

4

Milan Malcho - Jozef Jandacka
Tadeas Ochodek - Jan Kolonicny

**CORRELATIONS FOR HEAT TRANSPORT
BY NATURAL CONVECTION
OF CYLINDRICAL SURFACES SITUATED
ONE ABOVE THE OTHER**

12

Andrej Gasparec - Milan Saga - Peter Pechac
**NUMERICAL MODELING OF FERRITE
MATERIAL IMPACT
ON THE EFFECTIVENESS
OF INDUCTION HEATING PROCESS**

18

Michal Holubcik - Radovan Nosek
Katarína Sulovcova - Roman Weber
**FACTORS AFFECTING EMISSION
CONCENTRATIONS IN SMALL HEAT
SOURCES**

25

Jozef Broncek - Peter Jankejech
Peter Fabian - Norbert Radek
**INFLUENCE OF MECHANICAL
ANISOTROPY IN LOW CARBON
MICROALLOYED STEEL**

31

Jan Dizo - Miroslav Blatnický - Blanka Skocilasova
**COMPUTATIONAL MODELLING
OF THE RAIL VEHICLE MULTIBODY
SYSTEM INCLUDING FLEXIBLE BODIES**

37

Milan Zmindak - Leszek Radziszewski
Zoran Pelagic - Milos Falat
**FEM/BEM TECHNIQUES FOR MODELLING
OF LOCAL FIELDS IN CONTACT
MECHANICS**

47

Frantisek Brumerčik - Maria Tomasikova
Aleksander Nieoczym

EPICYCLIC GEAR TRAIN SYNTHESIS

51

Milan Zmindak - Zoran Pelagic - Martin Nagel
Lukas Smetanka - Zuzana Stankovicova
**SIMULATION MODELING OF BARREL
BORE WEAR UNDER DYNAMIC
PRESSURE LOAD**

57

Miroslav Neslusan - Tomas Hrabovsky
Maria Cillikova - Anna Micietova
**BARKHAUSEN NOISE EMISSION
IN MILLED SURFACES**

62

Libor Trsko - Otakar Bokuvka - Peter Palcek
Frantisek Novy - Katarina Mikova
**FATIGUE RESISTANCE OF C30
STRUCTURAL STEEL**

67

Pavel Kopeček - Milan Pinte
HOW TO SUPPLY ASSEMBLY LINES

72

Martin Krajcovic - Viktor Hancinsky
**PRODUCTION LAYOUT PLANNING USING
GENETIC ALGORITHMS**

78

Peter Bubenik - Filip Horak - Viktor Hancinsky
**ACQUIRING KNOWLEDGE NEEDED FOR
PULL PRODUCTION SYSTEM DESIGN
THROUGH DATA MINING METHODS**

83

Helena Samajova - Tongxing Li
OSCILLATORS NEAR HOPF BIFURCATION

88

Frantisek Brumerčik - Michal Lukac
Aleksander Nieoczym
**MECHANICAL DIFFERENTIAL
MATHEMATICAL MODEL**

COMMUNICATIONS

92

Maria Zihalova - Dana Bolibruchova - Dalibor Vojtech
**INFLUENCE OF VANADIUM AND
CHROMIUM ADDITION ON MORPHOLOGY
AND COMPOSITION OF IRON BASED
PHASES IN AlSi10MgMn ALLOY**

98

Radoslav Konar - Milos Mician
Jozef Mesko - Michal Sventek
**IDENTIFICATION OF LACK
OF FUSION AND PENETRATION
IN CIRCUMFERENTIAL FILLET WELD
BY PHASED ARRAY ULTRASONIC
METHOD IN GAS INDUSTRY**

103

Andrej Novak - Maria Mrazova
**RESEARCH OF PHYSIOLOGICAL FACTORS
AFFECTING PILOT PERFORMANCE
IN FLIGHT SIMULATION TRAINING
DEVICE**

108

Karol Grondzak - Juraj Branicky
ON THE OPTIMAL PIN SET GENERATION

113

Lukas Holesa - Karol Hrudkay
**THE IMPACT OF SELECTED FACTORS
OF UTILITY MOTOR VEHICLES
OPERATION CONDITIONS
ON THE ECONOMY DRIVING**

119

Jan Bitta - Irena Pavlikova - Ondrej Zavila
Pavel Platos - Jose Maria Caridad y Ocerin
**DOMINANT AIR POLLUTION SOURCE
DETERMINATION IN THE VICINITY
OF COKING PLANT BASED ON
STATISTICAL DATA ANALYSIS**



Dear Readers,

The core theme of the ongoing World EXPO 2015 in Milan (May 1 - October 31, 2015) is "Feeding the Planet, Energy for Life". Although the central theme focuses on nutrition of mankind, the attention is also paid to other related topics, namely environmental protection and natural biological task associated with a sustainable life.

The Slovakia Pavilion presents an incredible variety of countryside, from local traditions up to modern Slovak technologies. The Pavilion embodies a lively, dynamic country full of positive energy. The concept is made up of three pillars:

- *diversity - Slovakia is a country with diverse cultures, history, landscape and experience;*
- *symbiotic synergy - the mentioned diversity is a symbiotic synergy of the modern and traditional as well as local and global;*
- *positive energy - Slovakia is a country full of positive energy where everybody can "recharge their batteries".*

Energy, including also energy for life, is the measure of all forms of mass motion. In the isolated physical system the total energy does not change (the first law of thermodynamics), it is not the function of time, i.e. it can neither be created nor destroyed; it only changes its form.

Energy for life is closely associated with a general problem of energy usage, its conversion not only in relation with health and health risks but also with environmental factors having impact on biochemical changes.

The papers included in this volume of the Scientific Letters of Zilina University deal with the general idea of energy for life. Though, they offer concrete innovative solutions featuring a positive approach to the environment and sustainable life. The journal not only presents papers closely related to energy - its transfer, saving and impact of its conversion on the environment but also articles dealing with exergy as a convertible part of energy. Some articles pay attention to the modelling of processes connected with design and operation of products of engineering manufacturing. There are a few articles aimed at theoretical solutions of some problems not only in engineering but also in related branches. I hope you will find them interesting and motivating.

Vladimír Hlavna

Milan Malcho - Jozef Jandacka - Tadeas Ochodek - Jan Kolonicny *

CORRELATIONS FOR HEAT TRANSPORT BY NATURAL CONVECTION OF CYLINDRICAL SURFACES SITUATED ONE ABOVE THE OTHER

The paper presents a new criterion equation for calculating the Nusselt number for heat transport by natural convection from different numbers of cylindrical surfaces of heating sources. Horizontal cylindrical surfaces are situated one above the other and each of them is independently electrically heated by constant power output of Joule heating. Correlation relationships were derived on the basis of tens of measurements of heat outputs of the system of electrically heated horizontal cylindrical surfaces in a thermostatic chamber under defined conditions. The number of cylindrical surfaces, their distance and heat output to the horizontal cylinder varied during measurements. The derived criterion equation is significantly simpler compared to equations corrected by polynomial regression.

Keywords: Natural convection, cylindrical surfaces one above the other, criterial equations.

1. Introduction

Not only when providing heat distribution in buildings but also in many other technical applications especially in electrotechnics when cooling is ensured, heat is transported from oriented heat transfer surfaces by natural convection. The most frequently used oriented heat transfer surfaces are vertical slabs and horizontal cylindrical sources situated one above the other. In most of the so far published contributions the attention has been paid to modifications of the criterial equation for heat transfer by natural convection from an individual cylinder placed individually in space. Experimental experience from visualisation of density fields around oriented heat transfer surfaces [1] and numerical simulation of thermal fields at heat transfer from pipe heat sources by means of the CFD method [2] showed that the flow in the vicinity of horizontal cylindrical surfaces that are situated higher, is intensively influenced by air stream generated by natural convection onto cylindrical surfaces situated lower. Thus all cylindrical surfaces are flown around by flow field which differs significantly from the flow field generated by one individual horizontal cylindrical heat transfer surface. This is why the criterion equation for natural convection from one individual cylindrical surface cannot be used for the system of horizontally oriented heat transfer surfaces situated one above the other. The equation needs to be modified for a bundle of heat transfer surfaces or to find, on the basis of measurements performed in the thermostatic chamber, a new criterion equation for a bundle

of pipes. It is also possible to obtain a database of necessary data on the basis of numerical experiments, for example in ANSYS Fluent code.

2. Natural convection from a horizontal cylinder

The boundary layer around the horizontal cylinder with a higher temperature than the ambient temperature begins to develop in its bottom area. Its thickness gradually increases until the layer having a stable form is created on the surface (Figs. 1 and 2). The density of the local Nusselt number is, with respect to the thickness of the boundary layer, the highest in the lowest part and the lowest in the upper part of the boundary layer. The flow around the cylindrical surface has a laminar character along the whole circumference with a greater thickness of the boundary layer.

To determine the average Nusselt number along the circumference of the horizontal cylinder where the characteristic dimension is its outer diameter d , a simple relation according to Morgan is often used. It has the following form:

$$\overline{Nu}_d = \frac{\overline{\alpha} d}{\lambda} = CRa_d^n, \quad (1)$$

where:

\overline{Nu}_d is average Nusselt number,
 $\overline{\alpha}$ is heat transfer coefficient [W/m².K],

* ¹Milan Malcho, ¹Jozef Jandacka, ²Tadeas Ochodek, ²Jan Kolonicny

¹Department of Power Engineering, Faculty of Mechanical Engineering, University of Zilina, Slovakia

²Energy Research Center, VSB - Technical University of Ostrava, Ostrava - Poruba, Czech Republic

E-mail: milan.malcho@fstroj.uniza.sk

d is characteristic dimension [m],
 λ is coefficient of thermal conductivity of liquid [W/m.K].

C constant and n exponent are different for a range of the Rayleigh criterion number Ra_d .

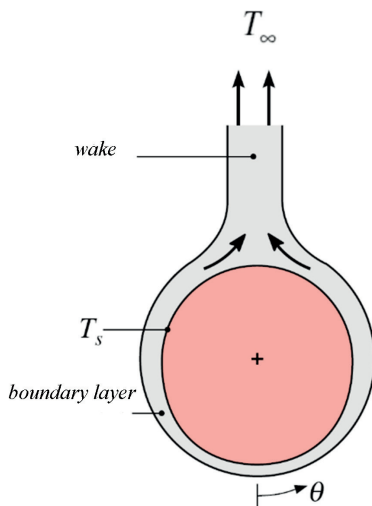


Fig. 1 Development of boundary layer in natural convection from the horizontal cylinder [2]

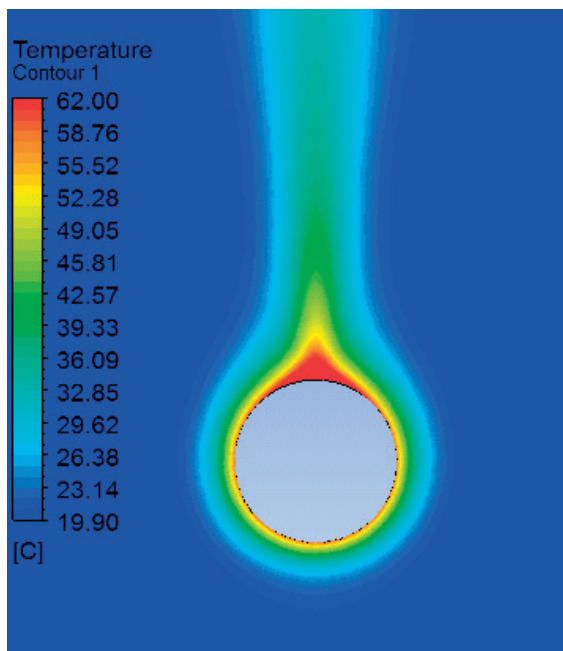


Fig. 2 Visualisation of the thermal field and boundary layer in natural convection from the horizontal cylinder (surface temperature 60.1°C; ambient temperature 20°C) gathered at simulation computations in ANSYS Fluent [3]

To compute the Nusselt number for a long horizontal cylinder and a wide range of the Rayleigh number, the relation according to Churchill-Chu [4] is recommended:

$$Nu_d = \left\{ 0.60 + \frac{0.387 Ra_d^{1/6}}{\left[1 + (0.559/Pr)^{9/16} \right]^{8/27}} \right\}^2$$

pre $10^{-5} < Ra_d < 10^{12}$, (2)

where:
 Pr is the Prandtl number.

For the range Ra_d of number the following relation holds for natural convection:

$$\overline{Nu}_d = 0.36 + \frac{0.518 Ra_d^{1/4}}{\left[1 + (0.559/Pr)^{9/16} \right]^{4/9}} .$$
 (3)

Past publications and research of natural convection from horizontal cylindrical heat transfer surfaces have not mentioned correlation relationships for the Nusselt number of the bundle of heat transfer surfaces which are most frequently used in heating and cooling technology and which would enable complex quantification of the total heat output of the bundle. The influence of pipe distance on the overall heat transfer in natural convection from the pipe bundle was analysed within the experiment by measurements of heat output of a model of a heating source consisting of 10 horizontal pipes having a diameter of 20 mm and length of 1000 mm [5].



Fig. 3 Arrangement of pipes in a thermostatic chamber at axial distance of pipes $1D$ [6]



Fig. 4 Arrangement of pipes in a thermostatic chamber at axial distance of pipes $5D$ [6]

An objective of analyses was to determine the impact of pipe distance on heat transfer from the pipe system and their impact on the overall heat output of the pipe bundle. The distances among the pipe walls were 0 mm (Fig. 3), 10 mm, 20 mm and 40 mm (Fig. 4). Measurements were done at temperature gradients $55\text{ }^{\circ}\text{C}/45\text{ }^{\circ}\text{C}$, $75\text{ }^{\circ}\text{C}/65\text{ }^{\circ}\text{C}$, $85\text{ }^{\circ}\text{C}/75\text{ }^{\circ}\text{C}$, the ambient temperature of $20\text{ }^{\circ}\text{C}$. The measurement was compared with a CFD mathematical model of heat transport from the system of pipes situated one above the other.

An extensive set of numerical experiments in the field of heat transport by natural convection from oriented heat transfer surfaces was performed by Kapjor [6] and experiments were done by Annunziata D'Orazio [7]. From the gathered material Kapjor created a new criterion relation for the computation of the Nusselt number for natural convection from “ n ” horizontally arranged cylindrical surfaces situated one above the other by means of polynomial regression. In ANSYS Fluent code tens of heat transport simulations were performed from ten pipes having an outer diameter of 20 mm situated one above the other. The wall temperature was $30\text{ }^{\circ}\text{C}$, $45\text{ }^{\circ}\text{C}$, $60\text{ }^{\circ}\text{C}$, $75\text{ }^{\circ}\text{C}$, $90\text{ }^{\circ}\text{C}$, $105\text{ }^{\circ}\text{C}$ and ambient temperature $20\text{ }^{\circ}\text{C}$. It was expected that the heat output in natural convection from “ n ” horizontal pipes situated one above the other is dependent on dimensionless spacing H/D as well as on dimensionless variable T_{∞}/T_s . At approximation the least square method for the function of two variables was used. Approximation polynomial regressions of higher orders ($n > 5$) were computed from functional dependencies of the Nusselt number of the bundle of horizontal pipes in ratio H/D and T_{∞}/T_s .

Analytical solutions and experiments show that heat transfer by natural convection from any surface depends on the surface geometry, on its orientation as well as on distribution

of temperature on the surface and also on thermo physical characteristics of liquid.

Reference temperature, from which physical characteristics needed for computation are determined, is the average temperature of the boundary layer:

$$T_f = (T_s + T_{\infty})/2 \quad [^{\circ}\text{C}]. \quad (4)$$

The flow of liquid in natural convection can be unstable due to the occasionality of turbulence. This instability is caused by flow disturbances which gradually get stronger and laminar flow becomes turbulent. As already mentioned, the flow character in natural convection determines the criterion of the Rayleigh's Ra .

3. Measurement and thermal analysis of horizontal heating pipes situated one above the other

The measurement of heat flows of the bundle of horizontal heat transfer surfaces was performed in a thermostatic chamber. During measurements, the temperature of the chamber inner walls was controlled so that the reference value of air temperature in the chamber, which was measured by Vernon resistance thermometer PT-100 DIN 1/5, would be stationary $20 \pm 0.5\text{ }^{\circ}\text{C}$.

The thermostatic chamber is controlled by Siemens Systematic S7-300. Visualization D2000 is programmed to the regulation system to visualise the situation in the thermostatic chamber. It provides a fully automated control of the chamber and helps to achieve equilibrium conditions at different measurement requirements within the range of measurability range.

Other experiments performed in the thermostatic chamber were measurements of thermal outputs from various systems of vertical arrangement of horizontal heated cylinders placed one above the other with an objective to design a new form of criterion equation for the computation of the Nusselt number of such a bundle. To obtain output and thermal parameters necessary for the creation of a new criterion relationship on the basis of which it would be possible to quantify the thermal output from “ n ” vertically arranged horizontal heated cylinders placed one above the other in natural convection, the measurements in the thermostatic chamber together with simulation analyses in ANSYS Fluent were performed gradually on three, five and ten horizontal cylinders situated one above the other. The principle and method of measurement were similar to those used for measurement and analysis of thermal output from one heated horizontal cylinder.

The measurement in thermostatic chamber consisted of the measurement of thermal and output parameters from three, five and ten electrically heated horizontal cylinders placed one above the other.

Ten, five and three heated cylinders were horizontally fixed on the stand in the thermostatic chamber (Fig. 5). During



Fig. 5 The fixing of a) ten, b) five and c) three horizontal heated cylinders on the stand in thermostatic chamber

measurement each cylinder was heated by the same electric output. The distance among individual cylinders gradually changed from 20 mm to 100 mm, with a step of 20 mm. The changing distance was defined by ratio H/D . Ratio H/D represents a dimensionless distance among the cylinders (Fig. 6). The temperatures, the cylinders achieved after the supplied equal electric output, were measured.

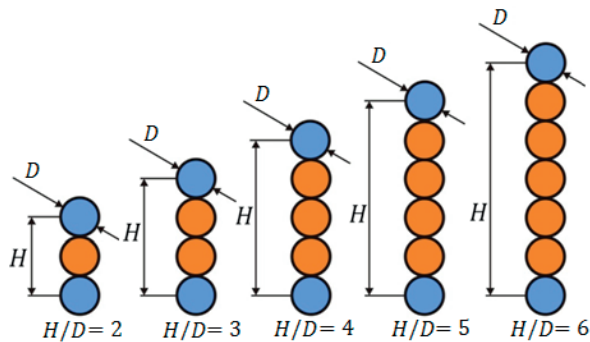


Fig. 6 Distance among individual cylinders in ratio H/D

Having connected all the heated cylinders to power sources, thermocouples to the central measuring station and having set all distances among individual cylinders, the measurements started. An objective of the measurements was to record surface temperatures of individual heated cylinders which changed due to changing distances among the individual cylinders with the supplied constant electric input. The reason why the experimental measurement was performed on bundles of ten, five and three horizontal heated cylinders is to obtain sufficient numbers of surface temperature values of individual cylinders for criterion numbers. It is obvious that at existing arrangements of pipe systems various thermal fields originate in the vicinity of the bundles. Due to thermal fields generated when arranging given bundles of cylinders, the surface temperatures of individual cylinders also change. The values are different for a bundle of

ten, five or three cylinders. This way a greater number of surface temperatures is obtained – data highly important for further analyses and final computations.

As obvious from the values of individual measurements shown in the previous tables, the change of distance among individual cylinders results in outstanding change of surface temperatures of horizontal heated cylinders situated one above the other. When the distance among cylinders is 20 mm and 40 mm (ratio $H/D=1$ and $H/D=2$), the surface temperatures of the cylinders increase. This growth of temperature is caused by the fact that a thermal field is formed in the vicinity of the cylinder, which influences the cylinder placed above; thus in the vicinity of the cylinder placed above a thermal field with a higher temperature is formed, which causes the increase of its surface temperature at the constant electric input. Changing the ratio $H/D=3$, at which the distance among individual cylinder gets the value of 60 mm, the growth of the surface temperature is lower as there is no more significant impact on the individual cylinders and the surface temperatures of cylinders do not tend to increase. From the values of surface temperatures of cylinders placed at the distance of 100 mm it is obvious that there is no influence of thermal fields from the heated cylinders situated above them. The heated cylinders thus obtain temperatures corresponding to the values which were recorded when measuring one heated cylinder.

Generated thermal fields near the individual bundles of cylinders that originate in heat transfer from their surfaces to environment and their interaction result in the already mentioned growth of surface temperature of individual cylinders. This phenomenon can be better seen in Fig. 7 which shows chosen visualisations of thermal fields gathered from simulation analyses from ANSYS Fluent around three, five and ten heater horizontal cylinders situated one above the other.

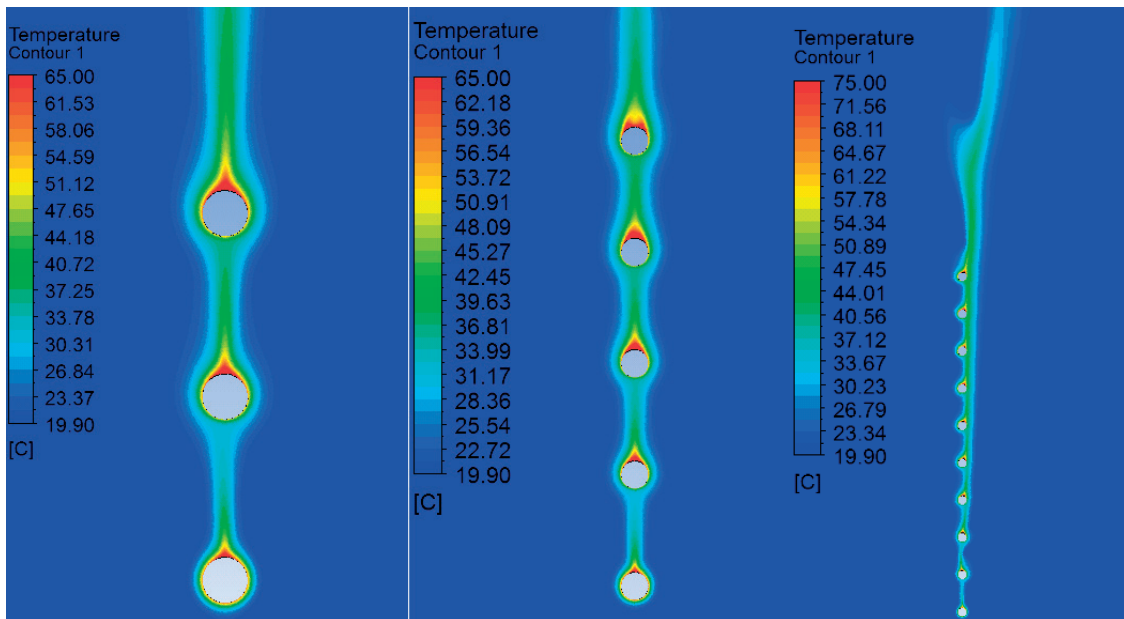


Fig. 7 CFD visualisations of thermal fields around bundles of heated horizontal cylinders (3, 5, 10) situated one above the other, with the initial temperature of a heated cylinder 60°C at the ambient temperature of 20°C and ratio $H/D = 4$

The new criterion relation for the Nusselt number, according to which thermal output can be quantified from “ n ” vertically arranged horizontal pipes placed one above the other in natural convection, was determined on the basis of data gathered from experimental measurements, simulation computations and analyses with the help of known mathematical methods. The criterion relation was formed on the basis of dimensional analysis with the help of a multiple linear regression.

4. Processing and analysis of data for creation of criterion relation

To create a new criterion relation for computing the Nusselt number from “ n ” vertically arranged horizontal pipes placed one above the other, processed and analysed data gathered from experimental measurements, simulation analyses and mathematical computations are used.

As already mentioned, the proposed criterion relation will be formed on the basis of dimensional analysis from measured and computed data with the help of a multiple linear regression in Microsoft Excel. In a general case, it will be an equation expressing physical dependence of n chosen relevant dimensionless quantities x_1, x_2, x_3 and x_4 in the form

$$y = b_0 \cdot x_1^{b_1} \cdot x_2^{b_2} \cdot x_3^{b_3} \cdot x_4^{b_4}, \quad (5)$$

where

y is an estimated value of the Nusselt number, $x_1 - x_n$ are values of independent variables, and $b_0 - b_4$ are regression coefficients.

Having logarithmized equation (5), it obtains the form (6)

$$\log y = \log b_0 + b_1 \log X_1 + b_2 \log X_2 + b_3 \log X_3 + b_4 \log X_4, \quad (6)$$

or (7)

$$z = a_0 + b_1 y_1 + b_2 y_2 + b_3 y_3 + b_4 y_4, \quad (7)$$

where the form is more suitable for the multi parametric linear regression. In its application various physical and geometric parameters were used as parameters X_1, X_2, X_3 and X_4 .

The following 4 dependent variable dimensionless quantities are assessed:

- changing distance among individual pipes - ratio $- H/D$,
- number of horizontal cylindrical surfaces - n ,
- Rayleigh number ($Ra = Gr \cdot Pr$) that includes changing temperatures of the wall temperatures to the ambient temperature through defining the average temperature difference Δt_{str} ,
- ratio of the ambient Prandtl number for the ambient non-influenced by temperature and the Prandtl number for surface temperature of one pipe - Pr/Pr_s whose value influences the thickness of boundary layers.

The regression constant b_0 and regression coefficients $b_1 - b_4$ were obtained through specific functions for multi parametric regression in a table processor MICROSOFT EXCEL. The values of standard deviation σ and correlation index R were also set. The standard deviation simply gives the average difference between a computed and real value of the Nusselt number. The reliability

of computed results obtained through correlation is given by the value of correlation index R . If this value exceeds 0.7, the results are generally acceptable; if this value exceeds 0.8, the results are good; if this value is higher than 0.9, the results are excellent.

After the analysis of the achieved results and their consequent processing we came to conclusion that the value of the Nusselt number from “ n ” vertically arranged horizontal pipes placed one above the other is mainly dependent on the changing distance among individual pipes, that is, on a dimensionless parameter, on the ratio H/D , on the number of heating pipes n , and also on the change of individual pipes situated one above the other. This change of surface temperatures is characterised by the average value of temperature difference Δt_{str} obtained from all the heating pipes. The values Δt_{str} are obtained from individual types of arrangements, from bundles of three, five and ten heating pipes. The ratio (Pr/Pr_s) contains the influence of temperature taken on the first pipe wall on the heat transfer from the bundle of pipes in which the value Pr was determined from ambient parameters and the value Pr_s from the temperature of the first bottom pipe wall.

Owing to heat transfer by natural convection, the determining parameter was the criterion number $Ra = Gr \cdot Pr$ whose values were computed similarly as in the case of natural convection from one pipe at $Ra = Gr \cdot Pr < 10^8$.

The multiple linear regression was done for two types of obtained values:

- For values obtained from simulation computations in ANSYS Fluent,
- For values obtained from experimental measurements in the thermostatic chamber.

From the values obtained from simulation computations in ANSYS Fluent, we processed data by the multiple regression in Microsoft Excel. On their basis we created the equation which, having been delogarithmized, gained the form

$$Nu = 32.25 \cdot (H/D)^{0.16} \cdot n^{-0.03} \cdot Ra^{-0.27} \cdot (Pr/Pr_s)^{-65.5} \quad (8)$$

Constant b_0 , regression coefficients $b_1 - b_4$, standard deviation σ and correlation index R have following values:

b_0	b_1	b_2	b_3	b_4	R	S
32.25	0.16	-0.03	-0.27	-65.5	0.9101	0.0212

Figures 8a - 8d show comparison of values of the Nusselt number computed according to the obtained equation (8) with the values computed from simulation results for individual bundles of pipes.

In a similar way we did computation from the values obtained from measurements on experimental device in the thermostatic chamber. The computation was done in Microsoft Excel through the multiple linear regression.

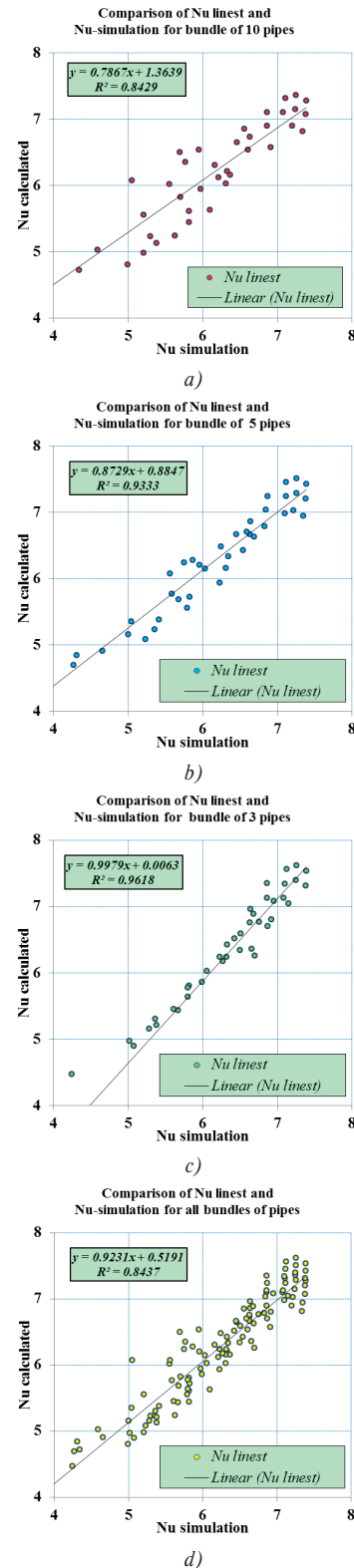


Fig. 8 Comparison of computed and simulated values of the Nusselt number for bundles of ten, five, three and all heated cylinders

The resultant criterion equation for natural convection from the bundle of pipes has the form

$$Nu = 4.705 \cdot (H/D)^{0.14} \cdot n^{-0.02} \cdot Ra^{-0.03} \cdot (Pr/Pr_s)^{-29} \quad (9)$$

For the constant b_0 , regression coefficients $b_1 - b_4$, standard deviation σ and correlation index R following values hold:

b_0	b_1	b_2	b_3	b_4	R	S
4.705	0.14	-0.02	-0.03	-29	0.958	0.0117

Figures 9a - 9d show comparison of values of the Nusselt number computed according to the obtained equation (9) with the values computed from measured results for individual bundles of pipes.

5. Conclusion

From the performed analyses follows that the criterion equation for a bundle of horizontal pipes regularly situated

vertically one above the other, proposed on the basis of a set of measured data shows a better correlation than the criterion equation determined from the data obtained from a numerical experiment by the CFD method.

A cause may be that the CFD model of natural turbulence captures only one shape of the flow field above the pipes (an image of current distribution of flow and thermal field). These fields are markedly non-stationary especially in the upper part of the bundle and change their shape so that the CFD method does not catch their average parameters in time. When measuring determining parameters, the temperatures of surfaces and air are naturally averaged in time due to thermal accumulation of pipes and sensors. Further averaging can be achieved through processing a greater number of data recorded by the central measuring station to a table process.

Comparing the criterion equation for heat transfer in natural convection on an individual horizontal pipe proposed according to Michejev in the form

$$Nu_1 = 0.5(Gr \cdot Pr)^{0.25} \cdot (Pr/Pr_s)^{0.25} \quad (10)$$

for $10^3 < Gr \cdot Pr < 10^6$,

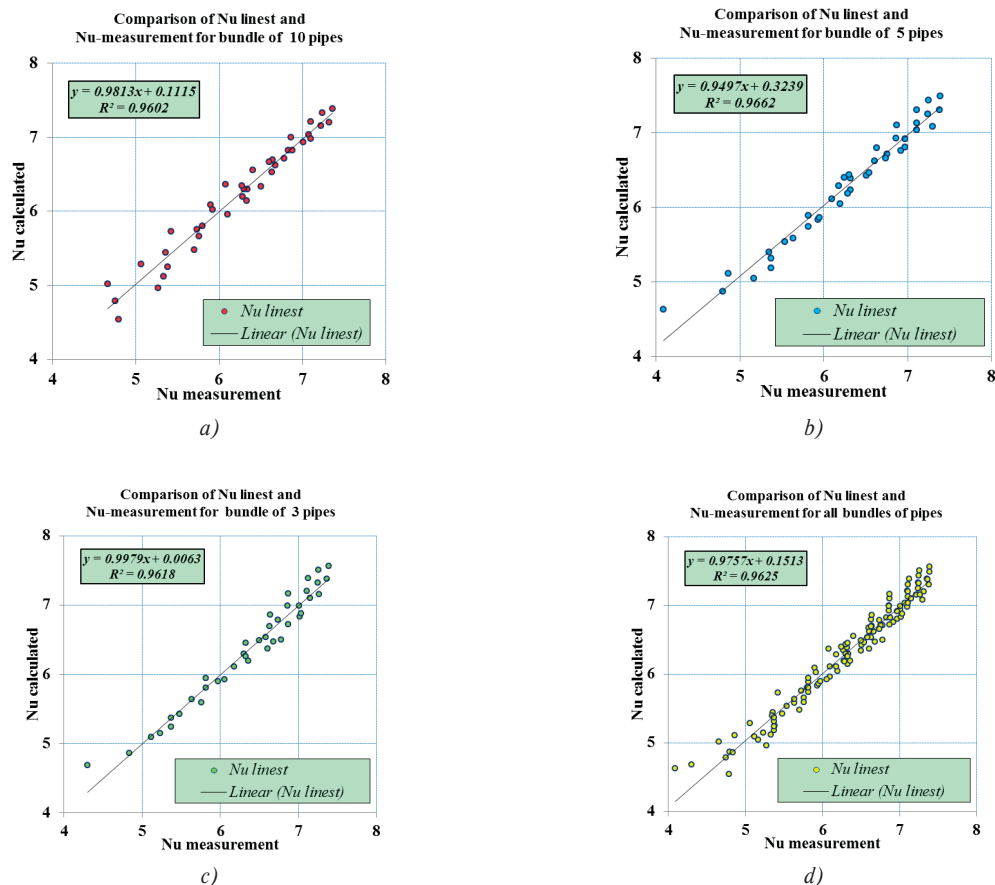


Fig. 9 Comparison of computed and measured values of the Nusselt number for bundles of ten, five, three and all heated cylinders

or a proposed relation according to Morgan in the form

$$Nu_1 = 0.48(Ra)^{0.25} \text{ for } 10^4 < Gr \cdot Pr < 10^7, \quad (11)$$

then for heat transfer of the bundle of horizontal cylinders vertically arranged one above the other a criterial equation can be proposed in the form:

$$Nu_{bundle} = Nu_1 \cdot f\{(H/D), n, Ra, (Pr/Pr_s)\}, \quad (12)$$

where for the relation of the first pipe according to Morgan, the resultant equation has the form

$$Nu_{bundle} = Nu_1 \cdot 9.8 \cdot (Gr \cdot Pr)^{-0.28} \cdot (H/D)^{0.14} \cdot n^{-0.02} \cdot (Pr/Pr_s)^{-29}. \quad (13)$$

The obtained forms of criterion equation are significantly simpler than equations with polynomial corrections at a good approximation of the Nusselt number determined from experimental measurements.

Acknowledgement

This paper has been elaborated in the framework of the project "Support of research and development in the Moravian-Silesian Region 2013 DT 1 - International research teams" (02613/2013/RRC). Financed from the budget of the Moravian-Silesian Region.



References

- [1] MARTYNYENKO, O. G., KHRAMTSON, P. P.: *Free - Convective Heat Transfer*. Springer : New York, 2005, ISBN - 10 3-540-25001-8.
- [2] GRESSAK, T., KAPJOR, A., HUZVAR, J., JANDACKA, J., MALCHO, M.: *Influence of Design Parameters of Floor Convector on its Performance*. Intern. Congress on Engineering and Technology - ICET, June 2013, Dubrovnik, 2013, ISBN 978-80-87670-08-8, pp. 153-158.
- [3] INCROPERA, F. P., DEWITT, D. P., BERGMAN, T. L., LAVINE, A.: *Fundamentals of Heat and Mass Transfer*. 6th ed., John Wiley : New York, 2007.
- [4] CHURCHILL, S. W., CHU, H. H. S.: Correlating Equations for Laminar and Turbulent free Convection from a Horizontal Cylinder. *Int. J. Heat Mass Transfer*, 18, 1049-1053, 1975.
- [5] SMATANOVA, H., JANDACKA, J., MALCHO, M., KAPJOR, A.: The Influence of Construction of a Ladder Heat Source on its Thermal Output (in Slovak), *Strojarnstvo-Strojirenstvi*, 6, 2009, extra edition, Kosice, p. 244, ISSN 1335-2938.
- [6] SMATANOVA, H., KAPJOR, A., HUZVAR, J., GRESSAK, T.: *Determination of the Maximum Heat Output of a Pipe Heat Source HDR 12 by a CFD Method (in Slovak)*, 32nd Session of Departments of liquid mechanics and thermomechanics, June 2013, Tatranska Lomnica : Zilina : Zilinska univerzita, 2013, ISBN 978-80-554-0715-9, pp. 73-76.
- [7] D'ORAZIO A., FONTANA L.: Experimental Study of Free Convection from a Pair of Vertical Arrays of Horizontal Cylinders at Very Low Rayleigh Numbers. *Intern. J. of Heat and Mass Transfer*, vol. 53, No. 15-16, July 2010, pp. 3131-3142. Available at: <<http://www.sciencedirect.com/science/article/pii/S001793101000147X> ISSN: 0017-9310.

Andrej Gasparec - Milan Saga - Peter Pechac *

NUMERICAL MODELING OF FERRITE MATERIAL IMPACT ON THE EFFECTIVENESS OF INDUCTION HEATING PROCESS

The article deals with numerical simulation of induction heating process as a coupling of electromagnetism and heat transfer. The article presents how the surrounding materials used in the induction heating process influence the resulting temperature. The scope of the article is to show impact of ferrite material on the resulting temperature of induction heating process.

Keywords: Induction heating, finite element method, electromagnetic field analysis, thermal analysis, Joule heat, Maxwell's equations.

1. Introduction

Induction heating has been used in industry over the past three decades. Due to its rapid heating and good reproducibility it is used in heat treatment as well as in applications for special use in mechanical engineering and chemical industry. Induction heating is a non-contact method of heating an electrically conductive material by the process of electromagnetic induction [1]. In a thin layer on the surface of parts alternating electromagnetic field generates currents which are called eddy currents [2]. Eddy currents generate heat due to resistive power losses, which are the main source of heat in the process of induction heating. The induction heating process is dependent on the electrical conductivity of the material, the size of the current in the inductor, the frequency of the applied electromagnetic field and the magnetic properties of the material [3]. Numerical modeling of induction heating allows the optimization of process variables. Using the finite element method, it is possible to calculate the temperature distribution across all components which are exposed to the induction heat. It is thus possible to optimize various process parameters. Induction heating can be addressed as coupling of the electromagnetic and thermal problem [1].

In the following chapters are summarized the fundamental equations and their simplification which are used to describe the physical behavior of materials under electromagnetic and thermal fields.

2. Electromagnetism equations

An electromagnetic field describes a set of equations known as Maxwell's equations. Equations consist of Faraday's law and Ampere's law with Maxwell extension.

The equations contain four different variables, the intensity of the electric field E , magnetic induction B , the intensity of the magnetic field H and the electric induction D [4].

Maxwell's equations are expressed as follows [5 and 4]:

$$\nabla \times E = -\frac{\partial B}{\partial t}, \quad (1)$$

$$\nabla \times H = J + \frac{\partial D}{\partial t}, \quad (2)$$

$$\nabla \cdot B = 0, \quad (3)$$

$$\nabla \cdot D = \rho. \quad (4)$$

where J is the current density, t is the time and ρ is the free volume charge density.

Constitutive relations between fields in a homogeneous isotropic environment are expressed as follows [5 and 4]

$$B = \mu H, \quad (5)$$

$$D = \varepsilon E, \quad (6)$$

$$J = \sigma E, \quad (7)$$

where μ is the permeability, ε is the permittivity of the dielectric and σ is the conductivity of the material.

We assume a harmonious solution to the sinus wave. In addition to these relations there is a vector of magnetic potential A in the following relation to

$$B = \nabla \times A. \quad (8)$$

* Andrej Gasparec, Milan Saga, Peter Pechac
Faculty of Mechanical Engineering, University of Zilina, Slovakia
E-mail: milan.saga@fstroj.uniza.sk

Maxwell's equations can then be written by diffusion equation as follows

$$\sigma \frac{\partial A}{\partial t} - \frac{1}{\mu} \nabla^2 A = J_s, \quad (9)$$

where J_s is the source current density in the inductor.

The diffusion equation (9) can be expressed in the same form for the electric and the magnetic field. In the case of the magnetic vector potential, it can be used in conjunction with any physically noticeable phenomenon of electromagnetic induction, as well as eddy currents induced voltage, inductor impedance, inductor induction. If the current stream as well as eddy currents are considered to be a sinus, and also time-harmonic, electromagnetic fields may be introduced by the following equation [6 and 7]

$$j\omega\sigma A - \frac{1}{\mu} \nabla^2 A = J_s. \quad (10)$$

Depending on the electrical and magnetic properties, there can be intermittent or continuous electromagnetic fields on each side of a common interface between two different materials.

At the interface between two media, the field must meet the following boundary conditions [4, 8 and 9]:

$$\hat{n} \times (E_1 - E_2) = 0, \quad (11)$$

$$\hat{n} \times (D_1 - D_2) = \sigma, \quad (12)$$

$$\hat{n} \times (H_1 - H_2) = J_s, \quad (13)$$

$$\hat{n} \times (B_1 - B_2) = 0. \quad (14)$$

The domain border is given by the normal unit vector \hat{n} and is directed from the surface normal of the surface 2 to surface 1 [10 and 11].

Boundary conditions can also be formulated in words such as:

- Components of the electric field are tangentially continuous through the interface of media 1 and 2.
- The electric flux component is interrupted through an interface with the size ρ for the electrically conductive medium, $\rho = 0$.
- The tangential components of the magnetic field intensity are disjointed via two media with size J_s . In the case of a zero surface current and if the medium has final conductivity, the tangential component is continuous [4 and 5].
- Normal component of magnetic flux density is continuous across the interface of media 1 and 2.

3. Heat transfer equations

The formulation of the problem of the energy balance is based on the first thermodynamics law [10]. When dealing with a heat

non-stationary event it is necessary to determine the dependence of temperature and the quantity of heat depending on the time for any point of the body. The first law of thermodynamics, heat transfer is characterized by this dependence, which is described by the following equation [12 and 13]:

$$\rho c \frac{\partial T}{\partial t} - \nabla \cdot (k \nabla T) = Q, \quad (15)$$

where ρ is the density, c is the specific heat capacity, thermal conductivity k , and Q is the heat generated in the material per unit of volume and time. Heat transfer equation (15) specifies the layout of the temperature in the environment as a function of time and space [14 and 15]. In the case that the temperature distribution is known, it is possible to calculate the heat flux (15) according to the equation inside the body or on its surface. The solution of the equation of heat conduction requires initial and boundary conditions. The boundary condition may be prescribed by a known temperature at the border or by prescribing heat flux using the flux or radiation [16].

The condition of the heat flux at the border can be defined by the relationship

$$q_n = -k \frac{\partial T}{\partial n}, \quad (16)$$

where n is normal to the surface towards the outside and q_n is a constant heat flux defined by

$$q_n = h(T_s - T_\infty)^\alpha + \sigma \epsilon [(T_s)^4 - (T_\infty)^4], \quad (17)$$

where h is the convection surface heat transfer coefficient, T_s is the surface temperature and T_∞ is the ambient temperature.

The first part of the boundary condition represents convective heat transfer and the second part of boundary condition (17) represents radiation.

Suppose that the temperature changes on the surface of the material in the sinusoidal mode. Then it can be shown that the amplitude of the changes will be smaller with increasing depth and with a certain time lag, i.e. the phase angle. If the temperature increases, the frequency attenuation and phase angle will increase [6 and 2]. This is the same phenomenon as in the case of electromagnetic waves, but in a different time scale because the electromagnetic field has a much shorter relaxation time.

In spite of the fact that the diffusion equation (10) has the same properties as heat conduction equation (15), their scales are different. Harmonic current in the device for induction heating is usually applied in the frequency range 50 Hz - 70 kHz. For this reason, the use of equation (10) can increase the thermal analysis at each time because the time scale of the electromagnetic problem is much shorter. This assumption is used in the numerical simulation of the solutions strategy [6 and 2].

4. Coupling of electromagnetic and thermal problem

The practical problem associated with the heat transfer is not usually possible to solve analytically, and especially if it has temperature-dependent and non-linear material properties. The current approach to getting a solution for these problems is to use the finite element method. The aim is to calculate temperature field distribution in the body on which it is applied harmoniously through oscillating current in the inductor.

It is possible to calculate magnetic vector potential from the equation (10). Eddy current J_e generated in the body is then calculated using the following relation [2, 3 and 9]

$$J_e = -j\omega\sigma A. \quad (18)$$

The source of the heat in the equation of heat conduction (15) is expressed by [3, 9 and 17]

$$Q = \frac{1}{2\sigma} |J_e|^2 = \frac{1}{2\sigma} J_e \cdot J_e^* \quad (19)$$

where J_e^* is the complex conjugate of the J_e .

At the external border area the magnetic vector potential is chosen so that it is zero at the interface (Dirichlet condition). From the equation (10) we can see that the magnetic vector potential is a long-term solution, a solution in which the characteristics of the material of the time step used the t_n . This is due to the fact that the time scale of the electromagnetic problem is much shorter than the thermal problem.

Figure 1 shows the strategy solutions in the time step. The problem is resolved using the material electromagnetic properties in the time step t_n . The thermal problem is calculated due to eddy currents in a time step t_{n+1} .

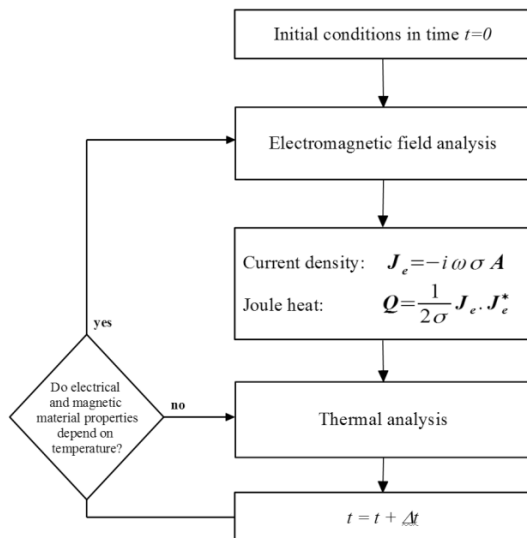


Fig. 1 Solution algorithm of coupling between electromagnetic and heat problem

5. Two dimensional model of coupled electromagnetic and thermal problem

Let us assume a general planar n-node element defined in the Cartesian nodal coordinate system $[x,y]$ [18].

For a finite n-node element is defined the interpolation of all calculated values in any point inside the element using values from the individual nodal points applying shape functions $N_i(x,y)$. For example, the temperature $T(x,y)$ in any point of element can be calculated by the following expression from element nodal temperatures T_i [13, 15 and 19]

$$T(x,y) = \sum_{i=1}^n T_i N_i(x,y). \quad (20)$$

Energy balance in the modeling area is dedicated to minimizing the energy functional in each node. This can be achieved by setting the first partial derivation of a functional in each node to zero. Instead of minimizing in each node, it is better to perform at the level of element.

The total energy associated to the entire modeling area is then equal to the sum of the energies of all the elements. As a result of the solution of algebraic equations of parallel system with respect to the magnitude of the magnetic vector potential gives an unknown value in each of the nodes. A set of equations can be written in the form

$$(V_e + jW_e) a_e = g_e, \quad (21)$$

where V_e and W_e are local matrices corresponding to finite element, a_e is the unknown vector of the magnetic vector potential of the corresponding finite element and g_e is the vector of the source current density of the corresponding finite element.

The other unknown quantities of the electromagnetic field are obtained using the following expressions [1, 3 and 9].

The intensity of the electric field E_z

$$E_z = -j\omega A_z. \quad (22)$$

Electric induction D_z

$$D_z = \epsilon_0 \epsilon_r E_z = -j\omega \epsilon_0 \epsilon_r A_z, \quad (23)$$

where ϵ_r is the relative permittivity and ϵ_0 is the vacuum permittivity.

Current density J_z

$$J_z = \sigma E_z + j\omega D_z = -j\sigma\omega A_z + \omega\epsilon_0 \epsilon_r A_z. \quad (24)$$

Joule heat Q_{AV}

$$Q_{AV} = \frac{1}{2} \text{real}(J_z \cdot \dot{E}_z), \quad (25)$$

where \dot{E}_z is transposed and conjugated (change the sign of the imaginary part of the complex numbers, all the opposite of) the vector of nodal values of electric field intensity E_z .

By the thermal transient analysis it is possible to solve the system of equations for different time steps, which can be written as follows:

$$C_e \frac{\partial T}{\partial t} + K_e T_e = f_e. \quad (26)$$

Individual matrices and vectors of this system are defined by the following relations:

C_e , the specific heat matrix defined by

$$C_e = \int_{\Omega} \rho c_p N^T N d\Omega = t \rho c_p N^T N. \quad (27)$$

K_e is the heat conductivity matrix defined by expression

$$K = \int_{\Omega} B^T D B d\Omega + \int_{\Gamma} h N^T N d\Gamma. \quad (28)$$

D is the heat conduction coefficient matrix defined as

$$D = \begin{bmatrix} k_x & 0 \\ 0 & k_y \end{bmatrix}, \quad (29)$$

where k_x and k_y are heat conduction coefficients for each direction. N is the matrix of shape functions and Ω is the matrix of their derivations.

In the above mentioned integrals, the represents the volume of the finite element and the represents the boundary of the finite element.

The first integral of the heat transfer matrix (28) characterizes heat conduction and the second integral characterizes heat convection.

The vector on the right side (26) is defined by

$$f_e = \int_{\Omega} G N^T d\Omega - \int_{\Gamma} q N^T d\Gamma + \int_{\Gamma} h T_{\infty} N^T d\Gamma, \quad (30)$$

where the first integral is characterized by a heat source in the volume, the second integral is characterized by heat flux through the surface area and third integral is characterized by convection through the surface area [13 and 16].

Transient thermal analysis given by a system of equations (26) can be then rewritten as follows

$$C T^{n+1} = (C - \Delta t K) T^n + \Delta t f^n. \quad (31)$$

The solution of the system of equations (31) in the time step "n" is the nodal temperature in the time step "n+1".

The system of equations (31) is Euler's explicit time integration solutions method (Forward difference) [15 and 20].

6. Computational model

Consider two dimensional problem of electromagnetic heating process of six parallel inductors to steel plate specimen. Martensitic annealed stainless steel is used as material for specimens. The scope of the FE study is to observe how different relative permeability of ferrite core material influences final temperature of heated steel plate specimen. The comparison had been done by the same input parameters shown in Table 1.

Input parameters

Table 1

Current	300	[A]
Frequency	3500	[Hz]
Heating time	50	[s]
Initial temperature	293.15	[K]

The chosen configuration for FE study runs is shown in Figs. 2 and 3.

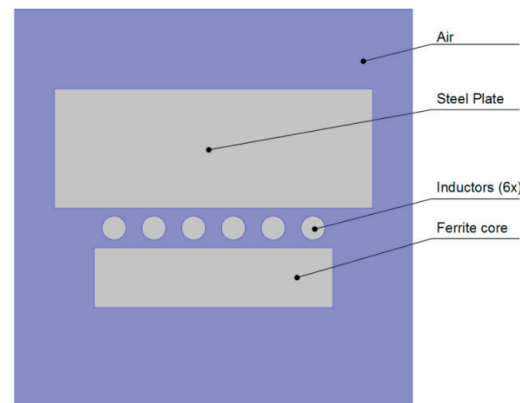


Fig. 2 Computational model

The model size and component dimensions are shown in Fig. 3.

The distances and diameter values are in millimeters [mm]. The length of the model in "z" direction is 100mm.

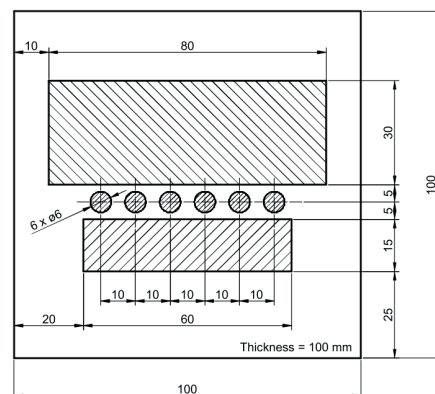


Fig. 3 Model size and component dimensions [mm]

Free triangular mesh with finer mesh in the areas with the highest value gradients in observed areas was chosen as the FE mesh shown in Fig. 4. The linear 3-node elements are used for interpolation [21].

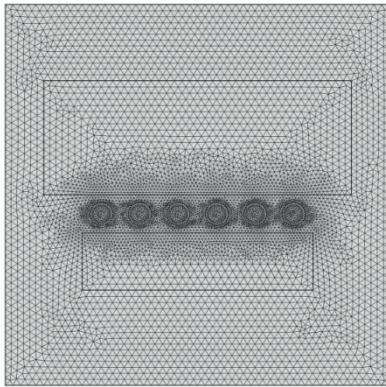


Fig. 4 Finite element mesh

Table 2 shows which material constants were used in FE studies. For the simplification, the constant material properties over the time were considered [22]. The relative permeability of ferrite core marked with (*) presents the range of the values used in FE runs.

The inductors were made of copper.

Material properties Table 2

Air	Material density	1.293	[kg/m ³]
	Specific heat	1.01 10 ³	[J/(kg K)]
	Thermal conductivity	26.0 10 ⁻³	[W/(m K)]
	Relative permeability	1.000 001 86	l
Copper	Material density	8930	[kg/m ³]
	Specific heat	340	[J/kg K]
	Thermal conductivity	384	[W/(m K)]
	Electrical resistance	1.7 10 ⁸	[ohm m]
	Relative permeability	0.999 99	l
Steel	Material density	7850	[kg/m ³]
	Specific heat	460	[J/(kg K)]
	Thermal conductivity	28	[W/(m K)]
	Electrical resistance	4.35 10 ⁻⁷	[ohm m]
	Relative permeability	1000	l
Ferrite	Material density	6600	[kg/m ³]
	Specific heat	700	[J/(kg K)]
	Thermal conductivity	20	[W/(m K)]
	Electrical resistance	50000	[ohm m]
	Relative permeability	1 to 100 (*)	l

7. Results

The scope of the numerical model is to calculate resulting temperature after certain heating time. Fig. 5 shows temperature distribution in [K] at 50s heating time and used ferrite core relative permeability value of 50 (*). Fig. 6 presents impact of ferrite material relative permeability resulting temperature of induction heating process.

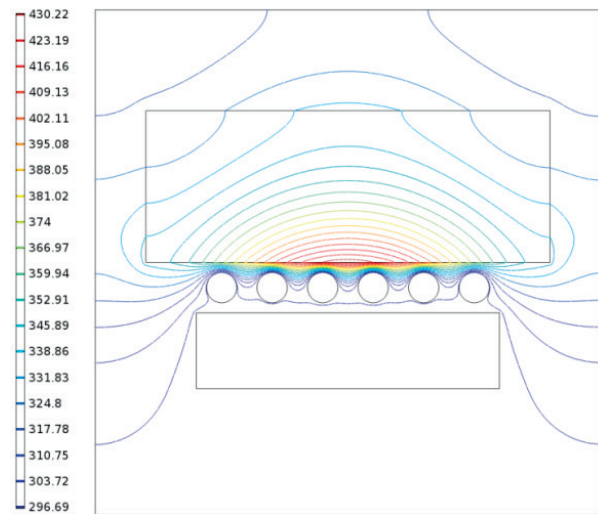


Fig. 5 Resulting temperature distribution at time 50s and ferrite core relative permeability value of 50(*)

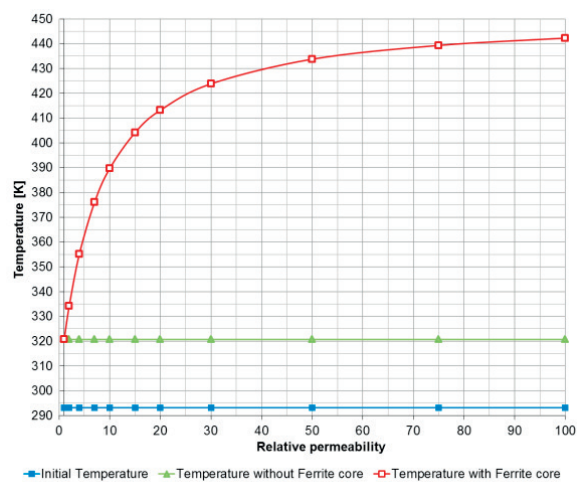


Fig. 6 Influence of ferrite core relative permeability (*) on resulting temperature of induction heating process

The red curve in Fig. 6 shows how relative permeability of ferrite core material influences the resulting temperature of heated material. The green line shows the resulting temperature of heated material without ferrite core. Both induction heating processes use the same process settings mentioned in Table 1.

8. Conclusion

In this article we applied equations of the electromagnetic and thermal field to solve problem of induction heating. The numerical simulation of induction heating process is shown as a coupling of electromagnetic and thermal problem leading to a system of thermal transient analysis by the explicit Euler method used in the time integration solutions.

By the FE solution of the electromagnetic and thermal problem it is possible to observe the effect of the individual variables related to electromagnetic induction as well as the resulting temperature or heat generated by the interaction of

the surrounding environments for different time steps. By this numerical approach we can observe how different material properties influence the resulting heat generated during the induction heating process and how the right combination of surrounding components influences the heating efficiency.

The numerical modeling of induction heating process allows optimization of the process parameters, material properties of components or geometry shape optimization.

Acknowledgements

This work has been supported by grant project VEGA No. 1/0234/13.

References

- [1] RUDNEV, V., LOVELESS, D., COOK, R., BLACK, M.: *Handbook of Induction Heating*. Inductoheat, Inc., 2003.
- [2] STOLL, R. L.: *The Analysis of Eddy Currents*. Oxford University Press : Oxford, 1974.
- [3] CLAIN, S., RAPPAZ, J., SWIERKOSZ, J., TOUZANI, R.: Numerical Modeling of Induction Heating for Two-dimensional Geometries. *Mathematical Models and Methods in Applied Sciences*, 3(6), 805-822, 1993.
- [4] STRATTON, J. A.: *Electromagnetic Theory*. IEEE Press : Piscataway, 2007.
- [5] KRISTENSSON, G.: *Elektromagnetisk vagutbredning*. Studentlitteratur, 1999.
- [6] HAMMOND, P.: *Applied Electromagnetism*. Pergamon Press : Oxford, 1985.
- [7] JIN, J.: *The Finite Element Method in Electromagnetics*, vol. 2, John Wiley & Sons, 2002.
- [8] DODD, C. V., DEEDS, W. E.: Analytical Solutions to Eddy-current Probecoil Problems. *J. of Applied Physics*, 39(6), 2829-2838, 1968.
- [9] CHABOUDEZ, C., CLAIN, S., GLARDON, R., MARI, D., RAPPAZ, J., SWIERKOSZ, M.: Numerical Modeling in Induction Heating for Axisymmetric Geometries. *Magnetics, IEEE Transactions*, 33(1), 739-745, 1997.
- [10] DAVIES, E. J.: *Conduction and Induction Heating*. No. 0-86341-174-6 in IEE Power Engineering Series 11. Peter Peregrinus Ltd. : London, 1990.
- [11] MATTEW, N., SADIKU, O.: *Elements of Electromagnetics*, vol. 3, Oxford University Press, 2001.
- [12] WANG, K. F., CHANDRASEKAR, S., HENRY, T., YANG, Y.: Finite-element Simulation of Induction Heat Treatment. *J. of Materials Engineering and Performance*, 1, 1992.
- [13] CARSLAW, H. S., JAEGER, J. C.: *Conduction of Heat in Solids, 2nd ed.*, Oxford University Press : Oxford, 1959.
- [14] CALLISTER, JR. W. D.: *Materials Science and Engineering: An Introduction*. John Wiley & Sons, 1999.
- [15] LEWIS, R. W., MORGAN, K., THOMAS, H. R., SEETHARAMU, K. N.: *The Finite Element Method in Heat Transfer Analysis*. John Wiley & Sons, 1996.
- [16] LEWIS, R. W., NITIRASU, P., SEETHARAMU, K. N.: *Fundamentals of the Finite Element Method for Heat and Fluid Flow*. Wiley : Chichester, 2004.
- [17] LABRIDIS, D., DOKOPOULO, P.: Calculation of Eddy Current Losses in Nonlinear Ferromagnetic Materials. *IEEE Transactions on Magnetics*, 25(3), May 1989.
- [18] JAKUBOVICOVA, L., KOPAS, P., HANDRIK, M., VASKO, M.: *Computational and Experimental Analysis of Torsion and Bending Loading of Specimen*. In-Tech 2010, September 2010, Prague, pp. 395-400.
- [19] ZMINDAK, M., NOVAK, P.: Particles Interactions in Composites Reinforced by Fibre and Spherical Inclusions. *Communications - Scientific Letters of the University of Zilina*, vol. 11, No. 2, pp. 13-18, 2009.
- [20] SAGA, M., VASKO, M.: Stress Sensitivity Analysis of the Beam and Shell Finite Elements. *Communications - Scientific Letters of the University of Zilina*, vol. 11, No. 2, 2009, pp. 5-12.
- [21] KWON, Y. W., BANG, H.: *The Finite Element Method using MATLAB*. CRC Press : University of Minnesota, 1996.
- [22] SAPIETOVA, A., DEKYS, V., VASKO, M.: A Numerical Modeling Rotating Machine Having Unbalance and the Measuring of its Dynamical Properties, *Metalurgija/Metallurgy*, vol. 492010, No. 2, pp. 503-507.

Michal Holubcik - Radovan Nosek - Katarína Sulovcova - Roman Weber *

FACTORS AFFECTING EMISSION CONCENTRATIONS IN SMALL HEAT SOURCES

Combustion of biomass fuel itself as a renewable energy source does not automatically ensure the best use of its energy content with low emission production. Biomass combustion with bad settings of combustion conditions can be ineffective and with a high production of emissions. The article discusses the impact of various aspects on the power and emission parameters of the heat source. The influence of the amount of combustion air, the temperature of combustion air, the relative humidity of combustion air, the fuel feeding and fuel moisture on thermal power and emission production in automatic boiler for combustion of wood pellets were specifically verified. The results show that appropriate setting of these aspects has an effect on concentration of emissions from the combustion of biomass.

Keywords: Emission, dendromass, temperature of combustion air, fuel moisture, air humidity.

1. Introduction

There is nowadays again great interest in more efficient use of energy because requirements for energy resources are ever increasing [1]. To enhance energy self-sufficiency, the increasing focus is on the improvement of power equipment efficiency and use of renewable energy sources [2 and 3]. One of the renewable energy sources is biomass.

1.1. Biomass combustion

One of the most commonly used forms of obtaining thermal energy from biomass is its direct combustion. There is possibility to burn wood in the form of logs, wood chips, briquettes and pellets, and also straw of cereals and oilseeds, energy plants in packages, briquettes and pellets [4]. The combustion of biomass fuel itself as a renewable energy source does not automatically ensure the best use of its energy content with low emission production [5]. Biomass combustion with bad settings of combustion conditions can be ineffective and with a high production of emissions.

Effective use of biomass by low-emission production requires the application of high quality technologies and their proper operation [6]. Biomass combustion in a heat source is influenced

by several aspects, e.g. type of fuel, the amount and distribution of combustion air, method of combustion, design and regulation of combustion appliance, etc. [7]. All those aspects influence the power and emission parameters of the heat source. Emissions are pollutants arising from the biomass combustion dispersed in the air. The basic emissions are carbon monoxide (CO), nitrogen oxides (NO_x), sulphur dioxide (SO₂), unburned products known as organic hydrocarbons (OGC) and particulate matters (PM) [8 and 9]. To maintain the environmental friendliness of biomass, states issue measures in the form of emission limits, which have to be respected [10].

1.2. The aim of the article

The article deals with the impact of various aspects on the power and emission parameters of the heat source. Special attention is paid to the verification of influence of the amount of combustion air, the temperature of combustion air, the relative humidity of combustion air, the fuel feeding and fuel moisture on thermal power and emission production in automatic boiler for combustion of wood pellets.

* ¹Michal Holubcik, ¹Radovan Nosek, ¹Katarína Sulovcova, ²Roman Weber

¹Department of Power Engineering, Faculty of Mechanical Engineering, University of Zilina, Slovakia

²Clausthal University of Technology, Institute of Energy Process Engineering and Fuel Technology, Clausthal-Zellerfeld, Germany

E-mail: michal.holubcik@fstroj.unizsa.sk

2. Methods for measuring thermo technical parameters of heat sources

2.1. Heat source

An automatic hot water boiler designed to burn wood pellets with a nominal heat output of 18 kW with a retort burner is used as a heat source. Fuel is supplied from a tightly closed container into the combustion chamber using a screw feeder. The air needed for combustion is forced through a fan into the intake system in the combustion chamber. The combustion of waste products takes place near the cast iron rectifier of flue gas. The regulatory control system of the boiler allows changing control algorithms where it is possible to change the amount of combustion air, operation time and standing time of the screw feeder for the fuel supply.

2.2. Used fuel

To minimise measurement mistakes during all the experiments, the fuel with the same properties was used. Wood pallets made from spruce sawdust without bark were used. The fuel was supplied by a company producing 2000 kg of biofuel per hour. The analysis of biofuels confirmed that the delivered wood pellets meet the specified requirements A1 in compliance with STN EN 14961-2 [11]. The pellet diameter was 6 mm and their length did not exceed 40 mm. The moisture content determined in compliance with STN EN 14774 [12] reached the value of 9.98%. The ash content determined in compliance with STN EN 14775 [13] reached the value of 0.452%. Mechanical resistance (DU) determined in compliance with STN EN 15210 [14] reached the value of 98.67%. The content of fine particles (F) determined in compliance with STN EN 15210 [14] reached the value of 0.239%. The calorific value determined in accordance with STN EN 14918 [15] reached the value of 17.58 MJ.kg⁻¹. The bulk density determined in accordance with STN EN 15103 [16] reached the value of 650 kg.m⁻³.

2.3. Measurement of thermal power of the heat source

Measurement of the heat source thermal power was performed on an experimental device for testing heat sources (Fig. 1) which consisted of the experimental heat source, equipment for heat consumption or regulation of heat produced by the hot water boiler, gaseous emission analyser, particulate matter analyser, logger connected with all the measuring devices which recorded the values every 20 seconds and a PC for evaluation of the measured data.

Thermal power of the heat source is determined in accordance with STN EN 303 - 5 [17]. Direct method, so called calorimetric method, was used to determine the thermal power of the heat

source. Thermal power is determined from the mass flow measured by a magnetic induction flow meter and from the temperature difference between outlet and inlet of heat transfer medium in the heat source measured by paired metal resistance thermometers PT100 according to equation [18]:

$$Q = m \cdot c_p \cdot (T_2 - T_1) \quad (1)$$

where Q is thermal power of heat source [kW], m is mass flow of heat transfer medium at the inlet and outlet [kg.s⁻¹], c_p is specific heat capacity of heat transfer medium [J.kg⁻¹.K⁻¹]. Specific heat capacity is dependent on the temperature of the heat transfer medium; T₁ is temperature of heat transfer medium at the outlet of heat source [K] and T₂ is temperature of heat transfer medium at the inlet of heat source [K]. During the determination of thermal power it was necessary to maintain the set temperature gradient by the temperature regulator. The regulating device consists of a heat exchanger, two circulation pumps controlled by frequency converters, two regulating valves and of control, regulatory and safety devices. During the measurements the constant chimney draft 12 ± 2 Pa was ensured with a flue fan. The flue fan speed was controlled by the frequency converter.

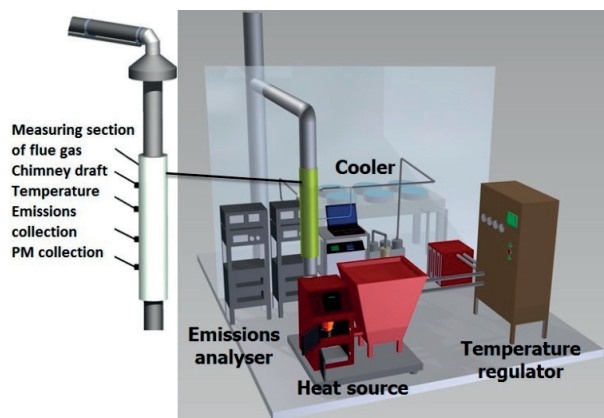


Fig. 1 Experimental device for testing heat sources

2.4. Measurement of emission production

The flue gases pass through the measuring section (Fig. 1) which is located in the flue system. In the measuring section of the flue gas the temperature measurement in the chimney, composition of the flue gases and chimney draft measurements were performed. The flue system is joined with an insulated flue gas measurement section. The production of CO and NO_x was determined by the flue gas analyser ABB AO 2020 [19]. The device works on the principle of infrared spectroscopy. The normalised oxygen concentration (O₂ standardised) in the flue gases from the central heat source has in accordance with

STN EN 303 - 5 [17] the value of 10%. The values of emission production were calculated based on the oxygen content in the flue gas according to the relation:

$$Y_{(10\% O_2)} = Y \cdot \frac{21 - O_{2\text{ standardised}}}{21 - O_{2\text{ avg}}} \quad (2)$$

where Y is the measured concentration of the emission [mg.m⁻³], $O_{2\text{ standardised}}$ is normalised oxygen concentration [%] and $O_{2\text{ avg}}$ is the average oxygen concentration in the flue gases[%].

3. Methodology for determining the influence of various aspects of the thermo - technical parameters of the heat source

3.1. Influence of the amount of combustion air

The tested boiler conception allowed regulating the amount of combustion air by the control system of the boiler via the fan speed controlled in the range of 10% - 100%. Regulation for fuel feeding was set at each measurement at the same value (18 seconds feeding and 25 seconds waiting time of the screw feeder) it means that fuel delivery was the same for all measurements.

The combustion air supplied by a fan in the area of retort burner was divided into primary and secondary combustion air. The amount of supplied air to the combustion process was measured by indirect method through an anemometer which measured the air flow velocity at inlet. Based on the velocity and flow section, the volume flow was calculated and, consequently, the mass flow of combustion air was calculated. Mass flow rate of combustion air supplied to the boiler reached the values ranging from 45 kg.h⁻¹ (for setting the fan at 10% of rated speed) to 142 kg.h⁻¹ (for setting the fan at 100% of rated speed).

3.2. Influence of the combustion air temperature

Combustion air temperature change was performed before entering the heat source. Combustion air supply was connected to the pipe with the heat exchanger which heats or cools supplied combustion air. The lowest supplied air temperature was -5°C and gradually increased in steps of 5°C to 40°C. Regulation for supply air temperature was set during measurement at the same value (18 seconds feeding and 25 seconds waiting time of the screw feeder, the fan was set at 40% of rated speed).

The heat exchanger was located behind the fan in a square duct made of steel sheet with service door. The heat exchanger was made of copper tubing with corrugated aluminium ribs used for better heat transfer. The size of aluminium ribs is 60 x 120 x 0.5 mm (v x d x h) with regular spacing 5 mm. The heat exchanger consists of four separate parts having the length of 170 mm. All four parts are connected by copper elbows into a single unit

while soldering is done by brazing. Inlet and outlet of heat from the heat exchanger is done by heat transfer medium - Thermal Glycol mixture with water in 1:1 ratio with solidification point -30 °C. Regulation of the fluid temperature was carried out by a circulating thermostat Julabo FP40 which was connected through the insulated pipe to the heat exchanger. The scheme of device for change of combustion air temperature is shown in Fig. 2.

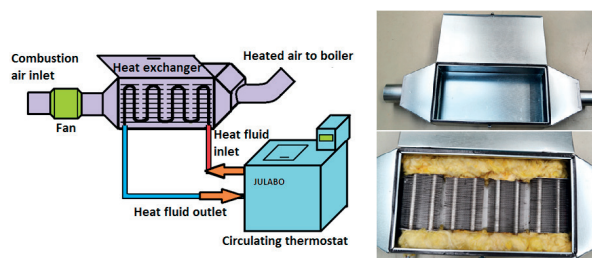


Fig. 2 The principle of combustion air heating

3.3. Influence of the relative humidity on combustion air

The relative humidity of combustion air was regulated in the polystyrene chamber with the following dimensions 1.5m x 1.0m x 1.0m (Fig. 3). Ambient air having a relative humidity 49% and temperature of 23°C was fed into the chamber. The water vapour was produced in a steam humidifier with the regulation of the relative humidity. The chamber was equipped with separating walls for more efficient mixing of ambient air with water vapour. The relative humidity of the combustion air was measured just before accession to the boiler and the examined values were as follows: 50%, 60%, 70%, 80%, 90% and 99%. The humidity of air progressed according to Mollier h-x diagram isothermally when to increase the relative humidity from 49% (at 23 °C) to 60% at a constant temperature, it was necessary to bring 2 g of water vapour per 1 kg of air. Combustion air temperature at the inlet to the heat source was the same as the temperature at the inlet to the polystyrene chamber.

Settings for the fuel supply and combustion air were the same for each measurement (18 seconds feeding, 25 seconds standing of the fuel conveyor, the fan was set at 40% of rated speed).



Fig. 3 The principle of combustion air humidification

Average values of combustion air mass flow, heat output, CO and NOx formation depending on the fan setting

Table 1

Fan settings	10%	20%	30%	40%	50%	60%	70%	80%	90%	100%
Mass flow rate [kg.h ⁻¹]	45	72	90	108	114	137	139	139	140	142
Thermal power [kW]	14.01	14.92	15.84	17.12	16.91	16.48	16.02	15.48	14.95	14.84
CO concentration [mg.m ⁻³]	9554	351	340	547	1328	1748	1697	1976	3330	3646
NOx concentration [mg.m ⁻³]	94	178	174	173	165	171	177	179	169	170

3.4. Effect of fuel moisture

In this section we investigated the influence of fuel humidity on thermo-technical parameters of the heat source; we did it by changing the humidity of fuel (wood pellets). Wood pellets with an initial moisture content of 9.98% were subsequently dried to a humidity of 0% and 5%; gradually adding water, the sample moisture content reached 10%, 15%, 20%, 25% and 30%. The individual samples were tested in automatic boilers for combustion of wood pellets in the same regulation setting of the boiler; fuel supply (18 seconds feeding, 25 seconds standing of the fuel conveyor) and supply of combustion air (fan was set at 40% of rated speed) remained the same during each measurement.

3.5. Influence of fuel feeding

Control of the heat output of small automatic heat sources was done by changing the time of both fuel feeding and combustion of supplied fuel. The recommended setting of fuel supply and combustion time is in many cases based on experience of manufacturers or on measurements of nominal and minimum performance of boiler during testing [20]. The user of the heat source has available variety of feeding and combustion time settings.

The tested automatic hot water boiler for burning wood pellets allows changing the operating time and the time of standing of the screw feeder for fuel supply. In the framework of the research three types of comparative measurements were carried out to determine the influence of fuel supply on thermo-technical parameters of the heat source. The first series of measurements was carried out at a constant time standing at 25 seconds and following time of fuel supply 18, 15, 12 and 9 seconds. The second series of measurements was carried out at a constant fuel supply of the 18 seconds and the standing times of 25, 28, 31 and 34 seconds. The third series of measurements was carried out at a constant time difference of 7 seconds between the time of fuel supply and standing time. The settings during the third measurements were as follows: 15/22 sec. (standing / supply), 18/25 sec., 20/27 sec. and 30/37 sec. The supply of combustion air was constant for all the measurements (the fan was set at 40% of rated speed).

4. Results of experiments

4.1. Amount of combustion air

Table 1 shows the average values of the combustion air mass flow, heat output, concentration of CO and NOx depending on the setting of the fan speed. The mass flow rate of combustion air increased proportionally to the increasing fan speed up to 60% of rated speed. The slightest increase in mass flow of the fan was recorded in the range of 60% to 100% of rated speed. Thermal power of the heat source increased with the fan speed to the value of 40%, subsequently it declined. The highest CO production was recorded at 10% of the fan speed which was caused by low excess air or incomplete combustion due to insufficient supply of oxygen to the flame.

The lowest CO concentrations were registered at the value of 20% and with the increasing amount of combustion air the CO formation increased as well. The NOx concentration was lowest in the minimum amount of combustion air, given by the small amount of nitrogen supplied to air and due to a lower temperature in the flame [21]. For other speeds the formation of NOx did not change much.

4.2. The temperature of combustion air

Table 2 shows the average values of heat power, concentration of CO and NOx depending on the temperature of combustion air. The boiler thermal power increased with the rising combustion air temperature due to the supply of certain energy into the warmer air. The CO concentration decreased with the increasing combustion air temperature due to a higher temperature in the combustion chamber and burning of CO to CO₂. The lowest NOx concentration was recorded at the lowest temperature of the combustion air; as the temperature raised the NOx formation increased. This was caused by high flame temperature when more NOx was formed [21 and 22].

Average values of heat output, CO and NOx formation depending on the combustion air temperature

Table 2

Combustion air temperature	-5 °C	0 °C	5 °C	10 °C	15 °C	20 °C	25 °C	30 °C	35 °C	40 °C
Thermal power [kW]	16.92	17.02	17.41	17.56	17.73	17.91	18.06	18.14	18.21	18.39
CO concentration [mg.m ⁻³]	468	537	511	487	479	421	436	396	409	378
NOx concentration [mg.m ⁻³]	154	159	158	164	173	171	178	181	183	187

4.3. Relative humidity of combustion air

Table 3 shows the average values of thermal power, CO and NOx formation depending on the relative humidity of combustion air. Higher humidity of combustion air caused the cooling of flame and it resulted in the reduction of thermal power. The experimental results also show that CO had a slightly rising trend. However, at 99% humidity the concentration of CO was more than seven times higher due to a lower flame temperature and imperfect combustion (less oxygen at the expense of the water vapour). From the results it can be seen that the NOx production is slightly decreasing with increasing air humidity caused by the cooling of the flame by water contained in the moist air. In the case of 99% air humidity the production of NOx decreased by more than 20%.

4.4. Effect of fuel moisture

Dependence of the average values of thermal power and emissions on fuel moisture is shown in Table 4. As expected, the boiler capacity decreased significantly with increasing moisture content of fuel due to a lower amount of flammable products in the humid fuel. In this case some energy was used to evaporate water during combustion. Table 3 shows that the CO production had increasing character with increasing moisture content of fuel. CO concentrations were 16 times higher at 30% moisture content of fuel compared to the combustion of dry fuel. This was due to imperfect mixing of fuel with an oxidant, creating

zones in the combustion chamber of the furnace with the lack of oxygen for total oxidation of the carbon, the instability of the temperature conditions in the combustion chamber of the furnace and temperature variations in the furnace because of the water content of the fuel. A significant decrease in NOx was observed with increasing moisture content of fuel due to the flame cooling by water contained in the wet fuel.

4.5. Influence of fuel feeding

Tables 5, 6 and 7 show the average values of thermal power, CO and NOx concentrations depending on the setting of fuel feeding. The measurements showed that the effect of setting the fuel feeding and fuel burning time (standing) had a major impact on the performance and emission parameters of the heat source. Reducing the time of fuel feeding at constant standing time had a linear effect on the heat output. The measurements of boiler at operating settings showed that the highest thermal performance was achieved in the following setting - 18/25 seconds (feeding/standing). The highest formation of CO was measured while achieving the maximum heat output of the heat source. For other settings of the boiler significantly lower concentrations of CO were measured. It follows that the nominal power would be needed to bring to the furnace higher amount of secondary air so as to deflagrate relatively large amounts of CO. The results of measuring the NOx concentration indicated that these are essentially constant and of relatively low value.

Average values of heat output, CO and NOx formation depending on the combustion air humidity

Table 3

Combustion air humidity	49%	50%	60%	70%	80%	90%	99%
Thermal power [kW]	16.91	16.90	16.8	16.6	16.5	16.4	16.2
CO concentration [mg.m ⁻³]	470	471	474	538	572	585	3381
NOx concentration [mg.m ⁻³]	320	319	317	315	312	309	252

Average values of heat output, CO and NOx formation depending on the fuel moisture

Table 4

Fuel moisture	0%	5%	10%	15%	20%	25%	30%
Thermal power [kW]	19.21	18.08	17.28	15.95	12.36	9.74	7.99
CO concentration [mg.m ⁻³]	268	322	355	784	1372	1978	4299
NOx concentration [mg.m ⁻³]	207	199	181	173	154	119	97

Average values of heat output, CO and NOx formation depending on the fuel supply Table 5

Fuel supply	18/25 s	15/25 s	12/25 s	9/25 s
Thermal power [kW]	17.93	15.42	11.91	9.24
CO concentration [mg.m ⁻³]	451	327	242	287
NOx concentration [mg.m ⁻³]	164	176	168	164

Table 6

Fuel supply	18/25 s	18/28 s	18/31 s	18/34 s
Thermal power [kW]	17.93	15.63	13.74	12.03
CO concentration [mg.m ⁻³]	451	283	224	235
NOx concentration [mg.m ⁻³]	164	171	172	169

Table 7

Fuel supply	15/22 s	18/25 s	20/27 s	30/37 s
Thermal power [kW]	15.54	17.93	15.87	14.26
CO concentration [mg.m ⁻³]	356	451	398	411
NOx concentration [mg.m ⁻³]	183	164	181	184

5. Conclusion

The results of experiments pointed out the fact that the combustion process can influence many aspects. Measurements show that these aspects affect the thermal performance of the heat source and the formation of CO and NOx. The obtained results (Fig. 4) show that the humidity of fuel has the highest impact on the combustion process. This factor significantly decreases the thermal power of the boiler and considerably increases the production of CO.

References

- [1] MESKO, J., FABIAN, P., HOPKO, A., KONAR, R.: Shape of Heat Source in Simulation Program SYSWELD using Different Types of Gases and Welding Methods. *Strojirenska tehnologija*, vol. 16, No. 5, 2011, 6-11.
- [2] KAPJOR, A., HUZVAR, J., FTOREK, B., VANTUCH, M.: Criterion Equations of Heat Transfer for “n” Horizontal Pipes one above another at Natural Convection in Linear Method of Approximation. *Communications - Scientific Letters of the University of Zilina*, vol. 16, No. 3A, 2014, 54-61.
- [3] PILAT, P., PATSCH, M., MALCHO, M.: *Solar Heat Utilization for Adsorption Cooling Device*, EPJ Web of Conferences, vol. 25, 2012.
- [4] CERNECKY, J., NEUPAUEROVA, A., JANOSKO, I., SOLDAN, M.: *Environmental Technology (in Slovak)*, Technicka univerzita Zvolen, 274 p., 2010.
- [5] DELIISKI, N., DZURENDA L., BREZIN V.: Calculation of the Heat Energy needed for Melting of the Ice in Wood Materials for Veneer Production, *Acta Facultatis Xylogologiae Zvolen* vol. 55, No. 2, 2013, 21-32.
- [6] SOOS, L., KOLEJAK, M., URBAN, F.: *Biomass - Renewable Energy Source (in Slovak)*, Vert: Bratislava, 2012.
- [7] HUZVAR, J., KAPJOR, A.: *Micro-cogeneration incl. the Conversion of Chemical Energy of Biomass to Electric Energy and the Low Potential Heat*, Proc. of AIP Conference, vol. 1337, 2011, 40-42.

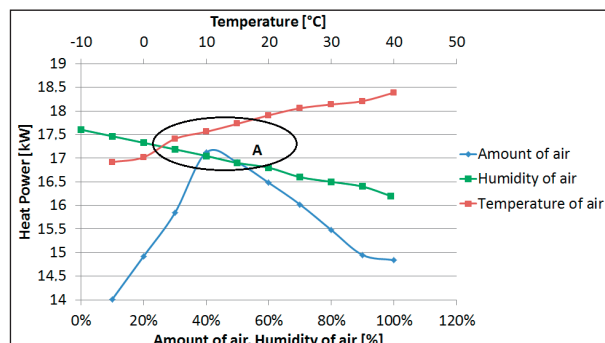


Fig. 4 Graph of thermal power dependence on different aspects (area A shows standard conditions of biomass combustion)

The amount of combustion air and its properties also have relatively significant effect on the combustion process. For optimal combustion of biomass it is necessary to ensure appropriate excess air given by the combustion stoichiometry (the lowest relative humidity and the highest temperature of combustion air). Area A (Fig. 4) indicates the optimal combustion conditions of the tested boiler when it is possible to achieve the ideal combination of high thermal power, low emission formation of commercially available fuel (wood pellets have a normal humidity around 10%) and air (combustion air temperature is normally about 15 - 20 ° C and relative humidity of about 40-60%). Based on the measured results we can conclude that the combustion process is influenced by many factors. For achieving the highest combustion efficiency with the lowest impact on the environment it is necessary to operate the heat source at optimal parameters.

Acknowledgement

This work was supported by the projects „Vyskumne centrum Zilinskej univerzity v Ziline ITMS 26220220183” and “Moderne zdroje tepla pre vykurovanie”KEGA 070ZU-4/2013.

- [8] VITAZEK, I., VITAZKOVA, B., PLOTH, J.: Production of Gas Emissions from Biomass Heat Source. *Engineering Mechanics*, vol. 20, 2013, No. 3/4, 289-298. ISSN 1805-4633.
- [9] TAUS, P., TAUSOVA, M.: Economic Analysis of FV Power Plants According to Installed Performance, *Acta Montanistica Slovaca*, vol. 14, No. 1, 2009
- [10] DZURENDA, L., DELIISKI, N.: Drying of Beech Timber in Chamber Drying Kilns by Regimes Preserving the Original colour of wood, *Acta Facultatis Xylogiae Zvolen*, vol. 55 No. 2, 2013, 31-42.
- [11] STN EN 14961-2, 2011: Solid biofuels. Fuel specifications and classes. Part 2: Wood pellets for non-industrial use
- [12] STN EN 14774, 2010: Solid biofuels. Determination of moisture content. Oven dry method
- [13] STN EN 14775, 2010: Solid biofuels. Determination of ash content
- [14] STN EN 15210, 2010: Solid biofuels. Determination of mechanical durability of pellets and briquettes.
- [15] STN EN 14918, 2010: Solid biofuels. Determination of calorific value
- [16] STN EN 15103, 2010: Solid biofuels. Determination of bulk density
- [17] STN EN 303 - 5: 2012: Heating boilers. Part 5: Heating boilers for solid fuels, manually and automatically stoked nominal heat output of up to 500 kW. Terminology, requirements, testing and marking
- [18] NEMEC, P., CAJA, A., MALCHO, M.: Mathematical Model for Heat Transfer Limitations of Heat Pipe, *Mathematical and Computer Modelling*, vol. 57, No. 1-2, 2013, 126-136.
- [19] HORAK, J., JANKOVSKA, Z., STRAKA, F., BURYAN, P., KUBESA, P., HOPAN, F., KRPEC, K.: Problems of Determination of Characteristic Temperatures of Biomass Ash Fusibility (in Czech), *Chemické listy*, vol. 107, No. 6, 2013, 502-509.
- [20] WERLE, S.: Impact of Feedstock Properties and Operating Conditions on Sewage Sludge Gasification in a Fixed Bed Gasifier, *Waste Management & Research*, vol. 32 (10), 2014, 954-960.
- [21] RIMAR, M., FEDAK, M., DUDINAK, P.: Process of Nitrogen Oxides Generation in Pressure Burners, *Manufacturing and Industrial Engineering*, No. 3, 2007, 81 - 84.
- [22] ADAMCZYK, W., WERLE, S., RYFA, A.: Application of the Computational Method for Predicting NOx Reduction within Large Scale Coal-fired Boiler, *Applied Thermal Engineering*, vol. 73, 2014, 341-348.

Jozef Bronceek - Peter Jankejech - Peter Fabian - Norbert Radek *

INFLUENCE OF MECHANICAL ANISOTROPY IN LOW CARBON MICROALLOYED STEEL

The energy industry is one of the most discussed topics in modern days. Among the critical areas belongs the production and sale of energy, including fuel extraction, manufacturing, refining and distribution. As today's society consumes large amounts of fuel, the energy industry is affecting the infrastructure and maintenance of all civilizations across the globe. Transportation of oil and natural gas through a pipeline system proves to be most efficient and safe. Most pipelines are made from steel. The quality and properties of steel used in this field are determined by the environmental safety requirements and industry regulations. The majority of steel pipe carrying oil and natural gas is the low representation of carbon and other alloys such as manganese and silicon. Manufacturers of this kind of steel have a stringent focus on quality testing such as tensile strength ratio, toughness and hardness. The purpose of this contribution is to focus on the microstructural anisotropy caused by chemical segregation and non-uniform distribution of inclusions in X65 pipeline steel, with focusing on the toughness properties and microstructural analysis.

Keywords: Toughness, microstructure, inclusions, pipeline steel, segregation.

1. Introduction

High grade pipeline steels are manufactured by using thermo-mechanical controlled rolling after which the product gains superior characteristics by controlling the deformation and the temperature of deformation during the hot rolling process. Thanks to the effect of plastic deformation above and below the recrystallization stop temperatures a fine grained microstructure is created with improved mechanical properties such as toughness and yield strength (Table 1) [1 and 2].

Typical microstructure of hot rolled low alloy steel is illustrated in Fig. 1. It can be seen that the microstructure consists of plainer patches of pearlite parallel to the rolling plane. Microstructural banding is often more pronounced in sections containing the rolling direction than in those containing the transverse direction [1].

These patches of pearlite are produced by homogenization of carbon during cooling through the austenite phase field. However, there are gentle variations which occur with the content of manganese, as carbon maintains a uniform chemical potential in the austenite. Manganese lowers the activity of carbon and hence the regions which are rich in manganese are associated with somewhat higher carbon concentration (Fig. 2) [1].

If the region contains relatively large sulphur concentrations, manganese sulphides then precipitate in the regions containing a large average concentration of manganese. As a consequence, manganese is bound in the sulphide which is surrounded by a manganese depleted zone where ferrite forms. The ferrite partitions carbon into the adjacent zones which have low average concentration of manganese that transforms into pearlite. The position of ferrite bands is thus shifted into locations where the average Mn concentration is large, but where the Mn is tied up as sulphides (Fig. 3) [1 and 3].

API specifications for X65 pipeline steel

Table 1

Grade	C	Mn	P	S	Nb	V
X65	≤ 0.26	≤ 1.46	≤ 0.04	≤ 0.05	≥ 0.005	≥ 0.005
Grade	EUL (MPa)		UTS (MPa)		Y/T Ratio	
X65	≥ 448		≥ 530		≤ 0.90	

* ¹Jozef Bronceek, ²Peter Jankejech, ³Peter Fabian, ³Norbert Radek

¹Department of Design and Mechanical Elements, Faculty of Mechanical Engineering, University of Zilina, Slovakia

²Department of Technological Engineering, Faculty of Mechanical Engineering, University of Zilina, Slovakia

³Department of Operation Engineering, Faculty of Mechatronics and Machine Design, Kielce, University of Technology, Poland

E-mail: jozef.bronceek@fstroj.uniza.sk

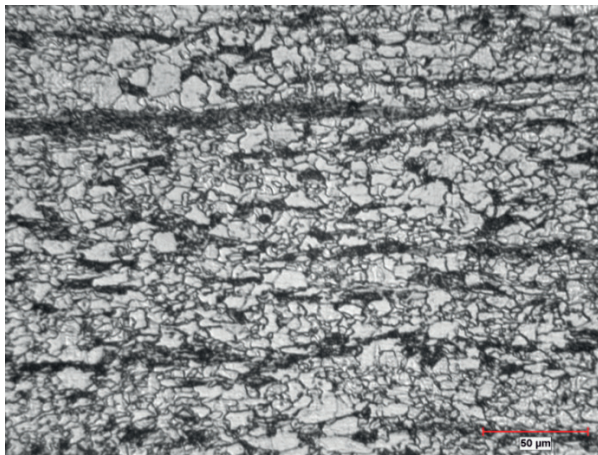
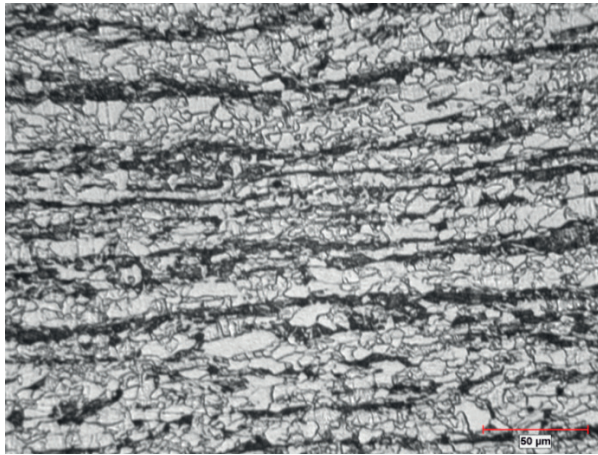


Fig. 1 Typical microstructure of hot rolled steel, in this case grade X70

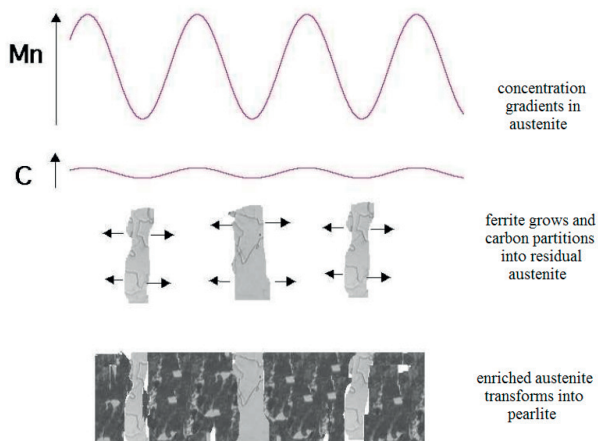


Fig. 2 Illustration of mechanism banding where locations with higher concentration of manganese become pearlite bands [1]

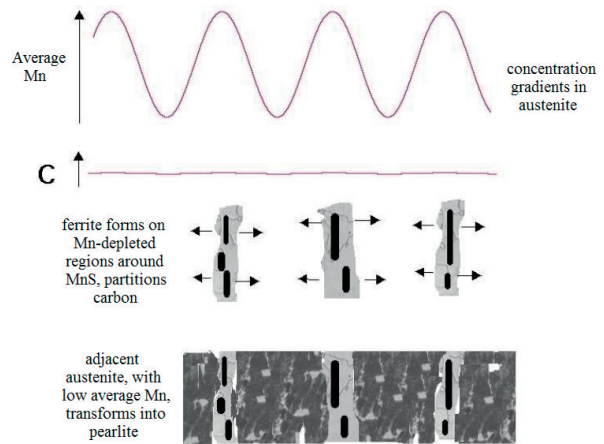


Fig. 3 Illustration of mechanism banding where steel contains substantial quantities of manganese sulphides [1]

2. Influence of anisotropy on mechanical properties

The orientation dependence of toughness is a well-known phenomenon for hot-rolled steels in general. There are three particular factors which influence mechanical properties of hot rolled steels:

- non-uniform distribution in the size and shape of inclusions,
- microstructural anisotropy due to chemical segregation with banding,
- elongated grain structure.

Inclusions influence anisotropy because they are often associated with the initial solidification process and any solidification induced chemical segregation. Others may participate in the austenite at high temperatures prior to the hot deformation that the cast steel is subjected to. Common inclusions include the manganese sulphides, silicates and alumina and combinations of oxides depending on the particular steelmaking route; the hot deformation needed to shape the steel has the effect of orienting these phases along the principal plastic strain directions (Fig. 4). Some phases such as manganese sulphides and silicate can deform along with the steel and hence become elongated, whereas others fragment and form stringers along these same directions. The inclusions can, as a consequence, lead to a variety of anisotropies, particularly with respect to tensile elongation, bend properties, fracture mode and fracture toughness [1, 4, 5, 3, 6, 7, 8 and 9].

Nonmetallic inclusion like MnS influence properties by nucleating cleavage or voids. It is often that the inclusions serve to concentrate stress so that adjacent and more brittle cementite particles can initiate cleavage (Fig. 5) [1, 2 and 3].

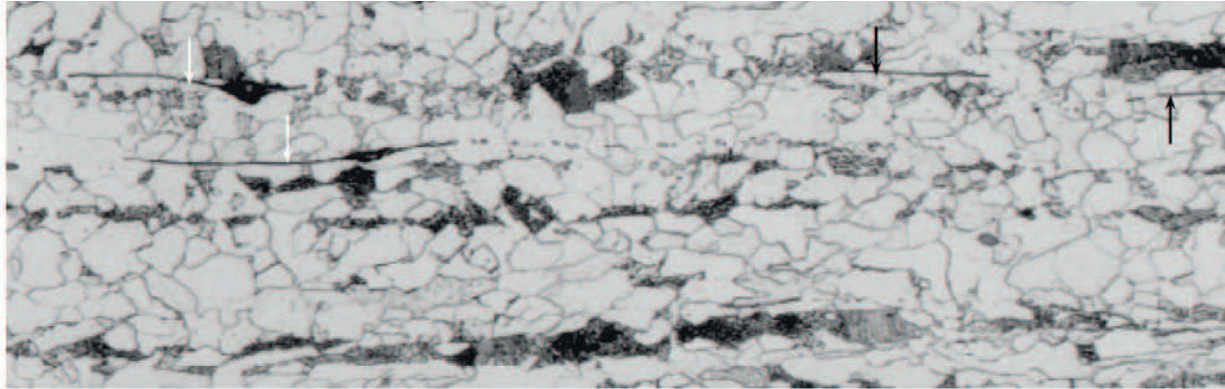


Fig. 4 Low carbon microalloyed steel consisting of ferritic grains, pearlite bands and flattened MnS (black arrows) and mixed oxide MnS (white arrows) [1]

This is because inclusions like MnS can lose cohesion with the matrix before the onset of cleavage. The tip of elongated inclusion provides the greatest stress concentration so loading normal to the plane of the inclusion leads to poor toughness in contrast to the case where the principal loading is parallel to the long axis when the stress concentration due to decohesion is of minor importance. This leads to anisotropy of toughness [1 and 10].

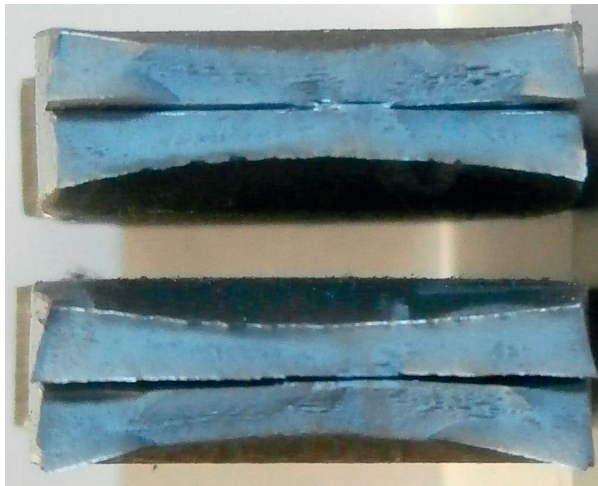


Fig. 5 Broken tensile specimen of X65 pipeline steel where the cleavage is initiated by nonmetallic inclusions

3. Experimental part

The material for testing was a pipe made from hot rolled microalloyed steel X65 whose chemical composition is shown in Table 2. This type of pipeline steel permits fluids to be transmitted at higher pressures with vital toughness and tensile properties, amongst other factors especially in ensuring susceptibility due to hydrogen induced cracking (HIC) which is caused by hydrogen sulphide gas.

The samples for impact testing were cut from the pipe as shown in Fig. 6. The set of samples marked by letter A represent the transverse orientation to the rolling direction (elongated grains) and set of samples marked by letter B represent longitudinal orientation that means parallel to the direction of rolling. One set contained three machined samples. The testing temperature was -45°C. Measured values are recorded in Table 2 and graphically illustrated in Fig. 7.

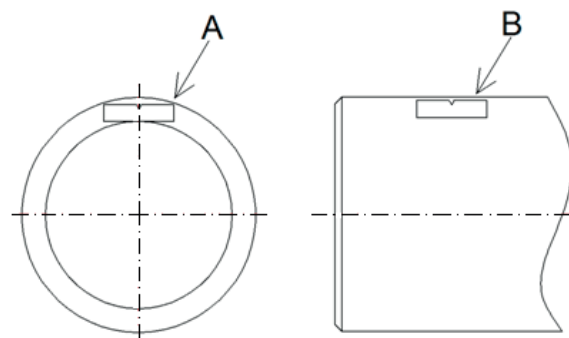


Fig. 6 Illustration of CVN sample orientation in the experimental material

Chemical composition of tested X65 pipeline steel

Table 2

C	Si	Mn	P	S	Co	Ni	Cr	Mo	V	Nb	Ti	B*
0.07	0.25	1.39	0.013	0.001	0.01	0.01	0.04	0.01	0.05	0.05	0.01	<1

* x. 1000

Measured values from impact testing

Table 3

Specimen size (mm)	Specimen orientation	Temp. (°C)	Specimen markings			Absorbed energy (J)			Average absorbed energy (J)
			A1	A2	A3	217.0	235.7	222.3	
55 x 10 x 10	Transverse	-45	A1	A2	A3	217.0	235.7	222.3	225
55 x 10 x 10	Longitudinal	-45	B1	B2	B3	245.6	247.0	273.0	255

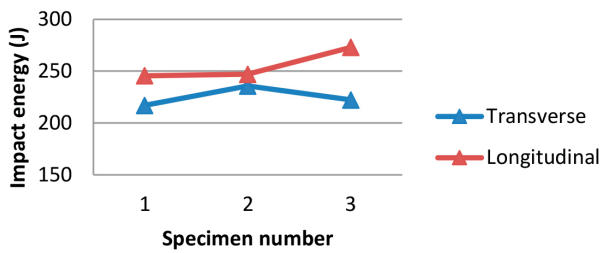
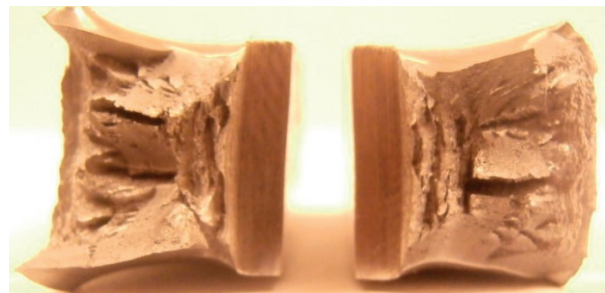


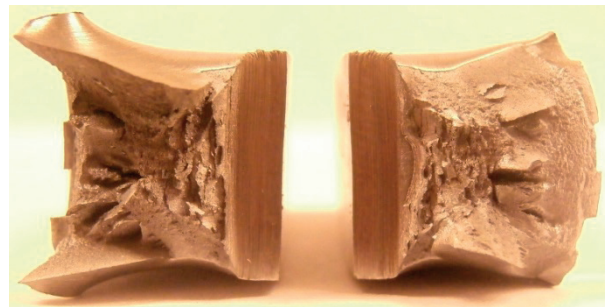
Fig. 7 Graphical illustration of measured values from impact testing

4. Conclusion

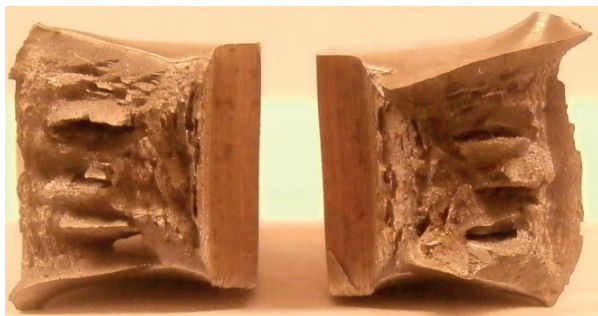
The purpose of this contribution was to find out how big the influence of chemical segregation and inclusions on toughness of examined X65 pipeline steel is. From the measured values (Table 3) it is possible to suggest that the toughness is higher parallel to rolling direction than in the transverse direction. The next phenomena which can be observed are splits on broken surfaces of the CVN specimens (Fig. 8) and tensile specimen (Fig. 5).



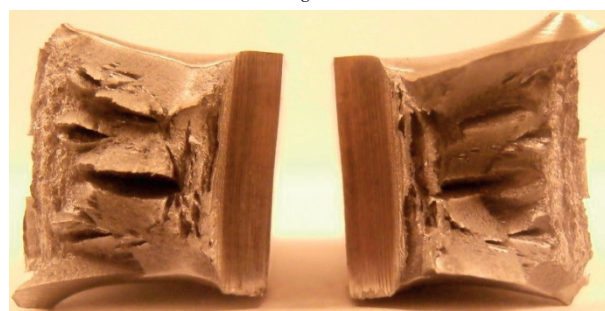
A3 Transverse



B1 Longitudinal



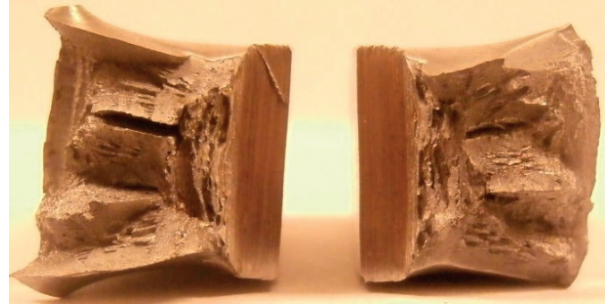
A1 Transverse



B2 Longitudinal



A2 Transverse



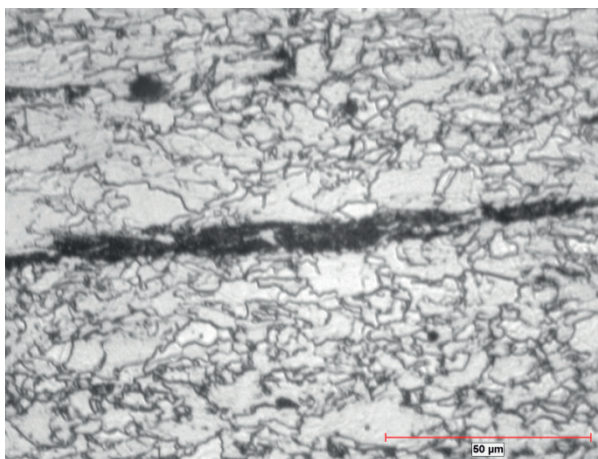
B3 Longitudinal

Fig. 8. Broken samples from Charpy impact testing

These splits can be caused by elongated inclusions such as manganese sulphides or by delamination. Due to the fact that the examined steel contains a little amount of sulphur (0.001%) it can be assumed that the main cause of splitting is delamination. Delamination is caused by the presence of microstructural banding with variations in crystallography between adjacent bands. As we can see in Figs. 9 and 10 these bands are located in the longitudinal and transverse direction of the examined steel. The difference is that the bands in the transverse orientation are more discontinuous than in the longitudinal direction. This is because the bands are more elongated with the grains in the process of hot rolling.



100x

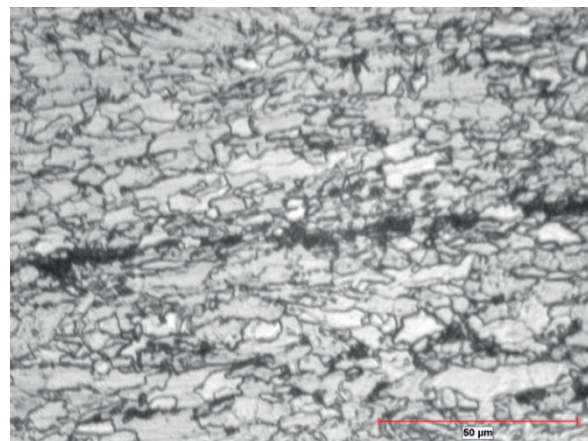


400x

Fig. 9 Microstructural bandings in the transverse orientation of elongated grains, Nital 2%



100x



400x

Fig. 10 Microstructural bandings in the longitudinal orientation of elongated grains, Nital 2%

To minimize the forming of these patches, manufacturers are trying to decrease the amount of phosphorus and sulphur to minimum. Also new methods of hot rolling (cross rolling) were developed to control the shape of the inclusions in combination with adding elements like zirconium, cerium and titanium. Thanks to these methods the anisotropy is reduced to the point that the thermo-mechanically rolled steels like grade X65 can meet the safety requirements.

Acknowledgments

The research work reported here was made possible by the project “Research Centre of University of Zilina”, ITMS 26220220183. Assistance provided by Proofstest Consulting Inc. was also highly appreciated.

References

- [1] JOO, M., SUH, D., BHADESHIA, K.: *Mechanical Anisotropy in Steels for Pipelines*. 2013, [online], (cit. 27.02.2015), http://www.msm.cam.ac.uk/phase-trans/2013/anisotropy_Joo_ISIJ_2013.pdf
- [2] BREZINOVA, J., GUZANOVA, A., MARUSCHAK, P., LORINCOVA, D.: Study of Wear Processes of Weld Clads, *Acta Metallurgica Slovaca*, vol. 20, No. 2, 2014, pp. 167-176, DOI 10.12776/ams.v20i1.273, ISSN 1335-1532
- [3] KONAR, R., MICIAN, M.: Numerical Simulation of Residual Stresses and Distortions in Butt Weld in Simulation Programme SYSWELD, *Communications - Scientific Letters of the University of Zilina*, vol. 14, No. 3, 2012, pp. 49-54, ISSN 1335-4205
- [4] RICHTARECH, L - BOLIBRUCHOVA, D.: Study of the Gas Content in Aluminium Alloys, *Manufacturing Technology: J. for Science, Research and Production*, vol. 13, No. 1, 2013, pp. 14-20, ISSN 1213-2489
- [5] PASTIRCAK, R.: Effect of Low Pressure Application during Solidification on Microstructure of AlSi Alloys, *Manufacturing Technology: J. for Science, Research and Production*, vol. 14, No. 3, 2014, pp. 397-402, ISSN 1213-2489
- [6] PETRU, M., BRONCEK, J., LEPSIK, P., NOVAK, O.: Experimental and Numerical Analysis of Crack Propagation in Light Composite Materials under Dynamic Fracture. *Communications - Scientific Letters of the University of Zilina*, vol. 16, No. 3A, 2014, pp. 82-89, ISSN 1335-4205
- [7] BREZINOVA, J., GUZANOVA, A., DRAGANOVSKA, D., BRONCEK, J.: Quality Evaluation of HVOF Coatings on the Basis of WC-Co in Tribocorrosive Conditions, *Material Science Forum*, vol. 811, 2015, DOI 10.4028/www.scientific.net/MSF.811.63 pp. 63-66
- [8] KOHAR, R., HRCEK, S.: Dynamic Analysis of a Rolling Bearing Cage with Respect to the Elastic Properties of the Cage for the Axial and Radial Load Cases. *Communications - Scientific Letters of the University of Zilina*, vol. 16, No. 3A, 2014, pp. 74-81, ISSN 1335-4205
- [9] HRCEK, S., KOHAR, R., MEDVECKY, S.: Usage of Dynamic Analysis to Determine Force Interactions between Components of Rolling Bearings. *Communications - Scientific Letters of the University of Zilina*, vol. 14, No. 3, 2012, pp. 62-67
- [10] KONAR, R., PATEK, M., MICIAN, M.: Experimental Measurements and Numerical Simulation of Bridge Construction Welding at Low Temperatures, *Communications - Scientific Letters of the University of Zilina*, vol.16, No. 3A, 2014, pp. 130-135, ISSN 1335-4205.

Jan Dizo - Miroslav Blatnický - Blanka Skocilasová *

COMPUTATIONAL MODELLING OF THE RAIL VEHICLE MULTIBODY SYSTEM INCLUDING FLEXIBLE BODIES

Tools for computer simulations are widely used in the field of a rail vehicle design. These means of virtual reality allow to perform static analyses of rail vehicle parts and dynamic analyses of a rail vehicle multibody system. For static analyses the finite element methods are most commonly used while the multibody system analyses are used for analyses of the rail vehicle dynamics. This paper deals with an implementation of flexible bodies into the rail vehicle multibody system. The implementation of flexible bodies into the rail vehicle multibody system extends the using of simulations, especially for an assessment of an influence of flexible bodies on running properties of the rail vehicle.

Keywords: Computational modelling, rail vehicle, multibody system, flexible bodies.

1. Introduction

In modern development process of rail vehicle computer aided simulations are employed. In this way costly experiments and prototypes can be reduced. Production of a rail vehicle is composed of several phases. There is a design phase, a development and optimisation phase, production of a rail vehicle, verification and validation of a rail vehicle and, in the end, commissioning of a rail vehicle. At this time computer software allows to perform complex simulations. Thus, shorter development periods and rising requirements like durability, efficiency or mass reduction demand precise simulations, which intensify the usage of lightweight structures.

2. Principles of rail vehicle multibody system with a flexible body

The need for more accurate models of a rail vehicle to describe the complex behaviour of flexible systems experiencing large motion while undergoing small elastic deformations motivated the development of many powerful analysis techniques. The most popular formulations use time-variant mass matrices to describe the inertia coupling between the rigid body motion and the elastic deformation [1].

To describe the dynamic behaviour of a rail vehicle mechanical system which undergoes large nonlinear working motions the

multibody system (MBS) approach is often most useful [2]. A classic MBS of a rail vehicle consists of rigid elements which are connected by ideal joints, coupling elements [3], contact elements [4 and 5] and force elements. The phenomena of the wheel/rail contact [6] significantly influence the rail vehicle properties and wheel/rail contact stress evaluation [7 and 8].

For applications in the field of rail vehicle analysis where the deformation of the bodies cannot be neglected, the method of flexible multibody systems has to be applied. In the flexible multibody system of a rail vehicle the approach is extended by flexible bodies.

The application of flexible bodies into the rail vehicle multibody system with the help of the finite element method introduces a large number of flexible degrees of freedom into the rail vehicle model. The reduction of the linear flexible degrees of freedom is the principal step for an efficient simulation of a flexible multibody system of a rail vehicle [9].

2.1 Foundations of flexible multibody dynamics

For the kinematic description of the motion of flexible bodies that are subjected to large displacements several methods are used. Among these methods are, for example, *the floating frame of reference*, *convected coordinate system*, *finite segment method* and *large rotation vector*. Large deformation problems in flexible

* ¹Jan Dizo, ¹Miroslav Blatnický, ²Blanka Skocilasová

¹Department of Transport and Handling Machines, University of Zilina, Slovakia

²Department of Machines and Mechanics, J. E. Purkyne University in Usti nad Labem, Czech Republic

E-mail: miroslav.blatnicky@fstroj.uniza.sk

multibody system can be efficiently solved using *the absolute nodal coordinate formulation* [10].

In the absolute nodal coordinate formulation, neither infinitesimal nor finite rotations are used as the element coordinates. The locations and deformations of the material points on the finite element are defined in the global coordinate system using the element shape function and nodal coordinates (Fig. 1).

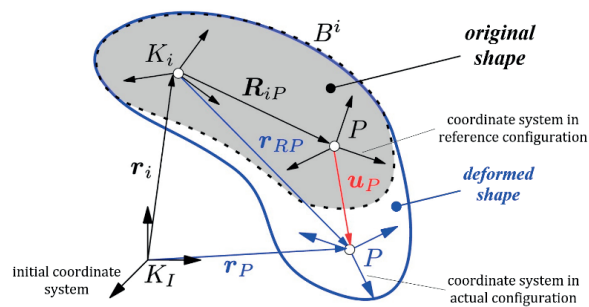


Fig. 1 Representation of the flexible body kinematics

The floating frame of reference formulation is currently the most widely used method in the computer simulation of flexible multibody systems [10 and 11]. It is used for the systems where the elastic deformation is small compared to the rigid body motion. The basic idea is to separate the motion of the body into a large nonlinear motion of the reference frame and a small linear elastic deformation with respect to the reference frame. The motion of a particular point P on the flexible body B^i is represented by the vector $r_p(t)$ (Fig. 1). A flexible body can be e.g. the bogie frame, the body of wagon or rail etc. Using the floating frame of reference formulation, the position vector $r_p(t)$ of the point is separated into a usually non-linear motion $r_i(t)$ of the reference frame and a superposed linear elastic deformation $u_p(t) = u(R_{iP}, t)$ with respect to the reference frame [11]

$$r_p(t) = r_i(t) + R_{iP} + u_p(t), \quad (1)$$

see Fig. 1. The vector R_{iP} corresponds to the position of the point P in the undeformed state.

A similar approach concerning the orientation of the coordinate system at point P leads to the small rotational motion $\vartheta_P(t) = \vartheta_P(R_{iP}, t)$ by elastic deformation. Once deformation disappeared, this kinematic formulation leads to exact modelling the rigid body dynamics of a rail vehicle. When this formulation is used, the modelling of a flexible multibody system of a rail vehicle can be divided into two parts (Fig. 2) [11].

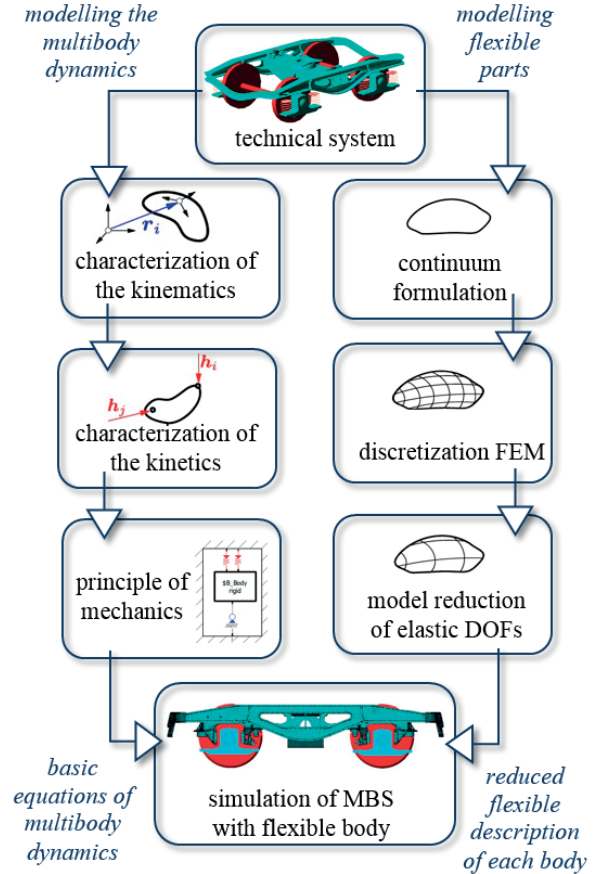


Fig. 2 Procedure of the rail vehicle multibody modelling and simulation with flexible bodies

This describes on the one hand the modelling of multibody dynamics and on the other hand the modelling of flexibility of selected bodies. Combination of these ways establishes the flexible multibody system.

3. Modelling of the multibody system of rail vehicle with flexible bodies

The Finite Element Method (FEM) is one of the most commonly used tools for the flexibility description [12 and 13]. It is an approximation and discretisation method for field problems formulated for differential equations. In structural dynamics the displacement field of a continuum is approximated by the Ritz approach and d’Alambert’s principle to get the equation of motion of a finite element model. The linear elastic deformation $u(R, t)$ and $\vartheta_p(R, t)$ are specified by the Ritz approach [11]

$$u(R, t) = \Phi(R) \cdot q_e(t), \vartheta(R, t) = \Psi(R) \cdot q_e(t), \quad (2)$$

where $q_e(t)$ refers to the nodal displacements of a finite element model and $\Phi(R)$ and $\Psi(R)$ are the elastic shape functions [9]. This results in the equation of motion of a flexible body

$$M_e \cdot \ddot{q}_e(t) + K_e \cdot q_e(t) = h_e, \quad (3)$$

as formulated in [9]. The matrices M_e and K_e are the mass and stiffness matrices of the flexible structure and have the following characteristics if the system is constrained sufficiently to avoid rigid body motion

$$M_e = M_e^T > 0, K_e^T > 0, \quad (4)$$

The generalised surface and volume forces are summarised in the force vector h_e . To consider the dissipative effects an additional damping matrix D_e is often introduced and can be approximated, e.g. by viscous damping (Rayleigh damping):

$$D_e = \alpha M_e + \beta K_e, \quad (5)$$

with the proportional factors $0 \leq \alpha, \beta \in \mathbb{R}$. The need for high precision and complex geometries often leads to a fine spatial discretisation. Mathematically the flexible bodies are described by a large set of linear ordinary differential equations, whose solution increases the computational effort of the simulation. Linear model reduction is a decisive component to efficient simulation. To get a representation used for some model reduction techniques the forces acting on the finite element structure are described by the time dependent excitation $u_e(t)$ and the input or control matrix $B_e \in \mathbb{R}^{N \times p}$. This matrix captures the spatial distribution of the boundary and coupling conditions. Further on, the output or observation matrix $C_e \in \mathbb{R}^{r \times N}$ is introduced for the calculation of the interesting displacements $y(t)$. In this case, equations of motion of a single flexible body can be formulated as a linear time-invariant second order multi input multi output system:

$$M_e \cdot \ddot{q}_e(t) + D_e \cdot \dot{q}_e(t) + K_e \cdot q_e(t) = B_e \cdot u_e(t), \quad (6)$$

$$y(t) = C_e \cdot q_e(t). \quad (7)$$

Due to increasing demands on the characteristics of technical products and their simulation, the requirements on the calculation accuracy and the calculation time are often extremely high. On the bottom line this trend means that the dimension of the equation of motion rises and the time to run the simulation should be as quick as possible. Such problems particularly require an adequate model order reduction to decrease the number of equations and keep the significant characteristics of the system. Using the floating frame of reference formulation and the linear model order reduction via projection of equation of motion (3), (5), (6) (see [9 and 11]) can be used. Therefore, the large number of degrees of freedom of the flexible coordinates $q_e \in \mathbb{R}^{N \times 1}$ are

approximated in a subspace \mathcal{V}_s of smaller dimension $n < N$ by the reduced displacement vector $\tilde{q}_e \in \mathbb{R}^{n \times 1}$

$$q_e \approx V \cdot \tilde{q}_e. \quad (8)$$

This subspace \mathcal{V}_s is described by the projection matrix $V \in \mathbb{R}^{N \times n}$. The use of this relation in FEM equations of motion (5) and (6) leads to an over-determined system and leaves a residuum because the exact solution q_e is generally not an element of the subspace \mathcal{V}_s . To obtain a unique solution the residual should be orthogonal on a second subspace \mathcal{W}_s represented by $W \in \mathbb{R}^{N \times n}$. The orthogonality conditions or Petro-Galerkin conditions result in the reduced FE equations

$$\tilde{M}_e \cdot \ddot{\tilde{q}}_e + \tilde{D}_e \cdot \dot{\tilde{q}}_e + \tilde{K}_e \cdot \tilde{q}_e = \tilde{B}_e \cdot u_e, \quad (9)$$

with the reduced matrices $\tilde{M}_e := W^T \cdot M_e \cdot V$, $\tilde{D}_e := W^T \cdot M_e \cdot V$, $\tilde{K}_e := W^T \cdot K_e \cdot V \in \mathbb{R}^{n \times n}$ and $\tilde{B}_e := W^T \cdot B_e \in \mathbb{R}^{n \times p}$, $\tilde{C}_e := C_e \cdot V \in \mathbb{R}^{r \times n}$.

The projection is called orthogonal if the subspaces are identical $V = W$ and oblique otherwise. This procedure leads to the reduced equations of motions of one flexible body:

$$\begin{bmatrix} M_r^i & M_{er}^i \cdot V \\ W^T \cdot M_{er}^i & \tilde{M}_e^i \end{bmatrix} \cdot \begin{bmatrix} \ddot{q}_r^i \\ \ddot{\tilde{q}}_e^i \end{bmatrix} + \begin{bmatrix} 0 \\ \tilde{K}_e \cdot \tilde{q}_e + \tilde{D}_e \cdot \dot{\tilde{q}}_e \end{bmatrix} = \begin{bmatrix} h_r^i \\ W^T \cdot h_e^i \end{bmatrix}. \quad (10)$$

A task of different reduction techniques is to find the projection matrices V and W .

4. Approach for the reduction of rail vehicle parts

For the simulation of the rail vehicle multibody system with flexible bodies some preprocessing steps for obtaining a reduced flexible body are necessary. It is possible to make in FEM software, for example in Ansys [14 and 15]. Ansys software allows engineers to construct computer models or structures, machine components or system, apply operating loads and other design criteria and study physical responses [16 and 17]. This software also allows to reduce flexible bodies for import into MBS software.

The general process to integrate flexible bodies into the rail vehicle multibody system consists of several operations:

- setting up the finite element model,
- integrating the finite element model into the MBS software,
- setting up the MBS model of the rail vehicle.

It is needed to reduce the size (number of freedom) of FEM model before working with the MBS interface. For this it is needed to perform several operations:

- define the interface nodes. The MBS interacts with the FEM superelement on these nodes.
- connect the interface nodes with structure. In Ansys it is recommended to use the following elements types:

- **rigid body element** - interface nodes have independent DOFs, coupling nodes on the FE structure have dependent degrees of freedom, dependent nodes perform rigid body motion only and independent node (interface node) defines this rigid body motion. Element types of rigid body elements for Ansys FEM code are CE, CERIG, MPC184 and RBE 2.
- **force distributing constraints** - interface node has dependent DOFs, coupling nodes on the FE structure have independent DOFs, motion at the interface node is the weighted average of the motion of the coupling nodes, forces and moments at the reference node are distributed either as forces or moments at the coupling nodes. Element types of force distributing constraints for Ansys FEM code are TARGE 170+CONTA173, TARGE 170+CONTA174.
- define the coupling nodes as retained nodes,
- define the retained DOFs. This step is important in the reduction process for yielding accurate superelement matrices [18].

Once the FEM model of a part of the rail vehicle is reduced, the input files generation for MBS software is required. The file with the flexible body input data is necessary for including flexible bodies in the MBS software. After loading the file with the FEM input data into the MBS software it is possible to define the interaction between flexible body and MBS system by using joints, constraints or force elements which apply loads to the flexible body. The flexible body deformation is caused by these loads [15].

For the needs of a rail vehicle simulation the FEM model of a bogie frame of a freight wagon was created. This is the most commonly used bogie in the Central and Eastern Europe - the Y25 bogie [19, 20 and 21].

4.1 Reduction of the bogie frame

In this section the procedure of preparation of the flexible model of the bogie frame is described.

The CAD model of the bogie frame was imported into the FEM software. For the preparation of the FEM data the software

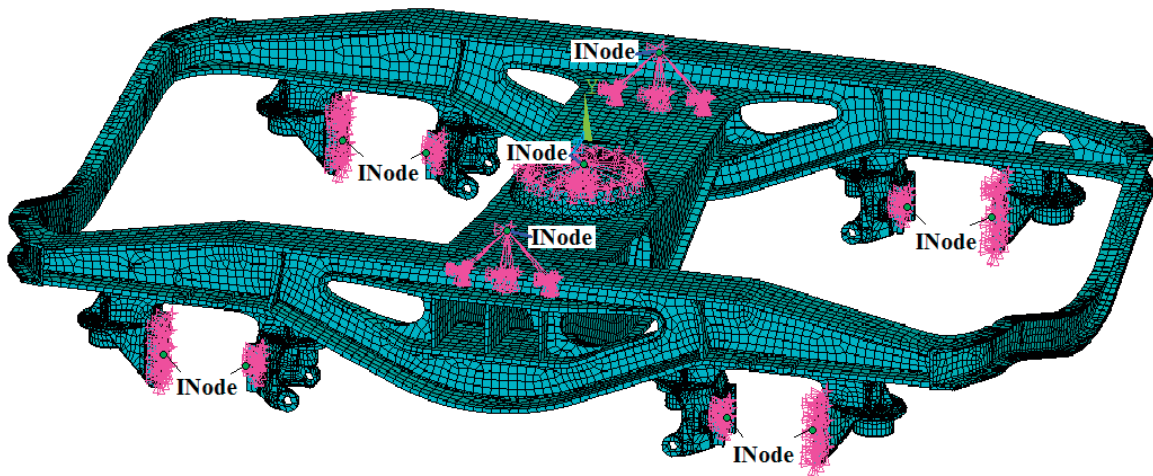


Fig. 3 FEM model of the bogie frame with interface nodes (INode)

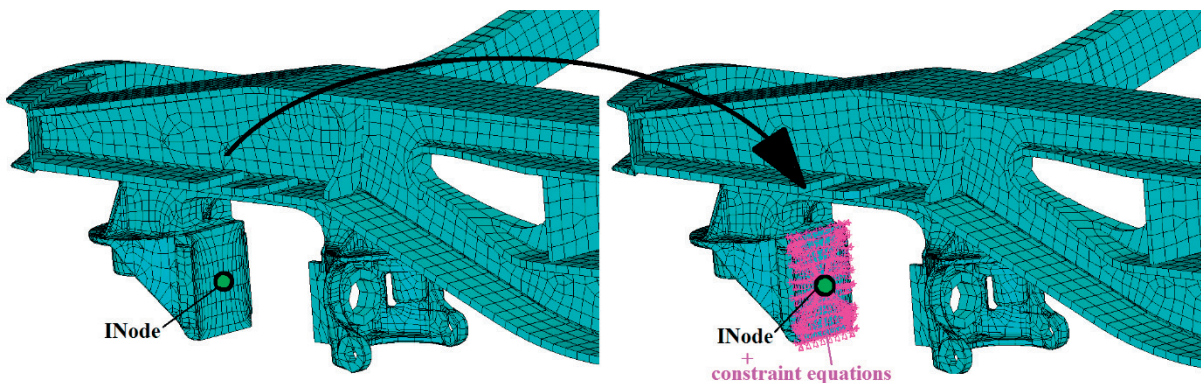


Fig. 4 Interface node (INode) on the friction surface (left) and constraint equations (right)

Ansys was used. In Ansys the FEM mesh and simulation of flexible body behaviour were performed [14 and 22]. For interface nodes the rigid body element was used. Interface nodes were defined in locations of joints, constraints and force elements (Fig. 3). In Fig. 3 interface nodes on the bogie frame created by using rigid elements are shown.

In Fig. 4 the example of interface node (INode) and relevant constraint equations created on the friction surface of the axle guide are shown. In this interface node friction forces between the bogie frame and the axlebox in the multibody system of the freight wagon are defined.

In the future research this FEM model of a bogie frame of a freight wagon will be used for importing into the MBS model of a freight wagon. After creation of the rail vehicle multibody system with flexible bodies analyses will be performed. These analyses will allow the better assessment of the freight wagon ride properties. It will be needed to consider that the freight wagon most commonly consists of two bogies. The created FEM model of a bogie will require much bigger computer capacity and will extend the computational time significantly.

5. Conclusion

The computer simulation is nowadays an integral part of the development process of rail vehicles. The flexible multibody dynamics is the field that encompasses several subjects such as rigid body dynamics, continuum mechanics, finite element method, numerical and computer method. Multibody simulations with flexible bodies enable more detailed analyses of a rail vehicle behaviour. The inclusion of the flexible body into MBS

simulation allows better optimization of rail vehicles design as well as prevention of potential problems during their long-term operation.

Acknowledgements

This paper was created during the processing of the project No. APVV-0842-11: "Equivalent railway operation load simulator on the roller rig". The work is also supported by the Scientific Grant Agency of the Ministry of Education of the Slovak Republic and the Slovak Academy of Sciences in project No. 1/0347/12: "Railway wheel tread profile wear research under the rail vehicle in operation conditions simulation on the test bench", project No. 1/0383/12: "The rail vehicle running properties research with the help of a computer simulation" and No. 1/1098/11: "Stress Distribution in a Braked Railway Wheel".



The Agency
of the Ministry of Education, Science, Research and Sport
of the Slovak Republic
for the Structural Funds EU



This contribution is the result of the project implementation: "Development of two types of freight wagons with bogies for non-standard wheelbase or track wheelset, complying with the criteria for interoperability, Environmental Issues, safety and reliability", ITMS code 26220220070, supported by the Operational Programme Research and Development.

"We support research activities in Slovakia / Project is co-financed from EU sources."

References

- [1] SCHIEHLEN, W.: Research Trends in Multibody System Dynamics. *Multibody System Dynamics*, 18, 2007, 3-13, Springer Science + Business Media B.V 2007. DOI 10.1007/s11044-007-9064-4.
- [2] SAGA, M., ZMINDAK, M., DEKYS, V., SAPIETOVA, A., SEGLA, S.: *Selected Methods of Analysis and Synthesis of Mechanical Systems*, VTS: University of Zilina, 2009, 360 p., ISBN 978-80-89276-17-2.
- [3] SAPIETOVA, A., SAGA, M., SHIMANOVSKY, A., SAPIETA, M.: Mobility of Multibody System in Terms of their Incorrectness. *Communications - Scientific Letters of the University of Zilina*, vol. 16. No. 3a, 2014, 33-39. ISSN 1335-4205.
- [4] LACK, T., GERLICI, J.: *Modified Strip Method Utilisation for Wheel/rail Contact Stress Evaluation*. 9th intern. Conference on contact mechanics and wear of rail/wheel system (CM2012): Southwest Jiaotong University, 2012. Presented in Chengdu, 2012.
- [5] GERLICI, J., LACK, T.: Contact Geometry Influence on the Rail/Wheel Surface Stress Distribution, *Procedia Engineering*, vol. 2, No. 1, 2010, 2249-2257.
- [6] LACK, T., GERLICI, J.: Wheel/rail Tangential Contact Stress Evaluation by Means of the Modified Strip Method. *Communications - Scientific Letters of the University of Zilina*, vol. 16. No. 3a, 2014, 33-39. ISSN 1335-4205.
- [7] LACK, T., GERLICI, J.: Wheel/rail Contact Stress Evaluation by Means of the Modified Strip Method. *Communications - Scientific Letters of the University of Zilina*, vol. 15. No. 3, 2013, 126-132. ISSN 1335-4205.
- [8] LACK, T., GERLICI, J.: *Tangential Stresses for Non-elliptical Contact Patch Computation by Means of Modified FASTSIM Method*. Inter. Association of Vehicles system Dynamics (IAVSD) 2013: 23rd intern. symposium on dynamics of vehicles on roads and tracks, August 2013, Qingdao : Chengdu : Southwest Jiaotong University, 2013. USB key, [6] p.

- [9] FEHR, J., EBERHARD, P.: *Simulation Process of Flexible Multibody Systems with Non-modal Model Order Reduction Techniques*. Multibody System Dynamics (2011) 25: 313-334, Springer Science + Business Media B.V, 2010. DOI 10.1007/s11044-010-9238-3.
- [10] SHABANA, A. A.: Flexible Multibody Dynamics: Review of Past Recent Developments. *Multibody System Dynamics*, 1: 189-222, 1997.
- [11] NOWAKOWSKI, Ch., FEHR, J., FISCHER, M., EBERHARD, P.: *Model Order Reduction in Elastic Multibody Systems using the Floating Frame of Reference Formulation*. Institute of Engineering and Computational Mechanics: University of Stuttgart: Germany.
- [12] VASKO, M., LEITNER, B., SAGA, M.: Computational Fatigue Damage Prediction of the Lorry Frames under Random Excitation, *Communications - Scientific Letters of the University of Zilina*, vol. 12, No. 4, 2010, 62-67.
- [13] LEITNER, B.: *Fatigue Damage Analysis and Fatigue Life Prediction of Lorry Frame under Random Excitation*. Transport means 2014. Proc. of the 18th intern. conference, October 2014, Kaunas University of Technology, 2014, 9-14, ISSN 1822-296X.
- [14] STASTNIAK, P., HARUSINEC, J., LACK, T., GERLICI, J.: *Structural Design of Freight Railway Wagon*. Proc. of conference Innovations in the conception, design, manufacture and testing of freight wagons I, 27-135, November 2014, Zilina: University of Zilina, ISBN 978-80-554-0955-9.
- [15] STASTNIAK, P., HARUSINEC, J.: Computer Aided Simulation Analysis for Computation of Modal analysis of the Freight Wagon. *Communications - Scientific Letters of the University of Zilina*, vol. 15. 2013, 73-79. ISSN 1335-4205.
- [16] SKOCILAS, J., SKOCILASOVA, B., SOUKUP, J.: *Determination of the Rheological Properties of Thin Plate under Transient Vibration*. *Latin American J. of Solids and Structures*. Brazil Society for mechatronics and Engineering. ISSN 1679-7817 (print), 1679-7825 (online).
- [17] SOUKUP, J., VALES, F., VOLEK, J., SKOCILAS, J.: *Transient Vibration of Thin Viscoelastic Orthotropic Plates*. Acta Mechanica Sinica, vol. 27, No. 1, pp. 98-107. The Chinese Society of Theoretical and Applied Mechanics; Institute of Mechanics, Chinese Academy of Sciences, co-published with Springer, ISSN 0567-7718 (Print, 1614-3116 (online).
- [18] SIMPACK documentation 2014, *user guide* (part of the program package).
- [19] DIZO, J.: *Simulation Analysis of a Freight Wagon Running on a Real Track*. Proc. of Innovations in the conception, design, manufacture and testing of freight wagons I, November, 2014, Zilina: University of Zilina, 2014, ISBN 978-80-554-0955-9, pp. 127-135.
- [20] DIZO, J., GERLICI, J., LACK, T.: *The Goods Wagon Equipped by Y25 Bogies Computer Simulation Analysis*. Transcom 2013, Proc. of the 10th European Conference of Young Researchers and Scientists, University of Zilina, ISBN 978-80-554-0695-4. – pp. 63-66.
- [21] HARUSINEC, J., DIZO, J., STASTNIAK, P.: The Computer Simulation of the Goods Wagon by Y25 Bogies (in Slovak). *Technolog*, pp. 245-250, 2013, University of Zilina, ISBN 1337-8996.
- [22] STASTNIAK, P., HARUSINEC, J., GERLICI, J., LACK, T.: Structural Analysis of the Construction Freight Bogie Wagon (in Slovak). *Strojirenska technologie - The J. for Science, Research and Production*, vol. 18, No. 2, 2013, 105-11. ISSN 1211-4162.

Milan Zmindak - Leszek Radziszewski - Zoran Pelagic - Milos Falat *

FEM/BEM TECHNIQUES FOR MODELLING OF LOCAL FIELDS IN CONTACT MECHANICS

This contribution contains description of modelling technique of contact problems of bodies with curved surfaces when assumption of infinitesimal displacements can be considered to give sufficient accuracy for both displacement and stress analysis. This assumption considers that the local configuration of the bodies in contact will not be influenced during the deformation process and only dimensions and shape of the contact surfaces and contact pressures will change by the load conditions. Such assumptions enable to reduce the contact problem considerably, if the local contact displacement and stress fields are modelled as local fields inside large elements (sub-domains) using superposition of a local Hertz type field and a smooth field modelled in a classical way using large FEM or BEM technique.

A technique of obtaining the complex solution of the bodies in contact as a combination of the local contact field defined by the Boussinesq's solution and the smooth field modelled by multi-domain BEM is described and considered to be a basis for the modelling and design of contact problems containing large gradient displacements.

Keywords: Point and line Hertzian contact, infinitesimal displacements, large element/sub-domain concept, FEM/BEM technique.

1. Introduction

If spherical bodies in contact have much different curvatures at least in one direction, like it is in roller bearings, the contact area is very small and under normal loading the contact pressure may occur in order of several thousand N/mm². The contact area can be small in both contact surface directions (called point contact) or in one direction only, when the difference of the curvatures in the other direction is small (called line contact).

The distribution of the externally applied load over the individual rolling elements and also the distribution of the contact pressure in the element contact area are important parameters, which influence the static and dynamic bearing capacity and life of the structural parts in contact. The elastic deformation of the adjacent components and the local deformation of the rolling elements and raceways at their contact area are decisive parameters for the distribution of the contact pressure. The very localised deformations and pressures in the flexible structure components make the problem high non-linear and the accurate analysis is necessary in order to obtain reliable results for the design of the whole bearing form and arrangements.

The detail distribution of the load over the individual rolling elements and the pressure distribution in the contact area of each element require very fine element mesh [1], high performance computers and effective software for the numerical modelling of the problem. The pressure distribution between the elements and the raceways follows the Hertz distribution approximation in the elliptic form only at the lower load levels.

Many authors [2 - 7] gave the analytic expressions for calculation of stress and displacement fields for contact problems of bodies of revolution using Hertz solution obtained from a half plane for 2D and for a half space for 3D problems. The analytic improvement for inclusion of frictional or tractive loads (Smith-Liu equations) was given in [8].

Several authors (e. g. [9 - 11]) used the Hertz solution, or more general Boussinesq solution (giving the displacements and stresses in a half space loaded by a concentrated force in the surface plane) to solve the contact problem of two bodies of rotation more generally.

The aim of the paper is to define an effective model for accurate enough stress and deformation analysis of the multi-body contact of the spherical parts of structure by the use of small number of large FE (finite elements) by effective

* ¹Milan Zmindak, ²Leszek Radziszewski, ¹Zoran Pelagic, ¹Milos Falat

¹Department of Applied Mechanics, Faculty of Mechanical Engineering University of Zilina, Slovakia

²Faculty of Mechatronics and Machine Building, Kielce University of Technology, Poland

E-mail: milan.zmindak@fstroj.uniza.sk

modelling of both the local displacement and stress fields. In such technique the global field is modelled in a classical way and the local effects containing large field gradients are defined by the Boussinesq solution, which satisfy the governing equations in all points of corresponding sub-domain and the boundary conditions at least in the local sense.

In the multi-body contact problems the deformation characteristics are computed first for some local sub-domain and the load distribution over the individual elements is modelled using the global model using special roller elements containing the non-linear contact stiffness of both the roller element and the raceways including the gap for corresponding rolling element [12].

The infinitesimal displacements are considered in the model. Under these assumptions, both the contact area and the contact pressure are to be determined from the topology of the undeformed bodies in the contact and from the resulting load conditions of each pair of contacted surfaces. However, the load distribution between the contacting bodies is considered to be result of the global analysis of all contacting bodies taking into account the non-linear contact stiffness, the finite but small rotations and bending and displacement of shafts, housing, etc. obtained from the global analysis.

The stiffness characteristic of the contacting pairs is obtained from a local model and it is defined as 1D contact pair if the contact surface is determined by the curvatures of contacted surfaces and it relates the contact force to normal displacements of contacted bodies. On the other side, it is defined as 2D contact if the position of the resulting force changes along one of the minor axes depending on the mutual rotation of contacting bodies and/or, if the curvature of contact surfaces changes along this axis. However, in each case, it is assumed that the topology of each contact surface does not change with the load and the contact element for the global model is considered to be 1D with the stiffness obtained from the 2D characteristic containing the dependence of the resulting force direction. In this way the contact characteristics can be obtained from the local model and the complex multi-body contact can be modelled by large elements, which leads to considerable saving of computational time and computer memory.

We do not take into account the frictional forces in this paper, but their inclusion is simple and straightforward as it is known from the referenced literature. The methodology used in this approach is not restricted to the contact problems of the bodies with curved surfaces, but can be used in some modifications to other problems like cracks inside the bodies or on their surface, small inclusions and inhomogenities, etc., i.e. all problems, in which the local effects cause large gradients in the displacement and stress fields.

2. Local solution

2.1 2D problems

All real contacts are three-dimensional (3D), and therefore theoretically demand a solution in the 3D theory of elasticity. But few solutions exist and where it is feasible to approximate the geometry to one or two dimensions, it may be that an exact solution thus facilitated is preferable to an approximate numerical solution to the exact problem. In this chapter, we shall be looking at plane problems. A simple, practical problem is the contact of two rollers of the same length. It is clear that the central portion is under plane strain, whilst ends are under plane stress. A second approximation is that the contacting bodies may be considered to be half-planes. We will first examine the displacement and stress field in the semi-infinite plane (Boussinesq problem) subjected to normal force (Fig. 1).

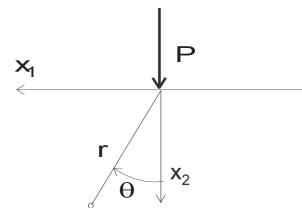


Fig. 1 Force acting on a half-plane

The stress components in terms of Cartesian coordinates are

$$\begin{aligned} \sigma_{11} &= -\frac{2}{\pi x_2} P \sin^2 \theta \cos^2 \theta = -\frac{2P}{\pi} \frac{x_1^2 x_2}{r^4} \\ \sigma_{22} &= -\frac{2}{\pi x_2} P \cos^4 \theta = -\frac{2P}{\pi} \frac{x_1 x_2^2}{r^4} \\ \sigma_{12} &= -\frac{2}{\pi x_2} P \sin \theta \cos^3 \theta = -\frac{2P}{\pi} \frac{x_1 x_2^2}{r^4} \end{aligned} \quad (1)$$

where

$$\begin{aligned} \sin \theta &= \frac{x_1}{\sqrt{x_1^2 + x_2^2}} = \frac{x_1}{r} \quad \text{with } r = \sqrt{x_1^2 + x_2^2} \\ \cos \theta &= \frac{x_2}{\sqrt{x_1^2 + x_2^2}} = \frac{x_2}{r}, \end{aligned} \quad (2)$$

and the displacements

$$\begin{aligned} u_r &= -\frac{P}{\pi E} \left(2 \frac{x_2}{r} \ln r + (1 - \nu) \frac{x_1}{r} \operatorname{arc} \operatorname{tg} \frac{x_2}{x_1} \right) + \\ &+ A \frac{x_1}{r} + B \frac{x_2}{r} \end{aligned} \quad (3)$$

$$\begin{aligned}
 u_r &= -\frac{P}{\pi E} \left(2\nu \frac{x_1}{r} + 2 \frac{x_1}{r} \ln r - (1-\nu) \frac{x_2}{r} \right. \\
 &\quad \left. \arctan \frac{x_2}{x_1} + (1-\nu) \frac{x_1}{r} \right) + A \frac{x_2}{r} - B \frac{x_1}{r} + Cr \quad (3) \\
 u_1 &= u_2 \frac{x_1}{r} + u_\theta \frac{x_2}{r} \quad u_1 = u_r \frac{x_2}{r} - u_\theta \frac{x_1}{r}.
 \end{aligned}$$

If we consider the stress state induced within a body by an arbitrary pressure $p(\xi)$, then the stresses are given by

$$\begin{aligned}
 \sigma_{11} &= +\frac{2}{\pi x_2} \int \frac{(x_1 - \xi)^2 x_2^2 p(\xi) d\xi}{[(x_1 - \xi)^2 + x_2^2]^2} \\
 \sigma_{22} &= +\frac{2}{\pi x_2} \int \frac{x_2^4 p(\xi) d\xi}{[(x_1 - \xi)^2 + x_2^2]^2} \quad (4) \\
 \sigma_{12} &= +\frac{2}{\pi x_2} \int \frac{(x_1 - \xi)^2 x_2^3 p(\xi) d\xi}{[(x_1 - \xi)^2 + x_2^2]^2},
 \end{aligned}$$

where the integrals are evaluated over the loaded area. The sign of pressure is defined in accordance with $p(x_i) = \sigma_{22}(x_i)$ and hence contact pressures will always be negative.

Similarly, expressions for the displacements can be found.

The contact problem of two cylinders pressed together with their axis parallel is a two dimensional equivalent of Hertzian contact. The following considerations apply:

1. The load is sufficiently small for the contact patch, of width $2a$, to be small in comparison with both R_1 and R_2 , which are the radii of curvature of the cylinders. This means that the assumption that the contacted bodies can be approximated by half-planes remains valid.
2. No surface shear tractions must arise, that is, both bodies have the same elastic constants, or the coefficient of friction must vanish.

This enables the relative normal approach of particles within the contact to be approximated by a parabola and gives an elliptic contact pressure distribution

$$p(x_1) = -p_0 \sqrt{1 - (x_1/a)^2}, \quad (5)$$

where p_0 is its peak value in the middle of the contact patch. The integrals are singular with the singularity in the surface point $x_2 = 0, x_1 = \xi$. So, appropriate technique has to be used for their evaluation as it is known from the Boundary Integral Equation Method (Boundary Element Method) [13].

Muskhelishvili [14] gives a solution for a circular disc loaded by two equilibrated forces (Fig. 2).

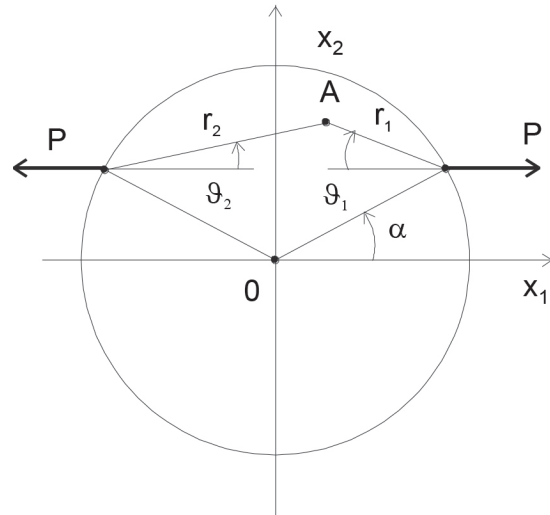


Fig. 2 Circular disc loaded by two forces

Stresses in a point A are

$$\begin{aligned}
 \sigma_{11} &= \frac{2P}{\pi} \left\{ \frac{\cos^3 \vartheta_1}{r_1} + \frac{\cos^3 \vartheta_2}{r_2} \right\} - \frac{P}{\pi R} \cos \alpha \\
 \sigma_{22} &= \frac{2P}{\pi} \left\{ \frac{\sin^2 \vartheta_1 \cos \vartheta_1}{r_1} + \frac{\sin^2 \vartheta_2 \cos \vartheta_2}{r_2} \right\} - \frac{P}{\pi R} \cos \alpha \\
 \sigma_{12} &= \frac{2P}{\pi} \left\{ \frac{\sin \vartheta_1 \cos^2 \vartheta_1}{r_1} + \frac{\sin \vartheta_2 \cos^2 \vartheta_2}{r_2} \right\}, \quad (6)
 \end{aligned}$$

and displacements

$$\begin{aligned}
 u_1 &= \frac{P}{4\mu\pi} \left\{ \frac{2(\lambda + 2\mu)}{\lambda + \mu} \ln \frac{r_2}{r_1} + \cos 2\vartheta_1 - \right. \\
 &\quad \left. - \cos 2\vartheta_2 - \frac{2\mu \cos \alpha}{\lambda + \mu} \frac{x_1}{R} \right\} \\
 u_2 &= \frac{P}{4\mu\pi} \left\{ \frac{2\mu}{\lambda + \mu} (\vartheta_1 + \vartheta_2) - \sin 2\vartheta_1 - \right. \\
 &\quad \left. - \sin 2\vartheta_2 - \frac{2\mu \cos \alpha}{\lambda + \mu} \frac{x_2}{R} \right\}, \quad (7)
 \end{aligned}$$

where R is radius of the disc and λ and μ are Lamé constants for the material of the disc.

Choosing the Hertz distribution of the contact force acting in the disc, the stress and displacement fields can be computed in a similar way (e.g. by integration of singular integrals) as given above for the half-plane.

The analysis of the stress state helps identify the critical maximum stresses in the contact region. They reveal vital information concerning the surface fatigue mechanism, plastic deformations and bearing capacity of the structure. Maximum shear stress which is in some depth below the surface and large stress gradients in the whole contact surface and sub-surface area require very fine mesh when they are to be evaluated with

required accuracy using classical numerical models like FEM or BEM.

Accuracy of the displacement analysis is responsible for the correct computation of load distribution on the rolling elements in the multi-body contact problems like rolling bearings.

2.2 3D problems

We will suppose infinitesimal elastic deformation of the bodies in contact. It means that contact pressure will be determined from mutual position of the contact surfaces assumed to be rigid in their local position. However, the local position of the contact surfaces is supposed to be determined by the total deformation of the complex system of elastic bodies, i.e. by bending of shafts, elastic deformation of housing, etc. The pressure distribution is then defined by the form of penetration of the surfaces and by the total force acting in the corresponding pair of contacting bodies. It means that the problem is non-linear and has to be solved iteratively.

We will call the 3D contact to be a point contact if the curvature of the contact surfaces does not change in the contact region. In such case the location of the contact is determined from the total deformation of the contact bodies as mentioned above and the contact surface is an ellipse. On the other side, if the contact surfaces have more general form, then we will call the contact to be a line contact. In such case the pressure distribution in the circumferential direction is defined similarly as it was in the 2D case in eq. (5), but the pressure function in longitudinal direction is not a unique function and it will depend on both geometry and location of resulting contact force for each pair of contacting bodies.

Similarly as in 2D, the basis for the numerical computation of the local contact stresses and displacements is the Boussinesq problem giving the response to a force acting in a point of the boundary of the half space.

The stresses for the problem of a concentrated normal force, P_3 , acting at the origin on the half space, $x_3 \geq 0$, are given [15] by

$$\begin{aligned} \sigma_{\alpha\beta} &= -\frac{P_3}{2\pi} \left\{ \frac{3x_\alpha x_\beta x_3}{r^5} - (1-2\nu) \cdot \right. \\ &\quad \left. \left[\frac{x_3}{r^3} \delta_{\alpha\beta} - \frac{\delta_{\alpha\beta}}{r(r+x_3)} + \frac{x_\alpha x_\beta (2r+x_3)}{r^3 (r+x_3)^2} \right] \right\}, \\ \sigma_{33} &= -\frac{P_3}{2\pi} \frac{3x_3^2}{r^5}, \\ \sigma_{3\alpha} &= -\frac{P_3}{2\pi} \frac{3x_\alpha x_3^2}{r^5}, \quad \text{with } (\alpha, \beta = 1, 2) \end{aligned} \quad (8)$$

and corresponding displacements

$$\begin{aligned} u_\alpha &= \frac{P_3}{4\pi\mu} \left[\frac{x_\alpha x_3}{r^3} - (1-2\nu) \frac{x_\alpha}{r(r+x_3)} \right], \\ u_3 &= \frac{P_3}{4\pi\mu} \left[\frac{x_3^2}{r^3} + \frac{2(1-\nu)}{r} \right], \quad \text{with } (\alpha = 1, 2). \end{aligned} \quad (9)$$

Similarly, the stresses for a concentrated tangential force [15], P_α , ($\alpha = 1, 2$), are

$$\begin{aligned} \sigma_{\alpha\beta} &= -\frac{P_\gamma}{2\pi} \left\{ \frac{3x_\alpha x_\beta x_\gamma}{r^5} - \frac{(1-2\nu)}{r(r+x_3)^2} \left[\frac{(3r+x_3)x_\alpha x_\beta x_\gamma}{r^2(r+x_3)} + \right. \right. \\ &\quad \left. \left. + \frac{(2r+x_3)}{r^2} x_\gamma x_3 \delta_{\alpha\beta} - (x_j \delta_{i\gamma} + x_i \delta_{j\gamma}) \right] \right\}, \\ \sigma_{3\alpha} &= -\frac{P_\gamma}{2\pi} \frac{3x_\alpha x_\beta x_\gamma}{r^5}, \\ \sigma_{33} &= -\frac{P_\gamma}{2\pi} \frac{3x_\gamma x_3}{r^5}, \quad \text{with } (\alpha, \beta, \gamma = 1, 2), \end{aligned} \quad (10)$$

and the displacements

$$\begin{aligned} u_\alpha &= \frac{P_\gamma}{2\pi\mu} \left[\frac{\delta_{\alpha\gamma}}{r} + \frac{x_\alpha x_\gamma}{r^3} + (1-2\nu) \left[\frac{\delta_{\alpha\gamma}}{r+x_3} - \frac{x_\alpha x_\gamma}{r(r+x_3)} \right] \right], \\ u_3 &= \frac{P_\gamma}{4\pi\mu} \left[\frac{x_\gamma x_3}{r^3} + (1-2\nu) \frac{x_\gamma}{r(r+x_3)} \right], \\ &\text{with } (\alpha, \gamma = 1, 2) \end{aligned} \quad (11)$$

The total stress and displacement fields for distributed load over the elliptical area on the half space boundaries are obtainable by integration over the area in two ways: using the cylindrical coordinates r , ϕ and x_3 , or, using the cartesian coordinates.

If, in the first case, the cartesian coordinates are chosen so that the main axes of the contact ellipse will be identical with the axes x_1 and x_2 and the half axes of the ellipse are a and b , respectively. Then r and ϕ are defined as

$$\begin{aligned} r \cos \varphi &= x_1 / a \\ r \sin \varphi &= x_2 / b. \end{aligned} \quad (12)$$

The numerical integration is performed using the Gauss quadrature rule for the r coordinate and by the equidistributed quadrature points in the circumferential direction, ϕ .

In the second case, the Gaussian quadrature rule is used for both x_1 and x_2 coordinate directions, using constant Gauss coordinate along the longer axis and variable integration limits in the second direction.

No equivalent closed solutions are available for 3D rolling elements like that for 2D cylinder given in the previous section.

3. Sub-domain formulation for the contact region

Very efficient formulation for modelling of displacement and stress fields in the contact regions can be obtained using Trefftz type reciprocity based elements. Here, the principles well known from the basic BEM formulations (see e.g. [16 and 17]) are used and so, we will give only the basic principles. For more details of the formulations used in the models see [18].

Weak formulation of equilibrium equations can be written using the principle of weighted residuals as

$$\int_{\Omega} (\sigma_{ij} + b_i) u_i^* d\Omega = 0, \quad (13)$$

where σ_{ij} and b_i are the stress tensor and body force vector, respectively. We can choose the weight functions u_i^* to be Trefftz (T-) displacement fields. The T-functions are the functions which satisfy all governing equations inside the domain and they have to satisfy the homogeneous equilibrium equations (with body force absent) of the same body in this case.

Applying both the integration per parts and the Gauss theorem to this equation two times, the following relation is obtained

$$\int_{\Gamma} t_i^* u_i d\Gamma = \int_{\Gamma} t_i u_i^* d\Gamma + \int_{\Omega} b_i u_i^* d\Omega, \quad (14)$$

where t_i are tractions acting on the domain boundaries Γ of the domain Ω . This equation expresses the reciprocity of works done by two systems of forces, the one without stars which is looked for, and another, reference state (for which all, displacements, stresses and tractions are known inside and on the domain boundaries), denoted by letters with stars.

The reciprocity equations are well known from the BEM formulations where the Kelvin fundamental solutions are used for reference state and lead to the singular integral equations. Using T-polynomials, or Kelvin solutions with the singular points located outside the domain, all integrals are regular. However, for more complex problems, the multi-domain formulation is advantageous because it leads to sparse matrices, as it is known from FEM. The displacements between the sub-domains are chosen to be compatible and the inter-domain equilibrium is satisfied in a weak, integral sense as follows

$$\int_{\Gamma_i} \delta u_i (t_i - \bar{t}_i) d\Gamma + \int_{\Gamma_i} \delta u_i (t_i^A - t_i^B) d\Gamma = \int_{\Gamma_e} \delta u_i t_i d\Gamma - \int_{\Gamma_i} \delta u_i \bar{t}_i d\Gamma = 0, \quad (15)$$

where Γ_i , Γ_t a Γ_e are the inter-domain boundaries, the boundaries with prescribed tractions and element (sub-domain) boundaries respectively and the letters with a bar denote the fields with prescribed value.

The equation (14) can be written in matrix form as

$$\mathbf{T}\mathbf{u}^e = \mathbf{U}\mathbf{t}^e + \mathbf{f}^b \quad (16)$$

and the last part of equation (15) in the form

$$\sum_e \mathbf{M}\mathbf{t}^e = \sum_e \mathbf{p}^e, \quad (17)$$

with summation over all elements.

Setting for tractions from (16) into (17), the following resulting system of discretised equations is obtained

$$\sum_e \mathbf{M}\mathbf{U}^{-1}\mathbf{T}\mathbf{u}^e = \sum_e (\mathbf{p}^e + \mathbf{M}\mathbf{U}^{-1}(\mathbf{f}^b + \mathbf{f}^p)), \quad (18)$$

or shortly

$$\mathbf{K}\mathbf{U} = \mathbf{p}. \quad (19)$$

Stresses of increased accuracy and smooth over the hole domain can be obtained from the nodal displacements and traction boundary conditions (for the points near or on the domain boundaries with prescribed static conditions) using T-functions as interpolators (see [19] for details). The convergence rate of both displacement and stresses is 4th order, when quadratic boundary elements are used in the formulation.

As the contact surfaces have mostly rotational shape, special sub-domains are used to model this kind of problems. The whole integration for obtaining the sub-domain matrices is performed over corresponding sub-domain boundaries (boundary elements) and so, the contact surfaces are easy to design. The contact sub-domain shapes are ring segments for the raceways, or full circles for the cylindrical roller elements for 2D problems and 3D ring segments and full 3D rolling elements for complex 3D problems.

The procedure of obtaining the stiffness characteristics of rolling elements in contact is an inverse procedure defined as follows:

- A. If the contact is 2D, or 3D with constant curvatures: choose both, the contact area and the pressure distribution according to the Hertz theory on the rolling element and raceways. As the problem is linear, the resulting contact force corresponding to the contact area is obtained from the penetration of both pairs of contact areas in the unloaded (initial) state and from the pressure and corresponding deformation of the contact surfaces. In this way the deformation characteristic is computed for a series of sizes of contact area and corresponding resulting contact force. The deformation characteristic gives the dependence of resulting contact force to the total deformation in direction of the resulting force.
- B. If the contact is 3D and the curvature changes in the longitudinal direction of the rolling elements (it is often

the shape obtained by the optimised design), or if some parts of both the raceway and the rolling elements are cylindrical and the resulting load is asymmetric, then we can proceed in similar way as in previous case, but we have to choose some asymmetric penetration positions (crossing longitudinal axes of rolling element and raceway) and to obtain the characteristics for several such positions and to interpolate between them for the specific conditions. The characteristics give dependence of four parameters: (1) the resulting force, (2) its position, (3) the total deformation and (4) the angle between the axes.

The rolling elements have the shape, which is advantageous to be modelled by BEM (small surface to volume ratio). The single domain formulation using T-functions is obtained directly using equation (14) for this purpose with Boussinesq's or Kelvin's functions with singularities located outside the domain for the weighting functions defining the reciprocal states. As we need to compute the stresses on and near the boundaries of such domains a very suitable procedure is defined as follows:

- A. Solve the equation (14) in the form (20) for unknown displacements from prescribed tractions in the boundary nodes (located in points on the radius R as shown in Fig. 3 for 2D problem) using the Kelvin's functions with source points y located outside the domain (on radius R_o):

$$\int_{\Gamma} T_{ij}(y,x)u_j(x)d\Gamma(x) = \int_{\Gamma} U_{ij}(y,x)t_j(x)d\Gamma(x) \quad (20)$$

where

$$U_{ij}(y,x) = -\frac{1}{16\pi(1-\nu)\mu r} \{(3-4\nu)\delta_{ij} + r_{,i}r_{,j}\} \quad (21)$$

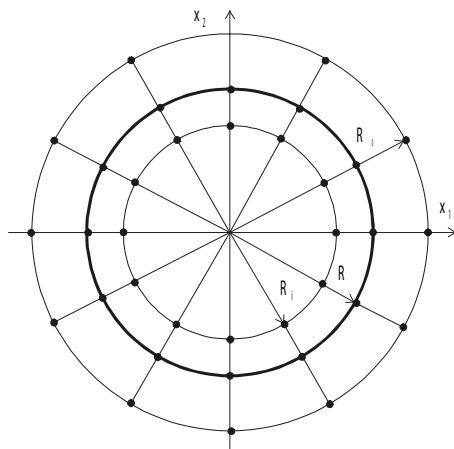


Fig. 3 2D rolling element

$$T_{ij}(y,x) = -\frac{1}{8\pi(1-\nu)r^2} \left\{ [(1-2\nu)\delta_{ij} + 3r_{,i}r_{,j}] \frac{\delta r}{\delta n} + (1-2\nu)(r_{,i}n_{,j} - r_{,j}n_{,i}) \right\} \quad (22)$$

for 3D problems. Similarly:

$$U_{ij}(y,x) = -\frac{1}{8\pi(1-\nu)\mu} \cdot \{(3-4\nu)\delta_{ij} + \ln(r) - r_{,i}r_{,j}\} \quad (23)$$

$$T_{ij}(y,x) = -\frac{1}{4\pi(1-\nu)r^2} \left\{ [(1-2\nu)\delta_{ij} + 2r_{,i}r_{,j}] \frac{\delta r}{\delta n} + (1-2\nu)(r_{,i}n_{,j} - r_{,j}n_{,i}) \right\} \quad (24)$$

for 2D problems.

- B. Compute the displacements in points y (radius R_i) inside the domain from the boundary displacements and tractions by equation (25)

$$u_i(y) = \int_{\Gamma} U_{ij}(y,x)t_j(x)d\Gamma(x) - \int_{\Gamma} T_{ij}(y,x)u_j(x)d\Gamma(x) + \int_{\Omega} U_{ij}(y,x)b_j(x)d\Omega(x) \quad (25)$$

- C. Define patch displacement fields from the nodal displacements in a node on the boundary (the point of interest) and in two neighbour nodal points on the boundary and one inside the domain and from the prescribed boundary tractions in the point of interest using (POI) second order T-polynomials with local origin of the co-ordinates in the POI. For such field it is simple to find corresponding stresses in the POI. Similarly we can proceed, when the stresses in points near the boundary are to be obtained, i.e. using the patches of nodal points which are closest to the POI.

When the displacement and stress field contain large gradients like Hertz contact fields, then the resulting field is split into the local part embodying the large gradients and the smooth part of corresponding field as

$$f^R = f^L + f^S \quad (f = u_i, \sigma_{ij}, t_i) \quad (26)$$

where the indices R , L and S denote the resulting, local and smooth part of corresponding field, respectively. The local field is described in an auxiliary region which can only partially coincide with the real region (Fig. 4). The auxiliary region contains the local field solution, whereas the real region is solved numerically with prescribed smooth boundary conditions and thus, it does not require very fine discretisation.

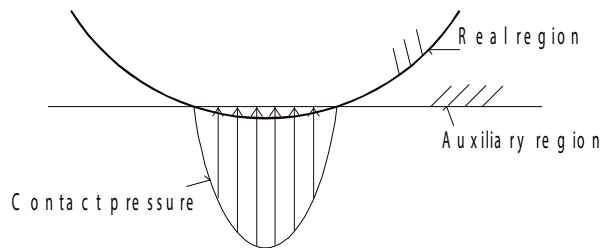


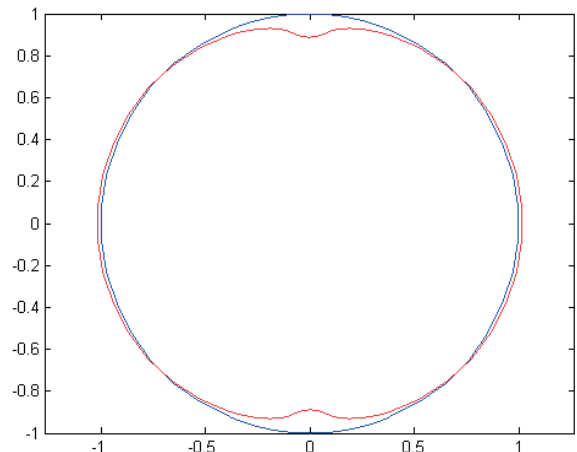
Fig. 4 Real and auxiliary region

The smooth fields are computed by the models described above, i.e. by the equation (19) for the MD formulation, or by the equation (20) for the single domain solution. When the intensity of the local field is known, then the problem can be split into local and smooth part according to (26) and solved separately for each of them, whereas in the case when its intensity is unknown (e.g. cracks, or other geometrical concentrators), then both the local displacements and traction boundary conditions have to be included into the formulation. As in the last case the local solution satisfies the governing equations in strong sense, the accuracy of the solution will not be destroyed by the large gradients and the fineness of discretisation is dictated by the smooth field part of the solution.

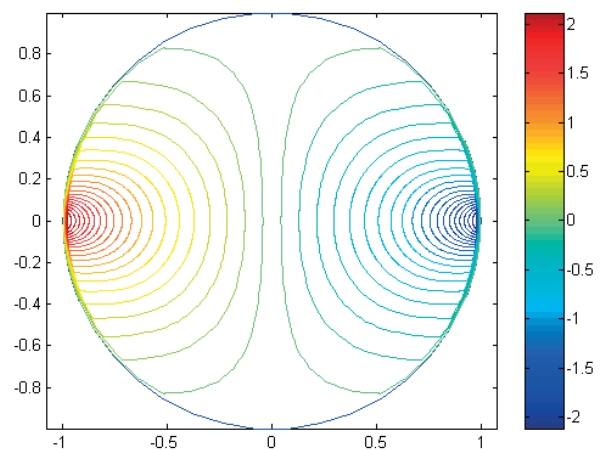
3.1 Some numerical results and discussion

The local 2D fields are studied on a cylindrical rolling element (Fig. 5). As we can see from Fig. 5, the smooth displacement field contributes to the total deformation of the cylinder by about the same amount as the local displacements. Note that the rolling contact element in the global model consists of the total displacement of the roller plus the local deformation of the raceways. The local deformation of the raceway is to understand the difference of its total displacements and the smooth field solution [18]. Figures 5e and 5f show the isolines of maximum shear stress which are responsible for plastic deformation and damage arising in some depth below the contact surface. Figure 5f contains the extreme region of this field and it is evident that the models give good results even in the close vicinity of integrand singularities.

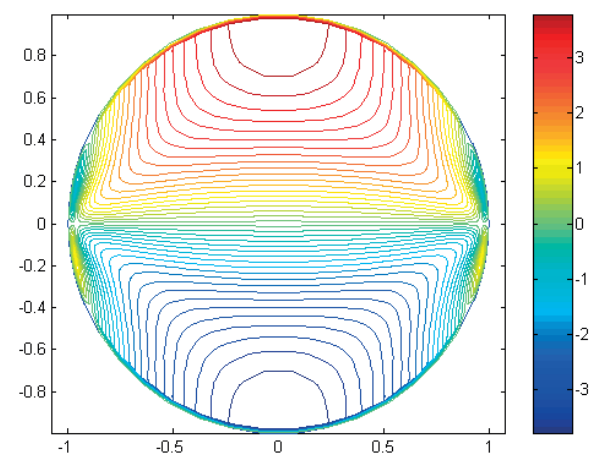
The integrals for the evaluation of the displacement and stress fields are singular, but Gauss quadrature formulas give good accuracy in all important points with except of the points on the contact surface where stresses are given by the contact pressure distribution. Generally, the stresses in this area are computed by the technique (T-polynomial interpolation from both the nodal displacements and the boundary tractions) described in the previous section.



5a: Deformation of the cylinder

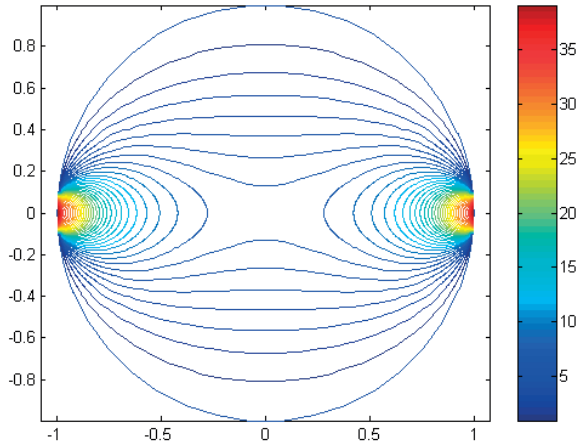


5b: u_1 displacements (in the direction of contact force)

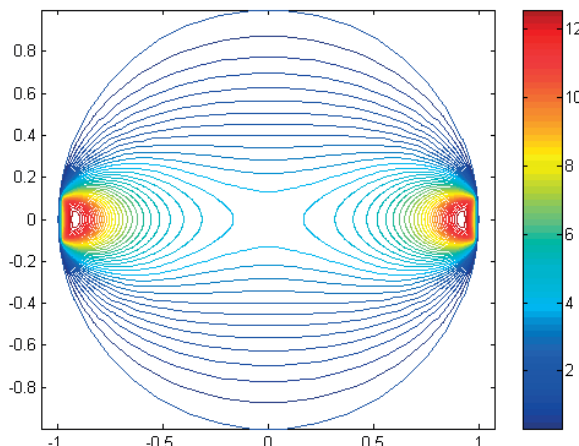


5c: u_2 displacements

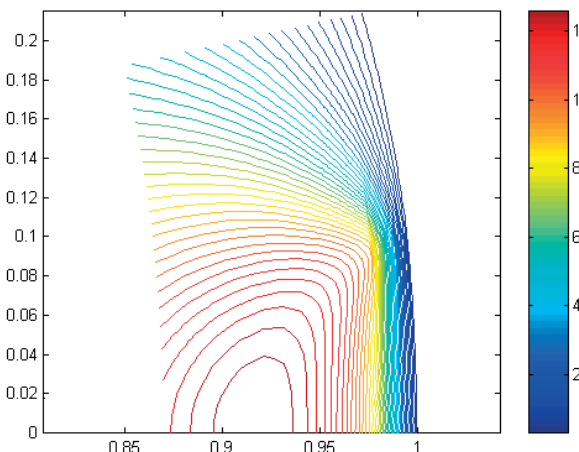
Fig. 5 Deformation and stresses in a cylinder under Hertz contact conditions



5d: Von Mises stress field



5e: Max. shear stress field



5f: Max. shear stress field in the contact zone

Fig. 5 Deformation and stresses in a cylinder under Hertz contact conditions

The raceways are modelled by the complete ring using similar technique as that for cylinders (equidistant integration points in circumferential direction), or by a ring segment both 2D and 3D problems. Examples of such elements deformed by pure bending are shown in Fig. 6 (2 x 5 quadratic boundary elements [BE] in circumferential direction and 2 x 1 BE in radial direction) and Fig. 7 (4 x 5 quadratic BE in circumferential direction and 2 x 1 BE in radial direction). Each of them defines one sub-domain. The pure bending states gave accurate displacements and stresses (with exception of truncation errors) and served for testing the accuracy of the formulation.

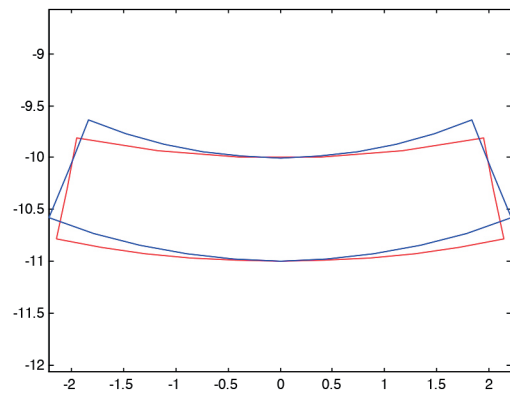


Fig. 6 2D ring segment element

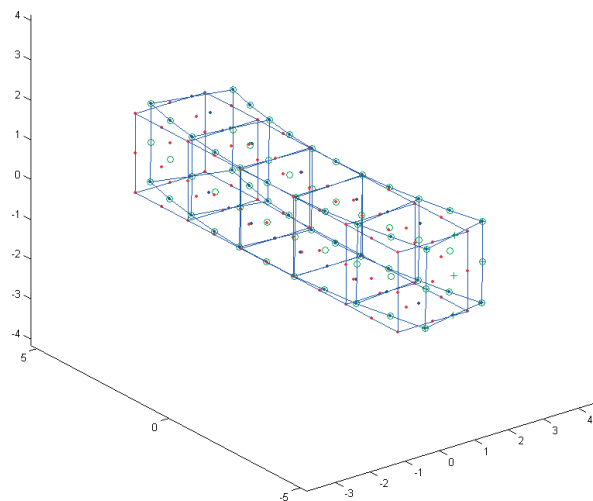


Fig. 7 3D ring segment element

Also more general forms can be used for the investigation of the local effects, but the geometry of the raceways should be defined as good as possible, e.g. it has to be modelled by the rotational surfaces.

The elliptical Hertzian contact can be solved using the potential methods of Boussinesq and Cerutti, fully described

by Love [20] and the complete solution for normal as well as shear tractions is introduced in Hills et al. [5]. Classical numerical way of integration by Gauss quadratures gives good results for some distance from the contact area, but not in very close vicinity of the contact surface.

4. Conclusions

We have shown that the contact of the bodies with cylindrical surfaces can be very effectively solved when the local fields are split out of the solution and the local problem is modelled using the Boussinesq half space solution. The other field, which is smooth enough, is then modelled by large elements. Special T-elements are introduced for the modelling of these fields in order to obtain high accuracy of the models. The stiffness matrix of the T-elements is obtained by integration over the element boundaries, which enables to conserve the cylindrical form of the contact surfaces in the computational models. This is important for the accurate enough definition of rolling contact elements for the multi-body contact problems like the rolling bearings as described in our previous model [15], in which, however, classical FE model using fine mesh was used to model the local fields.

The basic assumption by the modelling of contact problem is that the local topology of the contact region is not changed by the loading and thus the Hertz theory can be applied for each pair of contacting surfaces. Using this assumption, the

problem of obtaining the stiffness characteristics of the rolling elements is defined as an inverse problem, i.e. each body in the contact is modelled separately, which further simplifies the solution and increases the efficiency of computational models. The technique can be extended to more flexible bodies in contact when the curvature of the contact surfaces is taken into account by an iterative process. Also in such problems considerable improvements can be achieved in the rate of convergence and computer time and memory requirements reductions, because the changes are mostly not large and so small number of iteration steps can be expected to achieve the convergence, unlike it is by the classical numerical methods where many parameters (nodes) are contained in the contact area with the contact conditions changing in many of them during the iteration process.

Further improvements of the numerical treatment of the general 3D contact, as well as the use of presented method to other field problems are the aims of our current research.

Similar technique of the splitting the field containing large gradients into the local field with large gradient and another, smooth enough field, can be used also for other types of problems, e.g. problems with cracks, material inhomogenities, inclusions, etc.

Acknowledgement

The authors gratefully acknowledge support from the Slovak Grant Agency VEGA 1/0983/15.

References

- [1] PASTOREK, P., PELAGIC, Z., ZMINDAK, M.: *FEM Analysis of Stresses in Dynamic Contact Problems*. Proc. of Dynamics of Rigid and Deformable Bodies 2013, 11th intern. conference, October 9-11 2013, Usti nad Labem, 2013 ISBN 978-80-7414-607-7.
- [2] ESCHMANN, P., HASBARGEN, L., WEIGAND, K.: *Ball and Roller Bearings, Theory, Design and Applications*, John Wiley & Sons Ltd : Chichester, 1985.
- [3] CHANGSEN, W., *Analysis of Rolling Element Bearings*, Mech. Eng. Publications Ltd : London, 1987.
- [4] PILKEY, W. D.: *Formulas for Stress, Strain, and Structural Matrices*, John Wiley : New York, 1990.
- [5] HILLS, D. A., NOWELL, D., SACKFIELD, A. *Mechanics of Elastic Contacts*, Butterworth Heinemann Ltd : Oxford, 1993.
- [6] CASTLEBERRY, G. A.: *Analyzing Contact Stresses More Accurately*, Machine Design, 1984, pp. 92-97.
- [7] KALKER, J. J.: *An Algorithm for the Computation of the Frictionless Contact Pressure between Two Bodies of Revolution*, TH Delft, 1981.
- [8] SMITH, J. O., LIU, C. K.: Stresses Due to Tangential and Normal Loads on an Elastic Solid with Application to Some Contact Stress Problems, *J. of Appl. Mech.*, 21, 1953, 157-166.
- [9] TIMOSHENKO, S. P., GOODIER, J. N.: *Theory of Elasticity*, 3rd ed., McGraw-Hill : New York. 1970.
- [10] BLOKH, B. I.: *Theory of Elasticity (in Russian)*, Univ. Press : Kharkov, 1964.
- [11] KNOTHE, K., LE-THE, H.: A Contribution to the Calculation of the Contact Stress Distribution between Two Elastic Bodies of Revolution with Non-elliptical Contact, *Computers & Structures*, 18, 1984, pp. 025-1033.
- [12] SCHAUDE, B.: *Optimal Profiling of Rolling Elements of Cylinder Rollers (in German)*, Dissertation, University Karlsruhe, 1978.
- [13] VIJAYAKAR, S.: A Combined Surface Integral and Finite Element Solution for a Three-dimensional Contact Problems, *Int. J. Numer. Meth. in Engng.*, 31, (1991), 525-545.

- [14] MUSKHELISHVILI, N., I.: *Some Basic Problems of Mathematical Theory of Elasticity, (in Russian)*, Nauka : Moscow (1966).
- [15] KOMPIS, V.: HANDRIK, M., ELESZTOS, P., KOCH, F.: *Analysis and Design of Roller Bearings*, EAEC 2001 Congress, Bratislava, June, 2001, CD-ROM 2001.
- [16] BALAS, J. SLADEK, J. SLADEK, V.: *Stress Analysis by Boundary Element Methods*, Elsevier : Amsterdam 1989.
- [17] KUPRADZE, V. D.: *Potential Methods in Theory of Elasticity (in Russian)*, Nauka : Moscow, 1963.
- [18] KOMPIS, V.: *Selected Topics in Boundary Integral Formulations fo Solids and Fluids*, CISM Courses and Lectures, No. 433, Springer - Verlag : Wien, 2002.a
- [19] KUHN, G.: *Boundary Element Technique in Elastostatics and Linear Fracture Mechanics*, in E. Stein, W. L. Wendland, eds., *Finite Element and Boundary Element Techniques Form Mathematical and Engineering Point of View. CISM Courses and Lectures, No. 301*, Springer - Verlag : Wien, 1988, pp. 109-170.
- [20] LOVE, A. E. H.: *A Treatice on the Mathematical Theory of Elasticity*, Cambridge University Press : Cambridge, 1927.

Frantisek Brumerick - Maria Tomasikova - Aleksander Nieoczym *

EPICYCLIC GEAR TRAIN SYNTHESIS

The synthesis of an epicyclic gear train is a difficult task that can be solved by different methods with significantly various computational time demands. This article describes effective approach to the two-linked epicyclic gear train synthesis. The method described in this article is based on the fundamental gear ratio calculation for each possible combination of gearbox external elements connected to the internal planetary structure.

Keywords: Epicyclic gear train, synthesis, Willis formula.

1. Introduction

The two-linked epicyclic gear train synthesis rests in the all possible kinematic structure creation and the selection of its best alternative.

The starting point of the calculation is the definition of gear ratios in the solved gearbox via selected method. The most common method for the ratio calculation is the drive resistance method, which generates the minimum gear ratio and the method of the maximum velocity, which generates the minimum gear ratio [1].

After defining the couple of ratios, the main task of the synthesis is to find the optimal kinematic structure of the epicyclic gear train via the analytical method using the specific features of the kinematic equations of the two-linked planetary gear trains [2].

2. Single epicyclic gear kinematic equations

The basic equation, which characterises the epicyclic gear train with 3 basic elements (sun gear p , ring gear q and carrier r) and which has 2 degrees of freedom (DOF) is so called Willis formula

$$\omega_p - \omega_q u_v = \omega_r (1 - u_v), \quad (1)$$

where: ω_p speed of the central wheel p (sun gear),
 ω_q speed of the central wheel q (ring gear),
 ω_r speed of the carrier r ,
 u_v fundamental epicyclic gear ratio.

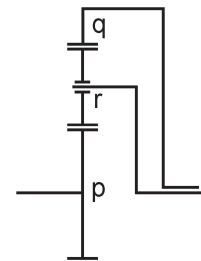


Fig. 1 Single epicyclic gear train with internal geared ring gear
 (Source: authors)

The fundamental epicyclic gear ratio is defined as

$$u_v = \pm \frac{z_q}{z_p} = \frac{\omega_p}{\omega_q} \Big|_{\omega_r = 0}, \quad (2)$$

where: z_q tooth number of the central wheel q ,
 z_p tooth number of the central wheel p .

The sense of the gear ratio is negative if the central wheel q has the internal gearing, which is the case of both of the two-linked simply epicyclic gear trains solved in this task (Fig. 3).

The Willis equation (1) has specific properties considering the fundamental epicyclic gear ratio u_v as negative [3] and [4]:

- it is linear and homogeneous,
- the summary of its constant coefficients is zero: $1 - u_v - (1 - u_v) = 0$
- the coefficient with the lowest absolute value is 1 and it is placed by the speed of the central wheel p ,

* ¹Frantisek Brumerick - ¹Maria Tomasikova - ²Aleksander Nieoczym
¹Faculty of Mechanical Engineering, University of Zilina, Slovakia
²Mechanical Engineering Faculty, Lublin University of Technology, Poland
 E-mail: brumerickf@fstroj.uniza.sk

- the coefficient with the highest absolute value is $|1 - u_v|$ and it is placed by the speed of the central wheel q ,
- the equation is valid for any epicyclic gear with three basic elements (p, q, r) with two degrees of freedom.

Every step-gearbox based on epicyclic gears has following external elements:

- Input A ,
- Output X ,
- Braking elements n , which represents the connection of the internal gearbox element to the gearbox frame to obtain the $DOF = 1$. The number of braking elements corresponds with the number of gear ratios [5] (excluding the ratio $i_{AX} = 1$ - direct drive)

Thus, the preferred ratio is shifted by the activating of the proper braking element ($n = 1, 2, \dots$).

The gear ratio between the input and output is defined as [6]

$$i_{AX} = \frac{\omega_A}{\omega_X}, \quad (3)$$

where: ω_A speed of the input A ,
 ω_X speed of the output X .

Consider the input A is connected to the central gear p , the output X is connected to the central gear q and the stopped braking element n is the carrier r (Fig. 2).

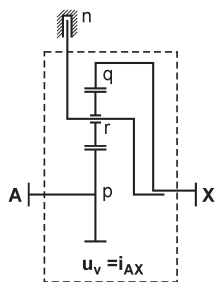


Fig. 2 Single epicyclic gear in the basic connection (Source: authors)

Then, the fundamental epicyclic gear ratio u_v is the same as the gear ratio between the input and output of the mechanism i_{AX} and the Willis formula can be represented also with the help of input and output speeds of the epicyclic gearbox and the gear ratio between input and output i_{AX} as

$$\omega_A - \omega_X i_{AX} = \omega_n (1 - i_{AX}), \quad (4)$$

where: ω_A speed of the input - central wheel p ,
 ω_X speed of the output - central wheel q ,
 ω_n speed of the braking element - carrier r ,
 i_{AX} desired gear ratio.

Each simple planetary gear (Fig. 1) can produce 6 gear ratios dependent on the motion state [7] and [8]. The motion state is described by the graphic expression ($p \rightarrow q |_{r=0}$). The input element is placed on the first place (p), the arrow symbol (\rightarrow) is expressing the power flow to the output element behind the arrow (q), whereby the stopped element (r) is described behind the vertical line ($|_{r=0}$). The example of the motion state is matching the gear structure in Fig. 2.

The relations $i_{AX} = f(u_v)$ and $u_v = f(i_{AX})$ are shown in Tables 1 and 2.

Relations between the gear ratio i_{AX} and the fundamental ratio u_v Table 1

Motion state	$i_{AX} = f(u_v)$	Motion state	$i_{AX} = f(u_v)$
$p \rightarrow q _{r=0}$	$i_{AX} = u_v$	$q \rightarrow p _{r=0}$	$i_{AX} = \frac{1}{u_v}$
$p \rightarrow r _{q=0}$	$i_{AX} = 1 - u_v$	$r \rightarrow p _{q=0}$	$i_{AX} = \frac{1}{1 - u_v}$
$q \rightarrow r _{p=0}$	$i_{AX} = \frac{u_v - 1}{u_v}$	$r \rightarrow q _{p=0}$	$i_{AX} = \frac{u_v}{u_v - 1}$

Relations between fundamental ratio u_v and the gear ratio i_{AX} Table 2

Motion state	$u_v = f(i_{AX})$	Motion state	$u_v = f(i_{AX})$
$p \rightarrow q _{r=0}$	$i_{AX} = u_v$	$q \rightarrow p _{r=0}$	$u_v = \frac{1}{i_{AX}}$
$p \rightarrow r _{q=0}$	$u_v = 1 - i_{AX}$	$r \rightarrow p _{q=0}$	$u_v = \frac{i_{AX} - 1}{i_{AX}}$
$q \rightarrow r _{p=0}$	$u_v = \frac{1}{1 - i_{AX}}$	$r \rightarrow q _{p=0}$	$u_v = \frac{i_{AX}}{i_{AX} - 1}$

3. Two-linked epicyclic gear kinematic equations

If the number of desired non-direct gear ratios is 2, there are 4 external elements needed to obtain the desired ratios [9]. The structure of such gearbox without connections between external and internal element connections is shown in Fig. 3.

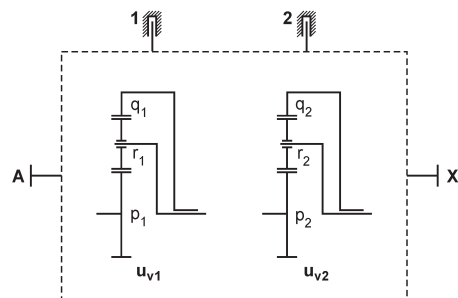


Fig. 3. Two-linked epicyclic gear - external and internal elements (Source: authors)

By the consideration of the upper described assumptions defined for single epicyclic gear, two basic equations describing the relations among the elements A, X, I and 2 respectively can be written:

$$\begin{aligned} \omega_A - \omega_X i_{AX1} &= \omega_1 (1 - i_{AX1}), \\ \omega_A - \omega_X i_{AX2} &= \omega_1 (1 - i_{AX2}) \end{aligned} \quad (5)$$

These are so called basic equations describing the relations between the speeds of the external elements A, X and I , or A, X and 2 considering that the desired gear ratio can be achieved with the help of one planetary gear set using the described external elements connected to the internal planetary gear elements ($p_1, q_1, r_1, p_2, q_2, r_2$) in so far unknown structure [10].

The other two so called derived equations can be obtained using the two basic equations (5). The product of this mathematical notation is the relations between the elements A, I and 2 , or X, I and 2 respectively. The equations can be written in the form of

$$\begin{aligned} \frac{\omega_A - (1 - i_{AX1})\omega_1}{i_{AX1}} &= \frac{\omega_A - (1 - i_{AX2})\omega_2}{i_{AX2}}, \\ -i_{AX1}\omega_X - (1 - i_{AX1})\omega_1 &= -i_{AX2}\omega_X - (1 - i_{AX2})\omega_2 \end{aligned} \quad (6)$$

After mathematical modification of the derived equations (6), they can be written as

$$\begin{aligned} \omega_A - i_{A12}\omega_X &= \omega_1 (1 - i_{A12}), \\ \omega_A - i_{X12}\omega_X &= \omega_1 (1 - i_{X12}) \end{aligned} \quad (7)$$

where: $i_{A12} = \frac{-(1 - i_{AX1})i_{AX2}}{i_{AX1} - i_{AX2}}, i_{X12} = \frac{-(1 - i_{AX1})}{i_{AX1} - i_{AX2}}$

The ratios marked $i_{AX1}, i_{AX2}, i_{A12}, i_{X12}$ can be considered as so called general ratio i_q , which will identify the internal structure of the mechanism in next calculations.

The general gear ratio i_q and the fundamental epicyclic gear ratio u_v are in mutual relation depending on connections between the external elements of the planetary gear train ($A, X, I, 2$) and internal planetary elements of the planetary gear train ($p_1, q_1, r_1, p_2, q_2, r_2$).

The relations $i_q = f(u_v)$ and $u_v = f(i_{AX})$ derived from Tables 1 and 2 are shown in Tables 3 and 4.

Relations between the gear ratio i_q and the fundamental ratio u_v Table 3

Motion state	$i_q = f(u_v)$	Motion state	$i_q = f(u_v)$
$p \rightarrow q _{r=0}$	$i_q = u_v$	$q \rightarrow p _{r=0}$	$i_q = \frac{1}{u_v}$
$p \rightarrow r _{q=0}$	$i_q = 1 - u_v$	$r \rightarrow p _{q=0}$	$i_q = \frac{1}{1 - u_v}$
$q \rightarrow r _{p=0}$	$i_q = \frac{u_v - 1}{u_v}$	$r \rightarrow q _{p=0}$	$i_q = \frac{u_v}{u_v - 1}$

The reciprocal table, which will be used by the synthesis, shows the relation between fundamental gear ratio of the simple epicyclic gear u_v as the function of the general gear ratio i_q (Table 2).

Relations between fundamental ratio u_v and the gear ratio i_q Table 4

Motion state	$u_v = f(i_q)$	Motion state	$u_v = f(i_q)$
$p \rightarrow q _{r=0}$	$u_v = i_q$	$q \rightarrow p _{r=0}$	$u_v = \frac{1}{i_q}$
$p \rightarrow r _{q=0}$	$u_v = 1 - i_q$	$r \rightarrow p _{q=0}$	$u_v = \frac{i_q - 1}{i_q}$
$q \rightarrow r _{p=0}$	$u_v = \frac{1}{1 - i_q}$	$r \rightarrow q _{p=0}$	$u_v = \frac{i_q}{i_q - 1}$

4. Synthesis of the two-linked epicyclic gear

The equations in Table 4 can be used by finding the proper possibilities of fundamental ratio u_v of all possible combinations of connections of external elements to internal gear train elements ($AX1, AX2, AI2, XI2$) using a simple algorithm, which calculates all the possible values of u_v that satisfy the specified criteria.

The most common criteria are the minimal planet gear bearings dimensions criteria $u_v \leq -1, 3$ and the radial gearbox dimensions criteria $u_v \geq -4$.

The motion state of the mechanism with satisfactory u_v value defines the connections between the external elements of the planetary gear train (A, X, n) and internal planetary elements of the planetary gear train (p, q, r).

If two gear ratios have to be achieved, there is two-linked epicyclic gear train needed. The calculation of the fundamental ratio u_v has to be done for every mechanism that is defined by the equations (5) and (7). The result of the calculation is the matrix with $4*6=24$ values of the fundamental epicyclic gear ratios.

The number of the two-linked epicyclic gear trains valid for the desired gear ratios varies according to the number of usable mechanisms calculated by the equation

$$C_k(n) = \binom{n}{k} = \frac{n!}{(n-k)!k!} \quad (8)$$

where: C number of combinations of the n elements taken k times,
 n number of basic and derived mechanism equations
 k number of planetary gear train links

If each of the mechanisms ($AX1, AX2, AI2, XI2$) satisfies the criteria for fundamental ratio u_v , there are

$$C_2(4) = \frac{4!}{(4-2)!2!} = 6 \quad (9)$$

combinations of possible two-linked epicyclic gear trains ($AX1-AX2, AX1-AI2, AX1-XI2, AX2-AI2, AX2-XI2, AI2-XI2$).

The motion states of the two-linked simple epicyclic gears with the satisfactory u_{v_1} and u_{v_2} values define then the connections between the external elements of the planetary gear train ($A, X, I, 2$) and internal elements of the planetary gear train ($p_1, q_1, r_1, p_2, q_2, r_2$) shown in Fig. 3.

5. Conclusion

The synthesis of two-linked epicyclic gears produces the planetary gearbox with two possible gear ratios shifted by braking

of two control elements. The way how to connect the external and internal elements of the gearbox according the desired gear ratios is based on the fundamental gear ratio calculation for each possible combination of gearbox external elements connected to the internal planetary structure and the control of its value that defines their motion state. The final structure is a two-linked epicyclic gear train built-up from two of valid simple gear combinations [11 and 12].

References

- [1] KOHAR, R., HRCEK, S., MEDVECKY, S.: Usage of Dynamic Analysis to Determine Force Interactions between Components of Rolling Bearings. *Communications - Scientific Letters of the University of Zilina*, vol. 14, No. 3, 2012, pp. 62-67.
- [2] KAMPF, R., LIZBETIN, J., LIZBETINOVA, L.: Requirements of a Transport System User. *Communications - Scientific Letters of the University of Zilina*, vol. 14, No. 4, 2012, pp. 106-108.
- [3] DROZDZIEL, P., KRZYWONOS, L.: The Estimation of the Reliability of the First Daily Diesel Engine Start-up During its Operation in the Vehicle. *Maintenance and Reliability*, 1(41), 2009, pp. 4-10, ISSN 1507-2711.
- [4] HANDRIK, M., VASKO, M., KOPAS, P., SAGA, M.: Effective Finite Element Solution and Post-processing for Wide Load Spectrum. *Communications - Scientific Letters of the University of Zilina*, vol. 16, No. 3A, 2014, pp. 19-26.
- [5] SAGA, M., VASKO, M., KOPAS, P., JAKUBOVICOVA, L.: Numerical Algorithm for Beam Residual Stress Identification. *Communications - Scientific Letters of the University of Zilina*, vol. 16, No. 3A, 2014, pp. 13-18.
- [6] DROZDZIEL, P., KOMSTA, H., KRZYWONOS, L.: An Analysis of Costs of Vehicle Repairs in a Transportation Company - Part I. *Transport Problems*, vol. 7, No. 3, 2012, pp. 67-75.
- [7] DROZDZIEL, P., KOMSTA, H., KRZYWONOS, L.: An Analysis of Costs of Vehicle Repairs in a Transportation Company - Part II. *Transport Problems*, vol. 7, No. 4, 2012, pp. 7-11.
- [8] SAPIETOVA, A., SAGA, M., NOVAK, P., JAKUBOVICOVA, L.: Multi-software Platform for Solving of Multibody Systems Synthesis. *Communications - Scientific Letters of the University of Zilina*, vol. 14, No. 3, 2012, pp. 43-48.
- [9] DROZDZIEL, P., KRZYWONOS, L., MADLENAK, R., RYBICKA, I.: Selected Aspects of Analyses of Failure Rates of Active Safety Systems in Buses. *Communications - Scientific Letters of the University of Zilina*, vol. 16, No. 3, 2014, pp. 114-119.
- [10] KOHAR, R., HRCEK, S.: Dynamic Analysis of a Rolling Bearing Cage with Respect to the Elastic Properties of the Cage for the Axial and Radial Load Cases. *Communications - Scientific Letters of the University of Zilina*, vol. 16, No. 3A, 2014, pp. 74-81.
- [11] BUKOVA, B., BRUMERCIKOVA, E., MADLENAK, R.: *Transport and e-commerce (in Slovak)*. Bratislava : Wolters Kluwer, 2014, 172 p., ISBN 978-80-8168-130-1.
- [12] BUKOVA, B., BRUMERCIKOVA, E., KOLAROVSKZI, P.: *Spedition and Logistics (in Slovak)*. Bratislava : Wolters Kluwer, 2014, 318 p. ISBN 978-80-554-0925-2.

Milan Zmindak - Zoran Pelagic - Martin Nagel - Lukas Smetanka - Zuzana Stankovicova *

SIMULATION MODELING OF BARREL BORE WEAR UNDER DYNAMIC PRESSURE LOAD

Wear is one of the major forms of material deterioration, often limiting both the life and the performance of the industrial components and requiring frequent replacement of the components. Wear is a very complex process and occurs by combination of several factors, such as the type of lubrication, loading speed, temperature materials, surface finishing and hardness. To simulate wear as a whole is very difficult, in many cases even not possible. The simulation by using the finite element method (FEM) is becoming increasingly popular and accessible. The FEM can also be used by solving mechanical wear, where it is critical to know the right way and method for arriving to the correct results. The method for obtaining additions of wear in the paper is developed on the base of previous practice, which used the combination of finite-element models and external algorithm for calculating wear. A FEM program ABAQUS has been used in this paper. The additions of degradation were obtained from an own developed script from MATLAB software, which is used to calculate selected equations and specific outputs in ABAQUS.

Keywords: Gun barrel bore dynamics, wear of materials, finite element method, pressure load.

1. Introduction

The presence of wear has been known for several millennia. Wear is one of the major forms of material deterioration, often limiting both life and performance of the industrial components. This phenomenon has not been fully explained till today. This is an unavoidable effect. Wear is affected by a variety of conditions, such as the type of lubrication, loading, speed, temperature, materials, surface finish and hardness. For example, nitrided steels are widely used due to their superior hardness and attractive surface hardness, fatigue life and tribological properties [1]. The prediction of wear is therefore an important part in mechanical engineering. The degradation of surfaces is not always an undesirable factor. Sometimes surface degradation is desired, for example a pencil drawing on paper, where the soft graphite is damaged. It is also desired by processing of materials, because without abrasion it is not possible to polish steel to the required surface roughness. Nevertheless, if the process of wear is known for a long time, the scientific studies of wear are relatively new. Consequently there are a few theories about wear not always the same.

Because of the complexity of the wear process, there are still lacks to fully understand the wear behavior. It is very

difficult directly to observe wear in contact of two moving bodies. Experiments must rely on the results and observations made after individual tests and then causes of wear can be considered.

There are two methods for grading of wear. The first are the conditions under which the wear occurs. It is, for example, the presence of lubricant, or solid abrasive particles. The second method is to choose one of the four operating mechanisms which were developed by Lim and Ashby [2]. These are seizing, melting, oxidation and plasticity. Plasticity is classified as the mechanical wear area.

The finite element method is known to be an effective numerical tool for the solution of boundary value problems on complex domains [3, 4 and 5]. Today, FEM methods are used for the analysis of every major engineering design and probably in every branch of scientific studies. The method is now used primarily through the application of commercial finite element programs ABAQUS, ANSYS, AUTODYN, etc. These programs are used on mainframes, workstations and PCs and are employed to solve very complex problems.

The main task of the FEM in the wear calculations is to compute the fields of contact stresses [6 and 7]. The elements of different type and shape with complex loads and boundary conditions can be used simultaneously. The method for

* ¹Milan Zmindak, ¹Zoran Pelagic, ²Martin Nagel, ³Lukas Smetanka, ¹Zuzana Stankovicova

¹Department of Applied Mechanics, Faculty of Mechanical Engineering University of Zilina, Slovakia

²DJH Engineering Center, INC., Martin, Slovakia

³Department of Transport and Handling Machines, Faculty of Mechanical Engineering University of Zilina, Slovakia

E-mail: milan.zmindak@fstroj.uniza.sk

obtaining additions of wear in this paper is developed on the base of previous practice, which used the combination of finite-element models and external algorithm for calculating wear. These practices were mainly from the works of Berabdallah and Olender [8].

The additions of degradation were obtained from an own developed script from MATLAB software, which is used to calculate selected equations from Lim and Ashby and specific outputs in FEM software ABAQUS.

2. The current state of modeling of shot dynamics

In modern times we get to the forefront of simulating of various processes in a wide spectrum of disciplines. Studying the dynamics of weapons is no exception. Experiments are often replaced by simulations to simplify and accelerate the acquisition of required results for research and customers. Every problem can have unmistakable properties, different initial and boundary conditions, various material properties, types or the load application. Making experiments in tasks with high number of variations is very expensive and time-consuming, which is in these times unfavorable for anyone. The FEM models allow assembling parametric tasks where it is possible to fast and effectively change the geometry, material properties, boundary conditions and loading, while the only cost is the computing time of numerical solution. Simulations of shooting are very complex; where it is often needed to take into account many simplifications. Therefore, it is necessary to compare the results of simulations with the results of experimental measurements. The FEM is using either modal or direct integration techniques. Given the complexity of the task, the way of direct integration with explicit numerical schemes is recommended [9].

Wear is divided into six types: adhesion, fatigue, abrasive, vibration, cavity and erosive. The mechanism of wear can be understood as a dynamic action, which is dependent on many parameters and on the prediction of the problem, defined as the initial value of the problem. Wear in general can be defined in the form of equation as:

$$\frac{dh}{ds} = f(\text{load, velocity, temperature, material properties, lubrication, etc.}) \quad (1)$$

where h represents the depth of wear and s represents the length of traveled path. Many wear models exist; their mathematic expressions differ from simple empiric relationship to difficult equation dependent on physical definition [10]. Parameters and coefficients are usable only for one solved task in many cases. Only few of them can be used to verify wear in practice. The most widely used model for linear wear is defined by an equation where the rate of wear is proportional to normal load

$$\dot{Q} = K\tilde{p} \quad (2)$$

where \dot{Q} is the rate of wear, K the coefficient of wear and \tilde{p} is the normalized pressure. This equation is described in literature as the Archard law of wear, despite its basic form was published by Holm [11] expressed as

$$\frac{V}{s} = K\frac{F_N}{H} \quad (3)$$

where represents the volume of wear, F_N normal force and H is the hardness of material. The wear coefficient K was introduced to better represent the agreement of simulation and experiment. According to Holm, it expresses the number of abraded atoms in mutual contact. According to Archard, it's the probability, that by mutual interaction of surface roughness particles of wear are created. The value of this coefficient should be obtained by an experiment and it is always lower than 1.

The depth of wear - h has a deeper meaning for engineering practice. Archard subtracted the contact surface A and obtained the equation

$$\frac{V}{As} = \frac{h}{s} = kp \quad (4)$$

where k is dimensional wear coefficient (Pa^{-1}) and p is the normal contact pressure (Pa). For linear wear of delamination we can write the expression

$$\frac{dh}{ds} = kp \quad (5)$$

Expanding eq. (2) by adding the influence of temperature we obtain [12]

$$\dot{Q}_{melt} = \frac{(T_{melt} - T_0)H}{T^* L_{melt} \beta \tilde{v}} \left(\alpha_{12} f_{Fr} \tilde{p} \tilde{v} \frac{T^* \beta}{T_{melt} - T_0} \right) \quad (6)$$

where T_{melt} is the melting temperature, T_0 is the ambient temperature, T^* represents the equivalent to melting temperature for steel, f_{Fr} is the friction coefficient, α_{12} and β represent constants, L_{melt} is latent heat of steel melting and \tilde{v} is the normalized speed.

2.1 Requirements on the model

Simulating shot dynamics by using parametrical models should be closest to reality, so the results can give good insight for different types of ammunition (displacement, velocity etc.). The current research is considered with these conditions [13]:

Precise geometry of the model: the weapon is composed of many parts, which are in contact with each other. Friction is also included in the model.

Shaped contact: is between projectile and segment created by notches. The segment carries motion through shaped contact on the projectile due to pressure of flue gases.

Explosion: is replaced with pressure load, which is applied to the barrel bore, segments, the grenade and on the tail fins. The area where the pressure load is applied is changing with time. Depending on the phase it is increasing or decreasing.

The damping mechanism depending on the weapon type is either a spring or hydraulic. Using the hydraulic concept the simulation is extended by the prescribed recoil force. For springs the recoil force function is the immediate recoil force.

The cylindricity of the barrel: the model must contain disorders because the barrel is not perfectly direct.

3. The models of weapon wear

An internal ballistics environment of weapon causes complications in experimental analysis. Therefore, the FEM is used to analyze the problem. The wear of the barrel bore is a complex task, therefore the analytical modeling is aimed on particular problems on a smaller scale. The approaches that can predict wear are empirical and computational [12 and 14].

The flowchart of the wear module is shown in Fig. 1.

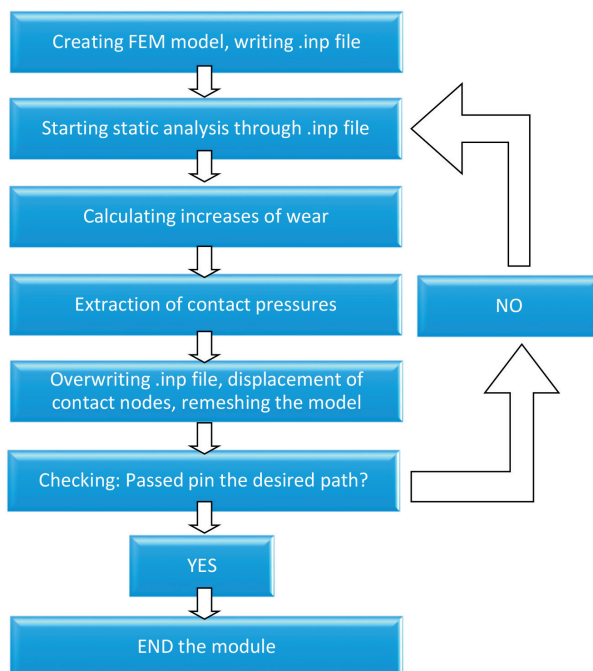


Fig. 1 Flowchart of the wear module

The script was made in the mathematical software MATLAB. In the first step the script starts the analysis in ABAQUS through background MATLAB on the base of the input file (*.inp) which was created to model the assembly.

For the solution of wear we need the contact pressures in selected nodes from the results. The script subsequently waits for the completion of the analysis. In the second step an output data file is processed so that it can be overwritten. In the third step the script calculates the corresponding increases of wear on the base of the selected equation of wear by Lim and Ashby. The values of increases assigns to the positions in the Y axis. The whole model is fitted from the contact area, therefore it needs to be re-meshed to the original contact position. The last step represents the cycle, which either starts the next simulation, or, depending on the total distance, ends the simulation process. During the computational process the computed increments of wear are displayed.

4. Transient analysis the dynamics of shot

For modeling the whole assembly of shooting from a barrel, all functional parts must be created and added to the simulation, in our case it is the housing with complete damping mechanism (hydraulic or spring), barrel inlaid to housing, bullet formed penetrator overlaid segments of the guide ring, wherein the segments are associated with a sealing ring. For our calculations it is sufficient to make a simplified 2D axis-symmetric assembly model consisting of 125 mm smooth tank barrel T-72, guide ring and of anti-tank warhead APFDS BM-15 penetrator.

4.1 Mesh

In areas where high pressures are anticipated there are smooth elements which are increased in the outward direction to save computational memory. The smallest elements have the size of 1x1 mm and they consist of regular bilinear elements. The transient areas were made up of triangles; they were used to increase magnification with elements through two layers of the size 4x4 mm. FEM model of the assembly is described in Fig. 2 and detailed view of the mesh is shown in Fig. 3.

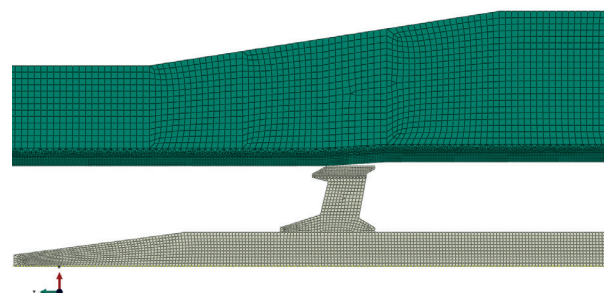


Fig. 2 FEM model of the assembly

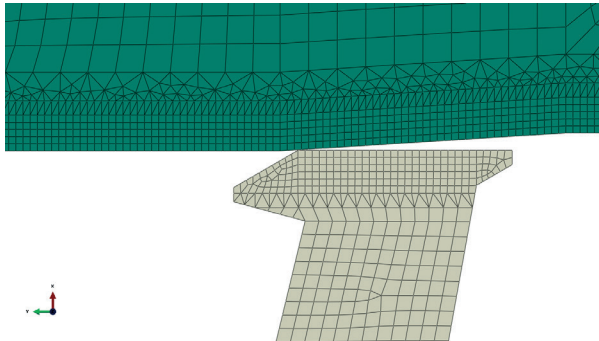


Fig. 3 Detailed view of the mesh

4.2 Materials

All the considered materials behave as elastoplastic materials. The barrel material is similar to steel STN 16 540 and it is stronger compared with the material of the guiding ring, which is similar to steel STN 16 240. The mechanical properties of used material are given in Table 1.

Material properties of used materials

Table 1

	E [MPa]	μ [-]	ρ [kg.mm ⁻³]	R_e [MPa]	R_m [MPa]
Barrel	210000	0.3	$7.84 \cdot 10^{-6}$	1185	1488
Segment	210000	0.3	$7.84 \cdot 10^{-6}$	600	894

4.3 Boundary conditions and loading

By real shot from a tank the barrel is present during the process in several mutual contact areas. These are the teeth penetrators with segments, the segments with guiding ring and tank barrel. The single parts were necessary to simplify and therefore only the contact between the segment and barrel bore was ultimately considered. The friction coefficient between steels is 0.8. The boundary conditions for the idealized case and referred to as direct loading are shown in Fig. 4.

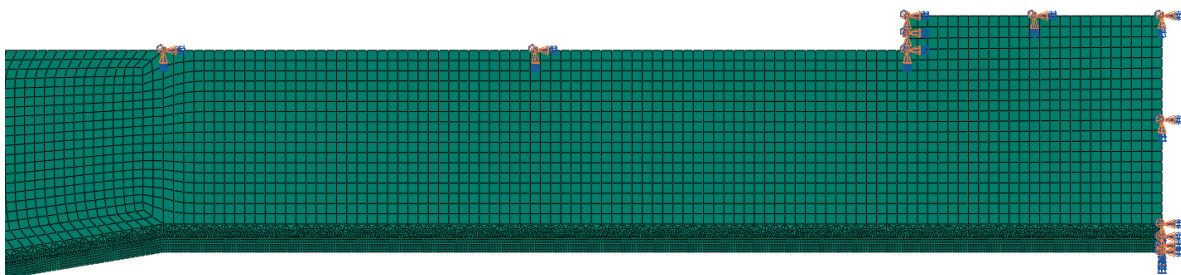


Fig. 4 Boundary conditions applied on the surface of the barrel

4.4 Results of the wear barrel bore module

In view of the amount of data the computational times of each cycle were different. For each area the complete analysis time was 30 cycles. One cycle was considered as one shot. The development of wear in the first examined area is described in Fig. 5. The graph in Fig. 6 shows details of history of the first shot.

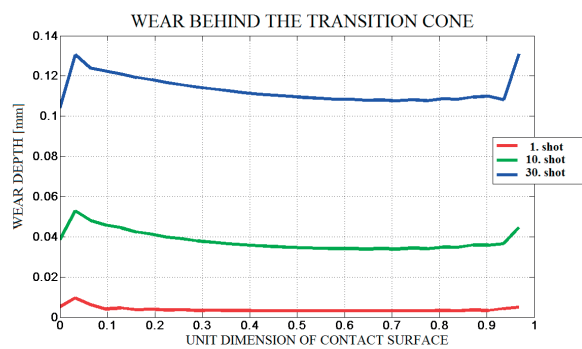


Fig. 5 Evaluation of wear in the contact surface during shots (area behind the transition cone)

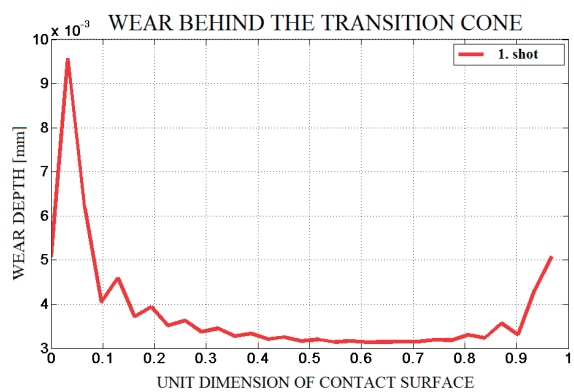


Fig. 6 Detail of wear in the contact surface after first shot

The value of maximal wear after 30 shots is around 0.13 μm . From the graph it is clear that the wear grows faster in the contact area with the leading edge. The maximal deviations of the barrel bore wear are actually on its end, therefore the load applied on the leading edge should be disregarded.

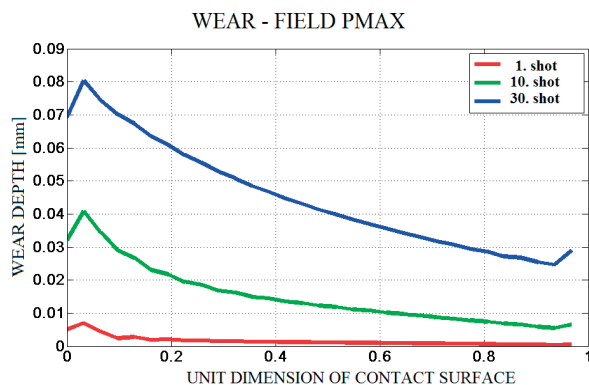


Fig. 7 Evaluation of wear on the contact surface in the field P_{max}

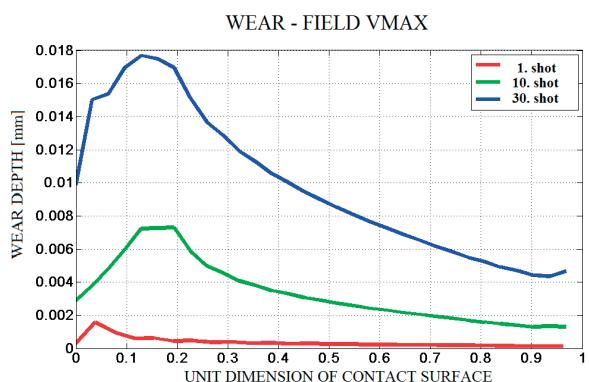


Fig. 8 Evaluation of wear on the contact surface in the field V_{max}

Figures 7 and 8 describe increases of wear in P_{max} and V_{max} fields. From these graphs it is clear that the more shots are fired from the chamber the less wear is on the barrel.

On the base of the obtained results the module was made which simulated the wear on examined areas by using a simplified FEM model of T-72 tank barrel bore. The module of calculation of wear used the equation (6). The minimal wear for areas 1, 2 and 3 amounted after 30 cycles the values 130, 80 and 18 μm as it is shown in the previous figures.

5. Conclusion

In this paper an algorithm for wear calculation is presented. The algorithm uses simple equation based on the delamination wear formulation with the combination with commercial FE code ABAQUS. The paper has shown on an example that it is possible to simulate wear of materials using interface coupling of a MATLAB code and commercial software to calculate the stresses needed as input data for the wear module. The main objective of this work was to extend the possibilities of the ABAQUS program and to include the possibility of modeling wear in dynamical analysis by including also some factors as temperature. This will increase the possibility of modeling of wear processes using ABAQUS or a similar FE software.

A two dimensional FE model of a barrel bore consisting of the barrel and a shot segment was modeled. The model was used to show wear depth through time at various distances, in this case the distance was considered in shot times. The results show the decreasing of wear depth with the time steps (shots). The contours have a good agreement with results presented in literature, and can be also verified experimentally.

Acknowledgement

The authors gratefully acknowledge the support of the Slovak Grant Agency VEGA 1/0983/15.

References

- [1] YANG, Z., NORTHWOOD, D. O., SUN, X., LUMBRERAS, R., BARBER, G. C., ZOU, Q.: *The use Nitriding to Enhance Wear Resistance of Cast Iron*. In: De Hosson, J. Th., M., Brebbia, C. A. (eds.), *Surface effects and contact mechanics XI*, Wit Press, 2013, pp. 171-182.
- [2] LIM, S. C., ASHBY, M. F.: *Wear Mechanism Maps*. *Acta Metall.*, 35(1):1-24. 1987.
- [3] BUCALEM, M. L., BATHE, K. J.: *The Mechanics of Solids and Structures - Hierarchical Modeling and the Finite Element Solution*. Springer, 2011.
- [4] BATHE, K. J.: *Frontiers in Finite Element Procedures & Applications - Chap. 1*. In: *Computational Methods for Engineering Technology*. B. H. V. Topping and P. Ivanyi (eds.), Saxe-Coburg Publications, Stirlingshire, U.K., 2014.
- [5] ZMINDAK, M., MIKUSIK, J., KLIMKO, J.: *Dynamical Rolling Contact Stress Analysis of Cylindrical Roller Bearings using FEM*. Proc. of the 10 Intern. Conference on Vibration Problems 2011, Liberec, 2011.

- [6] HANDRIK. M., VASKO, M., KOPAS, P., SAGA, M.: Effective Finite Element Solution and Post-processing for Wide Load Spectrum. *Communications - Scientific Letters of the University of Zilina*, vol. 3A, 2014, pp. 19-26.
- [7] MUKRAS, S., KIM, N. H., SAWYER, W. G., JACKSON, D. B., GERGUIST, L. W.: Numerical Integration Schemes and Parallel Computation for Wear Prediction Using Finite Element Method, *Wear*, 266, 2009, pp. 822-831.
- [8] BENABDALLAH, H., OLENDER, D: Finite Element Simulation of the Wear of Polyoxymethylene in Pin-On-Disk Configuration, *Wear* 261, 2006, pp. 1213-1224.
- [9] ECHES, N., COSSON, D., LAMBERT, Q., LANGLET, A., RENARD, J.: *Modelling of the Dynamics of a 40 mm Gun and Ammunition System during Firing*. 7th European LS-DYNA Conference, 2009.
- [10] MENG, H-C.: *Wear Modelling: Evaluation and Categorisation of Wear Models*. Dissertation, University of Michigan, 1994.
- [11] HOLM, R.: *Electric Contacts*. Uppsala : Almqvist and Wiksells Boktryckeri AB, 1946.
- [12] PODRA, P., ANDERSSON, S.: Simulating Sliding Wear with Finite Element Method, *Tribology International*, 32, 1999, 71-81.
- [13] JOHNSTON, I. A. *Understanding and Predicting Gun Barrel Erosion*, Weapons Systems Division, 2005.
- [14] RABINOWICZ, E.: *Friction and Wear of Metals*, John Wiley & Sons : New York, 1995.

Miroslav Neslusan - Tomas Hrabovsky - Maria Cillikova - Anna Micietova *

BARKHAUSEN NOISE EMISSION IN MILLED SURFACES

This paper deals with the non-destructive evaluation of surface made of roll bearing steel 100Cr6 after milling cycles via Barkhausen noise technique. The paper discusses magnetic anisotropy linked with the structure transformations with regard to variable flank wear of cutting tool. Effective value of Barkhausen noise (BN), Peak Position and Full Width at Half Maximum (FWHM) derived from the raw BN signals are compared with metallographic observations and residual stress profiles. Surface integrity is also expressed in term of surface roughness due to comparable BN sensitive layer and the height of surface roughness profile.

Keywords: Barkhausen noise, milling, surface integrity.

1. Introduction

Cyclic magnetization in a ferromagnetic material produces magnetic pulsation as a result of irreversible and discontinuous Bloch Walls (BW) motion. Discontinuous BW motion is due to interference of BW with microstructure features such as precipitates, dislocation cells, grain boundaries and other lattice defects [1 - 4]. This phenomenon is named Barkhausen noise [5]. Barkhausen noise (BN) technique has found high industrial relevance mainly for monitoring surfaces loaded near their physical limits. BN features are usually correlated with residual stresses, microhardness or structure transformations. This technique is mostly adopted for monitoring of surfaces after grinding cycles due to strong correlation among thermal over tempering, associated surface burn and the corresponding BN features [6 and 7]. Effect of thermal softening after grinding due to over tempering decreases dislocation density (and the corresponding surface hardness), transforms carbides shape and their morphology as well as produces tensile stresses [6 and 7]. All the above mentioned aspects contribute to the higher magnitude of BN. Being so, surface over tempering can be easily revealed by the use of the Barkhausen noise technique [7].

Nowadays, it can be found that BN technique has been employed for the next industrial applications. BN technique was successfully adapted for turning operations [8 and 9]. These studies indicate strong influence of flank wear VB on surface integrity expressed in such BN features as BN (represent its effective rms value), Peak Position or BN envelope profile. As it was found, remarkable decrease of BN values and the simultaneous increase of Peak Position along with the progressively developed VB are

linked with increasing dislocation density and the corresponding structure transformations [8 and 9]. Moreover, verification of such concept in the real industrial conditions also revealed strong correlation between surface integrity after turning cycles (expressed in BN values) and deformations (expressed in their ovality and roundness deviation) produced by the consecutive heat treatment (hardening). Being so, this paper reports about the similar problem of milling operation in which BN emission, metallographic observations and residual stress profiles are investigated on surfaces after milling cycles produced by inserts of variable VB . Aspect of surface roughness is also involved due to comparable BN sensitive layer and the height of surface roughness profile.

2. Experimental conditions

Experiments were conducted on samples made of annealed bearing steel 100Cr6. 10 pieces of dimension 60x43x25mm were prepared for long term test. Cutting process was monitored as a long term test where such aspects as flank wear VB , structure alterations and corresponding surface integrity expressed in magnetoelastic responses (BN) of the milled surface were investigated. Cutting and other conditions: milling machine - FA4 AV, dry cutting, cutting tool made of cemented carbides R300-1240E-PM, R300-050Q22 - 12M 262489 of diameter \varnothing 50mm with 2 inserts of variable flank wear VB (in the range from 0.05 to 0.8 mm), $a_p = 0.25$ mm, $v_f = 112$ mm.min⁻¹, $v_c = 78.5$ m.min⁻¹. Flank wear was measured for both cutting inserts and VB values indicated in the paper represent their average value.

* Miroslav Neslusan, Tomas Hrabovsky, Maria Cillikova, Anna Micietova

Department of Machining and Manufacturing, Faculty of Mechanical Engineering, University of Zilina, Slovakia
E-mail: miroslav.neslusan@fstroj.uniza.sk

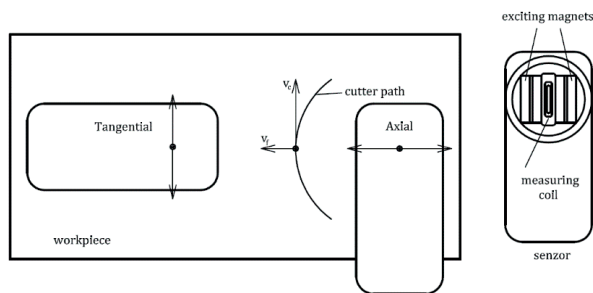


Fig. 1 Orientation of BN sensor

BN measurement was performed by the use of RollScan 300 and software package μ Scan in the frequency range of 10 to 1000 kHz (magnetizing frequency 125 Hz, magnetizing voltage 4 V). Each BN value was determined by averaging of 10 consecutive BN bursts (5 magnetizing cycles). Due to strong surface anisotropy, each surface was measured in two directions - tangential and axial as Fig. 1 illustrates. BN values indicated in the paper represent the effective (rms) value of BN signal. To reveal the microstructure transformations induced by milling 10mm long pieces were sectioned and routinely prepared for metallographic observations (etched by 2% Nital for 8s). Microstructure was observed in the direction of cutting speed. Residual stresses were measured by mechanical method based on electrolytic etching of (2 hours, 20% concentration of H_2SO_4 - electrolyte, 5V and 6A) machined surface and simultaneous measurement of a sample deformation. The details about principle, mathematic apparatus and measuring unit can be found in [10]. Surface roughness was measured by the use of Hommel Tester T 2000 in direction of feed speed (axial direction, see Fig. 1).

3. Results of experiments

Figure 2 depicts two different phases of flank wear VB. Turning operations are not usually performed with the inserts of flank wear VB above 0.5mm in order to avoid the excessive cutting forces and catastrophic tool failures. On the other hand, the flank wear is a major factor affecting the thickness of heat affected zone (HAZ), see Figs. 3, 4, 5 and 6. For this reason, quite large VB were employed to facilitate surface of relative thick HAZ; thus making more remarkable specific aspect of surface integrity investigated via BN. Microstructure observations show that milling with inserts of low VB (0.05 and 0.2mm) produces surface containing thin thermally softened layer which appears dark in the near surface region (see Fig. 3). HAZ is not continuous of variable thickness below $2\mu m$. As soon as the VB becomes more developed thickness of HAZ progressively increases. The higher VB is employed, the thicker HAZ can be produced (see Figs. 5 and 6).



a) sharp cutting insert, VB = 0.05 mm



b) VB= 0.8 mm

Fig. 2 Two different phases of flank wear VB



Fig. 3 Microstructure of milled surface, VB = 0.05 mm, HAZ ($2\mu m$)



Fig. 4 Microstructure of milled surface, VB = 0.4 mm, HAZ ($3.6\mu m$)



Fig. 5 Microstructure of milled surface, VB = 0.6 mm, HAZ (5 μm)



Fig. 6 Microstructure of milled surface, VB = 0.8 mm, HAZ (5.5 μm)

Figures 7, 8 and 9 depict influence of VB on surface roughness either illustrated by the raw roughness profiles (see Fig. 7) or via the extracted parameters (see Figs. 8 and 9). These figures reveal transformations in cutting edge geometry as well as intensification of plastic deformation of the machined surface. Due to a certain cutting edge radius a thin layer defined by the stagnation point undergoes severe plastic deformation during the time period corresponding the flank wear land. Both these aspects contribute to the progressive increase of surface roughness expressed in variable parameters. Furthermore, as the surface roughness profile increases in its height, the height of its irregularities

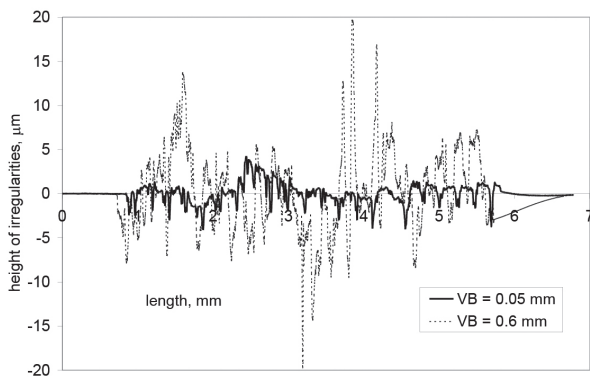


Fig. 7 Surface roughness profiles

becomes comparable with BN sensitive layer (the estimated BN sensitive thickness is about 40 μm). Being so, the volume of the structure within the surface roughness height (expressed in Rz parameter) contributing to the BN signal received on the free surface is reduced as the VB becomes more developed. It is considered that this effect contributes to the lower magnitude of BN obtained for surfaces produced by inserts of higher VB.

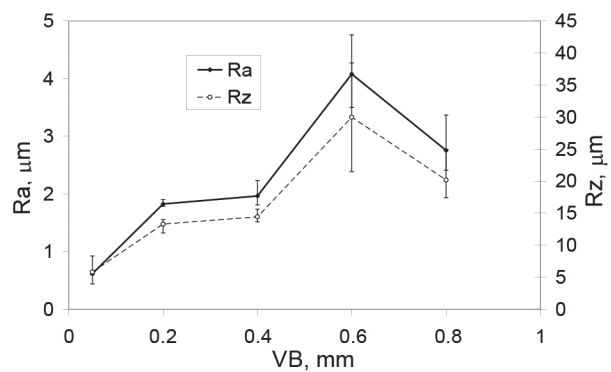


Fig. 8 Ra and Rz versus VB

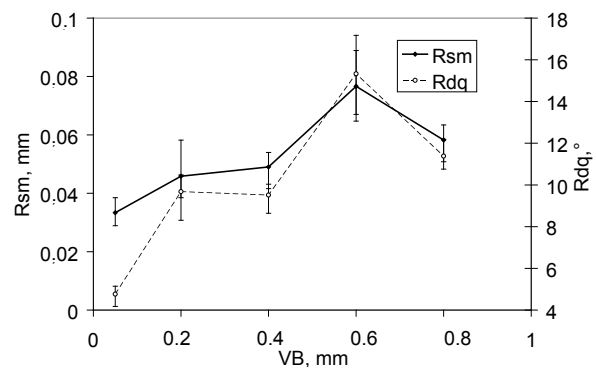


Fig. 9 Rsm and Rdq versus VB

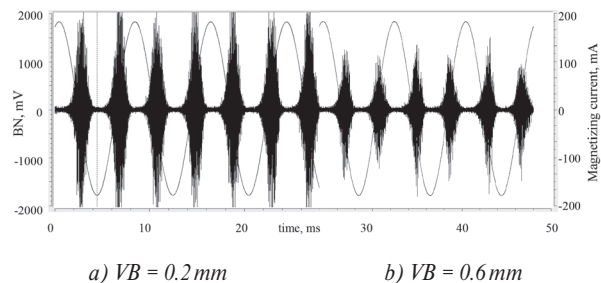


Fig. 10 BN signals in tangential direction

It is worth to mention that the generic term HAZ can not be associated with the pure thermal load (and corresponding thermal softening) of the near surface region. Due to a certain cutting edge radius and the corresponding stagnation point

a certain layer ahead of a cutting edge is not separated from the sample as a part of the chip but undergoes the cutting edge and forms the near surface region of machined surface exposed to the severe plastic deformation at elevated temperatures. It is well known that machined surface after turning or milling cycle usually contains near surface region in which effect of plastic deformation dominates whereas the deeper layers are mainly thermally softened. Both these (usually contradictory) effects (strain hardening and thermal softening) affect microstructure of machined surface; thus BW motion and BN emission. Both layers, near surface strain hardened and deeper thermally softened affects BN emission after milling cycle in a synergistic manner.

Figure 10 illustrates the BN signals obtained for tangential direction at two different VB. This figure shows that surface produced by inserts of lower VB emits BN signals of higher magnitude than that produced by the insert of higher VB. Figure 10 shows evolution of BN in the different directions. Figure 10 indicates richer BN emission in tangential direction (associated with the direction of cutting speed) than that in the axial direction (associated with the direction of feed speed). Strong magnetic anisotropy is due to unbalance between cutting and feed speeds as a result of stress anisotropy and associated effect of magnetostriction [11].

Figure 11 shows that BN drops down along with the progressive developed VB. Progressive decrease of BN versus VB in both directions is linked with the structure transformations in the near surface layer as a region mostly contributing to the BN signal obtained on the free surface. Gradual decrease of BN values in both directions indicates that effect of surface hardening dominates over the effect of thermal softening. Such behavior was previously explained (turned surfaces) through interference of BW with structure containing higher dislocations density [8] due to remarkable strain hardening at more developed VB. Higher dislocation density at higher VB is connected with two aspects as follows:

- transformations in cutting edge geometry (increasing cutting edge radius, more negative rake angle, etc.),
- longer time interval during which machined surface undergoes severe plastic deformation corresponding to the flank wear land.

As it was reported [8 and 12], both aspects affect BN in a synergistic manner. On the other hand, neither evolution of Peak Position nor FWHM indicate any remarkable variation versus VB (except Peak Position for VB = 0.8 mm), see Fig. 12. Also residual stress profiles (see Fig. 13) indicate mainly tensile stresses. As VB becomes more developed the higher magnitude of tensile stresses can be obtained. It is well known that tensile stresses are a product of thermal effect (unbalance in heating and cooling of neighboring layers - I type stresses). It is well known that tensile stresses contribute to the richer BN emission whereas compressive stresses reduce BN magnitude. Being so,

it is apparent that microstructure features (pinning sites in the structure interfering with BW) take the major role in BN emission whereas stress state is only minor.

It is also worth to mention that thermal softening in machining cycles becomes more significant in the case of hardened samples whereas surface strain hardening becomes more visible on metallographic observations (visible texture or refined white layer) when more negative tool geometry (rake angle) is employed. Moreover, such tool geometry also contributes to the remarkable increase of Peak Positions and transformation of BN envelopes profiles [8 and 12]. Nevertheless, BN emission in this study exhibits continuous drop down along with VB and

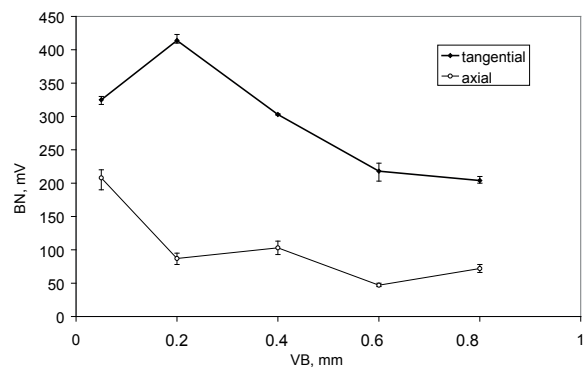


Fig. 11 BN versus VB

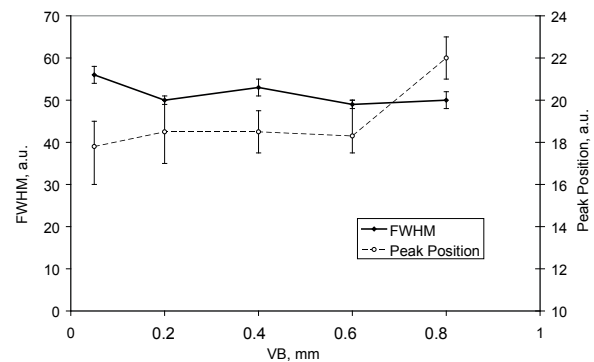


Fig. 12 Peak Position and FWHM versus VB

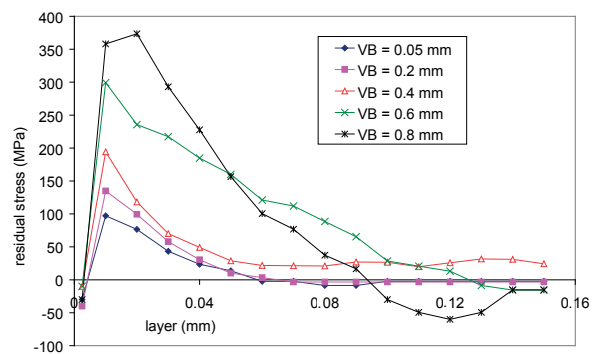


Fig. 13 Residual stress profiles

can be easily employed for non destructive monitoring of surface integrity after milling. On the other hand, further experiments focused on microhardness profile and measurement of dislocation density should be carried out to verify the above mentioned information.

4. Conclusions

BN technique has found a high industrial relevance for detection mainly grinding cycles when unacceptable thermal softening and tensile stresses contribute to the high BN values. Milling or turning processes form the different state of surface

integrity than that after grinding. Grinding cycles usually produce isotropic (from magnetic as well as stress point of view) surface whereas turning and milling cycles do not. However, this study demonstrates and proves the potential of BN technique for monitoring surfaces of high anisotropy. Industrial implementation of BN technique for real needs would avoid implementation of components of unacceptable surface; thus prevent their early crack initiation and machine premature failures.

Acknowledgement

This article was edited under the financial support of KEGA projects No. 005ZU - 4/2014, 009ZU - 4/2014.

References

- [1] KAMEDA, J., RANJAN, R.: Nondestructive Evaluation of Steels using Acoustic and Magnetic Barkhausen Signals - II. Effect of Intergranular Impurity Segregation, *Acta Metall.*, vol. 35/7 1987, pp. 1527-1531.
- [2] BUTTLE, D. J., SCRUBY, C. B., JAKUBOVICS, J. P., BRIGGS, G. A. D.: Magneto-acoustic and Barkhausen Emission: Their Dependence on Dislocations in Iron, *NDT & E Int.*, vol. 24 1991, pp.47-54.
- [3] GATELIER-ROTHERA, C., et al.: Characterization of Pure Iron and Carbon-iron Binary Alloy by Barkhausen Noise Measurements: Study of the Influence of Stress and Microstructure, *Acta Mater.*, vol. 46/14, 1998, 4873-4882.
- [4] RANJAN, R., JILES, D.C., RASTOGI, P.: Magnetic Properties of Decarburized Steels: An Investigation of the Effects of Grain Size and Carbon Content, *IEEE Trans. Magn.*, vol. 23/3, 1987, 869-1876.
- [5] BARKHAUSEN, H.: *Phys. Zeitschrift*, vol. 20, 1919, pp. 201.
- [6] MICUCH, M., CILLIKOVA, M., NESLUSAN, M., MICIETOVA, A.: Micromagnetic Study of Cutting Conditions and Grinding Wheel Wear Influence on Surface Integrity, *Manufacturing Technology*, vol. 14 2014, 66-71.
- [7] ROSIPAL, M.: *Application of Barkhausen Noise for Study of Surface Integrity of Machined Surfaces*, PhD. Dissertation, University of Zilina, 2012.
- [8] CIZEK, J., NESLUSAN, M., CILLIKOVA, M., MICIETOVA, A., MELIKOVA, O.: Modification of Steel Surfaces Induced by Turning: Non-destructive Characterization using Barkhausen Noise and Positron Annihilation, *J. of Physics D: Applied Physics*, vol. 47, 2014, 1-17.
- [9] DUBEC, J., NESLUSAN, M., FAKTOR, M.: Analysing the Influence of Tool Wear when Turning, on Bearing Rings Deformation through Barkhausen Noise, *Technolog*, vol. 1, 2013, 16-21.
- [10] NECKAR, F.: Influence of Cutting Process on Surface Integrity, Research report No. 400, CVUT : Praha, 1985.
- [11] HAJKO, V., POTOCKY, L., ZENTKO, A.: *Magnetization Processes*, ALFA : Bratislava, 1982.
- [12] DUBEC, J., NESLUSAN, M.: Multiparametric Analysis of Surface after Turning through Barkhausen Noise in Relation to Tool Wear, *MM Science*, July 2012.

Libor Trsko - Otakar Bokuvka - Peter Palcek - Frantisek Novy - Katarina Mikova *

FATIGUE RESISTANCE OF C30 STRUCTURAL STEEL

In this paper the authors present and discuss results of both fatigue life tests and fatigue crack growth rate tests performed for C30 steel which is used for railway axle manufacturing. The obtained results demonstrate the differences in fatigue strength and fatigue crack growth resistance in two different parts of one railway axle which are subjected to different levels of plastic deformation, namely the axle bolster body and axle body.

Keywords: Fatigue strength, crack growth resistance, C30 steel, railway axle.

1. Introduction

In spite of years of intensive research, fatigue of metals is still a serious engineering problem and fatigue fractures appear very frequently on common cyclically loaded structural components [1 and 2]. With respect to the technology used for manufacturing, different microstructural and work hardening states can be present in just one structural component. This means that different parts of the component can have different fatigue properties and tests done using specimens prepared from various parts are not equal [3 and 4].

Various tests can be performed to evaluate fatigue properties of materials. Most commonly used are standard fatigue life tests in which the specimen is cyclically loaded until it fractures and fatigue crack growth tests where the resistance of material to fatigue crack growth is evaluated. Even when both tests refer to fatigue resistance, each of them provides information about different material characteristics. Standard fatigue life tests provide information about number of cycles which are necessary for fatigue crack initiation and propagation through the whole cross section until complete fracture occurs. However, fatigue crack growth tests provide information about the resistance of the material microstructure to fatigue crack propagation. This means that correct interpretation of these test results is extremely important because they can provide even completely opposite results [2, 5 and 6].

The fatigue life and fatigue crack growth resistance of specimens prepared from different parts of a railway axle manufactured from C30 structural steel are analysed in this study. Results are discussed in the light of the ratio between

the number of cycles necessary for fatigue crack initiation and propagation and the ability of a material with lower strength to create a plastically deformed zone on the crack tip which slows down further fatigue crack propagation.

2. Material and methods

C30 steel obtained from a manufactured railway axle was used as experimental material. Quantitative chemical analysis (Table 1) confirmed that the chemical composition meets the standard prescribed for this steel [7 and 8].

C30 steel chemical composition in weight % Table 1

C	Mn	Si	P	S	Cu	Ni	Cr	Al
0.26	0.96	0.35	0.019	0.02	0.05	0.02	0.07	0.017

To produce a railway axle large steel ingots are used. They are hot-rolled to a bar-shaped semi-product. After hot-rolling, homogenisation annealing and normalising are carried out with the aim to homogenise the chemical composition and polyhedrisation of the deformed material grains. The microstructure is then formed by polyhedral ferritic and pearlitic grains [8 and 9]. This bar is then die forged to a shape very close to the final axle and machined for a final axle. The resulting mechanical properties are determined by the degree of plastic deformation during the die forging process. To assure high value of plastic deformation strengthening, large degree of area reduction during the die forging process is necessary and the hot rolled bar diameter must be at least double the size of the largest diameter of the final axle.

* ¹Libor Trsko, ^{1,2}Otakar Bokuvka, ²Peter Palcek, ^{1,2}Frantisek Novy, ¹Katarina Mikova

¹Research Centre of University of Zilina, Slovakia

²Faculty of Mechanical Engineering, University of Zilina, Slovakia

E-mail: libor.trsko@rc.uniza.sk

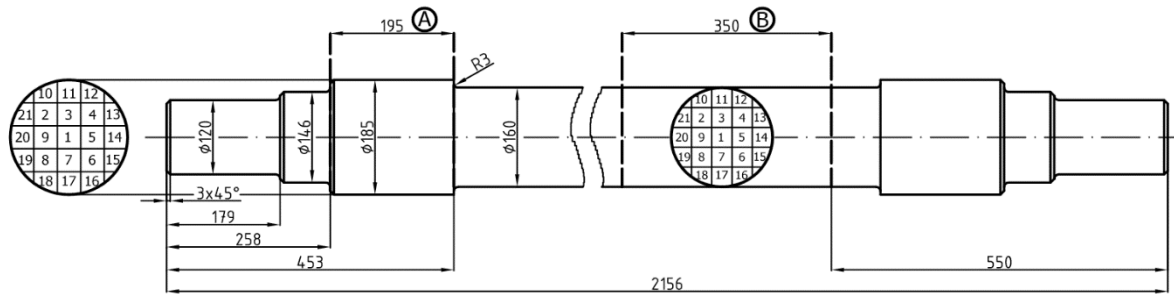


Fig. 1 Drawing of the tested railway axle and sketch of machining position of the specimens

Deformation strengthening by die forging is more significant on the surface than in the core of the material. However, during machining process a part of the strengthened surface layer is removed. The depth of removed layer is higher in the body of axle (the middle part of the axle with diameter of 160 mm in Fig. 1, marked B) than in the axle bolster (the part of the axle with diameter of 185 mm, marked A in Fig. 1).

Removing of the surface layer also causes compressive residual stress relief from the material. The stress relief is again more significant when a deeper surface layer of material is machined. Due to these facts, the mechanical properties of various parts of the axle can differ. Tensile test specimens and fatigue test specimens were machined from a new, not used railway axle (Fig. 1). One set was machined from the axle bolster (marked A in Fig. 1) and another from the axle body (marked B in Fig. 1). The position of the machined specimen, with respect to the cross section position, is described by the drawn mesh in the circles representing the cross sections (Fig. 1).

Specimens for ultrasonic fatigue tests (Fig. 2a) were machined from all 21 bars. Each specimen's gauge length was ground and polished by diamond metallographic emulsion. To obtain the mathematical dependence of the number of cycles to failure on the loading stress amplitudes, experimental results were approximated by the Basquin function, using the least square method [9]:

$$\sigma_a = \sigma'_f (N_f)^b \quad (1)$$

in which b is the exponent of fatigue life curve and σ'_f is the coefficient of fatigue toughness obtained by the extrapolation of stress amplitude on the first loading cycle.

Fatigue crack growth was measured using the specimens according to Fig. 2b, also with polished surface of the gauge length. Primary notch with 1 mm in diameter and depth of 0.8 mm was manufactured by drilling and served as initiator for the fatigue crack. From the rest of bars from positions marked 1, 3 and 11 specimens for tensile tests were machined (Fig. 2c.). Fatigue tests were performed in the high and ultra-high cycle region by ultrasonic tension-compression loading ($f = 20$ kHz, $R = -1$, $T = 20 \pm 3$ °C) [2, 10 and 11]. Fatigue crack growth measurement was performed using rotating-bending loading ($f = 40$ Hz, $R = -1$,

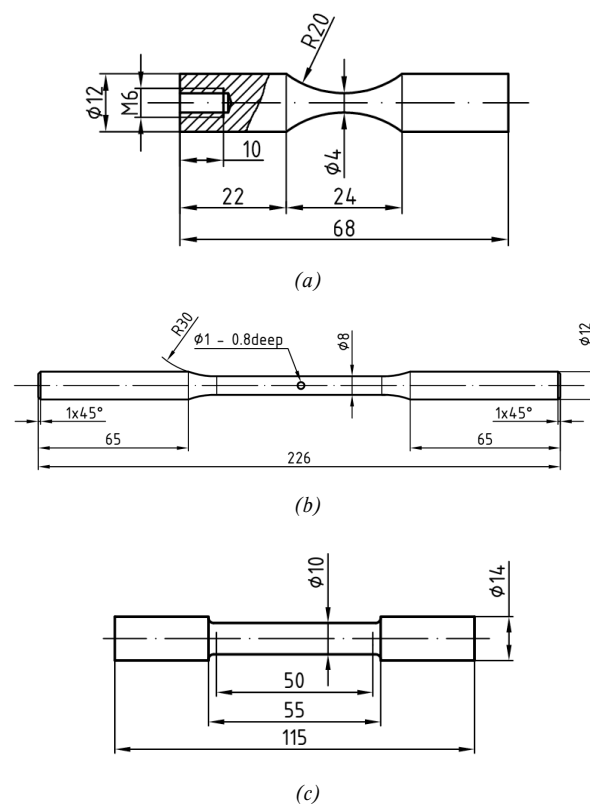


Fig. 2 Geometry of specimens used for ultrasonic fatigue tests (a), fatigue crack growth tests (b) and tensile tests (c)

$T = 20 \pm 3$ °C) on the testing equipment ROTOFLEX-UBM [9]. The specimens for fatigue crack growth (Fig. 2b) were loaded with cyclic bending stresses $R_o = 220$ MPa and $R_o = 240$ MPa ($R_o/R_m = 0.38$ and 0.41 , place A; 0.39 and 0.42 , place B). The length of the fatigue crack which was growing from the primary notch was regularly measured on the specimen's circumference after each $N = 10^4$ cycles with accuracy of 0.1 mm by a Brinell - Epignost optical microscope. $2a = f(N)$ dependencies were obtained from which fatigue crack growth rates $d2a/dN$ vs. stress intensity factor range ΔK dependencies ($d2a/dN = f(\Delta K)$) were evaluated. The applied stress intensity factor range ΔK was determined using the following equation [12]:

$$\Delta K = 1.03 \times \frac{2}{\pi} \times R_o \times (\pi \times a)^{\frac{1}{2}} \quad (\text{MPa}\cdot\text{m}^{1/2}) \quad (2)$$

in which R_o is bending stress (MPa), a is the half crack length including primary notch (m).

3. Experimental results

Tensile test results (as average values from the three tested specimens) are shown in Table 2. According to the results there is only a minor difference in the UTS of the specimens manufactured from different parts of the railway axle and the yield point is almost exactly the same. This means that when static loading is applied, there is no significant difference in the material properties of different axle parts.

The authors [9] determined by indirect ultrasonic resonance method [10] the modulus of elasticity of the specimen machined from position No. 14 (Fig. 1). For axle bolster (A) the value was $E = 2.06506 \times 10^{11}$ Pa and for axle body (B) $E = 2.05168 \times 10^{11}$ Pa. This means that there is also no significant difference in the values of modulus of elasticity, which describes the response of material to loading in the area of elastic deformation.

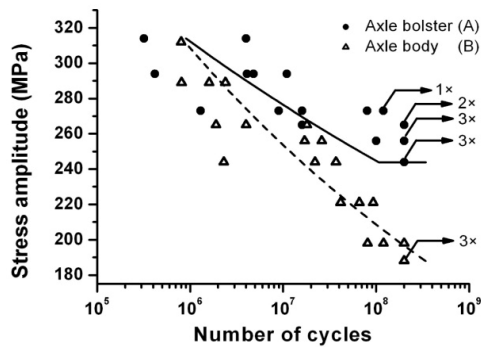


Fig. 3 Comparison of fatigue life of specimens machined from axle bolster and axle body, steel C30, tension-compression ultrasonic loading ($f = 20$ kHz, $R = -1$, $T = 20 \pm 3$ °C)

According to the results of fatigue tests (Fig. 3), the fatigue strength of specimens machined from the axle bolster is higher than that of the specimens machined from the axle body. Specimens fracture was observed even beyond the conventional fatigue limit, usually evaluated for $N = 10^7$ cycles and the fatigue

limit was estimated for $N = 2 \times 10^8$ cycles where the fatigue test was terminated and marked as run-out. Specimens were machined from the whole cross section of the axle parts which had different levels of deformation. This probably caused the high scatter of the results, but in general, the higher level of deformation in the axle bolster resulted in the fatigue limit (for $N = 2 \times 10^8$ cycles) $\sigma_a = 244$ MPa which is significantly higher than for the axle body where the fatigue limit was $\sigma_a = 188$ MPa.

Results of fatigue crack growth tests (Fig. 4), the dependence of fatigue crack growth rates vs. stress intensity factor range, show that material from the axle body has a higher resistance to the fatigue crack growth than material in the axle bolster. Again the high scatter of results is probably caused by different deformation levels of material from the surface and from the core of the railway axle.

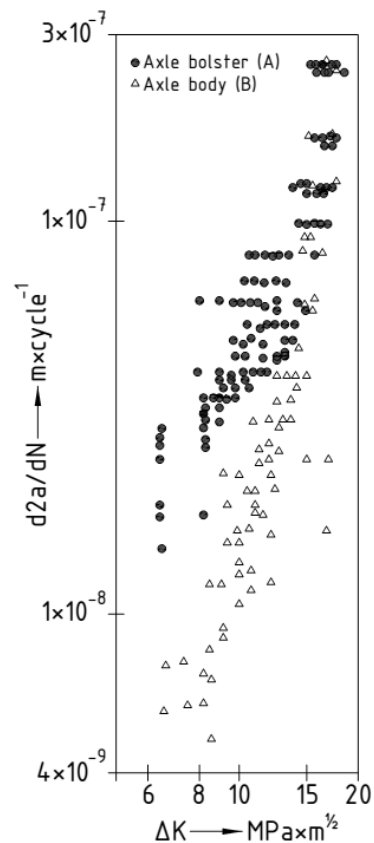


Fig. 4 Fatigue crack growth rate, steel C30, rotating-bending loading ($f = 40$ Hz, $R = -1$, $T = 20 \pm 3$ °C)

Results of tensile tests of steel C30

Table 2

Axle bolster (A)			Axle body (B)		
Yield point (MPa)	UTS (MPa)	Elongation (%)	Yield point (MPa)	UTS (MPa)	Elongation (%)
335.2	572.9	29.5	338.1	559.1	30.6

4. Discussion

Due to different deformation levels of various parts of just one structural component caused by the manufacturing process, the fatigue properties of these parts can significantly differ. This was confirmed by ultrasonic fatigue tests in the high and ultra-high cycle region where the fatigue limit of material in the area of axle bolster was higher than that of the material in axle body; the difference being $\Delta\sigma_a = 56$ MPa. This significant difference in fatigue properties, although expected on the basis of information about the manufacturing process, is neither reflected in the results of standard tensile test, nor in the value of ultimate tensile strength, nor in the value of yield point [11 and 13].

The fatigue crack growth resistance of material in the axle body is notably higher (the fatigue crack rates are lower) than of the material in the axle bolster and this seems to be in contradiction with the results of the performed fatigue tests. However, each fatigue degradation process consists of two main stages and that is the fatigue crack initiation and the fatigue crack propagation. In smooth specimens, the fatigue crack initiation represents more than 90 % of the total number of cycles to fracture. Presence of a notch on the surface significantly changes the ratio between number of cycles required for crack initiation and propagation ratio and this is the case of the fatigue crack growth tests where an artificial notch is used for acceleration and localisation of the fatigue crack initiation. According to authors of [2, 3, 14-21], materials with lower strength create on the crack tip a plastically deformed zone which slows down the fatigue crack propagation. In case of materials with higher strength this zone is not so significant and less influences (slows down) the fatigue crack propagation. The material in the axle bolster had a significantly higher resistance to fatigue crack initiation than the one in axle body, but when a crack was initiated from the artificial notch, the material in the axle body had higher resistance

to the fatigue crack propagation due to creation of this plastically deformed layer.

5. Conclusions

Tensile tests, ultrasonic fatigue tests and fatigue crack growth tests were carried out on specimens manufactured from two parts (axle bolster and axle body) of a C30 steel railway axle. Based on obtained results from these tests the following can be concluded:

- difference in mechanical properties (UTS, yield point, elongation, E) between specimens machined from axle bolster and axle body is negligible,
- specimens manufactured from the axle bolster show a significantly higher fatigue strength than the ones manufactured from the axle body,
- the difference in fatigue limit evaluated for $N = 2 \times 10^8$ cycles between the axle bolster and axle body material is $\Delta\sigma_a = 56$ MPa,
- specimens machined from the axle body show higher resistance against fatigue crack growth when compared to the specimens from axle bolster,
- different deformation levels of various parts of just one component created during the manufacturing processes resulted in significantly different fatigue properties, namely of fatigue strength and fatigue crack growth rate.

Acknowledgement

The research was supported by the European regional development fund and Slovak state budget by the project "Research centre of University of Zilina", ITMS 26220220183 (90%) and by project of bilateral cooperation APVV no. SK-CZ-2013-0047 (10 %).

References

- [1] GUAGLIANO, M., TRSKO, L., BOKUVKA, O., NOVY, F.: *Mater. Eng. - Mater. Inz.* 2012, vol. 19, No. 3, p. 117-123.
- [2] BOKUVKA, O., NICOLETTO, G., GUAGLIANO, M., KUNZ, L., PALCEK, P., NOVY, F., CHALUPOVA, M.: *Fatigue of Materials at Low and High Frequency Loading (in Slovak)*, Zilina: EDIS, 2014.
- [3] PALCEK, P., CHALUPOVA, M., NICOLETTO, G., BOKUVKA, O.: *Prediction of Machine Element Durability*, 1st ed., Zilina: EDIS 2003.
- [4] BURDACK, M.: *Eng. Fract. Mech.* 78(5), 2011, p. 742-753.
- [5] PETRAK, G.: *J. Eng. Fract. Mech.*, 6, 1974, p. 725.
- [6] ROMANIV, O. N.: *Proc. Basic Mechanisms in Fatigue of Metals*, ACADEMIA Praha, 1988
- [7] FURBACHER, I., MACEK, K., STEIDL, J.: *Catalogue of Technical Materials (in Czech)*, 1st ed., Prague : Verlag Dashofer, 2004.
- [8] SKOCOVSKY, P., BOKUVKA, O., KONECNA, R., TILLOVA, E.: *Material Science for Mechanical Engineers (in Slovak)*, 2nd ed., Zilina : EDIS, 2006.
- [9] TRSKO, L., BOKUVKA, O., NOVY, F., HADZIMA, B.: *Mater. Eng. - Mater. Inz.* 21 (3), 2014 pp. 104-108
- [10] PUSKAR, A.: *High Frequency Fatigue of Materials (in Slovak)*, 1st ed., Zilina : EDIS, 2014.

- [11] PUSKAR, A., BOKUVKA, O., PALCEK, P., MESKO, J.: *Machinery (in Slovak)*, 9, 1987.
- [12] KITAGAWA, O.: *Int. Conf. Stockholm*, Sweden, EMAS, 1982, p. 1051.
- [13] BOKUVKA, O., PUSKAR, A., NICOLETTO, G.: In Proc. of 8th DAS, Godollo, 1991, p. 36.
- [14] RITCHIE, R. D.: *Application of Fract. Mech. to Fatigue Crack Propagation*, Univ. California, 1981
- [15] BURSAK, M., BOKUVKA, O.: *Communications - Scientific Letters of the University of Zilina*, vol. 8, No. 4, 2006, pp. 34-37.
- [16] LUKAS, P., KLESNIL, M.: *Machinery (in Czech)*, 1, 1978, p. 36.
- [17] NOVY, F., BOKUVKA, O., TRSKO, L., CHALUPOVA, M.: *Annals of Faculty Engineering Hunedoara, Int. J. Eng.* X, 2, 2012, p. 231.
- [18] BOKUVKA, O., NICOLETTO, G., PALCEK, P.: *Proc. of Materials Development in Rail, Tire, Wing, Hull Transportation*, AIM : Genova, 1992, p. 1.123.
- [19] BURSAK, M., BOKUVKA, O.: *Communications - Scientific Letters of the University of Zilina*, vol. 11, No.1, 2009, pp. 27-30.
- [20] ZERBST, U., KLINGER, C., KLINGBEIL, D.: *Eng. Fail. Anal.*, 35(15), 2013, pp. 54-65.
- [21] OGNJANOVIC, M., SIMONOVIC, A., RISTIVOJEVIC, M., LAZOVIC, T.: *Eng. Fail. Anal.*, 17(7-8), 2010, pp. 1560-1571.

Pavel Kopecek - Milan Pinte *

HOW TO SUPPLY ASSEMBLY LINES

Great efforts are currently dedicated to cost engineering in industry. The lean production approach is a good way to lower production costs. Material flows and treatment should be planned and controlled neither too early nor too late, because early production leads to an increase of stocks of materials and late production to a backlog of orders. This task is especially important in serial production, e.g. in the automotive industry. A buffer stock could be connected with assembly lines in many ways, such as handcarts, fork lift trucks or special cableways. A modern method of material supply in an assembly workshop is the usage of tow trains consisting of a tow truck and several carts. The number of carts in a train can change but it cannot be high because of turnings and crossings. The task is to find and optimize transport routes. This task is considered to be NP-hard. The paper describes several approaches to solving the task.

Keywords: Material supplies, heuristic optimization, assembly lines, milk run VRP problem.

1. Task specification

There are two main possibilities for building tow trains in a central store:

- Using static milk run
- Using dynamic milk runs

The first case expects that transport routes are constantly designed. Assembly lines are operated with trains which run on fixed routes, sometimes in fixed periods. Optimization tasks are focused on finding good coverage of an assembly workshop with transport routes, and estimating the optimal number of trains and their lengths. Another task is to find a good solution for the bin packing problem of a cart. The optimization of such a system has been made by Ulrych and Raska [1].

A more interesting way of supplying assembly lines is the creation of routes and lengths of tow trains according to the momentary situation. There are demands from some assembly points for a new delivery of a material batch. The delivery must be in time. The criterion of optimization is a minimum sum of the length of all routes. The task is open, which means that during processing of an optimal schedule of tow trains new demands can appear. Trains on routes must carry out their orders but the rest of the demands are added to with new demands and newly optimized.

An example of such an assembly system is shown in Fig. 1. There is a central store, several assembly lines with work places and supply points. Tow trains can go in lanes. Lanes are mostly one-way. Trains cannot be overtaken and must wait when another train provides a supply point.

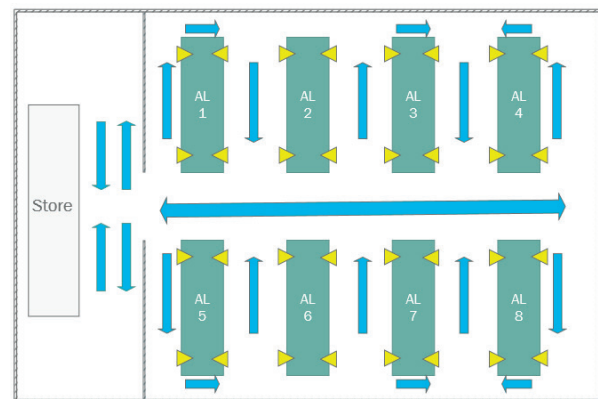


Fig. 1 Model of an assembly line (AL) supply system

This model can be represented in the form of a graph (Fig. 2). In this example, U00 represents the store, vertices Uxx supply points on assembly lines. Edges are evaluated by distances between them. Transport demands of U01, U05, U17, U18, U11, U13 and U14 can be covered by two cycles (red and blue) which represent routes of two supply trains.

If the length of a tow train is n carts then the task of optimizing the sum of lengths of routes can be represented by covering the graph with cycles going through maximal n vertices of the graph.

Groups of n demands ($1 < n < 20$) are randomly generated from vertices needing service by trains. Every group can be considered as a subgraph. The task is to cover the subgraph with cycles of a maximum of 5 vertices (start in the central store and

* Pavel Kopecek, Milan Pinte

Department of Industrial Engineering and Management, Faculty of Mechanical Engineering, University of West Bohemia, Czech Republic
E-mail: kopecek@kpv.zcu.cz

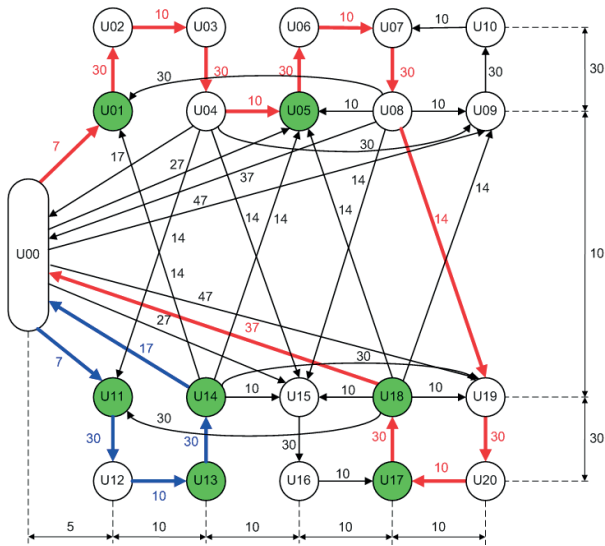


Fig. 2 Graph representation of assembly lines and supply routes

4 supply points in assembly lines) so that the total length of these cycles representing the routes of individual trains will be the shortest of them.

2. Related literature

Several approaches for solving this or similar tasks can be found in published papers.

Andras Kovacs [2] tries to minimize the order cycle time and the average picking effort. A probability model is used. Kovacs stated that “We showed that the milkrun system leads to a correlation among the request probabilities of items that can be exploited in a mathematical programming model”.

Some authors use artificial intelligence. Ediz Atmaca and Ayla Ozturk [3] use a simulated annealing solution. Zahalka [4], Tripathi [5], Montemani A.V. [6], Naqvi [7] and Lucka [8] use methods of an ant colony. Adamidis and others [9] use an evolutionary algorithm.

The vehicle routing problem is also described and solved by using a branch-and-price algorithm in [10]. Genetic algorithms are also used in [11]. Collection and Delivery problem is solved by Brian Coltin (minimizing energy and time, minimizing distances of a robot delivery) [12]. The task of supply of assembly lines was studied using a mathematical approach by Cardenas-Barron [13].

A very good overview of the related literature, a mathematical model and a heuristic approach is made by Satoglu and Sahim [14]. A case study of an assembly system is made by Emde and Boysen [15].

Selected Heuristic Methods Used in Industrial Engineering were published in DAAAM conference in Vienna 2013 [16].

3. Summary of related literature

Because the task of creating optimal routes for tow trains supplying assembly lines is NP-hard, the heuristic approach is considered to be a good solution for this task. A lot of authors use some genetic algorithms, ant colony systems or simulated annealing.

The weaknesses of these approaches can be found in the following areas:

- Complicated algorithms with long time solutions;
- Difficulties with determining or measuring real and valid input parameters that can change in time;
- Breakdowns and disturbances in a real production process which are unpredictable.

Solutions can be of long duration, sometimes hours and not seconds, changing parameters are not estimated with the necessary accuracy, unpredictable disturbances in workshops and simplifications in the abstraction arc from a real system to a mathematical model lead to no valid system.

4. A practical approach

It is interesting to observe a crane driver. If there are not many transport demands a crane driver has long idle times and the probability of some transport queues is low. If a lot of transport demands exist, the driver tries to solve the nearest demand. Sometimes he takes priorities into account. The simulation of this approach proved that the more demands there are, it is best for the driver to first prioritize and after that solve the nearest demand. The optimization could be done for queues of length under 10 by computing all permutations on a normal PC in times less than one second.

5. Hypotheses

Selection of the nearest demand

There is a simple deterministic solution – repeated selection of the nearest demand, then of the demand nearest to the goal of the last selected demand up to the maximum length of the train. The next trains are selected in the same way. This strategy could be good for a stacker in a FMS (Flexible manufacturing System) or in a store but not very appropriate for tow trains.

Simple crane or stacker in a FMS

For a small number of demands all permutations can be computed in a short time and for a great number of demands the strategy to select a nearest demand is also a good solution. The area between small and great number of demands could be covered by a selection from random generated permutations of demands.

Tow trains in assembly line systems

Let's say that the length of a train is maximal n. For less or equal demands than n all permutations can be computed (the practical length is under 7 carts). For more than n demands it is possible to randomly select several n-tuples of demands. Each n-tuple is optimized by computing all permutations. The random selection of n-tuples could be repeated many times. The number of repetitions is limited only by computer time (for example under 3 seconds).

6. Approval of hypotheses

Solution by brute force

The optimization problem is considered to be NP-hard. It is possible to solve it by brute force trying all permutations of high order up to 12 demands. To verify it, a test program has been developed. Results are shown in Table 1.

Times for solutions with brute force Table 1

n	factorial	Sec	min
2	2	0.000	0.000
3	6	0.000	0.000
4	24	0.000	0.000
5	120	0.000	0.000
6	720	0.000	0.000
7	5 040	0.000	0.000
8	40 320	0.003	0.000
9	362 880	0.029	0.000
10	3 628 800	0.277	0.005
11	39 916 800	3.020	0.050
12	479 001 600	36.082	0.601
13	6 227 020 800	489.931	8.166
14	87 178 291 200	7 000.000	116.667

Stacker

Simulation programs have been developed to validate the hypotheses.

It is possible to consider that demands for a stacker in a FMS have regular distribution of demands, which means that horizontal positions of all start and end points of demands could appear with the same probability. The task is to minimize the sum of the length of unloaded moves. With no optimization (FIFO - First In First Out), the ratio between unloaded and loaded moves is 100%.

Four strategies of optimization have been tested (Fig. 3):

- No optimization (FIFO).
- Selection of the nearest demand (Proximate).

- Repeated selection of random permutation (Random permutation).
- Brute force (all possible permutation up to 10 demands, then the computing time rises too much).

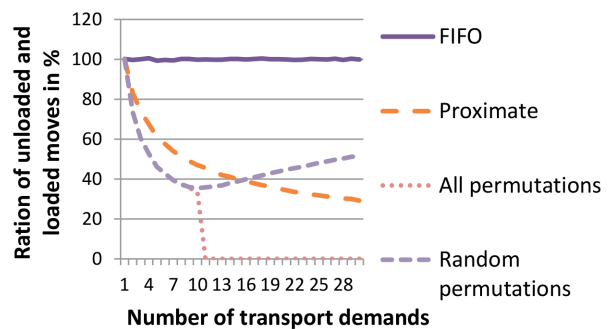


Fig. 3 Optimization of a stacker in a FMS

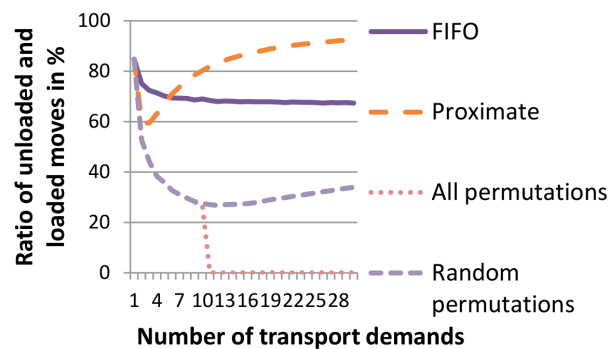


Fig. 4 Optimization of a stacker in a store

Stackers are often used in stores (Fig. 4). Moves of a stacker in a store are asymmetric which means that it either starts at one end (input place of a rack) and ends anywhere in a rack, or starts anywhere in a rack and ends at the same end (output place) where the input place is. This case was also simulated and optimized.

The simulations verified the hypotheses.

Tow trains in assembly line systems

The maximum length of a train was considered to be 4 carts and 1 tow truck. The optimum in a 4-tuple was found by testing all 24 possibilities. The task was to divide all transport demands into 4-tuples. Two strategies were used:

- selection of the proximate demand (deterministic),
- repeated random selection of 4-tuples, evaluation of lengths of routes for all tuples, the selection of the best selection (minimum length).

The worst selection was chosen for comparison.

This simulation verified that this method can decrease lengths of routes to about 70% of an unoptimized strategy (Fig. 5).

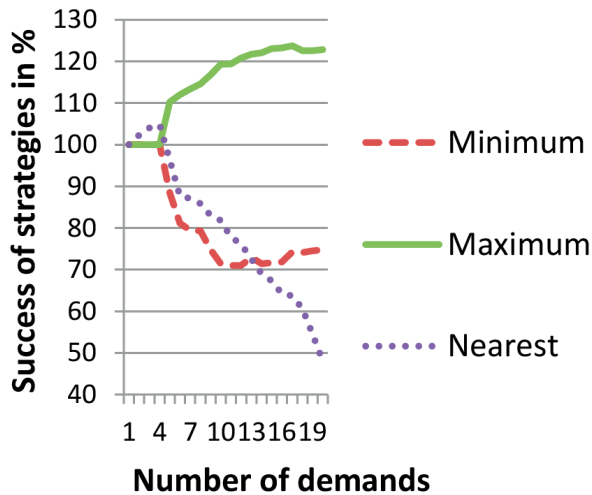


Fig. 5 Success of strategies (nearest demand, min and max random selection)

7. Conclusion

The research carried out on an “ad hoc” proposed model proved the hypothesis that a dynamic optimization of train creation and specification of supply routes of trains can be made in real time using relatively simple methods which are not

critically dependent on the accuracy of input data with good optimization results. Means of transportation and manpower can be saved in this way, and peaks of transport demands can be solved more quickly.

The model presented here has been developed theoretically, but inspired by an actual production system model of an assembly line. Subsequent research will be based on the one hand on optimization of larger production systems with the hypothesis of division of the optimized system into two or more parts, and on the other hand on specification of accurate data of an actual production system and experiments leading to optimization of its supply demands.

The optimization of a stacker in a FMS or in a store has been presented for comparison but this strategy was used in several production systems many years ago.

Repeated random selections could be a good solution when optimization tasks are considered for NP-complete. As has been shown above, some “ad hoc” deterministic strategies can also be used and compared with random selections.

Acknowledgements

The project presented in this article is supported by the project IGA ZCU SGS-2012-063. Results of the project OP VK n. CZ.1.07/2.3.00/09.0163 have been used.

References

[1] RASKA, P., Z. ULRYCH, Z.: *Simulation Optimization in Manufacturing Systems, Annals of DAAAM for 2012 & Proc. of the 23rd Intern. DAAAM Symposium*, B. Katalinic (Ed), DAAAM International: Vienna, 2012, pp. 221- 224

[2] KOVACS, A.: *Optimizing the Storage Assignment in a Warehouse Served by Milkrun Logistics, Intern. J. of Production Economics* 133, 2011, pp 312-318

[3] ATMACA, E., OZTURK, A: *Defining Order Picking Policy: A Storage Assignment Model and a Simulated Annealing Solution in AS/RS Systems, Applied Mathematical Modelling* 37, 2013, 5069-5079

[4] ZAHALKA, J.: *Econometric and Operation Research*, Faculty of Informatics and Statistic : University of Economics: Prague, 2008

[5] TRIPATHI, M., GLENN KURIGER, G., HUNG-DA WAN: *An ant Based Simulation Optimization for Vehicle Routing Problem with Stochastic Demands*, Proc. of the 2009 Winter Simulation Conference, University of Texas : San Antonio, 2009

[6] MONTEMANNI, R., GAMBARDELLA, L. M., A. E. RIZZOLI, A. E., DONATI, A. V.: *A New Algorithm for a Dynamic Vehicle Routing Problem Based on Ant Colony System*, Proc. of ODYSSEUS 2003, Palermo, May 2003

[7] NAQVI, N. Z., MATHERU, H. K., CHADHA, K.: *Review of Ant Colony Optimization Algorithms on Vehicle Routing Problems and Introduction to Estimation-Based ACO*, Intern. Conference on Environment Science and Engineering, IPCBEE vol. 8, IACSIT Press, Singapore, 2011

[8] LUCKA, M., PIECKA, S., 2009: *Multi-threaded Ant Colony Optimization with Asynchronous Communications for the Vehicle Routing Problem. Communications - Scientific Letters of the University of Zilina*, vol. 11, No. 4, 2009, pp. 5-8, ISSN 1335-4205

[9] ADAMIDIS, P., VOLIOTIS, C., PLIATSIKA, E.: *An Evolutionary Algorithm for a Real Vehicle Routing Problem, Intern. J. of Business Science and Applied Management*, vol. 7, No. 3, 2012

[10] VACCA, I., SALANI, M.: *The Vehicle Routing Problem with Discrete Split Delivery and Time Windows*, Ecole Polytechnique Federale : Lausanne, 2009

[11] KOLOCH, G., KAMINSKI, B.: *Nested vs. Joint Optimization of Vehicle Routing Problems with Three-dimensional Loading Constraints, Engineering Letters*, 18:2, EL_18_2_10 (Advance online publication: 13 May, 2010)

- [12] COLTIN, B.: *Multi-agent Pickup and Delivery Planning with Transfers*, tech. report CMU-RI-TR-14-05, Robotics Institute, Carnegie Mellon University, May, 2014
- [13] CARDENAS-BARRON, L. E, PORTER, D.: Supply Chain Models for an Assembly System with Preprocessing of Raw Materials: A Simple and Better Algorithm, *Applied Mathematical Modelling* 37, 2013, pp. 7883-7887
- [14] SATOGLU, S., I., SAHIN, E.: Design of a Just-in-time Periodic Material Supply System for the Assembly Lines and an Application in Electronics Industry, *Intern. J. of Advanced Manufacturing Technology*, 2013, 65:319-332
- [15] EMDE, S., BOYSEN, N.: Optimally Routing and Scheduling Tow Trains for JIT-Supply of Mixed-model Assembly Lines, *European J. of Operational Research* 217, 2012, pp. 287-299
- [16] KOPECEK, P.: *Selected Heuristic Methods Used in Industrial Engineering*, 24th DAAAM Intern. Symposium on Intelligent Manufacturing and Automation, 2013, B. Katalinic (Ed), Elsevier : Vienna, 2014, pp. 622- 629.

Martin Krajcovic - Viktor Hancinsky *

PRODUCTION LAYOUT PLANNING USING GENETIC ALGORITHMS

Globalisation of entrepreneurship has not only opened world markets but also global competition. The fundamental criteria for decisions on allocation of manufacturing capacities are currently not only costs (manufacturing, logistics, etc.), but mainly quality (of products, processes and services), flexibility (types of products, capacity, space, time) and a company's innovative capability.

Therefore the enterprise's facility layout needs to be more flexible to adapt to the rapidly changing environment. The need for flexibility of layout planning puts higher requirements for utilisation of layout and location problem solving methods. Classical methods, like linear programming, dynamic programming or conventional heuristics are being replaced by advanced evolutionary algorithms, which give better solutions to large-scale problems. One of these methods are also genetic algorithms.

This article describes the genetic algorithm utilisation in the production layout planning.

Keywords: Production layout, material flow optimisation, heuristics, genetic algorithms.

1. Requirements for the production layout planning

Current pressure on rapid innovations in the factory places increasing requirements also on the manufacturing and logistics systems design from the point of view of reduced laboriousness, consumption of time and costs for the whole system of technological design and, at the same time, on growth of quality, complexity and ability to testify the outputs generated from this process [1].

Based on the mentioned reasons it is possible to sum up the following fundamental requirements on the process of technological design [2]:

- rapid design of new solutions,
- maintenance of systematic approach in design,
- manufacturing systems design as part of digital factory concept,
- interactive design of a new manufacturing/logistics system,
- possibility of ongoing monitoring and assessment of proposed solution variants,
- implementation of optimisation approaches to design the time and spatial structure of the manufacturing system,
- proper visualisation and presentation of design outputs,
- possibility of dynamic verification of a proposed solution.

From the viewpoint of spatial arrangement of manufacturing and logistics structures, the following decision criteria are important [3]:

- minimisation of transport-related outputs and costs,
- minimisation of the areas needed,
- provision of occupational hygiene and safety,
- flexibility and the possibility of changes in the future,
- favourable conditions for team work,
- minimisation of reserves and continuous time,
- simple material flow,
- connection to an external logistics chain,
- possibility to flexibly optimise the arrangement in compliance with the changing production program.

2. Methods for layout planning

A key assumption of the "right" production layout proposal is correct preparation and analysis of input data. Fundamental layout planning data source is the technical preparation of production. Layout planning data contain information about products (assortment, bill-of-material, design parameters, production volume, etc.), production processes (operations, used

* Martin Krajcovic, Viktor Hancinsky

Department of Industrial Engineering, Faculty of Mechanical Engineering, University of Zilina, Slovakia
E-mail: martin.krajcovic@fstroj.uniza.sk

technologies, time standards, etc.) and production resources (machines, tools, personnel, etc.) [4].

The basic results of the input data analysis have to serve following data:

- information about material flow processed in “from-to” table (Fig. 1a) or information about relationships among workplaces in relationship chart,
- overall requirements of production resources (machine types and number of machines) as a result of capacity calculations (Fig. 1b).

These data sets form the basis for optimal layout planning of the manufacturing system.

	1	2	3	4	5	6
1	C K Datej	Ergonomic	SV 18 RA	TNC 20N	GBL 25 tyč	BUA 28x630
2	Ergonomic	0	10000	15000	0	0
3	SV 18 RA	0	0	10000	0	0
4	TNC 20N	0	0	0	0	15000
5	GBL 25 tyč	0	0	0	0	15000
6	BUA 28x630	0	0	0	0	0
7	SUI 50/1000 INDEX GU	0	0	0	0	0
8	600	0	0	0	0	5000
9	PF 150	0	0	0	0	0

a) from-to table

Machine type	Production unit time						Number of machines (calculated)	Number of machines (proposed)
	V1	V2	V3	V4	V5	V6		
Ergonomic	0.24		0.15	0.12			0.51	1
SV 18 RA	0.15						0.15	1
TNC 20N	3.24		2.18				5.41	6
GBL 25		1.81			0.73		2.54	3
BUA 28X630		0.36	0.36	0.39	0.34		1.45	2
SUI 50/1000				0.24	1.16		1.40	2
INDEX GU 600				1.33			1.33	2
PF 150					2.32		2.32	3
GAC						0.97	0.97	1
Inspection	0.05	0.02	0.03	0.09	0.04	0.02	0.25	1

b) machine requirements

Fig. 1 Data for layout planning

Proposing an ideal arrangement, it is advantageous to use optimisation methods and algorithms which can be classified as follows [5]:

- Graphical methods: they are suitable for solving simple problems, because a graphical presentation of spatial arrangement is used when looking for an optimal solution. Following methods belong to this group: Sankey chart, spaghetti diagram, relationship diagram, etc.
- Analytical methods: they are represented by optimisation methods of operational analysis. They are characterised by a mathematical model that describes an objective function and boundary conditions of the problem solution. Their disadvantage is high demand for calculation, complicated and often even impossible mathematical description of real

conditions in the system and low interactivity of a designer with a proposed solution. This group consists of methods of linear and non-linear programming, a transport problem, methods of dynamic programming, etc.

- Heuristic methods: they are based on simple algorithms of solving and investigation into the fulfilment of criteria (conditions) given by a particular algorithm. They feature relative simplicity, low demand for computing and high interactivity with a designer (the designer can interfere with the solution in any phase). However, they do not guarantee finding the global optimum and usually are unable to determine how close the found solution is to the optimum. Heuristic methods for proposal of spatial arrangement are divided into:
 - Construction procedures - based on the gradual insertion of system elements to the layout (starting with the elements with the highest transport intensity or with the strongest bonds); following methods belong to this group: CORELAP, ALDEP, PLANET, MAT, MIP, INLAYT, FLAT, etc.
 - Exchange procedures - based on the original placement, which they try to improve through the object interchange; following are some examples of the methods: CRAFT, MCRAFT, MULTIPLE, H63, FRAD, COFAD, etc.
 - Combined procedures - using a combination of the two above mentioned approaches (usually a construction procedure proposes the initial placement and an exchange procedure makes further improvement); examples of methods: BLOCPAN, LOGIC, etc.
- Metaheuristic methods: These methods produce the results of much higher quality than classical heuristics. Their advantage is the ability to leave - under certain conditions - found local extremes, which classical heuristics cannot do. Following methods belong to this group: genetic algorithms, simulated annealing, tabu search, Ant Colony optimisation, etc.

These mathematical methods use one of the following two basic types of layout quality assessment [6]:

1. Assessment based on scoring of adjacent relationships (Adjacency-based scoring): the objective is to maximise the resultant adjacency scoring for the proposed placement of objects. Data from the table of adjacency relations are used as inputs.

$$z = \sum_{i=1}^m \sum_{j=i+1}^m f_{ij} x_{ij}, \tag{1}$$

where f_{ij} is numerical adjacency-based scoring of relations among objects i and j , x_{ij} is the adjacent coefficient ($x_{ij}=1$ if the workplaces i and j are adjacent (neighbouring), $x_{ij}=0$ if they are not adjacent) and m is the number of workplaces.

2. Assessment based on total transportation outputs or costs (Distance-based scoring): the objective is to minimise the

total transportation output and transportation costs for a proposed spatial placement. Data from the matrix table of transportation relations are used as inputs.

$$z = \sum_{i=1}^m \sum_{j=i+1}^m f_{ij} c_{ij} d_{ij}, \quad (2)$$

where f_{ij} is the intensity of material flows between objects i and j , c_{ij} are transportation costs for one material unit on the distance unit between objects i and j and d_{ij} is the distance between objects i and j .

3. Genetic algorithms

Genetic algorithms are based on the principle of natural evolution, which was described in Darwin's book "On the Origin of Species by Means of Natural Selection, or the Preservation of Favoured Races in the Struggle for Life" (1859). In the seventies of the twentieth century, J. H. Holland proposed the idea of genetic algorithm as an abstraction of appropriate genetic processes [7]. A decade later, genetic algorithms became one of major rapidly developing fields of informatics and artificial intelligence. Figure 2 shows the basic procedure of genetic algorithm, which was divided into two main sections - evaluation and evolution [8].

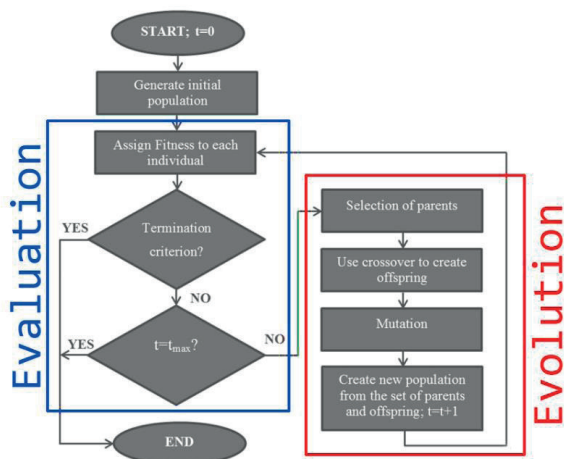


Fig. 2 Genetic algorithm

After generating the initial population, which can be created randomly, or based on historical/empirical data, the evaluation section takes place. The first step is to evaluate each individual in relation to the solved problem. Within genetic algorithms, we call the function that evaluates individuals as "fitness function". The basic principle of genetic algorithm is that individuals with better fitness must be unconditionally preferred in selection to next generation. However, with certain probability, it is possible for every solution to be selected. This ensures the diversity of the population.

The next steps after determining the fitness of all individuals in current population are two decision blocks, where the first evaluates, if the termination criterion is met (e.g. cost is below the specified value) and the second checks, if the maximum number of generations is not exceeded. If none of the above applies, the evolution section takes place. Within the evolution, the algorithm must first select the parents. As we mentioned, higher fitness means higher probability of individual being chosen. Several methods for choosing parents are known, we particularly can mention these [9]:

- Roulette mechanism with fitness-proportionate selection
- Roulette mechanism with rank selection
- Stochastic universal sampling
- Tournament mechanism
- Elitism

After determining the parents, genetic operators (Fig. 3) are applied, to create offspring. Crossover is an analogy to chromosomal recombination and reproduction in biology on which they are based. It is a genetic operator, which is responsible for mutual exchange of parts of chromosomes. Mutation is a genetic operator used to maintain genetic diversity of the population. Within mutation, one or more alleles in the chromosome are altered from their initial state. The main goal of mutation is to prevent algorithm from being stuck in the local extreme by preventing excessive similarity of individuals.

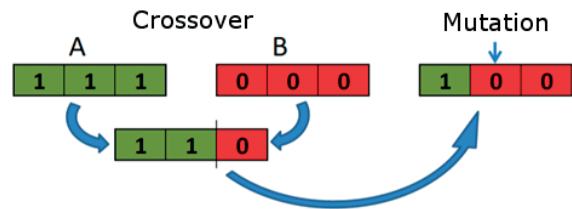


Fig. 3 Genetic operators - crossover and mutation

After application of genetic operators, new population is created, where both offspring and parents can be present, depending on the rules used within evolution. Subsequently, evaluation section calculates new fitness values and decides if another iteration is needed.

The main advantages of genetic algorithms include:

- They work with a population of possible solutions, thus it is less probable for the algorithm to end at a local optimum.
- They do not require any special knowledge about target function, they are universal.
- Genetic algorithms have very good results with problems with a large set of possible solutions.
- Versatility for a variety of optimisation problems.

Disadvantages include:

- They do not find optimal, but feasible solution.

- The implementation of the algorithm, the representation of solutions and the formulation of evaluation function can be difficult.

4. Layout planning using genetic algorithms

Currently, system for plant layout design is being developed at the Department of Industrial Engineering at the University of Zilina, utilising genetic algorithms. At this stage, input and results are transferred between Matlab and Excel spreadsheet, where simple user interface was created. In the spreadsheet, we input parameters such as number of machines, dimensions, types and probabilities of genetic operators or intensities between workstations/machines (Fig. 4).

After setting the input parameters we run the layout generator, coded in Matlab/ GNU Octave language. The algorithm creates initial solutions in a specified quantity and performs evolution. The chromosome structure was determined as $2*n$, where n is the number of machines. Therefore, we store information about

X and Y coordinates of each machine inserted into the layout. Mechanisms for machine overlap correction and desired layout dimension maintenance were also incorporated. After the run, following data are transferred back to Excel [10]:

- X-Y coordinates of each machine,
- fitness value of proposed solution,
- graphic interpretation.

Figure 5 shows the best initial solution from the first generation (a), average and best fitness values during the run (b), and final solution visualisation in Excel (c).

If we consider machines in layout as dimensionless (dimensions are not given in input section), the obtained result can be interpreted as “slots” for the machines (the layout dimensions are equal to the number of available slots in each direction), and the graphic interpretation in Excel is sufficient. However, for more accurate layout design it is necessary to take real dimensions into account, therefore there was a need for advanced drawing software. After consideration we decided to implement the interconnection with AutoCAD software (Fig. 6), where not only the obtained plant layout can be constructed, but

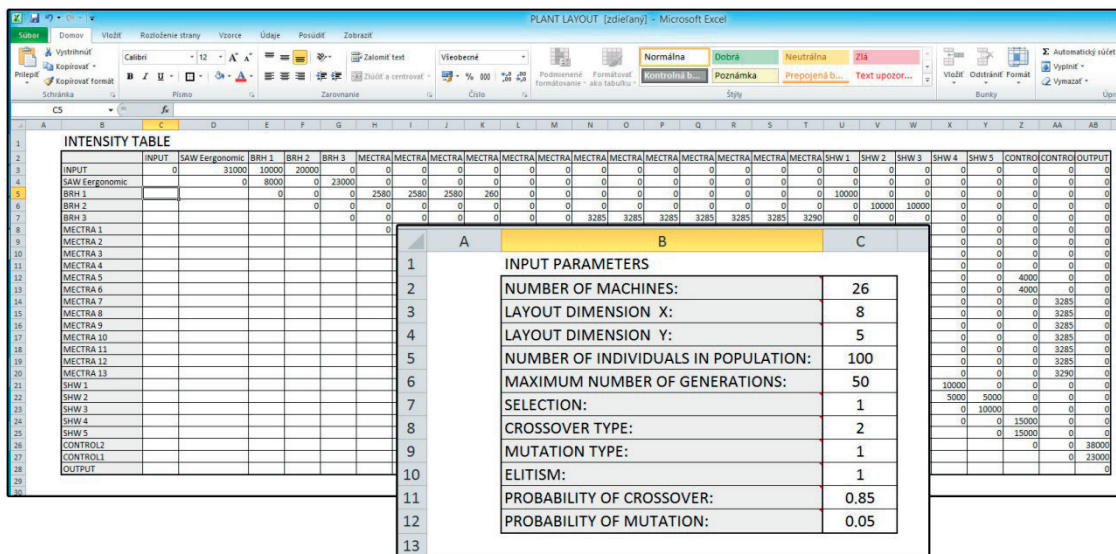


Fig. 4 Input sections of spreadsheet

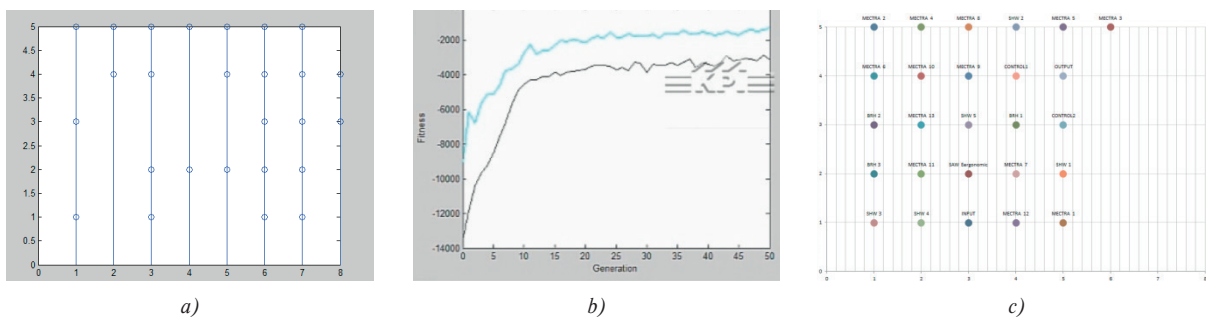


Fig. 5 Best initial solution, best and average fitness of the run, and the final solution

also thanks to installed FactoryCAD/ FactoryFLOW extensions, we can insert 3D models of machines in *.JT format, thus creating 3D model of machine layout and evaluate various aspects of the solution, such as material flow, aisle congestion, area structure or the possibility of milk run implementation with included tools. Also, thanks to SDX (Simulation Data eXchange) format, it is possible to evaluate obtained layout dynamically in another software solution by Siemens - Plant Simulation [11].

Thanks to these functionalities, we can not only get a possible layout solution, but also evaluate it both statically, and dynamically, which provides us with an advantage over solutions where only simple non-interactive block layout is created.

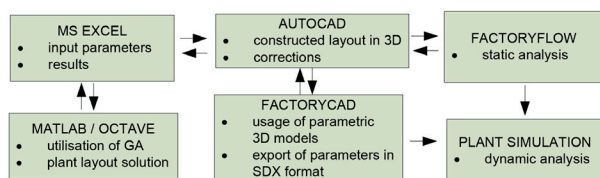


Fig. 6 Proposed integration of plant layout design utilising genetic algorithms

5. Conclusion

This paper describes the utilisation of genetic algorithms in the layout design of production systems. Authors' workplace addresses mentioned issues within the development of the digital factory concept and advanced industrial engineering methods

[12]. Described approach connects the algorithmic solution of the spatial arrangement problem (utilising genetic algorithms) with both static (FactoryFLOW) and dynamic (Plant Simulation) verification and also a graphical representation of the proposed production system (AutoCAD, FactoryCAD). The benefits of application of genetic algorithms are manifested mainly when solving large-scale problems of spatial arrangement, where genetic algorithms can effectively and more quickly converge to solution than traditional algorithms for spatial arrangement optimisation, described in Chapter 2.

Described layout design procedure provides:

- Reduction of the time needed to design the spatial arrangement of the large-scale production system.
- Increase of the design quality through the implementation of appropriate configuration of boundary conditions to the algorithm,
- Complex verification of an obtained spatial arrangement solution through static and dynamic verification of the proposed system.
- Cost reduction in a designed production system.
- Visualisation of the spatial arrangement through a 3D model of the production system, which can be further presented and utilised with the use of progressive computer technologies, such as virtual and augmented reality.

Acknowledgment

The authors gratefully acknowledge support from the Slovak Grant Agency VEGA 1/0583/12.

References

- [1] MICIETA, B, BINASOVA, V., HALUSKA, M.: The Approaches of Advanced Industrial Engineering in Next Generation Manufacturing Systems. *Communications - Scientific Letters of the University of Zilina*, vol. 16, No. 3A, 2014, Zilina, pp.101-105, ISSN 1335-4205
- [2] KRAJCOVIC, M.: *Modern Approaches of Manufacturing and Logistics Systems Design. (in Slovak)*, Digitalny podnik - cesta k buducnosti : zbornik prednasok, 10.-11.5.2011 Zilina : CEIT SK, 2011 [elektronicky zdroj], ISBN 978-80-970440-1-5, 12 p.
- [3] KRAJCOVIC, M. et al.: Intelligent Manufacturing Systems in Concept of Digital Factory. *Communications - Scientific Letters of the University of Zilina*, vol. 15, No. 2, 2013, Zilina, pp. 77-87, ISSN 1335-4205.
- [4] HNAT, J.: Virtual Factory Framework. *Industrial Engineering Moves the World - InvEnt 2012*. Zilina : University of Zilina, 2012, ISBN 978-80-554-0542-1, pp. 56-59.
- [5] FURMANN, R., STEFANIK, A.: Progressive Solutions Supporting Manufacturing and Logistics Systems Design Developed by CEIT SK, s.r.o. (in Slovak). *Produktivita a inovacie*, Zilinska univerzita : Ustav konkurencieschopnosti a inovacii, ISSN 1335-5961, vol. 2, No. 2, 2011, pp. 3-5.
- [6] LI, J., MEERKOV, S. M.: *Production Systems Engineering*. New York : Springer, 2009. 666 p., ISBN 0387755780.
- [7] NUR FADHILLAH BINTI SALEH, ABDUL RAZAK BIN HUSSAIN: Genetic Algorithms for Optimizing Manufacturing Facility Layout. [Online] 2008. [Date: 12. 10 2013.], <http://comp.utm.my/pars/files/2013/04/Genetic-Algorithms-for-Optimizing-Manufacturing-Facility-Layout.pdf>.
- [8] MISOLA, M. G., NAVARRO, B. B.: Optimal Facility Layout Problem Solution using Genetic Algorithm. *Intern. J. of Mechanical, Industrial Science and Engineering*, vol. 7, No. 8, 2013, pp. 622-627.

- [9] XIU, L., et al.: *An Adaptive Genetic Algorithm for Facility Problem in Cylinder Block Line*, IEEE, 2011, Proc. of intern. Scientific conference on Computer Science and Automation Engineering, pp. 749-753.
- [10] HANCINSKY, V., KRAJCOVIC, M.: *Genetic Algorithms and their Utilization in Production Scheduling (in Slovak)*. Prumyslove inzenyrstvi 2014, intern. student scientific conference, 2014, Kouty nad Desnou : SmartMotion, ISBN 978-80-87539-55-2, pp. 49-55.
- [11] ALTUNTAS, S., SELIM, H.: Facility Layout using Weighted Association Rule-based Data Mining Algorithms: Evaluation with Simulation. *Expert Systems with Applications*, 39 (1), 2012, pp. 3-13.
- [12] DULINA, L., BARTANUSOVA, M.: Ergonomics in Practice and its Influence on Employees' Performance. *Communications - Scientific Letters of the University of Zilina*, vol. 16, No. 3A, 2014, Zilina, pp.206-211, ISSN 1335-4205.

Peter Bubenik - Filip Horak - Viktor Hancinsky *

ACQUIRING KNOWLEDGE NEEDED FOR PULL PRODUCTION SYSTEM DESIGN THROUGH DATA MINING METHODS

Article deals with defining relationships for setting the optimal number of kanban cards in individual circuits of pull production systems, in order to minimize work in progress, while maximizing the number of completed orders in the observed time interval. To achieve this objective, data mining methods were used.

Keywords: Data mining, production planning, knowledge acquisition, genetic algorithm.

1. Introduction

In a pull production system, processes are based on customer demand. The main difference between classic push production systems and pull production systems is that the first one schedules work releases based on demand, and the latter one authorizes work releases based on system status. Among other advantages, pull production systems can provide low unit cost, good customer service, high external quality and flexibility. Unfortunately, pull systems cannot be applied to all business types, because they require initial conditions such as stable demand, low number of product types, etc.

However, by integrating pull systems in some of your production processes, you will be able to reduce your lead times, and perhaps associated costs. One of the most significant parameters of pull production system is a number of circulating kanban cards. Central topic of this article is a new approach to finding out an optimal setting of this crucial parameter by using methods and techniques such as data mining, simulation and genetic algorithms.

2. Pull Production System

Kanban became an effective tool in support of running a production system as a whole, and it proved to be an excellent way for promoting improvement. One of the main benefits of kanban is to establish an upper limit to the work in progress inventory, avoiding overloading of the manufacturing system.

Kanban cards are a key component of kanban and signal the need to move materials within a manufacturing or production facility or move materials from an outside supplier in to the production facility. The kanban card is, in effect, a message that signals that there is a depletion of product, parts, or inventory that, when received, the kanban will trigger the replenishment of that product, part, or inventory. Consumption therefore drives demand for more production, and demand for more products is signalled by the kanban card. Kanban cards therefore help create a demand-driven system [1].

3. Data mining

The manual extraction of patterns from data has occurred for centuries. Early methods of identifying patterns in data include Bayes' theorem (1700s) and regression analysis (1800s). The proliferation, ubiquity and increasing power of computer technology has dramatically increased data collection, storage, and manipulation ability. As data sets have grown in size and complexity, direct "hands-on" data analysis has increasingly been augmented with indirect, automated data processing, aided by other discoveries in computer science, such as neural networks, cluster analysis, genetic algorithms (1950s), decision trees (1960s), and support vector machines (1990s). Data mining is the process of applying these methods with the intention of uncovering hidden patterns in large data sets. It bridges the gap from applied statistics and artificial intelligence (which usually provide the mathematical background) to database management

* Peter Bubenik, Filip Horak, Viktor Hancinsky

Department of Industrial Engineering, Faculty of Mechanical Engineering University of Zilina, Slovakia
E-mail: peter.bubenik@fstroj.uniza.sk

by exploiting the way data is stored and indexed in databases to execute the actual learning and discovery algorithms more efficiently, allowing such methods to be applied to ever larger data sets. Knowledge exists in all business functions, including purchasing, marketing, design, production, maintenance and distribution, but knowledge can be notoriously difficult to identify, capture and manage [2]. Simply stated, data mining refers to extracting or “mining” knowledge from large amounts of data [3]. Due to large amounts of data generated and collected during manufacturing execution, manufacturing is a promising area of application for data mining to extract knowledge for optimization purposes [4].

4. Simulation in terms of data mining

Simulations lend meaning to data and can be updated and adapted as further data come in [5]. It often happens that provided historical data are not sufficient to derive relevant knowledge. This occurs for a number of reasons, the most common ones are:

- The unpredictability of external factors affecting the operation of the production system.
- Inadequate recording of the data needed for analysis.
- Incorrect data caused by human factor.
- Incompatible corresponding resolution of analyzed data.
- Lack of data due to newly implemented system.

In such cases, it is possible to use simulation, in which the listed historical data are used, if possible, in the following tasks:

- Elimination of attributes that do not affect the target parameter.
- Setting the probability distribution of the process attributes.
- Simulation model validation.

If the historical data are not available at all, as often happens in case of designing new production systems, simulation is the only way to obtain data necessary to derive applicable knowledge. The heart of data mining is knowledge discovery, as it enables to discover relevant objects and the relationships that exist between

these objects, while simulation provides a vehicle to represent those objects and their relationships [6].

5. Problem formulation

Figure 1 shows the pull production system, whose parameters are needed to be optimized. Simulation model was created in Simulink environment with use of SimEvents Toolbox [7]. In considered system, there are three circuits, in which kanban cards in the number of kb_1 , kb_2 and kb_3 circulate. The first circuit is shown first from the left in Fig. 1, to which belongs number of cards kb_1 , the next one, transport circuit with block *Trans_kanban* contains kb_2 kanban cards and for following block, kb_3 cards are allocated. The very last block on the right is used to generate production orders based on normal distribution. Also cumulative operations for defining the amount of work in progress run in this block.

The aim of the solution was to formalize relations that describe the impact of the selected combination of numbers of kanban cards on the amount of work in progress and the numbers of finished orders, as these factors are crucial in terms of the efficiency of the proposed system.

Since the chosen maximum number of kanban cards was $max[kb_i]=30$, in the case of simulating every possible case it would leave $n^k = 30^3 = 27000$ simulation runs. To reduce the number of simulation runs, optimization through genetic algorithms in Matlab environment was used in this case.

6. Acquiring data using genetic algorithms

If we label $f_{sim}(kb_1, kb_2, kb_3)$ as a function that describes the behavior of the simulation model, the optimization problem can be written as:

$$WIP_{opt} = \min_{kb_i \in Z^+} \{f_{sim}(kb_1, kb_2, kb_3)\} \quad (1)$$

where WIP_{opt} is the minimal amount of work in progress achieved with properly chosen combination of numbers of kanban cards in each circuit. Utilization of genetic algorithms in this case

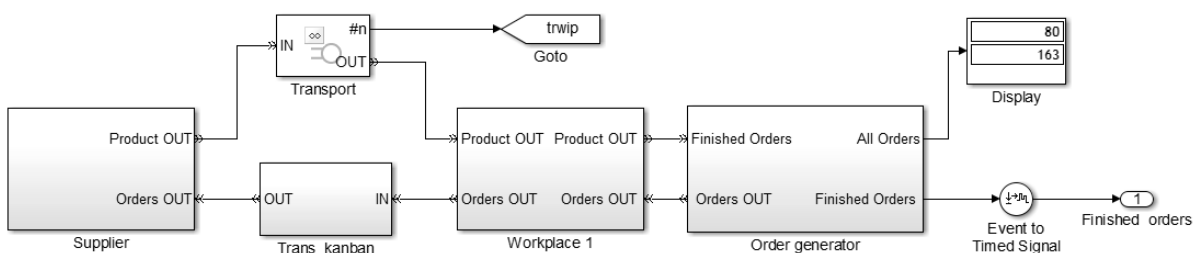


Fig. 1 Analyzed production system created in Simulink environment

reduced the number of simulation runs from 27000 to 1040 for optimization in terms of the amount of work in progress. For optimization in terms of the number of finished orders, a similar formula was used, with the difference that in this case, the aim was to maximize the number of finished orders.

$$FO_{opt} = \max_{kb_1 \in Z^+} \{f_{sim}(kb_1, kb_2, kb_3)\} \quad (2)$$

For optimization in terms of the number of finished orders, 880 simulation runs were executed. Values calculated in order to minimize WIP and maximize FO together make the dataset, which should also contain those combinations of numbers of kanban cards in particular circuits, which can be determined from which knowledge applicable to the production system can be determined. Figure 2 shows the resulting dataset of performed simulation run, where the color attribute describes the amount of work in progress.

From Fig. 2 it is clear that the amount of work in progress is increasing with the increasing number of kanban cards in each circuit. Figure 3 shows the same set of combinations of different

amounts of kanban cards, but in this case the number of finished orders is the evaluation criterion.

Search and formalization of knowledge through data mining algorithms

Following data mining algorithms were used to seek knowledge in the dataset:

- Neural networks.
- Random forests.
- Linear regression.

The solution was carried out in KNIME [8] environment and for testing the models in terms of suitability of use, equation (3) was used to calculate the mean square error.

$$MSE = \frac{1}{n} \sum_{i=1}^n (\hat{Y}_i - Y_i)^2 \quad (3)$$

where \hat{Y} is prediction vector and Y is the vector of actual values obtained from the simulation model. To use a neural network predictor, it was necessary to temporarily convert the data into $\langle 0,1 \rangle$ interval, using combinations of *Normalizer/Denormalizer* nodes. In this case, feedforward neural networks algorithm RProp

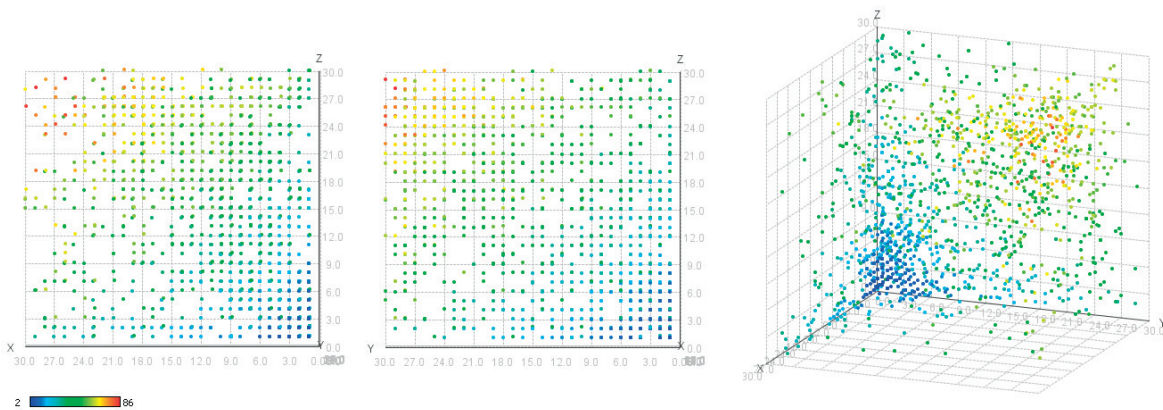


Fig. 2 Effect of combinations of numbers of kanban cards in particular circuits on the amount of work in progress ($x=kb_1, y=kb_2, z=kb_3$)

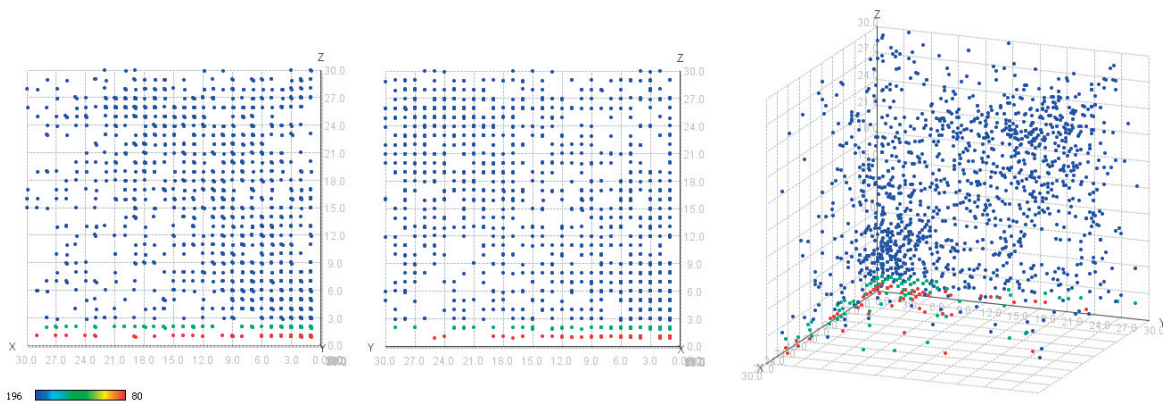


Fig. 3 Effect of combinations of numbers of kanban cards in particular on the number of finished orders ($x=kb_1, y=kb_2, z=kb_3$)

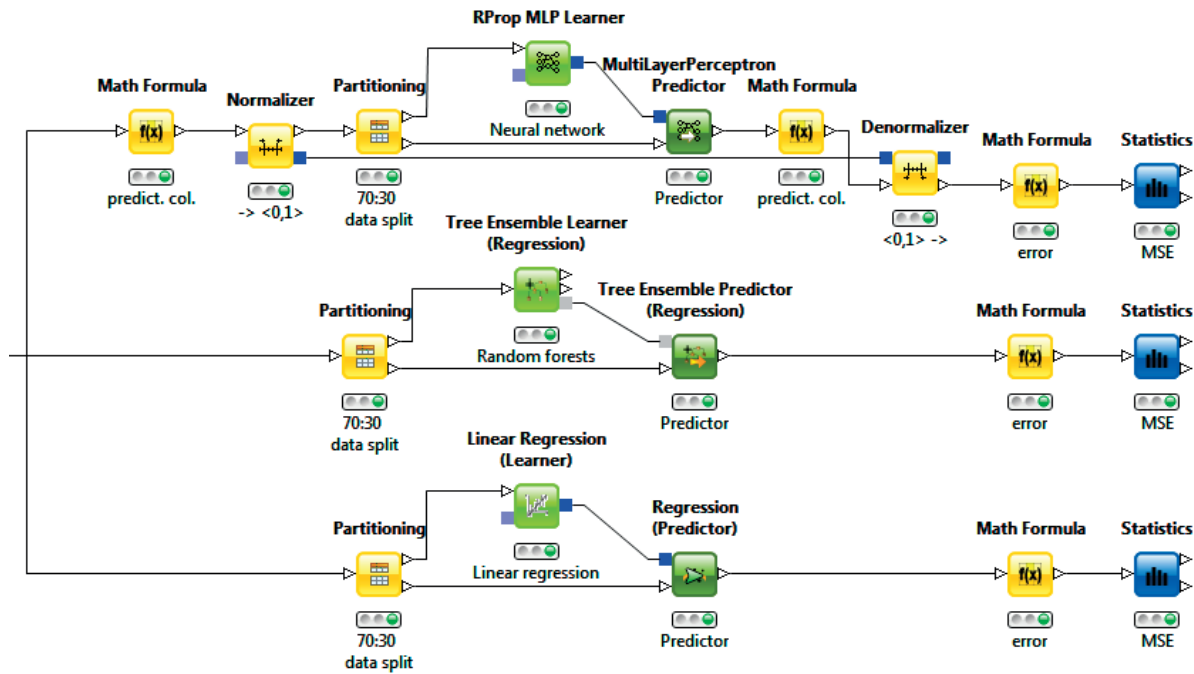


Fig. 4 Data processing stream and knowledge acquisition

MLP was used with the number of 100 iterations. As with other used algorithms, random selection was used to select training set of 30% size of the total analyzed data, based on which the mean square error was calculated according to equation (3) within model testing. Random forests algorithm was implemented by creating 50 random regression decision trees. It was not necessary to normalize the data. Further configuration of the algorithm for linear model prediction based on linear regression method was not necessary. Data processing stream and knowledge acquisition in KNIME environment can be seen in Fig. 4.

In this case, the aim was to seek knowledge about relation of combination of numbers of kanban cards kb_i in individual circuits i to amount of work in progress WIP . In the case of gaining knowledge about target parameter FO - number of finished orders, process topology remained unchanged (as can be seen in Fig. 4), only input dataset and its predicted columns were changed.

After executing transformation and mining operations, the results showed that for defining relations between number of kanban cards and amount of work in progress, the linear regression generated model performs the best. For determining the effect of kanban cards on number of finished orders, the best performing algorithm is random forests. In these cases, the mean square error was the lowest, as is shown in Table 1.

Calculated mean square error values for individual models Table 1

Predicted attribute	MSE		
	Rprop MLP	Random forests	Linear regression
WIP	6.467	37.42	0.106
FO	0.0587	0.011	1121.579

Tested models with the lowest error can be considered established and formalized knowledge. For the amount of work in progress, the model has the form:

$$WIP = 1.005 \cdot kb_1 + 0.9985 \cdot kb_2 + 1.0274 \cdot kb_3 \quad (4)$$

For the number of finished orders, the random forests algorithm derived model:

$$FO = \begin{cases} 80: kb3 < 1.5 \\ 154: kb3 \leq 2.5 \\ 196: kb3 > 2.5 \end{cases} \quad (5)$$

7. Conclusion

Acquired knowledge (4), (5) can be written in PMML format and added to the knowledge base, which is together with inference mechanism and user interface capable to form functioning knowledge system. Therefore, when designing pull production system it is necessary in terms of capacity to consider this knowledge, if we want to achieve the optimal amount of work

in progress together with the highest possible number of finished orders. In the case of appropriate choice of combination of kanban cards, the cost perspective would be also important, but if we consider that in the case of pull systems the highest costs come from delays, which results in a smaller number of completed

orders in due time, the most feasible combination of numbers of kanban cards should be [1 1 3]. Specific solution for the current situation, however, should be offered by the knowledge system, which would retrieve listed findings from knowledge base and optimize the resulting combination also in the terms of cost.

References

- [1] MICIETA, B., GREGOR, M., QUIRENC, P., BOTKA, M.: *KANBAN: Slovak Centre for Productivity (in Slovak)*, Zilina, 2001, ISBN 8096832425
- [2] HARDING, J. et al.: Data Mining in Manufacturing: A Review, *J. of Manufacturing Science and Engineering*, 2006, vol. 128, p. 969-976, ISSN: 1087-1357
- [3] HAN, J., KAMBER, M.: *Data Mining: Concepts and Techniques*, 2nd ed., edited by J. Gray, San Francisco: Morgan Kaufmann Publishers, 2006, p. 5, ISBN: 1-55860-901-6
- [4] GROGER, CH., NIEDERMANN, F., MITSCHANG, B.: *Data Mining-driven Manufacturing Process Optimization*. Proc. of the World Congress on Engineering, 2012, London. ISBN: 978-988-19252-2-0
- [5] LYTTON, W., STEWART, M.: Data Mining Through Simulation. *Neuroinformatics*. ISBN 978-1-58829-720-4, 2007, vol. 401, pp. 155-166
- [6] ALNOUKARI, M.: *An Integrated Data Mining and Simulation Solution*, 2010, p. 929, Available online: <http://www.academia.edu/190456/An_Integrated_Data_Mining_and_Simulation_Solution>
- [7] *SimEvents*, 2012. Available online: <<https://www.mathworks.com/products/datasheets/pdf/simevents.pdf>>
- [8] *KNIME Quickstart Guide*. 2011 Available online: < http://tech.knime.org/files/KNIME_quickstart.pdf> .

Helena Samajova - Tongxing Li *

OSCILLATORS NEAR HOPF BIFURCATION

In this paper the differential transformation method (DTM) is employed to solve a system of linear differential equations derived for energy optimal control theory and nonlinear differential equations and their systems for oscillators near Hopf bifurcation. They are given by differential equations in a complex plane. Different types of forced terms are considered. The approximate solutions are given in the form of series with required accuracy. Some numerical examples are provided.

Keywords: Oscillators, systems of ordinary differential equations, differential transformation method.

1. Introduction

The collective behaviour of oscillators and coupled oscillators represents the complex dynamic system. It demonstrates interest in experimental as well as numerical research. Examples of such applications may be found in mechanical oscillators, limit cycle oscillators, semiconductor lasers, superconducting Josephson junction or pacemakers. Synchronization, where individual oscillators oscillate at a common phase and frequency, depends on coupling force. A weak coupling leads to the character of non-coupled oscillators, for stronger coupling the considering of both frequency and amplitude is required. An approach used in the investigation is based on the study of the stability - the system is linearized near zero [1]. The solving of differential equations or their systems by DTM avoids such a restriction. This paper presents two main goals. Firstly, we apply the differential transformation method for oscillators and coupled oscillators. Secondly, we reduce a system of linear equations in an engineering application to the system of linear equations to energy optimal control of motors.

2. DTM - differential transformation method

In this section we bring a brief overview of the differential transformation method that proposes a technique which does not evaluate the derivatives symbolically; the differential transformation DT of the n^{th} derivative of a function $y(t)$ is defined by

$$Y(n) = \frac{1}{n!} \left[\frac{d^n y(t)}{dt^n} \right]_{t=t_0}, \quad (1)$$

where $y(t)$ is an original and $Y(t)$ is a transformed function.

An inverse transformation of $Y(n)$ leads to

$$y(t) = \sum_{n=0}^{\infty} Y(n)(t - t_0)^n. \quad (2)$$

If $t_0 = 0$, then the representation of the function reduces to

$$y(t) = \sum_{n=0}^{\infty} Y(n)t^n. \quad (3)$$

The properties of the DT with their proofs are published in [2 - 4]; the used ones of them are introduced below.

Let functions $G, G_i, i = 1,2,3$ be the differential transformations of functions $g, g_i, i = 1,2,3$, then the following correspondences hold

$$g(t) = g_1(t) + g_2(t) \rightarrow G(n) = G_1(n) + G_2(n) \quad (4)$$

$$g(t) = \lambda g_1(t) \rightarrow G(n) = \lambda G_1(n) \quad (5)$$

$$g(t) = g_1(t)g_2(t) \rightarrow G(n) = \sum_{l=0}^n G_1(l)G_2(n-l) \quad (6)$$

$$g(t) = t^k \rightarrow G(n) = \delta(n-k) \quad (7)$$

$$g(t) = e^{\beta t} \rightarrow G(n) = \frac{\beta^n}{n!} \quad (8)$$

$$g(t) = \frac{d^k g_1(t)}{dt^k} \rightarrow G(n) = \frac{(n+k)!}{n!} G_1(n+k) \quad (9)$$

* ¹Helena Samajova, ²Tongxing Li

¹Department of Appl. Mathematics, Faculty of Mechanical Engineering, University of Zilina, Slovakia

²School of Control Science and Engineering, Shandong University, Jinan, China

E-mail: helena.samajova@fstroj.uniza.sk

$$g(t) = \prod_{i=1}^3 g_i(t) \rightarrow G(n) = \sum_{s_1=0}^n \sum_{s_2=0}^{n-s_1} G_1(s_1)G_2(s_2) \cdot G_3(n-s_1-s_2) \quad (10)$$

where $\delta(n-k)$ is the Kronecker delta symbol, $n, l, k \in N^0$.

3. Oscillators near Hopf bifurcation

3.1 Differential equation for an oscillator with a real parameter ω .

We consider nonlinear differential equation used for oscillators [1] near Hopf bifurcation [5] with different types of forcing terms

$$y'(t) = y(t) [1 + j\omega + |y(t)|^2] + f(t), \quad (11)$$

where $j^2 = -1$, $\omega \in \mathbf{R}$, with the initial condition $y(0) = a$ and $a \in C$ is a constant. With the use of $y(t) = u(t) + jv(t)$ and a forcing term $f(t) = f_1(t) + jf_2(t)$ the equation (11) is equivalent to the system of two equations

$$\begin{aligned} u'(t) &= u(t) - \omega v(t) + u^3(t) + u(t)v^2(t) + f_1(t) \\ v'(t) &= v(t) + \omega u(t) + v(t)u^2(t) + v^3(t) + f_2(t) \end{aligned} \quad (12)$$

Using the properties (4) - (10), the resulting system of the DTM is

$$\begin{aligned} U(n+1) &= [U(n) - \omega V(n) + \sum_{s_1=0}^n \sum_{s_2=0}^{n-s_1} U(s_1)U(s_2) \cdot \\ &\cdot U(n-s_1-s_2) + \sum_{s_1=0}^n \sum_{s_2=0}^{n-s_1} U(s_1)V(s_2) \cdot \\ &\cdot V(n-s_1-s_2) + F_1(n)] / (n+1) \end{aligned} \quad (13)$$

$$\begin{aligned} V(n+1) &= [V(n) + \omega U(n) + \sum_{s_1=0}^n \sum_{s_2=0}^{n-s_1} V(s_1)U(s_2) \cdot \\ &\cdot U(n-s_1-s_2) + \sum_{s_1=0}^n \sum_{s_2=0}^{n-s_1} V(s_1)V(s_2) \cdot \\ &\cdot V(n-s_1-s_2) + F_2(n)] / (n+1) \end{aligned}$$

Now we will consider the cases with forcing terms of different types.

R1. Consider equations (12) without any forcing term and with the initial conditions $u(0) = 0.5$, $v(0) = 0.75$ and a parameter $\omega = 2$. The transformation of functions $f_1(t) = f_2(t) = 0$ yields $F_1(n) = F_2(n) = 0$.

The Matlab program is involved and gives numerical solutions as follows

$$\begin{aligned} u(t) &= 0.5 - 0.3906t - 0.4091t^2 + 2.9799t^3 + 6.6069t^4 + 8.7719t^5 + \dots \\ v(t) &= 0.75 + 2.1562t + 1.2397t^2 + 0.7014t^3 + 2.5814t^4 + 5.9462t^5 + \dots \end{aligned} \quad (14)$$

R2 a). For the forcing term of the power type $f(t) = t^k + jt^l$, where k, l are nonnegative integers the DT of $f_1(t)$ and $f_2(t)$ are $F_1(n) = \delta(n-k)$, $F_2(n) = \delta(n-l)$. The solutions for the same conditions as in R1. and $k = 3, l = 4$ are

$$\begin{aligned} u(t) &= 0.5 - 0.3906t - 0.4091t^2 + 2.9799t^3 + 6.8569t^4 + 8.8594t^5 + \dots \\ v(t) &= 0.75 + 2.1562t + 1.2397t^2 + 0.7014t^3 + 2.3814t^4 + 6.311t^5 + \dots \end{aligned} \quad (15)$$

b) Solutions under the initial conditions $u(0) = 0.5$, $v(0) = 0.75$ and parameters $\omega = 2$ and $k = 3$ are given as

$$\begin{aligned} u(t) &= 0.5 - 0.3906t - 0.4091t^2 + 2.9799t^3 + 6.8569t^4 + 8.8563t^5 + \dots \\ v(t) &= 0.75 + 2.1562t + 1.2397t^2 + 0.7014t^3 + 2.3814t^4 + 6.1993t^5 + \dots \end{aligned} \quad (16)$$

R3. If the forcing term is of the exponential type $f(t) = e^{\alpha t} + je^{\beta t}$, the DT of $f(t)$ is $F(n) = F_1(n) + jF_2(n)$,

$$\text{where } F_1(n) = \frac{\alpha^n}{n!}, F_2(n) = \frac{\beta^n}{n!}.$$

For $\alpha = 2, \beta = 1$ and for identical initial condition we obtain following solutions

$$\begin{aligned} u(t) &= 0.5 - 0.6093t - 1.4345t^2 + 9.6199t^3 + 29.8612t^4 + 75.7508t^5 + \dots \\ v(t) &= 0.75 + 3.1562t + 4.2701t^2 + 7.0497t^3 + 19.3663t^4 + 55.678t^5 + \dots \end{aligned} \quad (17)$$

In the special case $\alpha = \beta = 1$

$$\begin{aligned} u(t) &= 0.5 - 0.6093t - 0.9345t^2 + 8.8282t^3 + 28.7231t^4 + 71.9794t^5 + \dots \\ v(t) &= 0.75 + 3.1562t + 4.271t^2 + 6.4976t^3 + 17.6488t^4 + 50.7307t^5 + \dots \end{aligned} \quad (18)$$

Remark: From the theory of Taylor series and relations (7), (8) and (13), it is evident that the influence of the power type right hand side (RHS) manifests from the term of the lower degree of k, l unlike the RHS of exponential type changes all the terms of solutions.

3.2 Differential equation for an oscillator with a complex parameter ω .

Consider the equation (11) with $\omega = \omega_1 + j\omega_2 \in C$. The equation is separated into

$$\begin{aligned} u'(t) &= u(t)(1 + \omega_1) - \omega_2 v(t) + u^3(t) + \\ &+ u(t)v^2(t) + f_1(t) \end{aligned} \quad (19)$$

$$\begin{aligned} v'(t) &= v(t)(1 + \omega_2) + \omega_1 u(t) + \\ &+ v(t)u^2(t) + v^3(t) + f_2(t) \end{aligned}$$

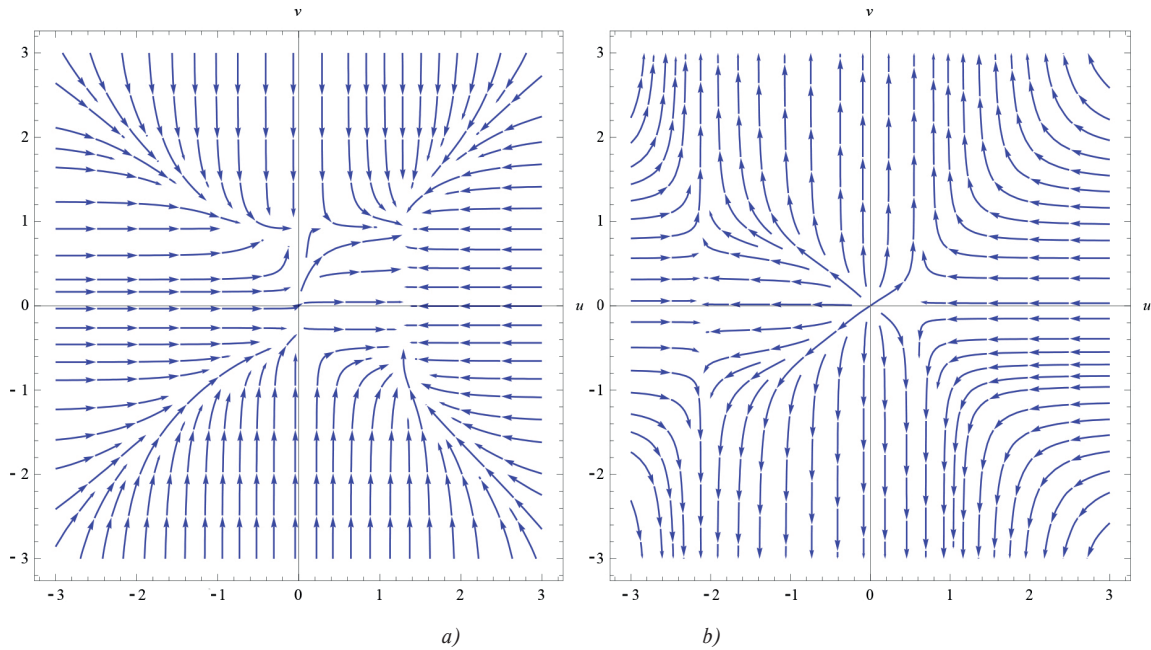


Fig. 1 Vector fields

Such kind of a system could be regarded as coupled oscillators with two different frequencies ω_1, ω_2 .

The DM of $u(t), v(t)$

$$\begin{aligned}
 U(n+1) = & [(1 + \omega_1)U(n) - \omega_2 V(n) + \sum_{s_1=0}^n \sum_{s_2=0}^{n-s_1} U(s_1) \cdot \\
 & \cdot U(s_2)U(n-s_1-s_2) + \sum_{s_1=0}^n \sum_{s_2=0}^{n-s_1} U(s_1)V(s_2) \cdot \\
 & \cdot V(n-s_1-s_2) + F_1(n)]/(n+1)
 \end{aligned} \quad (20)$$

$$\begin{aligned}
 V(n+1) = & [(1 + \omega_2)V(n) + \omega_1 U(n) + \sum_{s_1=0}^n \sum_{s_2=0}^{n-s_1} V(s_1) \cdot \\
 & \cdot U(s_2)U(n-s_1-s_2) + \sum_{s_1=0}^n \sum_{s_2=0}^{n-s_1} V(s_1)V(s_2) \cdot \\
 & \cdot V(n-s_1-s_2) + F_2(n)]/(n+1)
 \end{aligned}$$

The difference of two frequencies $\Delta = |\omega_1 - \omega_2|$ and a coupling constant K introduced in the system of differential equations (23) have a decisive influence on the behaviour of such systems of coupled oscillators. It could be one of the parameters which may be the reason of quenching of oscillators' amplitudes.

The numerical solutions of (21) are given for the initial conditions $u(0) = 0.5, v(0) = 0.75$ and frequencies $\omega_1 = 1, \omega_2 = 2$

$$\begin{aligned}
 u(t) = & 0.5 - 0.1563t - 0.1143t^2 + 0.7296t^3 + 2.4144t^4 + 6.4313t^5 + \dots \\
 v(t) = & 0.75 + 2.3594t + 3.6802t^2 + 7.8027t^3 + 19.3675t^4 + 48.2082t^5 + \dots
 \end{aligned} \quad (21)$$

Vector fields for solutions of equation (19) near Hopf bifurcation with initial conditions $u(0) = v(0) = 0.001, \omega = 5 + 6j, n=20$ are in Fig. 1 with forcing term a) $f(t) = t - jt^4$; b) $f(t) = e + je^{-3}$.

3.3 System of differential equations for coupled oscillators with real parameters ω_1, ω_2 .

Now, let us consider the system of two coupled oscillators with a constant K , which represents the coupling as considered in [1] and $\omega_1, \omega_2 \in \mathbf{R}$

$$\begin{aligned}
 y_1'(t) = & y_1(t) [1 + j\omega_1 + |y_1(t)|^2] + K(y_2(t) - y_1(t)) \\
 y_2'(t) = & y_2(t) [1 + j\omega_2 + |y_2(t)|^2] + K(y_1(t) - y_2(t))
 \end{aligned} \quad (22)$$

Similarly to the case of one equation we may separate it into the system

$$\begin{aligned}
 u_1'(t) = & u_1(t) - \omega_1 v_1(t) + u_1^3(t) + \\
 & + u_1(t)v_1^2(t) + K(u_2(t) - u_1(t)) \\
 v_1'(t) = & v_1(t) + \omega_1 u_1(t) + u_1^2(t)v_1(t) + \\
 & + v_1^3(t) + K(v_2(t) - v_1(t)) \\
 u_2'(t) = & u_2(t) - \omega_2 v_2(t) + u_2^3(t) + \\
 & + u_2(t)v_2^2(t) + K(u_1(t) - u_2(t)) \\
 v_2'(t) = & v_2(t) + \omega_2 u_2(t) + u_2^2(t)v_2(t) + \\
 & + v_2^3(t) + K(v_1(t) - v_2(t))
 \end{aligned} \quad (23)$$

and the DT is

$$\begin{aligned}
 U_1(n+1) &= [U_1(n) - \omega_1 V_1(n) + \sum_{s_1=0}^n \sum_{s_2=0}^{n-s_1} U_1(s_1) \cdot \\
 &U_1(s_2) U_1(n-s_1-s_2) + \sum_{s_1=0}^n \sum_{s_2=0}^{n-s_1} U_1(s_1) V_1(s_2) \cdot \\
 &\cdot V_1(n-s_1-s_2) + K(U_2(n) - U_1(n))] / (n+1) \\
 V_1(n+1) &= [V_1(n) + \omega_1 U_1(n) + \sum_{s_1=0}^n \sum_{s_2=0}^{n-s_1} V_1(s_1) \cdot \\
 &U_1(s_2) U_1(n-s_1-s_2) + \sum_{s_1=0}^n \sum_{s_2=0}^{n-s_1} V_1(s_1) V_1(s_2) \cdot \\
 &\cdot V_1(n-s_1-s_2) + K(V_2(n) - V_1(n))] / (n+1) \\
 &\quad (24) \\
 U_2(n+1) &= [U_2(n) - \omega_2 V_2(n) + \sum_{s_1=0}^n \sum_{s_2=0}^{n-s_1} U_2(s_1) \cdot \\
 &U_2(s_2) U_2(n-s_1-s_2) + \sum_{s_1=0}^n \sum_{s_2=0}^{n-s_1} U_2(s_1) V_2(s_2) \cdot \\
 &\cdot V_2(n-s_1-s_2) + K(U_1(n) - U_2(n))] / (n+1) \\
 V_2(n+1) &= [V_2(n) + \omega_2 U_2(n) + \sum_{s_1=0}^n \sum_{s_2=0}^{n-s_1} V_2(s_1) \cdot \\
 &U_2(s_2) U_2(n-s_1-s_2) + \sum_{s_1=0}^n \sum_{s_2=0}^{n-s_1} V_2(s_1) V_2(s_2) \cdot \\
 &\cdot V_2(n-s_1-s_2) + K(V_1(n) - V_2(n))] / (n+1)
 \end{aligned}$$

Considering the parameters of previous numerical examples $u_1(0) = u_2(0) = 0.5$, $v_1(0) = v_2(0) = 0.75$, $\omega_1 = 2$, $\omega_2 = 1$, $K = 2$, the components of the solutions are as follows

$$\begin{aligned}
 u_1(t) &= 0.5 - 0.5938t - 1.4111t^2 - 1.1733t^3 - 2.7805t^4 - 4.5852t^5 + \dots \\
 v_1(t) &= 0.75 + 2.3594t + 2.1489t^2 + 5.4193t^3 + 11.1783t^4 + 25.7515t^5 + \dots \\
 u_2(t) &= 0.5 + 0.1563t - 0.8018t^2 - 0.5712t^3 + 0.3199t^4 + 0.2545t^5 + \dots \\
 v_2(t) &= 0.75 + 1.8594t + 3.3677t^2 + 4.7132t^3 + 11.9392t^4 + 26.1863t^5 + \dots
 \end{aligned} \quad (25)$$

4. An engineering application

Let us demonstrate the exploitation of DTM principles on the problem describing an electric motor presented in [6 and 7]. Mathematical analysis of energy optimal speed and position control of the drive with PMSM (permanent

magnet synchronous motor) takes into account time varying load torque and motor copper losses.

Generally, we consider the system of linear differential equations

$$\begin{aligned}
 y_1'(t) &= y_2(t) + f_1(t) \\
 a_1 y_2'(t) &= y_3(t) - y_4(t) + f_2(t) \\
 y_3'(t) &= a_2 y_2(t) - a_3 y_3(t) + f_3(t) \\
 y_4'(t) &= f_4(t)
 \end{aligned} \quad (26)$$

The DTM brings the resulting system

$$\begin{aligned}
 Y_1(n+1) &= Y_2(n) + F_1(n) \\
 a_1 Y_2(n+1) &= Y_3(n) - Y_4(n) + F_2(n) \\
 Y_3(n+1) &= a_2 Y_2(n) + a_3 Y_3(n) + F_3(n) \\
 Y_4(n+1) &= F_4(n)
 \end{aligned} \quad (27)$$

The system (26) with $f_i(t) = 0$, $i = 1, 2$, $f_3(t) = 0.39$ and $f_4(t) = a_4 t + a_5$ is studied in [6]. Parameters for this model of an engine are given in [8]. The numerical solution by Matlab computed for initial conditions $y_1(0) = y_2(0) = y_3(0) = y_4(0) = 0$ and parameters

$$a_1 = 0.05, a_2 = -\frac{1}{1.3}, a_3 = 0.39^2, a_4 = a_5 = 1 \text{ is}$$

$$\begin{aligned}
 y_1(t) &= 3.9t^2 - 3.333t^3 - 5.833t^4 + 2.412t^5 + \dots \\
 y_2(t) &= 7.8t - 10t^2 - 23.33t^3 + 12.06t^4 + 18.315t^5 + \dots \\
 y_3(t) &= 0.39t - 3t^2 + 2.412t^3 + 4.578t^4 - 1.716t^5 + \dots \\
 y_4(t) &= t + 0.5t^2
 \end{aligned} \quad (28)$$

5. Conclusion

We used the differential transformation method DTM for two different problems - coupled nonlinear oscillators and energy optimal speed and position control of PMSM drive. Solutions to linear and nonlinear systems of ODE are calculated for systems with power and exponential types of RHS.

Acknowledgements

The first author gratefully acknowledges the Scientific Grant Agency (VEGA) of the Ministry of Education of the Slovak Republic and the Slovak Academy of Sciences for supporting this work under Grant No. 1/1245/12.

References

- [1] ARONSON, D. G, ERMENTROUT, G. B., KOPELL, N.: *Amplitude Response of Coupled Oscillators*, Physica D, 41, 1990, pp. 403-449.
- [2] MIRZAEI, F.: Differential Transform Method for Solving Linear and Nonlinear Systems of Ordinary Differential Equations, *Applied Mathematical Sciences*, vol. 5, 2011, No. 70, pp. 3465-3472.
- [3] KHAN, Y., SVOBODA, Z., SMARDA, Z.: Solving Certain Classes of Lane-n Type Equations Using the Differential Transformation Method, *Advances in Difference Equations*, 2012, 174.
- [4] REBENDA, J., SMARDA, Z.: Stability and Asymptotic Properties of a System of Functional Differential Equations with Nonconstant Delays, *Applied Mathematics and Computation* 219, 2013, pp. 6622-6632.
- [5] MARSDEN, J. E., MCCRACKEN, M.: The Hopf Bifurcation and Its Applications, Springer-Verlag, *Applied Mathematical Sciences*, New York, 1976.
- [6] VITEK, J., FTOREK, B., BUTKO, P., FEDOR, T.: Energy Optimal Control of PMSM Drive for Time-varying Load Torque, *Applied Mechanics and Materials*, vol. 710, 2015, pp. 67-75.
- [7] FTOREK, B., ORSANSKY, P.: *Some Analytic Solutions of a Time-delay Differential System*, Proc. of Interaction and feedbacks 2012: XIX-th national seminar, Prague: Institute of Thermomechanics, AS CR, 2012, pp. 5-10.
- [8] VITEK, J., FTOREK, B.: Energy Efficient Speed and Position Control of Electric Drives with PMSM, *Communications - Scientific Letters of the University of Zilina*, vol. 16, No. 1, 2014, pp. 64-71.

Frantisek Brumerick - Michal Lukac - Aleksander Nieoczym *

MECHANICAL DIFFERENTIAL MATHEMATICAL MODEL

The simulation of a road vehicle requires also the model of a mechanical differential. This article describes one of the possibilities how to build a mechanical differential model by the selected vehicle model structure.

Keywords: Simulation, mathematical model, mechanical differential.

1. Introduction

In cars and other double-tracked wheeled vehicles, a differential couples the drive shaft to half-shafts that connect to the front or rear driving wheels. The differential gearing allows the outer drive wheel to rotate faster than the inner drive wheel during a turn [1] and [2]. This is necessary when the vehicle turns, making the wheel that is travelling around the outside of the turning curve roll farther and faster than the other one. Average of the rotational speed of the two driving wheels equals the input rotational speed of the drive shaft. An increase in the speed of one wheel is balanced by a decrease in the speed of the other.

2. Vehicle model concept

Special blocks that enable sequencing and creating of string structures are also called two-terminal blocks. They have one input i and one output o on each side of the block (Fig. 1).



Fig. 1 Two-terminal block (Source: authors)

The principle of the string-concept vehicle modelling can be used by the classic drivetrain vehicle model, which consists from two-terminal block models of the drivetrain subsystems and the

three-terminal block model of the rear axle mechanical differential (Fig. 2).

The vehicle drivetrain model consists of blocks which are connected in alternating order of the blocks defining inertias (engine, gearbox, differential, vehicle body, wheels) and the blocks defining the torque or force law between connected components (clutch, torque converter, elastic shafts, tire) [3] and [4].

The blocks can be then divided into two groups:

- inertia blocks with the inner structure defining the inertia of the engine, gearbox, differential, wheels and the car body, which calculate the component speed,
- torque and force blocks, which calculate the torque of the clutch (alt. torque converter), torque on the shaft ends and forces between the tires and the track or the wheels respectively.

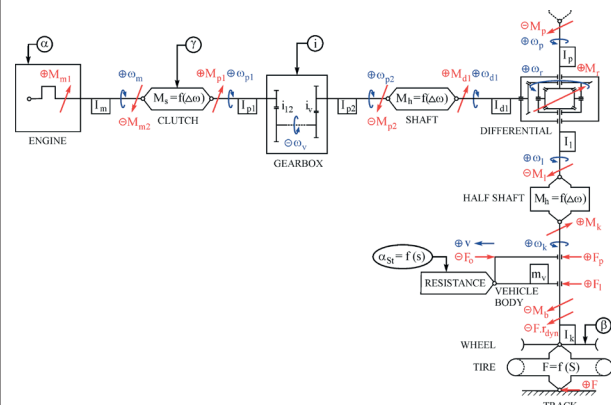


Fig. 2 Classic vehicle drivetrain model (Source: authors)

The string structure is completed with the:

- control parameter blocks (round shaped with the arrow towards the controlled block), which represent the position

* Frantisek Brumerick, Michal Lukac, Aleksander Nieoczym
 Faculty of Mechanical Engineering, University of Zilina, Slovakia
 Mechanical Engineering Faculty, Lublin University of Technology, Poland
 E-mail: brumerickf@fstroj.uniza.sk

of the gas, brake and clutch pedal and the shifted gear according the driver discrete event system (DES) model [5],

- environment resistance block, which is defined by the track and vehicle characteristics (grade resistance) [6] or the environment (aerodynamic drag).

3. Differential model structure

A differential (Fig. 3) consists of one input, the drive (propeller) shaft, and two outputs – half shafts, which are connected to the drive wheels [7]. The rotation of the drive wheels are coupled by their connection to the track via the tires. Under normal conditions, with small tire slip, the ratio of the speeds of the two driving wheels is defined by the ratio of the radii of the paths around which the two wheels are rolling, which in turn is determined by the track-width of the vehicle (the distance between the driving wheels) and the radius of the turn.

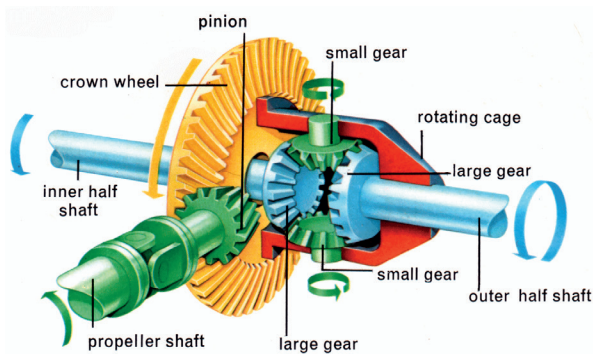


Fig. 3 Structure of a common vehicle mechanical differential (Source: <http://www.mrclutchnw.com/services/differential-rebuilding/>)

4. Model equations

The model of the differential has to be a three-terminal according to the vehicle drivetrain model structure described above (Fig. 4).

The kinematics of the three-shaft differential basic elements are defined according to the Willis formula as

$$\omega_p - \omega_l u_v = \omega_r (1 - u_v), \quad (1)$$

where: ω_p speed of the central wheel p ,
 ω_l speed of the central wheel l ,
 ω_r speed of the carrier r ,
 u_v fundamental differential ratio.

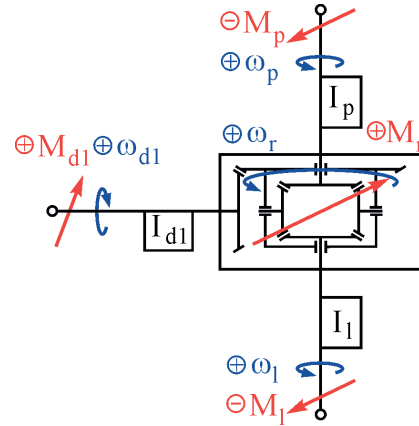


Fig. 4 Structure of the three-terminal differential block model (Source: authors)

The fundamental differential ratio is defined as

$$u_v = \pm \frac{z_l}{z_p} = \frac{\omega_p}{\omega_l} \Big|_{\omega_r = 0}, \quad (2)$$

where: z_l tooth number of the central wheel l ,
 z_p tooth number of the central wheel p .

The relations between the torques in the differential are described via the torque equilibrium equation

$$M_p + M_l + M_r = 0, \quad (3)$$

where: M_p torque on the central wheel p ,
 M_l torque on the central wheel l ,
 M_r torque on the carrier r .

The power equilibrium has to be applied in the same time. Then, if the efficiency losses are ignored, the power balance equation is defined as

$$M_p \omega_p + M_l \omega_l + M_r \omega_r = 0, \quad (4)$$

which is modified by the stopped differential rotating cage – carrier r ($\omega_r = 0$) into the form

$$M_p \omega_p + M_l \omega_l = 0. \quad (5)$$

If the differential is the vehicle one ($z_p = z_l$ opposite speed of the wheels p and l by the stopped carrier r), the fundamental differential ratio has the value $u_v = -1$. The Willis formula (1) is then changing to the form

$$\omega_p + \omega_l = 2\omega_r. \quad (6)$$

The speeds of both differential output shafts can be also calculated with the help of the rotation superposition [8] and [9]. The final speed equations are superposed from the speeds of both

output shafts with the carrier connected to a fixed unit and the relative speed of the central wheels towards the stopped carrier. The equation of the relative speeds is given by

$$\begin{aligned} \omega_p &= \omega_r + \omega_{pr} \\ \omega_l &= \omega_r + \omega_{lr} \end{aligned} \quad (7)$$

where: ω_{pr} relative speed of the central wheel p towards the stopped carrier r ,
 ω_{lr} relative speed of the central wheel l towards the stopped carrier r .

The equation above is the condition of the relation between the speed derivations (accelerations) in the form

$$\begin{aligned} \dot{\omega}_p &= \dot{\omega}_r + \dot{\omega}_{pr} \\ \dot{\omega}_l &= \dot{\omega}_r + \dot{\omega}_{lr} \end{aligned} \quad (8)$$

The acceleration component $\dot{\omega}_r$ of the described fixed unit of both output shafts with the carrier rotating with the speed ω_r is applicable to derive from the motion equation [10]

$$I_{dr} \dot{\omega}_r = M_r + M_p + M_l, \quad (9)$$

where: I_{dr} inertia of the differential fixed unit reduced to the carrier r .

Reduced moment of inertia I_{dr} of the unit consisting of differential input shaft with the differential pinion, carrier with the differential crown wheel and both output half shafts is calculable via the mass and force reduction method comparing the reduced unit kinetic energy and the kinetic energy of the unit components as

$$\begin{aligned} \frac{1}{2} I_{dr} \omega_r^2 &= \frac{1}{2} I_{dl} \omega_{dl}^2 + \frac{1}{2} I_p \omega_r^2 + \frac{1}{2} I_l \omega_r^2 = \\ &= \frac{1}{2} I_{dl} i_d^2 \omega_r^2 + \frac{1}{2} (I_p + I_l) \omega_r^2 \end{aligned} \quad (10)$$

where: I_{dl} inertia of the pinion and the rotating cage (carrier) reduced to the differential input shaft,
 $I_{p,l}$ inertia of the output (half) shafts p and l ,
 i_d ratio between the differential pinion and the crown wheel,
 ω_{dl} differential input shaft speed (pinion speed),
 ω_r differential crown wheel speed (rotating cage/carrier speed).

The ratio between the pinion and the crown wheel is defined by the equation

$$i_d = \frac{\omega_{dl}}{\omega_r}. \quad (11)$$

The torque ratio between the pinion and the crown wheel is defined with no losses by the equation

$$i_d = -\frac{M_{d2}}{M_{dl}} = \frac{M_r}{M_{dl}}, \quad (12)$$

where: M_{d2} reaction torque on the crown wheel.

The angular accelerations of the output shafts can be calculated by the following motion equations [8] and [9]:

$$\begin{aligned} I_{pr} \dot{\omega}_{pr} &= \left(I_p + \frac{I_l}{u_v^2} \right) \dot{\omega}_{pr} = M_p + \frac{M_l}{u_v}, \\ I_{lr} \dot{\omega}_{lr} &= (I_l + I_p u_v^2) \dot{\omega}_{lr} = M_l + M_p u_v \end{aligned} \quad (13)$$

where: I_{pr} inertia of both output shafts reduced to the central wheel p shaft,

I_{lr} inertia of both output shafts reduced to the central wheel l shaft.

The final angular acceleration equations of the all three differential shafts by the help of equations (8) through (13) can be defined either general as

$$\begin{aligned} \dot{\omega}_p &= \dot{\omega}_r + \dot{\omega}_{pr} = \frac{M_r + M_p + M_l}{I_{dr}} + \frac{M_p + M_l u_v^{-1}}{I_{pr}} \\ \dot{\omega}_l &= \dot{\omega}_r + \dot{\omega}_{lr} = \frac{M_r + M_p + M_l}{I_{dr}} + \frac{M_p + M_l u_v}{I_{lr}} \\ \dot{\omega}_r &= \frac{\dot{\omega}_p + \dot{\omega}_l}{2} = \frac{M_r + M_p + M_l}{I_{dr}} \end{aligned} \quad (14)$$

or particular for the vehicle differential ($u_v = -1$; $I_p = I_l$) as

$$\begin{aligned} \dot{\omega}_p &= \dot{\omega}_r + \dot{\omega}_{pr} = \frac{M_r + M_p + M_l}{I_{dr}} + \frac{M_p + M_l}{I_p + I_l} \\ \dot{\omega}_l &= \dot{\omega}_r + \dot{\omega}_{lr} = \frac{M_r + M_p + M_l}{I_{dr}} + \frac{M_l + M_p}{I_p + I_l} \\ \dot{\omega}_r &= \frac{\dot{\omega}_p + \dot{\omega}_l}{2} = \frac{M_r + M_p + M_l}{I_{dr}} \end{aligned} \quad (15)$$

5. Conclusion

Mathematical model of the mechanical differential is an important component of the complex vehicle drivetrain model. It can be built by different approaches according to the modelled system structure [11 and 12]. This article shows how to build a three-terminal mechanical differential block model calculating the shaft speeds according the acting torques, which is suitable for string structure drivetrain mathematical models.

References

- [1] DROZDZIEL, P., KOMSTA, H., KRZYWONOS, L.: An Analysis of Unit Repair Costs as a Function of Mileage of Vehicles in a Selected Transport Company. *Transport Problems*, vol. 9, No. 4, 2014, pp. 73-81.
- [2] HANDRIK, M., VASKO, M., KOPAS, P., SAGA, M.: Effective Finite Element Solution and Post-processing for Wide Load Spectrum. *Communications - Scientific Letters of the University of Zilina*, vol. 16, No. 3A, 2014, pp. 19-26.
- [3] SAGA, M., VASKO, M., KOPAS, P., JAKUBOVICOVA, L.: Numerical Algorithm for Beam Residual Stress Identification. *Communications - Scientific Letters of the University of Zilina*, vol. 16, No. 3A, 2014, pp. 13-18.
- [4] DROZDZIEL, P., KRZYWONOS, L.: The Estimation of the Reliability of the First Daily Diesel Engine Start-up During its Operation in the Vehicle. *Maintenance and Reliability*, 1(41), 2009, pp. 4-10, ISSN 1507-2711.
- [5] DROZDZIEL, P., KOMSTA, H., KRZYWONOS, L.: Repair Costs and the Intensity of Vehicle Use. *Transport Problems*, vol. 8, No. 3, 2013, pp. 131-138.
- [6] KOHAR, R., HRCEK, S.: Dynamic Analysis of a Rolling Bearing Cage with Respect to the Elastic Properties of the Cage for the Axial and Radial Load Cases. *Communications - Scientific Letters of the University of Zilina*, vol. 16, No. 3A, 2014, pp. 74-81.
- [7] DROZDZIEL, P., KRZYWONOS, L., MADLENAK, R., RYBICKA, I.: Selected Aspects of Analyses of Failure Rates of Active Safety Systems in Buses. *Communications - Scientific Letters of the University of Zilina*, vol. 16, No. 3, 2014, pp. 114-119.
- [8] KAMPF, R., LIZBETIN, J., LIZBETINOVA, L.: Requirements of a Transport System User, *Communications - Scientific Letters of the University of Zilina*, vol. 14, No. 4, 2012, pp. 106-108.
- [9] HRCEK, S., KOHAR, R., MEDVECKY, S.: Determination on the Maximum Roller Bearing Load with Regards to Durability thereof using FEM Analysis. *Communications - Scientific Letters of the University of Zilina*, vol. 14, No. 3, 2012, pp. 55-61.
- [10] SAPIETOVA, A., SAGA, M., NOVAK, P., JAKUBOVICOVA, L.: Multi-software Platform for Solving of Multibody Systems Synthesis. *Communications - Scientific Letters of the University of Zilina*, vol. 14, No. 3, 2012, pp. 43-48.
- [11] BUKOVA, B., BRUMERCIKOVA, E., MADLENAK, R.: *Transport and e-commerce*. Bratislava : Wolters Kluwer, 2014, 172 p., ISBN 978-80-8168-130-1.
- [12] BUKOVA, B., BRUMERCIKOVA, E., KOLAROVSKZI, P.: *Spedition and Logistics*, Bratislava : Wolters Kluwer, 2014, 318 p., ISBN 978-80-554-0925-2.

Maria Zihalova - Dana Bolibruchova - Dalibor Vojtech *

INFLUENCE OF VANADIUM AND CHROMIUM ADDITION ON MORPHOLOGY AND COMPOSITION OF IRON BASED PHASES IN AlSi10MgMn ALLOY

Application of secondary Al-Si alloys is mostly influenced by amount of impurities. Detrimental effect of iron, as the most harmful impurity, refers mainly to morphology of iron intermetallic phases. Morphology of iron phases can be influenced by several methods from which the most common is addition of some elements. In primary alloys manganese is commonly used, but its influence is not such favourable in high iron levels because of so-called sludge phase formation. Higher iron content thus requires other alloying elements which can be vanadium, chromium or others. In this article, vanadium and mutual vanadium and chromium influence on iron phase morphology and chemical composition is analysed by optical microscopy, SEM observations and EDX analysis.

Keywords: AlSi10MgMn alloy, iron based intermetallic phase, vanadium, chromium.

1. Introduction

In recent years much effort is being expended to protect the earth's environment and one of the most desirable concepts that have been established through these developments is the recycling of waste materials. Aluminium waste must be one of the most desirable materials for recycling or re-using. This is because the energy costs involved in its production can be reduced by up to 95% by recycling Al scrap, as the production of Al from its ore, bauxite, is an energy consuming and very expensive process [1]. However, the increasing use of recycled aluminium casting alloys warrants strict process control to remove the ill effects of impurity elements [2]. From impurity elements, the most harmful is thought to be iron [3 - 5].

Presence of iron in Al-Si cast alloys is a common problem in primary alloys but it becomes more important in secondary (recycled) aluminium alloys made from scrap materials. The reason why iron has such detrimental influence is that although iron is highly soluble in liquid aluminium and its alloys, it has very little solubility in the solid (max. 0.05 wt. %) and so it tends to combine with other elements to form intermetallic phase particles of various types [5]. Intermetallic phases present in the alloys then decrease mechanical properties of the alloy and also porosity of final casting can be increased by iron phases.

A variety of Fe-rich intermetallic phases have been observed in aluminium alloys. In Al-Si-Fe system there are five main Fe-rich

phases: Al_3Fe (or $Al_{13}Fe_4$), $\alpha-Al_8Fe_2Si$ (possibly $\alpha-Al_{12}Fe_3Si_2$), $\beta-Al_5FeSi$, $\delta-Al_4FeSi_2$ and $\gamma-Al_3FeSi$ [6]. The most common intermetallic phase is $\beta-Al_5FeSi$ that is also considered to have the most detrimental effect on mechanical and foundry properties of Al-Si type alloys. The platelet-like morphology of the Al_5FeSi phase allows it to act as a stress raiser, consequently undermining the mechanical properties of the cast part, mainly tensile strength and elongation [5]. As the fraction of insoluble phase increases with increased iron content, casting properties such as fluidity and feeding characteristics are also adversely affected. Iron also lead to the formation of excessive shrinkage porosity defects in castings [7]. If Mg is present with Si, an alternative phase can form, $\pi-Al_8FeMg_3Si_6$ [5]. Phase $\pi-Al_8FeMg_3Si_6$ occurs in script-like morphology and it has a negative impact on ductile properties of Al-Si-Mg alloys [8]. For the more usual Al-Si-Mg cast alloys of modest Mn contents, the $Al_{15}(Fe,Mn)_3Si_2$ phase often has an appearance of Chinese script in section, being irregular or convoluted. If Fe and Mn are sufficiently high, primary $Al_{15}(Fe,Mn)_3Si_2$ phase may appear as hexagonal, star-like, or dendritic crystals.

There is still only little information about vanadium influence on iron-based intermetallic phases in aluminium alloys. In the cast 99.5 Al alloy V addition in amount of 0.1 wt. % exhibits more cubic $\alpha-AlFeSi$ phase than in V-free version in both the as-cast and homogenised conditions, although the effect became more pronounced after homogenisation [9]. Vanadium addition (0.2

* ¹Maria Zihalova, ¹Dana Bolibruchova, ²Dalibor Vojtech

¹Department of Technological Engineering, Faculty of Mechanical Engineering, University of Zilina, Slovakia

²Institute of Chemical Technology, Department of Metals and Corrosion Engineering, Faculty of Chemical Technology, Prague, Czech Republic

E-mail: maria.zihalova@fstroj.uniza.sk

wt. %) in Al-Si cast alloys containing 3.0 ÷ 12.0 wt. % of Si, 0 ÷ 0.4 wt. % of Mg and 0.3 ÷ 2.3 wt. % of Fe have also a beneficial influence on length of β -Al₅FeSi but there was a negligible amount of V detected in platelets [10]. Previous work [11] shows also a beneficial influence of V addition on microstructure and mechanical properties of AlSi6Cu4 alloy but vanadium was not detected in iron intermetallic phases at all.

It has been reported that Cr addition can have similar effect on iron intermetallics as Mn [12]. Chromium improves aluminium alloys strength at indoor and higher temperatures (precipitation of intermetallic compositions of Cr inhibits the growth of grains) and mildly deteriorates elongation. But the presence of Cr phases Al₁₃(CrFe)₄Si₄ and Al₂(CrFe)₅Si₈ can increase brittleness [10]. Cr addition leads to improvement of mechanical properties of as-cast AlSi7Mg0.3 alloy while the maximal value of tensile strength and elongation was measured at 1.0 wt. % of Cr [13 - 16].

There is no available information about the mutual V and Cr influence in Al-Si alloy. In the article, vanadium and mutual V and Cr influence on iron based intermetallics is analysed in AlSi10MgMn cast alloy by optical microscopy, SEM observations and EDX analysis.

2. Materials and methodology

Commercial AlSi10MgMn alloy was used to perform the experiments. Selected alloy was in the first step of experiments polluted by iron by addition of AlFe10 master alloy. Alloy with 0.98 wt. % of iron was obtained this way (marked as AlSi10MgMnFe1). Vanadium was added to such prepared secondary alloy in amount of 0.2 wt. % of V. Combined V and Cr influence was evaluated on the alloy prepared by chromium addition to vanadium treated alloy in the amount of 0.5 and 1.0 wt. % of Cr. Required amounts of V and Cr were added in the form of AlV10 and AlCr20 master alloys. The melts were not purified, modified or grain refined. Prepared melts were after reaching pouring temperature (760 °C) poured into a permanent mould preheated to 200 °C. Chemical composition of the alloys is shown in Table 1. Accurate values of Cr level in alloys with added V and Cr could not be measured due to uncommonly high Cr addition that is out of range of the used spectrometer.

Samples for metallographic observations were prepared from the castings by standard procedure containing cutting,

grinding, polishing and etching. Chemical composition of selected intermetallic particles was analysed by EDX analysis.

3. Results

Typical microstructure of AlSi10MgMn1 alloy is shown in Fig. 1. As the alloy was not modified, eutectic silicon is present in the form of platelet particles surrounded by aluminium dendrites. Significant amount of iron based intermetallics is also present in the microstructure, mostly in the form of thick needles. Position of the iron phases seems to be preferentially along the eutectic Si. Chemical analysis of the needle-like particle (Fig. 2) shows mainly the presence of Al, Si and Fe, but low amount of Mn was detected as well. Generally, it can be described as β -AlSiFe, probably Al₅FeSi.

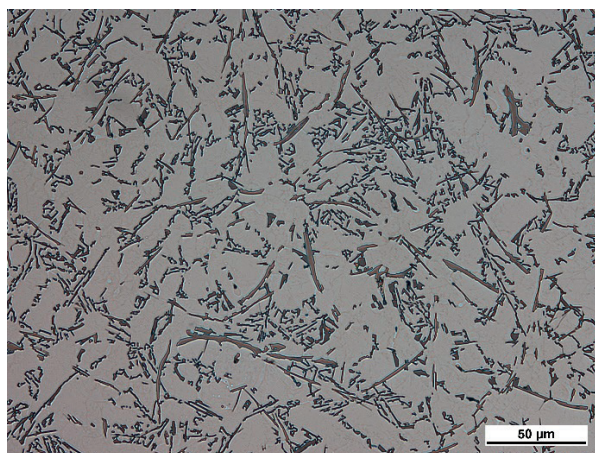


Fig. 1 Typical microstructure of AlSi10MgMnFe1 alloy, etch. 0.5% HF

Vanadium addition in amount of 0.2 wt. % leads to the formation of increased amount of script-like iron phases, but platelets were still in higher number. As it can be seen in Fig. 3, vanadium caused increasing of needle-like particles compared to AlSi10MgMnFe1 alloy but thickness was decreased. EDX analysis showed the presence of small V amount in script-like particles (Fig. 4).

Chemical compositions of prepared alloys in wt. %

Table 1

Alloy	Si	Mg	Mn	Fe	Ti	Zn	Cu	V	Cr	Al
AlSi10MgMn	10.220	0.277	0.108	0.448	0.046	0.029	0.047	0.010	0.006	rest
AlSi10MgMnFe1	9.73	0.313	0.118	0.980	0.041	0.026	0.048	0.009	0.037	rest
AlSi10MgMnFe1 + 0.2 wt. % V	9.133	0.265	0.116	1.588	0.034	0.026	0.046	0.216	0.166	rest
AlSi10MgMnFe1 + 0.2 wt. % V + 1.0 wt. % Cr	8.996	0.291	0.119	1.446	0.033	0.029	0.047	0.139	>0.480	rest
AlSi10MgMnFe1 + 0.2 wt. % V + 0.5 wt. % Cr	8.539	0.290	0.098	1.182	0.031	0.028	0.053	0.135	>0.480	rest

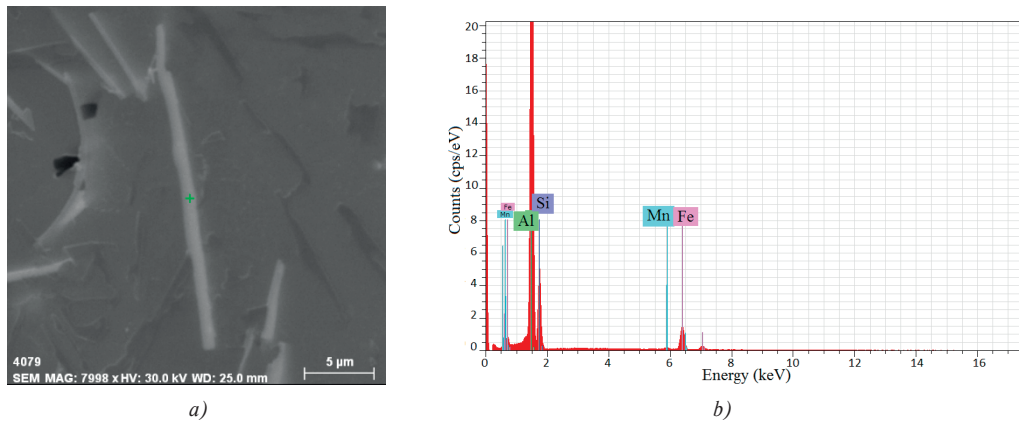


Fig. 2 EDX analysis of needle-like phase in AlSi10MgMnFe1 alloy: a) SEM image of analysed place, b) EDX spectrum

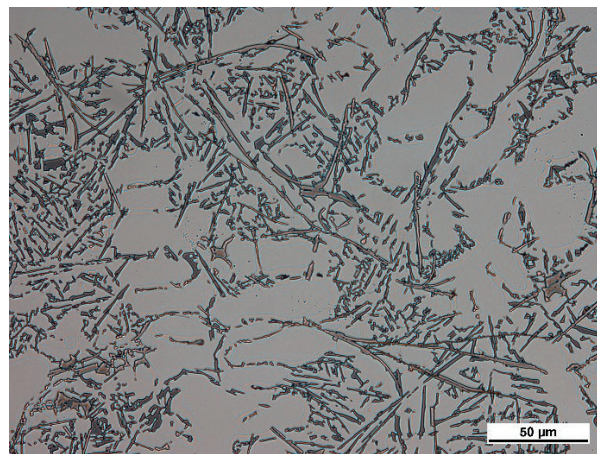


Fig. 3 Typical microstructure of AlSi10MgMnFe1 alloy with 0.2 wt. % of V, etch. 0.5% HF

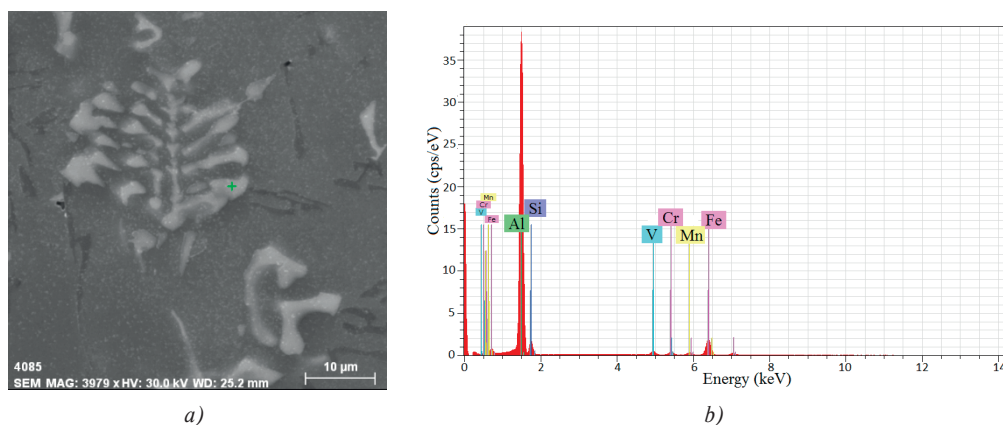


Fig. 4 EDX analysis of script-like phase in AlSi10MgMnFe1 alloy with 0.2 wt. % of V: a) SEM image of analysed place, b) EDX spectrum

Mutual V and Cr addition leads to the formation of so called “sludge phases”. Amount of sludge phases increased with Cr addition, lower amount was present after addition of 0.5 wt. % of Cr (Fig. 5) and higher in the alloy with 1.0 wt. % of Cr (Fig. 6). Size and amount of needle-like particle was after the V and Cr

addition decreased but the formation of sludge phases is thought to be even more deleterious compared to needles or script-like particles. This is due to its high melting point, high specific gravity and hardness which causes the increasing wear of melting devices and deteriorating of the alloy machinability [14]. Except of this,

once the sludge phase is formed, it cannot be removed from alloy by further re-melting or refining process. Chemical composition of script-like phase present in alloy with 0.5 wt. % Cr addition shows presence of both V and Cr in analysed place (Fig. 7) while

in alloy with 1.0 wt. % of Cr only chromium was detected (Fig. 8). Moreover, the amount of Cr was lower in a script-like phase after higher chromium addition.

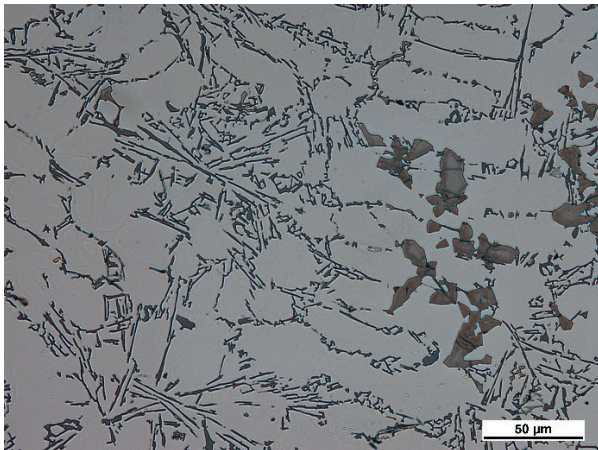


Fig. 5 Typical microstructure of AlSi10MgMnFe1 alloy with 0.2 wt. % of V and 0.5 wt. % of Cr, etch. 0.5% HF

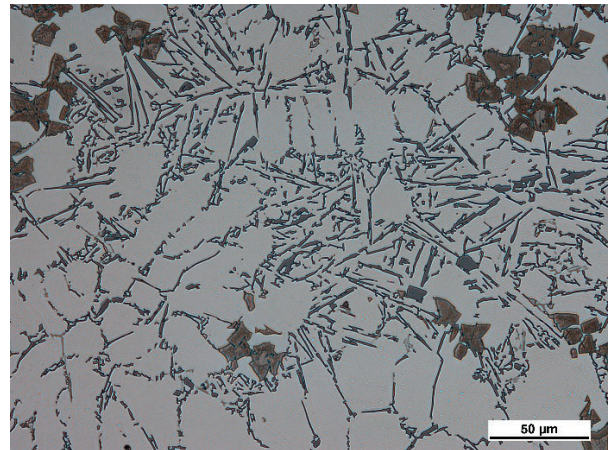
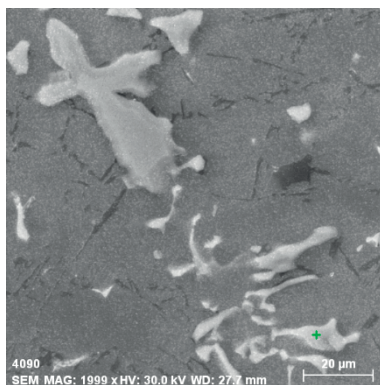
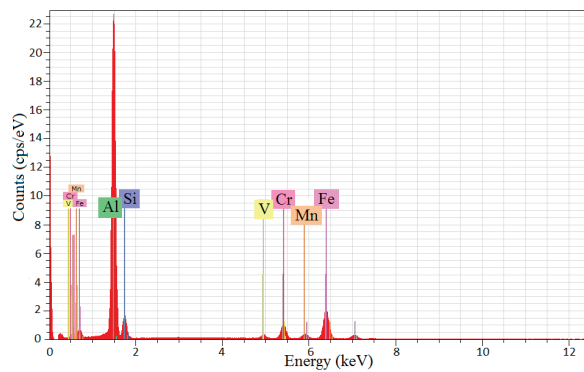


Fig. 6 Typical microstructure of AlSi10MgMnFe1 alloy with 0.2 wt. % of V and 1.0 wt. % of Cr, etch. 0.5% HF

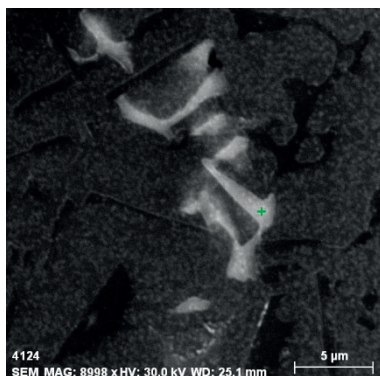


a)

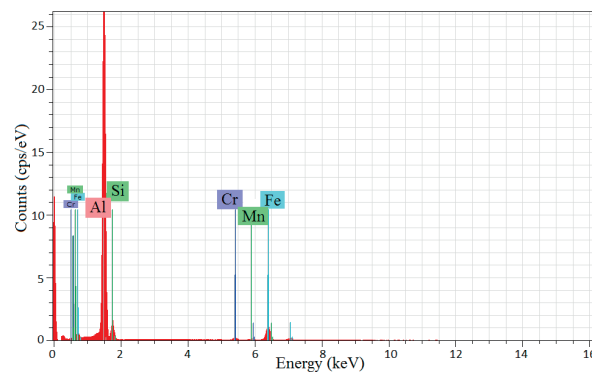


b)

Fig. 7 EDX analysis of script-like phase in AlSi10MgMnFe1 alloy with 0.2 wt. % of V and 0.5 wt. % of Cr: a) SEM image of analysed place, b) EDX spectrum



a)



b)

Fig. 8 EDX analysis of script-like phase in AlSi10MgMnFe1 alloy with 0.2 wt. % of V and 1.0 wt. % of Cr: a) SEM image of analysed place, b) EDX spectrum

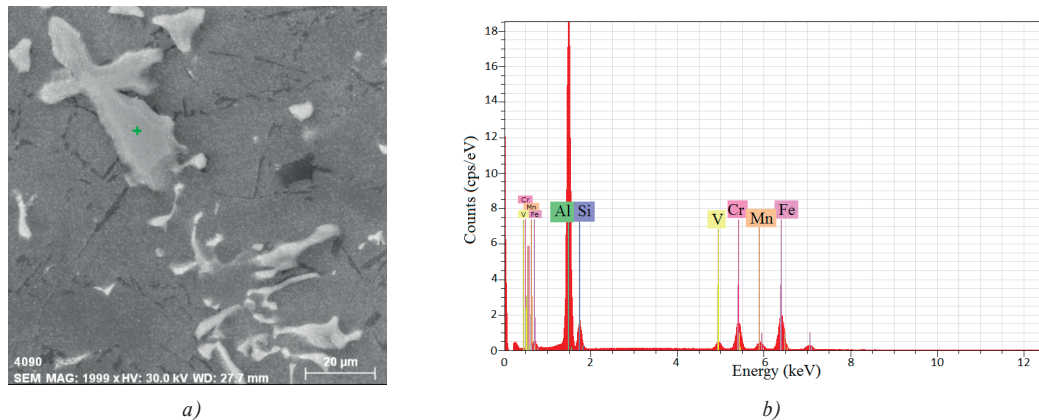


Fig. 9 EDX analysis of sludge phase in AlSi10MgMnFe1 alloy with 0.2 wt. % of V and 0.5 wt. % of Cr: a) SEM image of analysed place, b) EDX spectrum

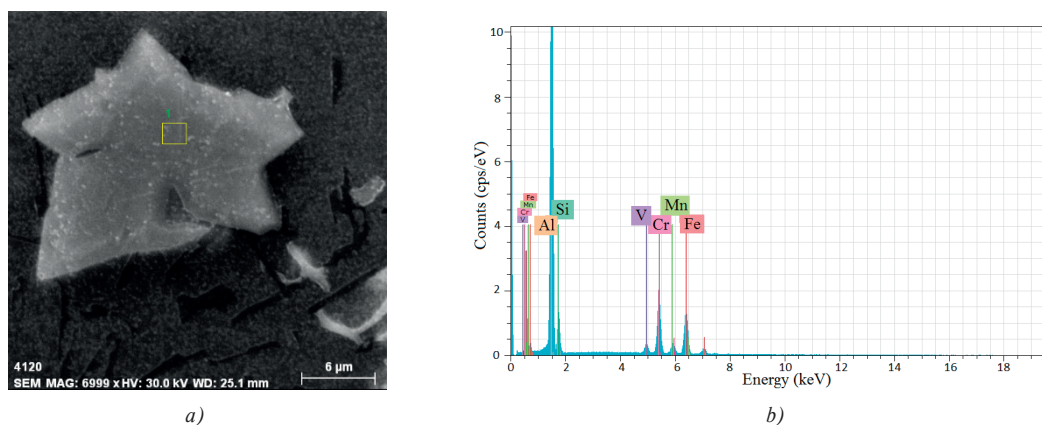


Fig. 10 EDX analysis of sludge phase in AlSi10MgMnFe1 alloy with 0.2 wt. % of V and 1.0 wt. % of Cr: a) SEM image of analysed place, b) EDX spectrum

Sludge phase chemical observations in both Cr treated alloys (Fig. 9 and 10) show presence of Al, Si, Fe, Cr, Mn and V. Amount of Cr in sludge phase seems to be higher with increasing Cr addition.

4. Discussion

Iron addition in the amount of 0.98 wt. % in AlSi10MgMn alloy leads to formation of thick needle like intermetallic phases β -AlFeSi. Manganese neutralisation effect on iron in such alloy composition is then insufficient because the Mn to Fe ratio is only 0.12 (recommended value 0.5 [5, 7 and 14]). Vanadium influence as the iron corrector was analysed in addition of 0.2 wt. % V. Formation of higher amount of script-like phases was observed. Vanadium also caused change of the needle-like length and thickness. Length of the phases rises in disagreement with the literature [10 and 11], but thickness was reduced. Some needle-like phases have a curved shape (Fig. 3) what might be probably the result of the accidental mechanical hindrance to

the straightening action which was observed by other authors [7] and it might be a sign of higher strength of these phases against the loading. Vanadium presence was detected in script-like phases together with Al, Si, Fe, Mn and Cr. Number of needle-like particles rapidly decreased after mutual V and Cr addition but a high amount of sludge phases were observed. The formation of this kind of particles had been observed by many authors [11, 13 and 14] and it is thought to be detrimental to mechanical, foundry properties and machinability of the alloy [14]. Influence of sludge phases on mechanical properties of Al-Si-Mg alloys is still not clear and in spite of the presence of sludge phases in AlSi7Mg0.3 alloy the tensile properties can increase as it has been shown in [13]. EDX analysis in alloys shows decreasing of V level present in script-like phases with alloys after Cr addition. Vanadium and also chromium level rises in the sludge phases with increasing of the Cr addition. It is possible that not only Cr, Mn and Fe are sludge forming elements, but also V belongs to that group at its higher levels.

5. Conclusions

Influence of V and mutual V and Cr addition in AlSi10MgMn alloy were analysed by optical microscopy, SEM observations and EDX analysis. Following conclusions can be drawn from the results:

- (1) Detrimental iron effect in the AlSi10MgMn alloy leads to formation of thick platelets of AlSiFe (probably Al_5FeSi) phase placed mainly near the eutectic Si.
- (2) Vanadium has an influence on the formation of higher amount of script-like phases and it acts like an iron corrector.

Also thickness of the needle-like particles was reduced by V addition but the length of needles increased.

- (3) Cr in amount of 0.5 and 1.0 wt. % leads to the formation of sludge phases which might deteriorate mechanical properties of alloy. More sludge phases formed at higher Cr level.
- (4) Sludge phases also contain certain amount of V that might be also a sludge formation element when the content of Fe, Mn and Cr exceeds a critical value.
- (5) Vanadium addition in amount of 0.2 wt. % has the most beneficial effect on morphology and chemical composition of iron intermetallics.

References

- [1] YAMAGIWA, K., WATANABE, Y, FUKUI, Y, KAPRANOS, P.: Novel Recycling System of Aluminum and Iron Wastes -in-situ Al- Al_3Fe Functionally Graded Material Manufactured by a Centrifugal Method, *Materials Transactions*, vol. 44, No. 12, 2003, 2461-2467, ISSN 1347-5320.
- [2] SREEJA KUMARI, S.S, PILLAI, R. M., RAJAN, T. P. D., PAI, B. C.: Effects of Individual and Combined Additions of Be, Mn, Ca and Sr on the Solidification behaviour, Structure and Mechanical Properties of Al-7Si-0.3Mg-0.8Fe Alloy. *Materials Science and Engineering A*, vol. 460-461, 2007, 561-573, ISSN 0921-5093.
- [3] HURTALOVA, L., TILLOVA, E., CHALUPOVA, M.: Influence of Intermetallic Phases on the Fracture Surfaces in Secondary Aluminium Cast Alloy. *Acta Metallurgica Slovaca - Conference*, vol. 3, 2013, 65-74. ISSN 1338-1156.
- [4] BRUNA, M., KUCHARCIK, L., SLADEK, A.: Complex Evaluation of Porosity in A356 Aluminium Alloy using Advanced Porosity Module. *Manufacturing Technology*, vol. 13, No.1, 2013, 26-30. ISSN 1213-2489
- [5] TAYLOR, J.A.: Iron-containing Intermetallic Phases in Al-Si Based Casting Alloys. *Procedia Materials Science*, vol. 1, 2012, 19-33. ISSN 2211-8128.
- [6] JI, S., et al: Effect of Iron on the Microstructure and Mechanical Property of Al-Mg-Si-Mn and Al-Mg-Si Die Cast Alloys. *Materials Science & Engineering A*, vol. 564, 2013, 130-139. ISSN 0921-5093.
- [7] TILLOVA, E., CHALUPOVA, M., HURTALOVA, L.: Evolution of Phases in a Recycled Al-Si Cast Alloy during Solution Treatment. *Scanning Electron Microscopy*, InTech: Croatia, 2012, 412-438. ISBN 978-953-51-0092-8
- [8] CAO, X., CAMPBELL, J.: Morphology of Al_5FeSi Phase in Al-Si Cast Alloys. *Materials Transactions*, vol. 47, No. 5, 2006, 1303-1312. ISSN 1347-5320.
- [9] ZHU, S. et al: Influences of Nickel and Vanadium Impurities on Microstructure of Aluminum Alloys. *JOM*, vol. 65, No. 5, 2013, 584-592. ISSN 1543-1851.
- [10] PETRIK, J., HORVATH, M.: The Iron Correctors in Al-Si Alloys. *Annals of Faculty Engineering Hunedoara - Intern. J. of Engineering*, 2011, 401-405. ISSN 1584-2673.
- [11] ZIHALOVA, M., BOLIBRUCHOVA, D.: Possibilities of Iron Elimination in Aluminium Alloys by Vanadium. *Manufacturing Technology*, vol. 13, No. 3, 2013, 289-296. ISSN 1213-2489
- [12] GUSTAFSSON, G., THORVALDSSON, T., DUNLOP, G.L.: The Influence of Fe and Cr on the Microstructure of Cast Al-Si-Mg Alloys. *Metallurgical Transactions A*, vol. 17A, 1986, pp. 45-52. ISSN 1543-1940.
- [13] BOLIBRUCHOVA, D., RICHTATECH, L., ORLOWICZ, W.: Possibilities of Eliminating the Higher Amount of Iron in Secondary AlSi7Mg0.3 Alloy by Chrome. *Communications - Scientific Letters of the University of Zilina*, vol. 16, No. 3A, 2014, 119-123. ISSN 1335-4205.
- [14] TILLOVA, E., CHALUPOVA, M.: *Structural Analysis of Al-Si Alloys* (in Slovak). EDIS ZU : Zilina, 2009, 191 p. ISBN 978-80-554-0088-4
- [15] HONZATKO, R., MICHNA, S., CAIS, J.: The Influence of Porosity on Mechanical Properties of Casts Produced from Al - Si Alloys. *Manufacturing Technology*, vol. 13, No. 3, 2013, 289-296. ISSN 1213-2489
- [16] NOVOTNY, J., CAIS, J., NAPRSTKOVA, N.: Analysis of Aluminium Alloys AlSi7Mg0.3 and AlMg3 by Means of X-Ray Diffraction. *Manufacturing Technology*, vol. 14, No. 3, 2014, 392-397. ISSN 1213-2489.

Radoslav Konar - Milos Mician - Jozef Mesko - Michal Sventek *

IDENTIFICATION OF LACK OF FUSION AND PENETRATION IN CIRCUMFERENTIAL FILLET WELD BY PHASED ARRAY ULTRASONIC METHOD IN GAS INDUSTRY

The article deals with non-destructive ultrasonic identification of lack of fusion and penetration in circumferential fillet welds in gas industry by using Phased Array method. These types of welds are used mainly for repairs of gas pipelines during operation. The main aim of this paper is to compare results of measurements of the weld with and without defect. Phased Array testing procedures for circumferential fillet welds methods are also described in this article.

Keywords: Phases Array, lack of fusion, incomplete penetration, ultrasonic testing.

1. Introduction

Until recently, pipeline weld inspection has been traditionally solely the domain of radiography. With the advent of modern ultrasonic technique Phased Array (PA), ultrasonic testing has proven to be an effective option to detect weld defects in gas pipeline welds oriented unfavourably for radiography. Ultrasound testing can be used for gas pipelines according to current standards. Standard STN EN 12732 affords to replace X-ray by ultrasound technique in the control steel pipelines.

One of these serious weld defects is also lack of fusion and incomplete penetration in weld. It produces the notch effect, which can cause pipeline destruction during operation. This defect can be reliably identified by modern ultrasonic technique PA.

2. Ultrasonic technique Phased Array

PA ultrasonic is an advanced method of ultrasonic non-destructive testing. Ultrasonic waves at a frequency of 20 kHz are used for testing. The two main types are longitudinal (L-waves) and transversal waves (S-waves). L-waves have the particle motion and propagation in the same direction, while transversal waves have particle and propagation at right angles to each other [1].

The formulas for longitudinal and transverse waves are:

$$c_L = \sqrt{\frac{E \cdot (1 - \mu)}{\rho \cdot (1 + \mu) \cdot (1 - 2\mu)}} \quad (1)$$

$$c_T = \sqrt{\frac{E}{2 \cdot \rho(1 + \mu)}} \quad (2)$$

where:

E - modulus of elasticity (Young`s modulus) [$N \cdot m^{-2}$],
 μ - Poisson`s ratio [$\mu = (2GE) \cdot (2G)^{-1}$],
 ρ - mass density [$kg \cdot m^{-3}$] [2].

Conventional ultrasonic transducers for NDT commonly consist of either a single active element that both generates and receives high-frequency sound waves, or two paired elements, one for transmitting and one for receiving. PA probes, on the other hand, typically consist of a transducers assembly with 16 to as many as 256 small individual elements that can each be pulsed separately. These can be arranged in a strip (linear array), 2D matrix, a ring (annular array), a circular matrix (circular array), or more complex shape. As is the case with conventional transducers, phased array probes can be designed for direct contact use, as part of angle beam assembly with a wedge, or for immersion use with sound coupling through a water path [3].

* ¹Radoslav Konar, ¹Milos Mician, ¹Jozef Mesko, ²Michal Sventek

¹Department of Technological Engineering, Faculty of Mechanical Engineering, University of Zilina, Slovakia

²MONT IRP s.r.o., Zilina, Slovakia

E-mail: radoslav.konar@fstroj.uniza.sk

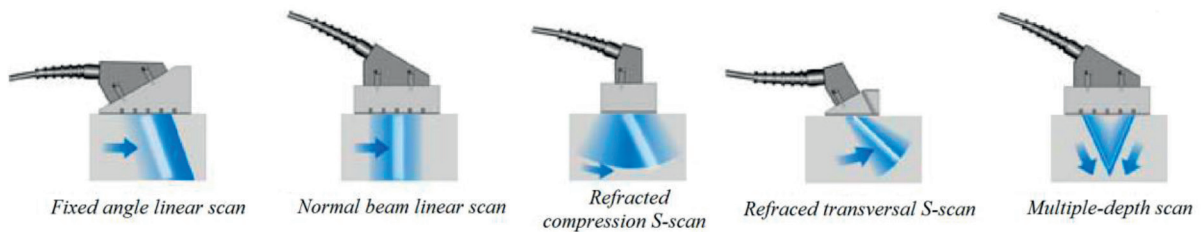


Fig. 1 Phased Array probes principle [3]

Transducer frequencies are most common in the 2 MHz to 10 MHz range. A PA system also includes a sophisticated computer based instrument that is capable of driving the multielement probe, receiving and digitizing the returning echoes, and plotting that echo information in various standard formats. Unlike conventional flaw detectors, phased array systems can sweep a sound beam through a range of refracted angles or along a linear path, or dynamically focus at a number of different depths (Fig. 1), thus increasing both flexibility and capability in inspection setups [2].

3. Lack of fusion and penetration

Lack of fusion and penetration, also called cold lapping or cold shuts, occurs when there is no fusion between the weld metal and the surfaces of the base material. This defect can be seen in Fig. 2.

The most common cause of lack of fusion is a poor welding technique. Either the weld puddle is too large (travel speed too slow) and/or the weld metal has been permitted to roll in front of the arc. Again, the arc must be kept on the leading edge of the puddle. When this is done, the weld puddle will not get too large and cannot cushion the arc [5 - 6].

Another cause is the use of a very wide weld joint. If the arc is directed down the centre of the joint, the molten weld metal will only flow and cast against the side walls of the base plate without melting them. The heat of the arc must be used to melt the base material. This is accomplished by making the joint narrower or

by directing the arc towards the side wall of the base plate. When multipass welding thick material, a split bead technique should be used whenever possible after the root passes. Large weld beads bridging the entire gap must be avoided [4 and 7].

Lack of fusion is a common gas pipelines weld defect. This defect occurs mainly at repair of gas pipelines. Cause of the lack of fusion is rapid dissipation of heat from the weld edges during welding, which is due to the effects of the flow gas in the pipeline [8].

4. Identification of lack of fusion and penetration by Phased Array method on experimental samples

Identification of lack of fusion by ultrasonic method is very difficult. Difficult identification is caused by smooth surface defect, which does not direct reflect the ultrasonic energy back into the probe. Defects can be identified only by the reflected beam from the weld shape. The procedure of testing options is described in this chapter.

Three experimental samples with artificial lack of fusion were produced for ultrasonic testing. One of the samples was without defect (Fig. 3) and two samples were with artificial defect - lack of fusion on the pipe side. The samples were made of S355 steel plate with thickness of 8 mm to simplify the weld joint geometry. This geometry is very similar to the real geometry of the weld on the pipe with a diameter of 300 mm at repair of gas pipeline with steel sleeve and steel patch [9 and 6].



Fig. 2 Lack of fusion and penetration [4]

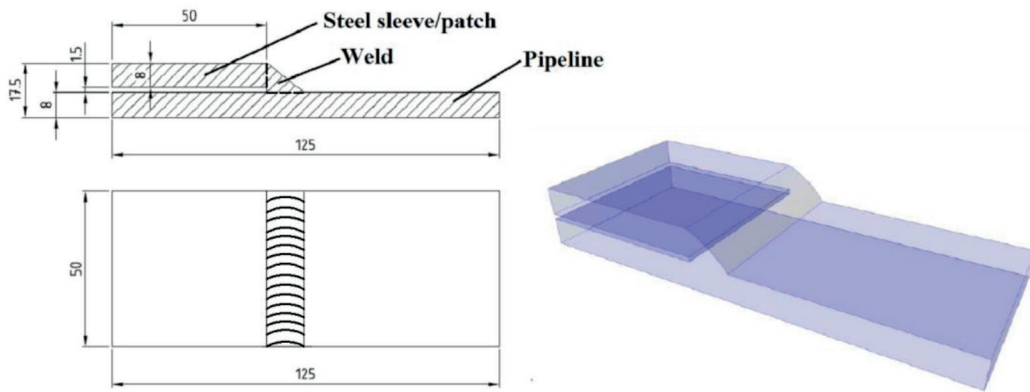


Fig. 3 Experimental sample without defect

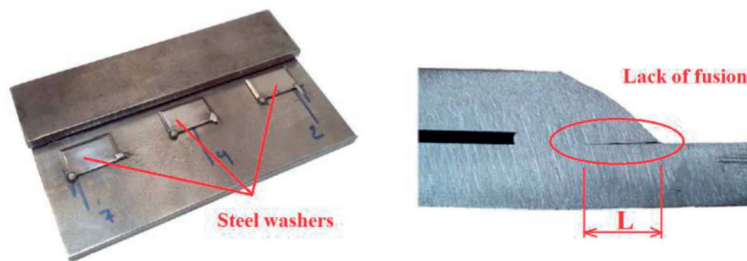


Fig. 4 Steel washers (left) and lack of fusion macrostructure (right)

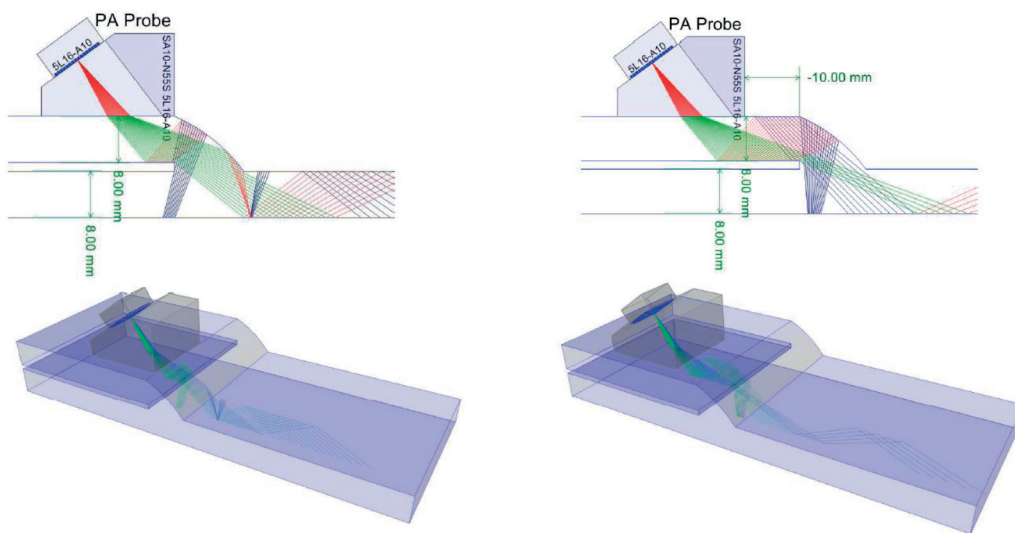


Fig. 5 Simulated testing probe position

Lack of fusion on the pipe side was manufactured with steel washers of dimension 40x35x2 mm. Defect originated during metal active gas (MAG) welding by partial melting of the surface of the steel washers. Steel washers and lack of fusion macrostructure are shown in Fig. 4. Depth of lack of fusion (L in Fig. 4) is 3.6 mm and 12.7 mm and its length is approximately 30 mm.

PA ultrasonic defectoscope OLYMPUS Omni Scan MX2, probe 5L16-A10 and wedge SA10-N55S were used for testing. The samples were tested with transversal ultrasonic waves with frequency 5 MHz (wavelength $\lambda = 0.6416$, $c_T = 3208$ m.s⁻¹). The sensitivity of the ultrasound system was set by the DAC \varnothing 2 mm curve + additional gain 8 dB. Ultrasonic gel EchoMix was used to ensure acoustic contact coupling.

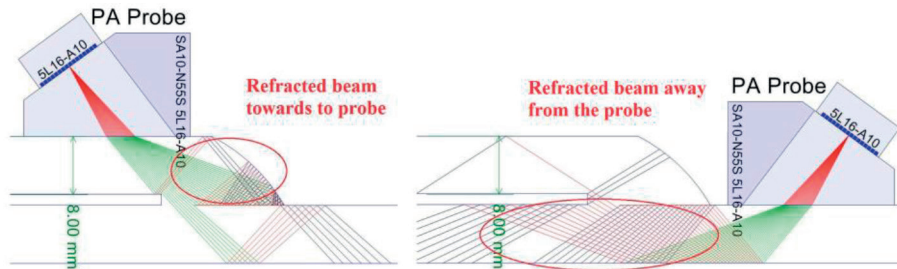


Fig. 6 Correct testing probe position from sleeve/patch: direct beam (left), reflected beam (right)

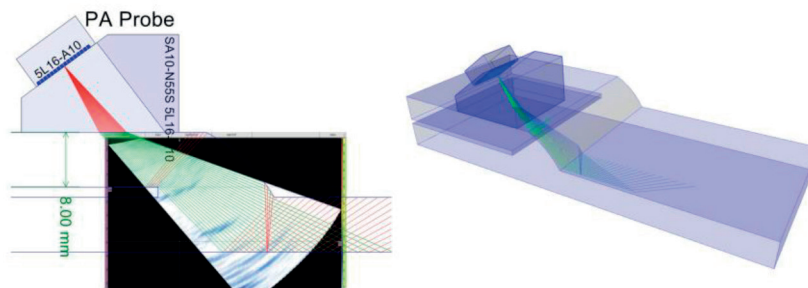


Fig. 7 PA ultrasonic record from sample without defect

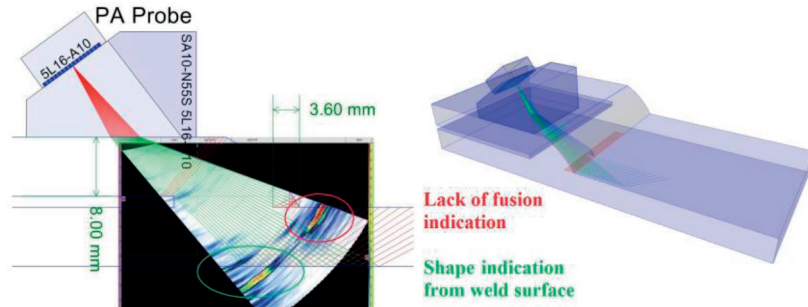


Fig. 8 PA ultrasonic record from sample with defect (defect depth $L = 3.6$ mm)

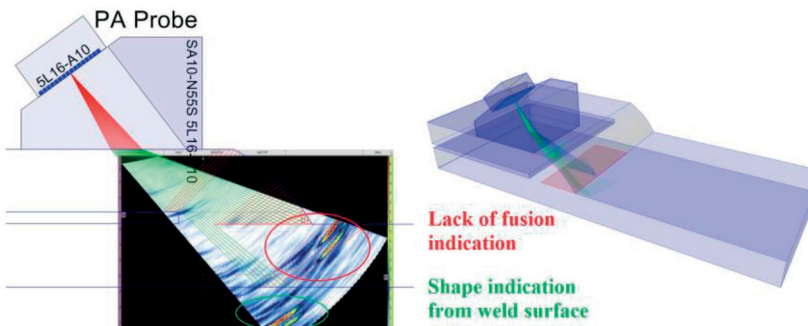


Fig. 9 PA ultrasonic record from sample with defect (defect depth $L = 12.7$ mm)

The correct position of the probe was designed in the program BeamTool, which allows to simulate the propagation of ultrasonic waves in the testing material. Beam Tool ultrasonic propagation simulation in samples with defect is in Fig. 5. From the picture it

is clear that the ultrasonic lack of fusion indication from sleeve (patch) side is shown through the reflected ultrasound beam from the surface of the weld. Any indications are not recorded from probe position on pipe side, because ultrasonic energy

after reflection is not returned back to ultrasonic probe. Correct position for testing is therefore position by patch (sleeve) side [5].

Two probe positions on patch (sleeve) side are necessary for the correct examination of the entire weld. Ultrasonic testing with direct beam is in the first position and the reflected beam in the second probe position. Correct testing probe position from sleeve (patch) side is shown in Fig. 6.

Ultrasonic testing was performed manually. Mechanised testing in practice is inappropriate method because of the irregular geometry of the sleeve. The results of ultrasonic testing samples without defect are in Fig. 7.

Significant indications are not shown in the ultrasound recording from the sample without defect – lack of fusion, because the whole ultrasonic energy is distributed to sample and no energy is reflected back to the probe.

The results of ultrasonic testing samples with defect are in Figs. 8 and 9. A clear ultrasonic indication is seen on both ultrasound records. Two different indications are shown on records of which the first indication originates from lack of fusion obtained by reflected beam and second indication is shape indication from weld surface, which can be also seen in the weld without defect.

Differences between error indications are in angular sector view. Lack of fusion indication with depth 3.6 is angular sector of indication view about 10° (60-70° angular sector) and for the defect with a depth of 12.7 mm is the angular sector of indication view about 15° (55-70° angular sector). Based on this observation the approximate size of the defect can be assumed. The exact

dimensions of the defect cannot be determined because ultrasonic indication was not received by them directly but reflected beam. Reflected beam is not obtained from real defect but from the weld surface due to the occurrence of the defect [8 and 10].

5. Conclusion

This article describes experimental ultrasonic testing of lack of fusion in repair gas pipeline weld joints. Experimental testing was carried out on simplified samples with and without the presence of lack of fusion. Performed experiments confirmed the unequivocal identification of lack of fusion in gas pipelines weld joint. The lack of fusion is displayed on the screen as angular sector indication. The problem is to determine the exact size of the defect. From the angular sector we provide only an approximate value of identification defect. According to results of measurements it is obvious that the main positive contribution of experiments is clear detection of lack of fusion, which is one of the most dangerous defects in gas pipeline welds. Ultrasonic testing procedure referred in article is accordance with the applicable gas standards and regulations.

Acknowledgment

This work has been supported by the Scientific Grant Agency of the Ministry of Education of the Slovak Republic, grant VEGA: 1/0836/13, KEGA: 034ZU-4/2015 and KEGA: 014ZU-4/2015.

References

- [1] LANGENBERG, K., MARKLEIN, R., MAYER, K.: *Ultrasonic Nondestructive Testing of Materials - Theoretical Foundations*, CRC Press : New York, 2012, 772, ISBN 978-1-4398-5588-1.
- [2] KOPEC, B. et al.: *Nondestructive Testing of Materials and Structures (in Czech)*, CERM, s.r.o. : Brno, 2008, p. 573, ISBN 978-80-7204-591-4.
- [3] OLYMPUS: *Phased Array Testing - Basic and Theory for Industrial Applications*, Olympus NDT : Waltham, 2012, p. 124.
- [4] CONSONNI, M., WEE FUN, CH., SCHNEIDER, CH.: *Manufacturing of Welded Joints with Realistic Defects*. NDT 2011 - 50th annual conference of the British Institute of Non-Destructive Testing, 13-15 Sept., 2011. Telford, UK
- [5] SCHMERR, L.: *Fundamentals of Ultrasonic Phased Arrays*, Springer : New York, 2015, 382, ISBN 978-3-319-07271-5.
- [6] RADEK, N. et al.: Laser Treatment of WC-Cu Coatings (in Polish), *Technolog*, vol. 6, No. 2, 2014 ISSN 1337-8996.
- [7] SLADEK, A., et al.: The Roundness and Microstructure of Thin-wall Bearing Rings, *Manufacturing Technology*, vol. 12, No. 13, 2012, 237-241, ISSN 1213-2489.
- [8] KONAR, R., PATEK, M., MICIAN, M.: Experimental Measurements and Numerical Simulation of Bridge Construction Welding at Low Temperatures, *Communications - Scientific Letters of the University of Zilina*, vol.16, No. 3A, 2014, 130-135, ISSN 1335-4205.
- [9] FABIAN, P., JANKEJECH, P., KYSELOVA, M.: Simulation of Roundness, Hardness and Microstructure of Bearing Rings with thin Cross Sections by using SYSWELD, *Communications - Scientific Letters of the University of Zilina*, vol. 16., No. 3A, 2014, 124-129, ISSN 1335-4205.
- [10] KONAR, R., MICIAN, M.: Numerical Simulation of Residual Stresses and Distortions in butt Weld in Simulation Programme SYSWELD, *Communications - Scientific Letters of the University of Zilina*, vol. 14, No. 3, 2012, 49-54, ISSN 1335-4205.

Andrej Novak - Maria Mrazova *

RESEARCH OF PHYSIOLOGICAL FACTORS AFFECTING PILOT PERFORMANCE IN FLIGHT SIMULATION TRAINING DEVICE

Physiological factors can easily affect a pilot performance and jeopardise the safety of the flight. Therefore, the research is based on the observation of student pilots' decision making and flying abilities during different flight conditions predetermined for the flight in simulation training device. The use of flight simulation training device is helpful as it is possible to vary flight parameters and consequently observe the pilot's reactions to different situations. The combination of pilot error statistics and subjective questionnaire enable to determine the influence of external conditions on the pilot's psychological state and subsequent performance during critical flight tasks.

Keywords: Training, fatigue, pilot performance, simulation training device.

1. Introduction

Many health factors and physiological effects are linked with flying. Some of them are minor, whilst others require a focus of attention in order to ensure safety of the flight. Moreover, there are a large variety of factors that may cause unsafe behaviour that will cause unsafe flight operations. Most of the worst pilot performances that still occur are attributed to human errors and therefore it is inevitable to analyse human error, workload, stress and other physiological conditions and their relationship with pilot performance during flight tasks [1]. Generally, the human being is most reliable under adequate levels of workload that do not change suddenly, unpredictable and immediately when the workload is excessive [2]. Errors arise from the inability of the human operators to deal with high information rates that come from the external environment [3].

1.1 Influence of physiological factors on pilot performance

For the purpose of this research, we focus on the performance measurements monitoring pilot behaviour during changing predetermined physiological conditions in order to seek and determine the level of successful or unsuccessful flight tasks.

Moreover, workload for a pilot varies due to the diverse features of the flight - different phases of flight represent different workloads for the pilot. For instance, Instrument Flight Rule (IFR) flight creates significantly higher workload than Visual

Flight Rule (VFR) flight. Also, pilots show higher workload for the Take-off phase or Landing phase compared to Cruise or VFR flight phase. Indeed, workload is modified further through other factors that are not under the control of the flight crew, such as weather conditions, visibility, traffic density or even communication requirements [4]. However, physiological factors may cause change and degradation of basic cognitive abilities and it can also degrade the pilot's rational thinking and concentration that lead towards higher error rate during the flight [5]. On the other hand, it also requires the ability of the pilot to depersonalise himself from the adverse effects of critical situations and keep a cool mind, clear and correct evaluation of current flight situations. The influence of those factors prolongs the reaction time that is linked with later pilot performance of checklist and it also increases the number of pilot errors [6].

This paragraph deals with measured physiological and psychological factors, such as heat, noise, hypoglycaemia and fatigue. These factors were chosen due to the fact that it is easy to activate them with the FSTD environment in simulation training devices. During the 24 hours prior to blood sugar measurement, the pilots had a limited consumption of sugar and they also started without food-intake. Moreover, blood sugar was measured, where specific values of all pilots are illustrated in the following subchapters and the impact of this factor on the ability and flight control accuracy during the final landing phase is detailed. The impact of noise was simulated by enhanced engine sounds and by ongoing communication (radio chatter) from the ground air traffic control. Pilot workload was increased by the need to confirm the dispatcher's instructions. Moreover, any phase of

* Andrej Novak, Maria Mrazova

Air Transport Department, University of Zilina, Slovakia
E-mail: andrej.novak@fpedas.uniza.sk

flight is accompanied by noise, especially during take-off phase and also during the landing, by use of the thrust reversers. Fatigue measurement was performed after high physical and mental pilot workload (was simulated after at least 24 hours conditions based on continuous wakefulness) which caused the individual's lower concentration during flight tasks and it also delayed responses during simulated crisis situations. In the case of heat measurements and their impact on pilot performance we used environmental conditions based on increased air temperature inside the FSTD cockpit temperatures of circa 47°C with the aid of an external 9kW heat exchanger normally used for heating the air of the engine during the winter season.

2. Research methodology

Flown trajectory

For the purpose of pilot performance measurements using an FSTD we chose ILS approach procedure at the airport Zilina - Dolny Hricov (LZZI) for runway 06 as the base procedure during which the measurement will take place. This procedure was chosen for several reasons. Firstly, in this procedure there are segments with prescribed flight altitude and final approach segment with a clearly defined glide path angle allowing measurable deviations from both the glide slope and localizer. This will allow well-defined, measurable parameters for evaluation of performance. Secondly, majority of the pilots surveyed in this activity are familiar with this procedure, as they are actively flying this approach procedure during their training at the Air Training and Education Centre of the University of Zilina and often perform these approaches during their active career. Therefore, this procedure eliminated varying efficiency due to unfamiliarity with the approach procedure i.e. any learning effect. Lastly, the procedure is not monotonous, and by its nature every precision approach procedure produces significant load on the pilot.

Every consequential approach was followed by missed approach procedure, as published in the approach chart. It eliminated the documentation required for the flight to a single chart, linking the approach procedure with the missed approach.

2.1 Procedure for objective measurement

Measured variables

For the purpose of objective measurement without being influenced by changes in other external factors, it was necessary to find appropriate variables that are only affected by the measured physiological influence and the resulting pilot state.

Three variables were created and they were based on the number of pilot errors in the flown segment. The first variable is measured at relatively lower workload. It is the number of

exceedance of the assigned flight altitude by more than 100 feet¹ (ft) in the outbound segment of initial approach after crossing the NDB - non-directional radio beacon ZLA to the final approach point. The measurements were carried out in 10-second intervals in order to also capture the deviation length.

The second variable measured at lower workload is the number of speed exceedance greater than 10 knots. The assigned speed for this segment is 200 knots and measurements were carried out at 10-second intervals. The third measurement was carried out in the time of high workload during the approach for landing. The measured variable is the deviation from the glide path (G/S) by more than one dot on the indicator. This deviation was monitored at intervals of 100 ft in height, and from 3900 ft to 1700 ft. Similarly, the fourth variable was measured simultaneously in the same phase, it was characterised as a departure from the lateral guidance (LOC) by more than one dot on the indicator. This deviation was monitored at intervals of 100 ft in height, and from 3900 ft to 1700 ft. The last measured variable was deviation from the reference airspeed of more than 10 knots, where the assigned airspeed for the purpose of measuring was set to 140 knots. This deviation was monitored at intervals of 100 ft in height, and from 3900 ft to 1700 ft.

Processing of measurement

The measurement was processed by statistical methods. We used the mean that was obtained by dividing the sum of observed values by the number of observations. For each pilot (pilot 1, 2, 3, 4, 5, 6 and 7) we count the mean for each factor (reference², hypoglycaemia, fatigue, heat and noise). Consequently, we count the average for all the data that was obtained for a particular influence.

3. Research outcomes

As mentioned above, the subjects of our research were seven pilots with different amount of flying hours. The flight was evaluated in 2 phases - initial and intermediate approach segment and also final approach segment. An instructor was monitoring the student pilot's behaviour during selected flight phases where external factors were changed after every 5 final approaches. For each physiological factor we count the average values that provide us with factors that have the most severe impact on the pilot performance during the flight tasks (Table 1).

¹Feet (ft) - a unit of length. It makes 0.3048 meters.

²Reference - for the purpose of this research, reference means the flight without any external conditions that could have any impact on pilot performance.

Illustration of the total average values related to external researched factors [author]

Table 1

Influence	Altitude	Airspeed	ILS	Total average
Reference	1.90	1.36	2.10	5.36
Noise	1.94	1.82	2.97	6.74
Hypoglycaemia	3.06	3.00	3.97	10.03
Heat	2.03	2.29	6.69	11.00
Fatigue	2.17	1.17	8.69	12.03

Reference column represents average number of pilot errors during the whole measurement cycle without any aggravated conditions for the selected flight task. Consequently, other columns (Noise, Hypoglycaemia, Heat and Fatigue) represent an effect of changing aggravated conditions that has different impact on the pilot performance during the intermediate and final approach. Following Fig. 1 we can see that the highest impact of fatigue factor that was mostly visible during ILS approach linked with deviations from the flight altitude by more than 100 feet and it was also followed by deviations from the specified airspeed - by more than 10 knots.

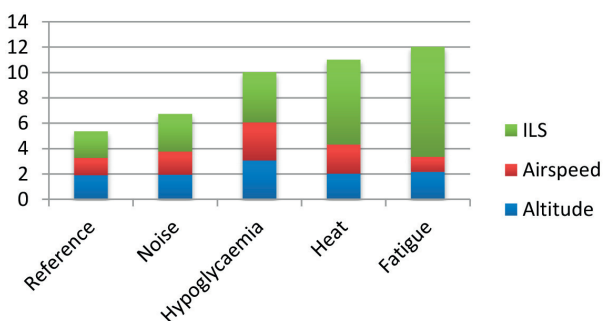


Fig. 1 Illustration of researched physiological factors [author]

NOTE:

All figures have the same graphical structure that is based on these characteristics: the x-axis represents researched physiological factors (reference, noise, hypoglycaemia, heat and fatigue), whereas the y-axis shows number of pilot errors.

In addition, Figs. 2, 3 and 4 represent three researched parameters that were regarded (altitude, airspeed and ILS). As can be seen in Fig. 2, according to Altitude parameter it is obvious that many pilot's errors were made due to the hypoglycaemia effect. Figure 3 illustrates that Airspeed parameter shows the same hypoglycaemia effect. According to Fig. 4 we can see that ILS parameter (sum of glide path errors, localizer errors and air speed errors) in the final approach segment was mostly influenced by the fatigue factor. Today, the issue of fatigue is still being argued and therefore this research also concentrates on this parameter as one of the serious problems in an effort to decrease the risks associated with it.

Altitude

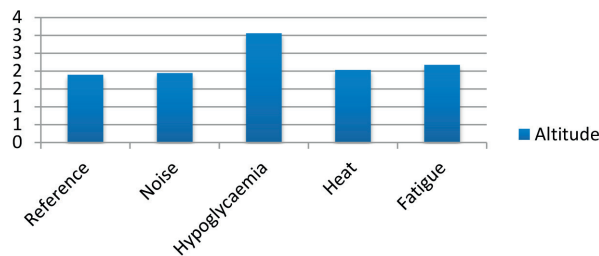


Fig. 2 Impact of physiological factor on Altitude [author]

Airspeed

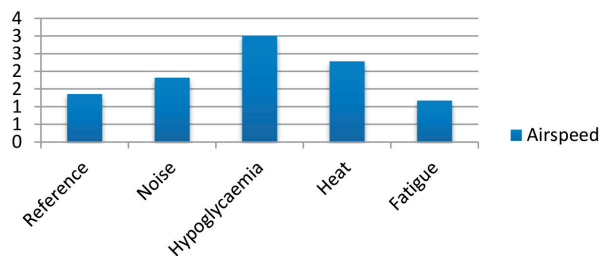


Fig. 3 Impact of physiological factor on Airspeed [author]

ILS

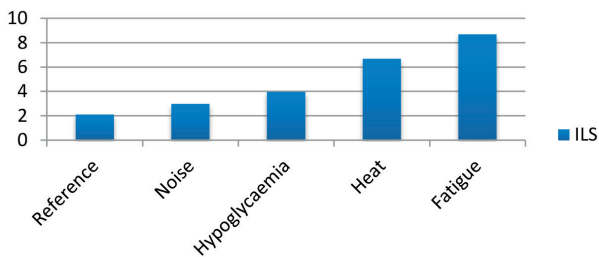


Fig. 4 Impact of physiological factor on ILS [author]

Moreover, Pilot 1 has about 300 flying hours and as can be seen in Fig. 5, the most significant factor that influenced Pilot 1 during the flight tasks was fatigue mainly during the final approach segment (ILS parameter). The Pilot's errors related to Airspeed parameter were influenced mostly by the noise factor and Altitude parameter was affected by the fatigue factor.

Furthermore, Pilot 2 has about 50 flying hours and his flight tasks was influenced during the final approach segment, similarly to the case of Pilot 1, by the fatigue factor. Consequently, Altitude parameter was affected in the same way by hypoglycaemia and noise factors. Equally, Airspeed parameter was influenced by the noise factor as in the case of Pilot 1.

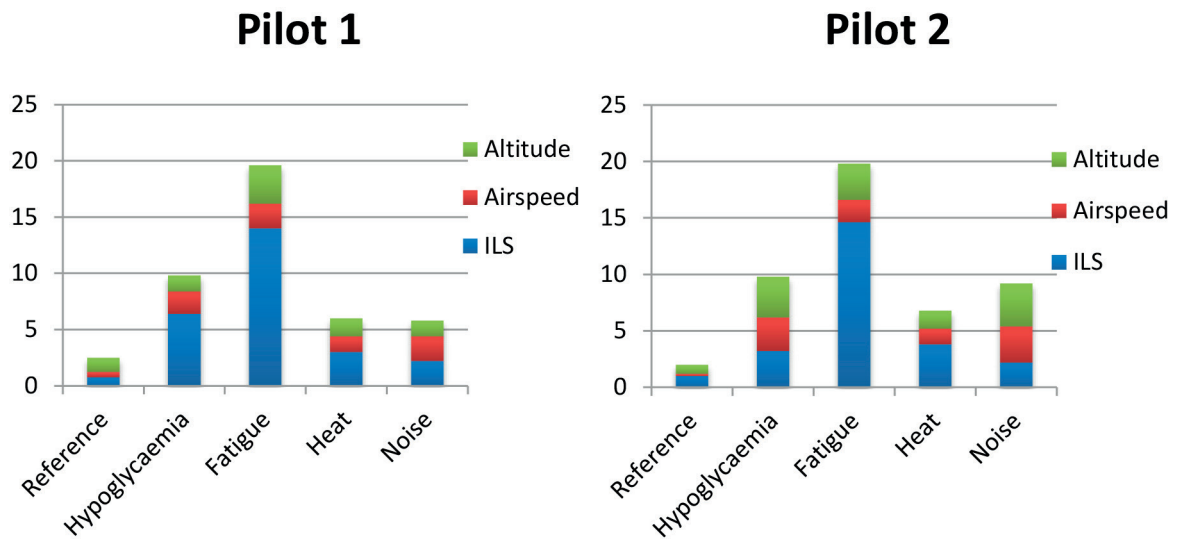


Fig. 5 Illustration of physiological factors' impact on performance related to Pilot 1 and Pilot 2 [author]

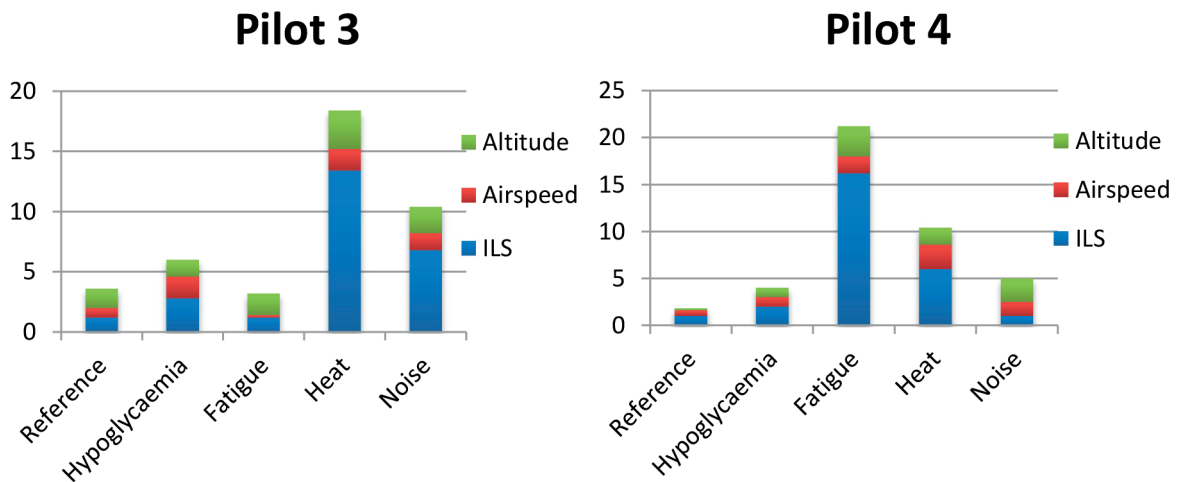


Fig. 6 Illustration of physiological factors' impact on performance related to Pilot 3 and Pilot 4 [author]

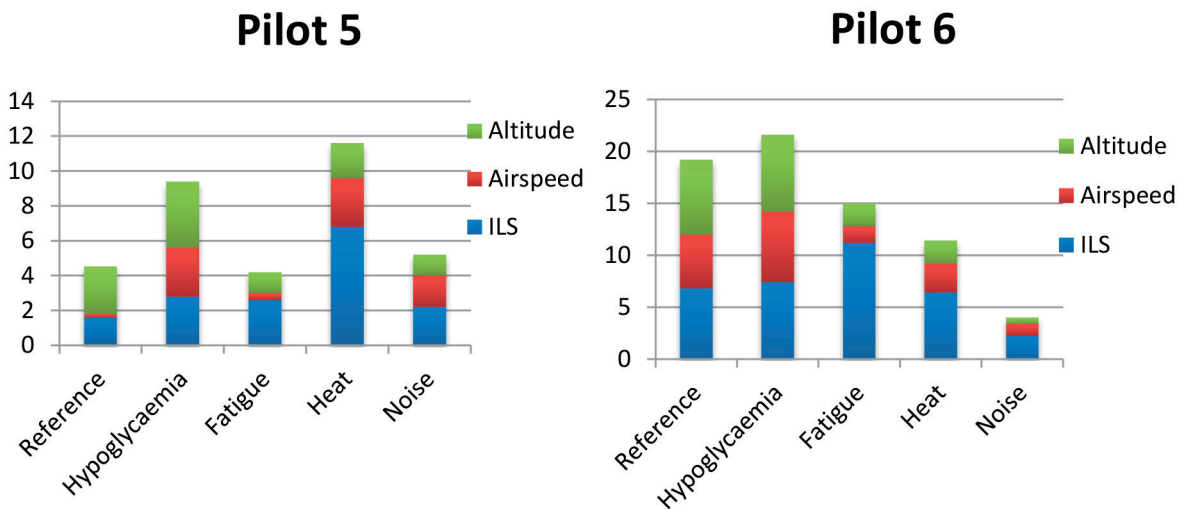


Fig. 7 Illustration of physiological factors' impact on performance related to Pilot 5 and Pilot 6 [author]

Figure 6 illustrates the performance of Pilot 3 and Pilot 4. In the case of Pilot 3 (about 150 flying hours) it is evident that the most significant impact was caused by the heat represented by ILS and Altitude parameter, while Airspeed parameter was mostly influenced by the hypoglycaemia factor. Pilot 4 has about 160 flying hours and his performance was mostly influenced by the fatigue factor during the final approach segment. Also, the pilot has many errors due to the heat factor (when Airspeed parameter was researched) and Altitude parameter was influenced mostly by the noise and fatigue factors.

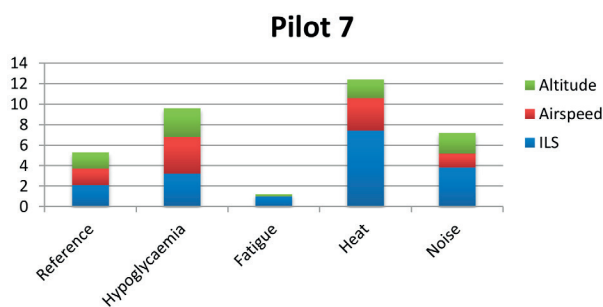


Fig. 8 Illustration of physiological factors' impact on performance related to Pilot 7 [author]

Figure 7 illustrates the performance of Pilot 5 and Pilot 6. Firstly, Pilot 5 has about 160 flying hours and ILS parameter was mostly influenced by heat factor while altitude parameter was mostly affected by hypoglycaemia effect. Besides, Pilot 6 has about 155 flying hours and in this case ILS parameter was mostly influenced by fatigue factor while altitude parameter was affected by the hypoglycaemia factor. Pilot 7 has about 45 flying hours and his performance was mostly influenced by heat factor whereas Altitude and Airspeed parameters were affected by the hypoglycaemia factor, as can be seen in Fig. 8 above.

4. Conclusion

Firstly, this research has shown that the most significant impacts were caused by the fatigue and hypoglycaemia factors. The other selected factors had just minor impact on the pilots' performance. We can also see that pilots' errors were most notable during the final approach segment where the ILS parameters were studied. Moreover, all measurements and their related features were measured during 6 months in an attempt to characterise different individual mental states of the tested student pilots and also in order to estimate the activity of the central nervous system (CNS) related to the defined flight tasks.

Secondly, the pilot's performance decrements resulted more from inadequate interface than from a depletion of mental resource. Moreover, it is necessary to realise that the pilot has to hold a large amount of important information in his working memory while attending to another task, such as answering a radio call and this is indicative of a mental workload problem. During our research it often happened due to the fact that pilots were required to do a flight task that was not expected. As the pilots were selected according to different amounts of flying hours, our research does not confirm that the number of pilots' errors is proportional to the number of flying hours, but it unfolds from the physical and mental conditions of the pilot.

In brief, practical contribution of this research offers another possibility to extend the group of studied physiological and psychological factors, such as heart rate, mental fatigue or drowsiness in order to improve the safety of flight operations.

Acknowledgement

This paper is published as one of the scientific outputs of the project: "The research on virtual reality elements application: the significant improvement of simulator performance characteristics", ITMS: 26220220167".



References

- [1] ENDSLEY, M.: Measurement of Situational Awareness in Dynamic Systems. *Human Factors* 37 (1), p. 33, 1995.
- [2] GANDER, P. H., NGUYEN, D., ROSEKIND, M. R., CONNELL, L.J: Age, Circadian Rhythms, and Sleep Loss in Flight Crews. *Aviation, Space and Environmental Medicine* 64 (3), pp. 189-190, 1993.
- [3] YEH, Y. Y., WICKENS, CH. D.: Dissociation of Performance and Subjective Measures of Workload and Performance. *Human Factors* 30, pp. 678-679, 1988.
- [4] WILSON, G. F.: Air-to-ground Training Missions: A Psychophysiological Workload Analysis. *Ergonomics* 36 (9), pp. 1072-1073, 1993.
- [5] BENO, L., BUGAJ, M., NOVAK, A.: Application of RCM Principles in the Air Operations, *Communications - Scientific Letters of the University of Zilina*, vol. 7 (2), 24 p., 2005.
- [6] BORGHINI, G., ASTOLFI, L., VECCHIATO, G., MATTIA, D.: Measuring Neurophysiological Signals in Aircraft Pilots for the Assessment of Mental Workload, Fatigue and Drowsiness. *Neuroscience and Biobehavioral Reviews*, pp. 3-5, 2012.

Karol Grondzak - Juraj Branicky *

ON THE OPTIMAL PIN SET GENERATION

Security of the information is one of the recent topics, attracting attention of security professionals as well as common people. With deep penetration of electronic devices into our everyday life the challenge to protect our privacy is increasing. Simple mechanism for authentication is shared secret in the form of password. In this paper we describe a method for generating a set of passwords in the form of Personal Identification Number (PIN), which can be used to provide an authentication mechanism for simple electronic devices with limited input possibilities.

Keywords: Information security, PIN code generation, maximum clique, genetic algorithm.

1. Introduction

Information is the value of today. We experience a deep penetration of modern information and communication technologies into our everyday life. With this, electronic crime is a serious threat. Smart phones, tablets and similar devices contain a lot of sensitive data about their owners. The protection of privacy has become a serious topic for electronic devices manufacturers.

There are different levels of security depending on the sensitivity level of protected information. For very sensitive, personal data the highest levels of security should be applied. For such purposes special cryptographic tokens are available.

On the other hand there are situations, when some kind of authorization is requested, but the security hazard is not very high. As an example let us consider a shared office printer. Many employees share the printer and some of the print jobs are not to be seen publicly. In such case it could be possible to add a security feature to the printer. A print job can be assigned some authorization code and only upon typing this code on the printer keyboard the job would be printed. The same mechanism could be used to protect an access to some special features of the printer. Modern office printers can serve as copy machines, fax machines, etc. If the management wants to restrict access to these services to a limited set of employees, the password protection is one of the possible mechanisms. The easiest way is to assign each employee unique secret information, which can identify her/him. Because of the limits of the input device capabilities usually the password has to consist of digits only. Such password is known as a Personal Identification Number (PIN).

Another example of PIN application for authentication is the access to land lines from company's private telephone network. If there is a request for different levels of landline access - e.g. limit the access to the local telephone network, or allow a long-distance calls, some kind of authentication mechanism is required. Then the access to landline is granted only after entering the authentication code (PIN).

This simple form of authentication exhibits several security risks. Let us consider two different cases. In the first case we consider that above mentioned authentication mechanism is used in a hostile environment, e.g. there are persons who want to gain illegal access to the services of electronic device, or to the information stored in it. In the second case we consider friendly environment, without illegal attempts to break into device.

In the case of hostile environment, the attackers' strategy can be to simply try different values of the PIN until they succeed. If there is no measure applied, the attackers sooner or later succeed in their attempts.

The second case might seem to be without security risks, but there is at least one. If the user of electronic device enters by mistake some misspelled PIN and this value would be evaluated by device as a valid code, then access to a protected resource can be granted to a person who is not allowed to use it. Primary goal of this paper is to demonstrate a method, how to avoid such a situation.

According to the best authors' knowledge this problem has not been solved yet. Our approach to use graph theory and maximum clique algorithm presents a unique and new idea to tackle this problem.

* Karol Grondzak, Juraj Branicky
Faculty of Management Science and Informatics, University of Zilina, Slovakia
E-mail: Karol.Grondzak@fri.uniza.sk

2. Formulation of the problem

For the purpose of this paper, we will consider that electronic device is equipped with some input device (e.g. keyboard), with limited number of characters (e.g. cellular phone keyboard). Let us denote the set of characters, which can be entered on the keyboard as:

$$\mathbf{S} = \{s_0, s_1, \dots, s_{k-1}\}, \quad (1)$$

where s_i is i -th character and k is number of different characters, available on the keyboard. Then the set of all available PIN codes of length n can be constructed by Cartesian product:

$$\mathbf{P} = \mathbf{S}^n = \underbrace{\mathbf{S} \times \mathbf{S} \times \dots \times \mathbf{S}}_n. \quad (2)$$

Number of available PIN codes is then given by the size of set \mathbf{P} :

$$N_p = |\mathbf{P}| = |\mathbf{S}|^n, \quad (3)$$

and the elements of set \mathbf{P} are in the form of n -tuples:

$$\mathbf{p} = \{(s_1, s_2, \dots, s_n) \mid s_i \in \mathbf{S}, i = 1, 2, \dots, n\}, \quad (4)$$

If all possible PIN values were assigned to the users, then any mistake when entering PIN code leads to granting access to protected resource. It would mean that any entered PIN code is valid and simply hitting neighboring key by chance would mean wrong user identification. It is not acceptable in situations when correct user identification is important, e.g. when the management wants to keep track of how many pages were copied by the particular employee. To reduce this possibility, only subset of all possible PIN codes should be assigned to the users. Such subset can be generated by the following procedure.

Let us consider a set of PIN values, defined by (2). To decrease the possibility of incorrect user identification caused by entering value of PIN code assigned to another user, we want to choose only subset of that set. The requirements on the subset are:

1. PIN codes in the selected subset should minimize the possibility of incorrect user identification,
2. subset should contain as many PIN codes as possible while preserving previous requirement.

To meet the first requirement, we need a qualitative criterion according to which we choose elements of the subset. We want to avoid the possibility that mistyped value of PIN code is recognized as correct one. This will happen when two PIN codes are "similar" to each other, e.g. when they differ only in one digit and these digits are close on the keyboard. One can easily see that it is relatively easy to enter PIN code 1112 instead of 1111, if keys 1 and 2 are close on the keyboard. It is much more difficult to hit by mistake key 9 instead of key 1 than it is for key 2. To formalize this empiric observation, we proposed to define a metric for PIN codes, based on the distance between characters of the input device.

This metric is defined such a way that it would help us to compare the PIN codes when constructing their subset. We start with metrics of single character and then we expand it to the whole PIN code. Let us denote the distance of two characters:

$$d_s(s_i, s_j), \forall s_i, s_j \in \mathbf{S}. \quad (5)$$

Then distance of any two PIN codes, defined by (4) is:

$$d(\mathbf{p}_i, \mathbf{p}_j) = \sum_{m=1}^n d_s(s_m^i, s_m^j), \forall \mathbf{p}_i, \mathbf{p}_j \in \mathbf{P}, \quad (6)$$

where s_m^i is m -th character of the PIN code \mathbf{p}_i . Having defined metrics, we can transform qualitative requirement that PIN codes in some subset should minimize the possibility of incorrect user identification into quantitative criterion.

Let us choose some minimal value of distance between PIN codes according to defined metrics (6), called threshold (T). We can expect that when we construct subset of PIN codes set such that the distance (as defined by (6)) of any PIN code from all other PIN codes in the subset will equal or will be larger than given threshold T , the possibility of incorrect user identification will be reduced. So we satisfy the first requirement by construction of subset \mathbf{P}_o such that:

$$\mathbf{P}_o = \{p_i \mid p_i \in \mathbf{P} \wedge \forall \mathbf{p}_i, \mathbf{p}_j \in \mathbf{P}_o : d(\mathbf{p}_i, \mathbf{p}_j) \geq T\}. \quad (7)$$

It is obvious that construction of some subset which holds property (7) can be accomplished without any difficulties. The problems will be more difficult if subset with maximum possible number of PIN codes has to be constructed, which the second requirement is.

To make sure that subset with maximum number of elements was obtained, it is necessary to construct all possible subsets of set \mathbf{P} and then find one with maximum number of elements. These subsets form a power set of set \mathbf{P} and it is well known that a superset of some set contains $2^{|\mathbf{P}|}$ elements.

The problem of finding maximum subset of PIN codes can be formulated using the terms of graph theory. Let us construct a weighted undirected graph G :

$$G(V, E), \quad (8)$$

where V is the set of vertices and E is the set of edges. Vertices represent elements of all possible PIN codes of set \mathbf{P} . The graph is complete, e.g. there is edge between any two vertices in the graph. Edges are weighted by the value of distance of the PIN codes which are connected by the edge.

To construct subset \mathbf{P}_o according to (7), the edges with smaller weight than chosen threshold value T are removed from the graph. Resulting graph G' is in general not complete. To obtain subset \mathbf{P}_o with maximum number of elements, maximal clique of graph G' has to be extracted.

This way we have transformed the problem of determination of optimal PIN set for the task of user identification into a problem of searching for a maximum clique in an undirected graph.

The problem of maximum clique determination is well known NP-complete problem. It is a combinatorial problem which can be solved either by exact algorithm or by different heuristic methods.

Exact algorithm for finding maximum clique in general constructs and evaluates all possible subsets of set P defined by (2). Many techniques have been proposed to reduce the amount of evaluated subsets. Some of them are based on the branch-and-bound algorithm, proposed by Carraghan and Pardalos [1 and 2]. We can mention here the work of Konc and Janezic [3], Ostergard [4] or Tomita and Kameda [5]. For many practical problems the size of the graphs does not allow to apply exact algorithm.

As the maximum clique problem is applicable for many theoretical and practical problems, a lot of heuristic methods were proposed to solve it. We can mention the simulated annealing approach proposed by Geng, Xu, Xiao and Pan in [6], the ant colony optimization approach proposed by Solnon and Fenet in [7] or the genetic algorithm approach proposed by Marchiori [8]. Local search algorithm was proposed by Katayama, Hamamoto and Narihisa in [9]. The published algorithms were tested on DIMACS benchmark set [10], which is available on Internet (<ftp://dimacs.rutgers.edu/pub/challenge/graph/benchmarks/cliq/>). It consists of graphs of different properties concerning the density and maximum clique size. Reference implementation of the exact algorithm is also available for download at DIMACS site.

3. Experimental results

To test the possibility of optimal PIN set generation, we considered the following configuration. The device access to which should be protected by the PIN code is equipped with a simple keyboard containing keys to enter digits from zero to nine (Fig. 1). For simplicity we will refer to each key by the character it is representing, e.g. key with symbol zero is zero character, or zero key, etc. Keys are arranged into two-dimensional lattice. Each key is assigned position in the lattice in the form of tuple describing the row and column of the lattice where the key is located. Upper left corner of the lattice has coordinates $(0,0)$ and they increase in the directions to the right and down. To calculate the distance between any two characters on the keyboard we use Manhattan metrics:

$$d_s(s_i, s_j) = |r_i - r_j| + |c_i - c_j|, \quad (9)$$

where s_p, s_j are any characters of the keyboard, r_p, r_j are row coordinates and c_p, c_j are column coordinates of the corresponding characters s_p, s_j respectively.

From (9) it is clear that the distance between digits one and nine is:

$$d(1, 9) = |0 - 2| + |0 - 2| = 4. \quad (10)$$

It is also obvious for the keyboard setup as shown in Fig. 1 that maximum distance between any two characters cannot be

larger than four. The distance for PIN codes of length n can be calculated using above mentioned formula (6) and maximum distance between any two PIN codes, considering keyboard in Fig. 1 cannot be larger than $4n$.

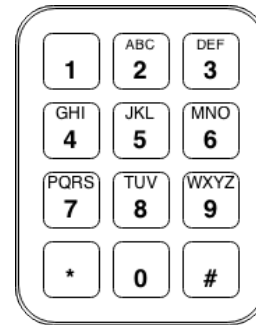


Fig.1 An example of the keyboard configuration

To verify our proposal and to better understand the properties of PIN codes sets, we have experimented with PIN codes of length two, three and four digits. Four digits PIN codes are quite popular for real devices, smaller sizes (two and three) are suitable for verification of the algorithms because of fast evaluation of the cliques.

As was mentioned in the previous paragraph, DIMACS library contains referential implementation of branch-and-bound algorithm. This algorithm was used to evaluate exact solutions for graphs, for which it was possible to find the solution in reasonable time. These results gave us some general information about the properties of graphs, which represent the optimal PIN set problem.

We also experimented with heuristic algorithm for finding maximum clique. We choose the Marchiori's algorithm, which is combination of genetic and simple novel heuristic. The novel heuristic is executed in each step of the genetic algorithm and is based on three steps. In the first step, the relaxation algorithm is executed to randomly enlarge particular solution. Next, there is executed the repair algorithm to extract the clique from the enlarged solution. Finally the extend algorithm is executed to enlarge the clique using simple greedy algorithm. Detailed description of the algorithm can be found in [8].

All experiments were performed on commodity computer equipped with two Intel CPUs (Intel(R) Xeon(R) CPU E5530 2.40GHz) and 4GB of RAM memory and the results are summarized in Table 1. First columns denote the size of the PIN code and the value of the threshold.

Following are the columns describing the properties of the graphs obtained after applying the above described algorithm. As we expected, when the threshold value increases, the amount of edges in graph decreases. Next column represents the minimum value of node degree. It can be seen that for larger thresholds nodes with zero degree appear in the graph. For thresholds

Results of heuristic

Table 1

PIN code size	Threshold Value	Edge count	Min Degree	Count of 0-degree	Max Degree	Density	Exact solution size	Size of the heuristic solution	In iteration	Time to find solution [s]
2	2	4690	91	0	97	0.9475	52	52	4	0.02
2	3	4012	65	0	90	0.8105	15	15	3	< 0.01
2	4	2908	25	0	78	0.5875	10	10	4	< 0.01
2	5	1678	0	1	59	0.3390	5	5	0	< 0.01
2	6	722	0	9	37	0.1459	4	4	0	< 0.01
2	7	208	0	35	16	0.0420	2	2	0	< 0.01
2	8	32	0	75	4	0.0065	2	2	0	< 0.01
3	2	495600	987	0	996	0.9922	N/A	504	10	2.02
3	3	480360	924	0	984	0.9417	N/A	94	210	7.79
3	4	441752	740	0	956	0.8844	N/A	59	570	13.82
3	5	371576	425	0	896	0.7439	N/A	20	157	2.68
3	6	275504	125	0	794	0.5516	15	14	5	0.07
3	7	173976	0	1	644	0.3483	8	8	125	1.78
3	8	90456	0	13	464	0.1811	6	6	5	0.07
3	9	37212	0	76	281	0.0745	3	3	0	0.02
3	10	11440	0	260	134	0.0229	3	3	0	0.03
3	11	2368	0	575	44	0.0047	2	2	0	0.03
3	12	256	0	875	8	0.0005	2	2	0	0.03
4	2	49943000	9983	0	9995	0.9990	N/A	4992	40	1073.07
4	3	49672200	9867	0	9977	0.9935	N/A	605	1327	3752.56
4	4	48746280	9371	0	9925	0.9750	N/A	354	747	870.15
4	5	46432752	8005	0	9790	0.9287	N/A	90	185	87.5
4	6	41968304	5525	0	9502	0.8395	N/A	60	123	38.69
4	7	35097872	2625	0	8962	0.7020	N/A	26	1020	229.55
4	8	26503760	625	0	8090	0.5301	N/A	19	73	14.02
4	9	17672856	0	1	6851	0.3535	N/A	10	937	156.45
4	10	10188920	0	17	5327	0.2038	9	8	28	4.35
4	11	4968168	0	133	3701	0.0994	4	4	0	2.26
4	12	1995400	0	629	2225	0.0399	4	4	13	1.8
4	13	636544	0	1995	1104	0.0127	3	3	2	0.27
4	14	152320	0	4475	424	0.0030	2	2	0	1.97
4	15	24576	0	7375	112	0.0005	2	2	0	1.96
4	16	2048	0	9375	16	0.0000	2	2	0	1.93

smaller than half of the PIN code size minimum degree is nonzero, but significantly larger than the size of found maximal cliques. It means that newly generated graphs are still complex and finding maximal clique by exact algorithm is time consuming procedure. To be able to compare our graphs with graphs contained in DIMACS benchmark set, we have calculated other graphs characteristics, like maximum node degree, number of nodes with zero degree and the graph density.

Finally the last columns contain information about the maximum clique size found by exact algorithm and by a simple genetic algorithm published by Marchiori [8].

Only the results for sparse graphs could be obtained by exact algorithm in reasonable time. Unfortunately these results are not very useful as the resulting cliques are small (only of size of tens). Such small cliques are not sufficient for practical problems when we usually have to assign hundreds of PIN codes for the users.

But the algorithm is useful to verify that heuristic algorithm is working properly.

When comparing the maximum cliques solutions found by exact and heuristic algorithms (when applicable), we can see that the difference between the solution size is mostly zero and in a few cases it is one. This gives us the confidence that heuristic algorithm can give us almost optimal solution in a reasonable time.

Taking into consideration the obtained results, we can conclude that reasonable large set of PIN codes is obtained when the value of threshold is approximately one quarter of maximum possible threshold value. The results demonstrate that for company with several hundreds of employees minimum reasonable PIN code size is four.

4. Conclusions

In this paper, we have presented the problem of finding set of PIN codes for unique user authentication applied for simple electronic device equipped with limited capabilities keyboard. We have proposed a procedure how to obtain maximum possible set of PIN codes by converting the problem into the problem of maximum clique search. As this problem is one of the fundamental and well-studied problems, there are many algorithms proposed to

solve it. In our paper we present the results of two algorithms applied to PIN code of sizes from two to four. Exact algorithm gives result only for sparse graphs and was used to verify the results of the heuristic algorithm. Using simple genetic algorithm, we were able to find maximum cliques for all the PIN code sizes and threshold values.

As a future work, we would like to study the properties of graphs, obtained by the proposed procedure into more details. To be able to obtain solution for larger PIN codes, we plan to parallelize the exact and heuristic algorithms. We also plan to extend our research by applying other maximum clique search heuristics, like simulated annealing, particle swarm optimization or differential evolution.

Acknowledgment

This paper is supported by the following project: University Science Park of the University of Zilina (ITMS: 26220220184) supported by the Research & Development Operational Program funded by the European Regional Development Fund.



References

- [1] CARRAGHAN, R., PARDALOS P. M.: An Exact Algorithm for the Maximum Clique Problem, *Operations Research Letters*, 9, 1990, 375-382.
- [2] PARDALOS, P. M., RAPPE, J., RESENDE, M. G. C.: *An Exact Parallel Algorithm for the Maximum Clique Problem*. High Performance and Software in Nonlinear Optimization, Kluwer Academic Publishers, 1997, 279-300.
- [3] KONC, J., JANEZIC, D.: An Improved Branch and Bound Algorithm for the Maximum Clique Problem, *Commun. Math. Comput. Chem.*, 58, 2007, 569-590.
- [4] OSTERGARD, P. R. J.: A Fast Algorithm for the Maximum Clique Problem, *Discrete Applied Mathematics*, 120 2002, 197-207.
- [5] TOMITA, E., KAMEDA, T.: An Efficient Branch-and-bound Algorithm for Finding a Maximum Clique with Computational Experiments, *J. of Global Optimization*, 37, 2007, 95-111
- [6] GENG, X., XU, J., XIAO, J., PAN L.: A Simple Simulated Annealing Algorithm for the Maximum Clique Problem, *Information Sciences*, 177, 2007, No. 22, 5064-5071
- [7] SOLNON, CH., FENET, S.: A Study of ACO Capabilities for Solving the Maximum Clique Problem, *J. of Heuristics*, 12, 2006, 155-180
- [8] MARCHIORI, E.: *A Simple Heuristic Based Genetic Algorithm for the Maximum Clique Problem*, Proc. of ACM Symp. Appl. Comput.: 366-373, 1998.
- [9] KATAYAMA, K., HAMAMOTO, A., NARIHISA, H.: An Effective Local Search for the Maximum Clique Problem, *Information Processing Letters*, 95, 2005, 503-511
- [10] HASSELBERG, J., PARDALOS, P. M., VAIRAKTARAKIS, G.: Test Case Generators and Computational Results for the Maximum Clique Problem, *J. Global Optim.*, 3, 1993, 463-482.

Lukas Holesa - Karol Hrudkay *

THE IMPACT OF SELECTED FACTORS OF UTILITY MOTOR VEHICLES OPERATION CONDITIONS ON THE ECONOMY DRIVING

Article analyzes the specific conditions of operating commercial vehicles and deals with their influence on the operation economy of a selected vehicle category. The article results are the empirically determined factors of the selected conditions that have the strongest (greatest) influence on variability of the average fuel consumption of selected vehicles. These factors are also supported by appropriate calculations. The next part of the article is creating a regression model through which it is possible to measure the impact of the factor changes on an observed variable.

Keywords: Operational conditions of road vehicles, average fuel consumption, telematics information systems in transport, correlation, regression.

1. Introduction

Within the research and development of intelligent transport systems there is an effort to determine individual groups of factors which affect the final price of transport output the most and which could create complete calculating formula for dynamic illustration of expenses for necessary transport. In this article we focus on specific group of external factors which create surrounding of the vehicle and distinctively affect consumption of fuel within utility vehicles. The aim was to methodically define field of these factors from total volume with documented narrowest connection on operation efficiency of selected utility vehicles and price of transport output.

2. Definition of used means and methods

Expenses on fuel present more than a third of expenses per kilometer and the importance of this item within cost structure of transport companies will be still more significant. Within monitoring of variable costs the largest attention is dedicated especially to them. Transport companies as well as producers of traffic engineering are seeking for constant solutions leading to reduction of fuel consumption and therefore given partial results of research in the area of possible factors on the price of

transporter performance are trying to offer new look on these problems.

After agreement with individual experts from cooperating transport companies, we set range of 8 primary criteria from the previous 36 available where we assumed the strongest connection with operation fuel consumption. For further research of their influence on monitored quantity there were chosen 2 approaches. First called empirical-expert approach (AHP method) determined which of the individual criteria has the largest relative importance on the compared consumption within monitored goods vehicles of the selected category. Second exact approach using methods of mathematical statistics (correlation and regression analysis), measured power of connection among entered variables (selected criteria) in comparison to fuel consumption variable.

2.1 Characteristics of monitored file unit

In order to fulfill target of research, we focused on extraction of required data from vehicle control units, within particular sample. We also used possibilities of telematic applications MAN TeleMatics and OptiFleet. Access passwords were provided by PROCAR a.s. (joint-stock company) and AVEmoto s.r.o. (limited by shares). From the point of statistic file observance there were assured comparable atmospheric-climatic conditions as well as

* Lukas Holesa, Karol Hrudkay
University Science Park of the University of Zilina, University of Zilina, Slovakia
E-mail: holesal@azet.sk

the same technical parameters of the selected vehicles. These were parameters connected with:

- average gross train weight,
- vehicle category,
- vehicle model,
- axles,
- curb weight of the serviceable vehicle,
- capacity weight.

2.2 Description of selected way of observance and obtaining of factors (parameters) within vehicle operation

Current specific solutions of world producers of articulated vehicles enable analysis of selected conditions within vehicle operation during fulfilling of shipping tasks, with provable effect on drive efficiency. According to information outputs of control units, it is possible to monitor and analyze conditions of vehicle operation, as illustrated in the following picture - Fig. 1.

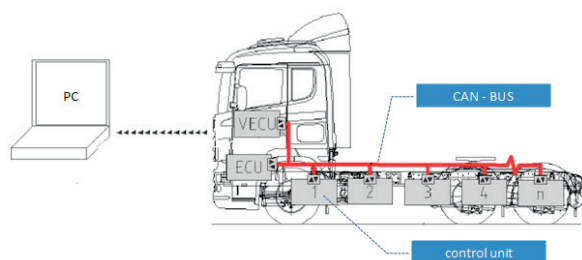


Fig. 1 Transfer data from control units to PC with the appropriate software of the system

Source: Prepared by the author on the basis of the information society as PROCAR and AVEmoto Ltd.

Through MAN TeleMatics and OptiFleet applications it is possible to examine individual statements of vehicle operation (aggregate statement, time statement, statement on fuel consumption, statement of surrounding conditions, statement of recorded data and so on), which are part of company fleet. Microsoft Office Excel is the most suitable way of extraction of the individual parameters of operation in xls format what was enabled only by OptiFleet, whereas using the MAN TeleMatics the necessary data had to be transcribed manually.

2.3 Determination of data files with key parameters of operation on selected sample of vehicles

Information was derived from company fleets and under the conditions described in more details in 1.1 and 1.2 chapters. Specifically it was concerned with 80 vehicles driving on various routes. Following converted statistic operations, file was reduced

to 72 items. Reason of the reduction were some bad numerical values recorded by control unit in certain time intervals of drive. From aggregate statements of vehicles, there were completely exported 42 parameters of operation.

From the point of data inaccessibility to the character of roadway we took into account only parameter of construction condition of roadways, specific altitude profile which is characterized by macro profile of concerned passage of roadway. In order to express average vertical distance and average longitudinal slope of passages within selected routes there were used MapSource 6.13.5 and Map&Guide. Both these software applications are map software which can draw high-altitude profile of route on correspondent base map. Monitored vehicles moved in countries like Slovakia, Czech Republic, Hungary, Austria, Germany, countries of Benelux, and the UK. Values of an average slope within routes were among $<0.2 \text{ }^\circ\text{>$ and vertical distance among $<1.3 \text{ m}>$. We can draw a conclusion that it is a slightly undulated territory.

3. Application of selected mathematical and statistical methods on obtained indices

3.1 Multi-criteria analysis

From all obtained parameters mentioned in 1.3 subhead, selection we worked with was further reduced to 8 key parameters (see Table 1). Selection has been made following the consultations with competent staff (working with given issues) from cooperating companies. In order to express significance of selected criteria on fuel consumption, one of the most suitable methods seemed to be AHP method.

Evaluation criteria for the establishment of matrix Table 1

K1	service break distance
K2	engine brake distance
K3	average driving speed
K4	optimal speed range
K5	average gross train weight
K6	consumption with CC
K7	overrun (proportion of driven distance)
K8	accelerator position

Source: Author

The basis of this method was to record subjectively selected values of significances, which were compared among alternatives for decision matrix. Experts (5 persons) kept at disposal so called descriptors in order to determine preference among compared criteria. Descriptors serve for graduation of significance between each pair of criteria, in case of equal criteria one point is used [1, 2, 3 and 4] and a problem of the same significance is eliminated.

Calculated weight criteria

Table 2

	critierion	product elements	ninth root of product	the final weight criteria
1.	K1	0.0037125	0.571434748862014	0.0607599932490068
2.	K2	4.1184	1.15205404339426	0.122496568573273
3.	K3	20.9454545454545	1.3555295172092	0.144131879411394
4.	K4	2166.66666666667	2.15565477372526	0.229208268764845
5.	K5	2692.30769230769	2.20298971307321	0.23424133789645
6.	K6	0.00005580357142857	0.375548645092112	0.0399316513143662
7.	K7	0.0404040404040404	0.725508457751585	0.0771424717920476
8.	K8	0.237416904083571	0.866066347660978	0.0920878289986174
		$\Sigma =$	9.40478624676862	1

Source: Author

Due to the limitation of article scope, in the following part there will be provided only a table with calculated respective significance weights of the individual criteria (see Table 2).

From the provided review of criteria determination it is clear that the highest priority was assigned to K5, K4 and K3 criteria and the lowest to K6 criterion. The outputs were taken into account in further processes and solutions.

3.2 Partial correlation analysis

Question analysis will serve to consider strength of connection (correlation) among pairs of variables, or one value from the other values [5] from n monitored values (criteria) $X_1, X_2 \dots X_n$ (see Table 1). Firstly, we used multiple correlation in order to find out significances of the individual criteria (variables) on one monitored value of average operation fuel consumption (dependent variable). As in the previous chapter, object of correlation are at the moment only values of parameters obtained from control units (8 criteria from AHP method) [6].

This correlation deals with correlating of one value with other measured values. After unsatisfactory results a partial correlation has been worked out in order to find out so called clear correlation of 2 values eliminating impact of other measured values (other criteria). We used SAS Learning edition 4.1 and Minitab 16.1.0 software for creating correlation matrix and correlograms. In the following pictures (see Figs. 2 - 9) you can see outputs of partial correlation of 8 selected criteria towards monitored value of consumption. As well as in case of multiple correlation we used SAS software.

Pearson Partial Correlation Coefficients, N = 72 Prob > r under H0: Partial Rho=0	
	average operation consumption
engine brake distance	0.15070 0.2308

Fig. 2 Partial correlation no. 1 - engine brake distance

Pearson Partial Correlation Coefficients, N = 72 Prob > r under H0: Partial Rho=0	
	average operation consumption
service break distance	-0.00456 0.9713

Fig. 3 partial correlation no. 2 - service break distance

Pearson Partial Correlation Coefficients, N = 72 Prob > r under H0: Partial Rho=0	
	average operation consumption
overrun (proportion of driven	0.26318 0.0342

Fig. 4 partial correlation no. 3 - overrun

Pearson Partial Correlation Coefficients, N = 72 Prob > r under H0: Partial Rho=0	
	average operation consumption
optimal speed range	-0.22558 0.0708

Fig. 5 Partial correlation no. 4 - optimal speed range

Pearson Partial Correlation Coefficients, N = 72 Prob > r under H0: Partial Rho=0	
	average operation consumption
average driving speed	-0.16122 0.1995

Fig. 6 Partial correlation no. 5 - average driving speed

Pearson Partial Correlation Coefficients, N = 72 Prob > r under H0: Partial Rho=0	
	average operation consumption
consumption with CC	-0.16536 0.1880

Fig. 7 Partial correlation no. 6 - consumption with CC

Pearson Partial Correlation Coefficients, N = 72 Prob > r under H0: Partial Rho=0	
	average operation consumption
average gross	0.46206 0.0001

Fig. 8 Partial correlation no. 7 - average gross

Pearson Partial Correlation Coefficients, N = 72 Prob > r under H0: Partial Rho=0	
	average operation consumption
accelerator position	-0.00204 0.9871

Fig. 9 Partial correlation no. 8 - accelerator position

Individual figures show respective partial empirical correlation coefficients (always the first value in the second column) determined again by point estimates, this time obtained pursuant to the relation 1. It is theoretically assumed with this type of correlation as compared to the previous (multiple) one that Y and Z are some random variables and (X_1, X_2, \dots, X_p) is their vector. The partial correlation coefficient gives here the correlation rate of variables Y, Z with exclusion of the vector effect (X_1, X_2, \dots, X_p) . Further assuming that $(y_1, z_1, x_{11}, x_{21}, \dots, x_{p1})$, $(y_2, z_2, x_{12}, x_{22}, \dots, x_{p2})$, ..., $(y_n, z_n, x_{1n}, x_{2n}, \dots, x_{pn})$ is random selection of range $n \times z(p+2)$ - of random dimensional vector (Y, Z, X_1, \dots, X_p) , that R is empirical correlation matrix of the random vector (X_1, X_2, \dots, X_p) and that r_{YX} is correlation coefficient of variables Y, $X_i (i=1, 2, \dots, p)$, then r_{ZX} is empirical correlation coefficient of variables Z, $X_i (i=1, 2, \dots, p)$. We should further mark line vectors

of empirical correlation coefficients $R(Y, X) = (r_{yX1}, r_{yX2}, \dots, r_{yXp})$, $R(Z, X) = (r_{zX1}, r_{zX2}, \dots, r_{zXp})$ and their column vectors $R(X, Y) = (r_{yX1}, r_{yX2}, \dots, r_{yXp})$, $R(X, Z) = (r_{zX1}, r_{zX2}, \dots, r_{zXp})$, where then r_{YZ} is empirical correlation coefficient of variables Y, Z (see the relation 1).

The second value in the second column represents statistical significance of each criterion (P - value). Same as with multiple correlation, on the grounds of the selected level of significance ($\alpha = 0.05$) those parameters that meet the condition, or can significantly near the selected level of significance, respectively, can be considered statistically significant ($P - value < \alpha$).

Criteria service braking, motor speed range and full load condition (see Figs. 3, 5 and 8) can be considered statistically significant. Compared to the multiple correlation the statistical significance of criteria narrowed from five to three particular criteria. The criterion motor speed range can be to a certain extent arguable, as it remained in the zone of negative correlation ($r_{YZ/X} = -0.22558$) and moves very closely around the selected level of significance (P-value = 0.0708), which is, however, according to [3] still acceptable. As there is a certain linearity of data and acceptable significance achieved, this criterion can be included in the short model of selected criteria. Said negative correlation can be caused by the fact that the percentage share of zone of optimal speed in which the vehicle remained within the whole passed route, was taken into account.

As the good result of the selected correlation we can regard also the fact that coverage of the mentioned criteria has been found out (service break distance, optimal speed range, average gross train weight) within AHP method, where these criteria were assigned a significant importance weight and results of the partial correlation. With the AHP method, said criteria achieved relatively important significance weights, namely criteria such as optimal speed range (0.2292) and average gross train weight (0.2342), representing the highest assigned weights, and the criterion service break distance achieved the value (0.0607) what can be interpreted as not the lowest value reached among the compared criteria (see Table 2). The important thing is that all these three criteria among all 8 criteria within partial correlation appeared as the only statistically significant on the selected α level and reach the closest dependence (relation) with monitored variable (operation consumption) what is proven by their correlation indices (service break distance = $r_{YZ/X} = 0.26318$, average gross train weight = $r_{YZ/X} = 0.46206$ and optimal speed range = $r_{YZ/X} = |0.22558|$) (see Figs. 3, 5 and 8).

$$r_{Y,Z/X} = \frac{r_{YZ} - R(Y, X) \cdot R^{-1} \cdot R(X, Z)}{\sqrt{(1 - R(Y, X) \cdot R^{-1} \cdot R(X, Z)) \cdot (1 - R(Z, X) \cdot R^{-1} \cdot R(X, Z))}} \quad (1)$$

4. Creating of multi-criteria linear regression model according to parameter significances

Only those criteria which reached statistical significance at the selected level of significance such as service break distance, optimal speed range (optimal speed range zone) and average gross train weight (see. partials covariance) were incorporated into the said model. We used Minitab software to create this model (see Table 3).

The output of the software for criteria Table 3

model parameters	values	error of the mean value	Prob> T
limits	23.112	1.442	0.001
par 1	0.12993	0.04464	0.005
par 2	-0.10406	0.01991	0.001
par 3	0.4466	0.07372	0.001
<hr/>			
R ² [%]	76.3		

Relevant model describes approximately 76.3 percent of variability of used data as it is apparent from the value of coefficient of determination. We have not included model with all expert specified criteria (parameters) into the article since it is not relevant from the general point of view. When creating it, we proceeded in a similar way as in regression model. Assumption that after dropping statistically insignificant parameters a coefficient of determination will increase, turned up to be the right one. In outputs where the model included all 8 criteria, it was only at the level R²= 0.49. Statistical significance of the individual regression coefficients (second column Table 3) reflects statistical significance reached within partial correlation of three concerned criteria. It is necessary to mention significant improvement of parameter 2 (optimal speed range) from 0.071 (values reached at regression analysis with all 8 criteria) to 0.001 (see fourth column in Table 3 - P-value). Such process of model creating is generally favorable because of its simple economic interpretation as well as simpler procedures when statistically estimating parameters and testing statistical significance.

According to this output from software (see Table 3), it is possible to construct required regression model containing only three primary key criteria (see relation 2). According to [7, 8 and 9], if value of R² is not below 0.7, given model has not only theoretical meaning but it is also applicable in practice. It is possible to apply within a range of defined parameter values (criteria - operational and road) the created model where a 95 per cent confidence interval was used,

$$y_{PS} = 23.112 + 0.12993x_{1t} - 0.10406x_{2t} + 0.44660x_{3t} \quad (2)$$

Through this model it is possible to empirically compare how value decrease or increase of some parameters affects the

monitored variable. Change of any value has to be within the range of values used for creating of corresponding regression model.

The following relations demonstratively show how the average operation fuel consumption would be changed if average gross train weight increased by 50 per cent in comparison to the former one under the same conditions of other operation parameters as well as routes grade. We can assume from values on route no. 2, which is one of the routes where measured operation data were exported from the vehicle control unit.

$$y_{PS} = 23.112 + 0.610671 - 5.400714 + 8.932 = 27.30 \text{ l/100 km} \quad (3)$$

$$y_{PS} = 23.112 + 0.610671 - 5.400714 + 13.398 = 31.10 \text{ l/100 km} \quad (4)$$

In relation 3 the former values of all three parameters are used and the result differs compared to the real fuel consumption (27.10 l/100km) by 0.20 liter which is deviation of only around 0.73 %. In relation 4 the value of average gross train weight increased from 10t to 30t with remaining conditions constant. As it is apparent from the given relationship, with such change operation fuel consumption would increase to 31.10 l/100 km what represents an increase by around 4.4 liter, so 12.86 per cent. In a similar way we can even empirically present the effect of other 2 parameters (criteria), how a monitored quantity would change at their nominal increase or decrease. The values of all three criteria may be changed but only in a specified range for routes undertaken on flat or slightly undulating territory.

According to the results from calculations, it is possible to say that ridden routes were only on slightly undulating territory (routes going through countries of Central and Western Europe). Therefore we assumed that available parameters of altitude profiles of routes will have an important effect (binding) on monitored fuel consumption what was confirmed when making partial correlation and subsequent attempt to stop the model with particular parameters. From this reason, the appropriate model is not mentioned in the article.

5. Conclusion

According to the results from both selected approaches, we discovered "overlap" of significances in three specific criteria from which a particular model has been built in the mentioned subhead. These are operation factors (criteria) which according to calculated and nominal proven outcomes can be assessed as the factors with the largest effect on operation fuel consumption of vehicles (among all other obtained factors). This influence of selected factors may be also numerically expressed by the said model. The particular model reached average 0.22 per cent deviation among extrapolated and real values of average operation

fuel consumption within selected sample of vehicles. According to subjective opinion of authors as well as opinion of addressed experts (evaluators within AHP method), it is possible to say that this deviation is from the theoretical point of view and also for the carrier himself at acceptable (minimum) level.

In the article we managed to define a small group of external factors proved to have the largest effect on monitored quantity. These factors belong to the whole group of factors which can enter into price for hauling performance.

Acknowledgement

This paper is supported by the following project: University Science Park of the University of Zilina (ITMS: 26220220184) supported by the Research&Development Operational Program funded by the European Regional Development Fund.

References

- [1] KALCEVOVA, J.: *Study Materials - Multi-criteria Analysis (in Czech)*, [elektronicky zdroj], [cit. 2015-02-23], 2008, <http://jana.kalcev.cz/vyuka/kestazeni/EKO422-KriterialniMatice.pdf>.
- [2] FIALA, P. at al.: *Multi-Criteria Decision Making*, VSE : Praha, 1994, ISBN 80-70709-748-7.
- [3] SAATY TH. L., VARGAS L. G., WENDELL R. E.: Assessing Attribute Weights by Rations. *Omega, Intern. J. of Management Science*, vol. 2, No. 1, pp. 9-13, 1983, Priority Setting in Complex Problems. In: Hansen, P.: *Essays and Surveys on Multiple Criteria Decision Making*. Proc. of the Fifth Intern. Conference on Multiple Criteria Decision Making, Berlin/Heidelberg/NewYork : Springer-Verlag, pp. 326-336, 1983., *Axiomatic Foundation of the Analytic Hierarchy Process in Management Science*, 32, No. 7, pp. 841-847, 1986.
- [4] TRIANTAPHYLLOU, E.: *Multi-Criteria Decision Making: A Comparative Study*. Dordrecht : Kluwer Academic Publishers, 2000, ISBN 0-7923-6607-7.
- [5] MARKECHOVA, D., STECHLIKOVA, B., TRPAKOVA, A.: *Statistical Methods and their Applications (in Slovak)*, Nitra : UKF, 2011, 515 p., ISBN 978-80-8094-807- 8.
- [6] STOPKA, O., KAMPF, R., KOLAR, J., KUBASAKOVA, I.: Identification of Appropriate Methods for Allocation Tasks of Logistics Objects in a Certain Area, *Our Sea, Intern. J. of Maritime Science & Technology*, vol. 61, No. 1-2, 2014, ISSN: 0469-6255.
- [7] CHAJDIK, J.: *Statistics Simply - 1st ed. (in Slovak)*, Bratislava : STATIS, 2003, 196 p., ISBN 80-85659-28-X.
- [8] STOPKA, O., KAMPF, R., KOLAR, J., KUBASAKOVA, I., SAVAGE, CH.: Draft Guidelines for the Allocation of Public Logistics Centres of International Importance, *Communications - Scientific Letters of the University of Zilina*, vol. 16 (2), 2014, pp. 14-19, ISSN: 1335-4205.
- [9] STOPKA, O., KAMPF, R. Draft Methodology for Selecting the Appropriate Storage Area Design in Intermodal Logistics Center, *Applied Mechanics and Materials*, vol. 708, 2014, Chapter 5. pp 300-305. ISSN 1662-7482.

Jan Bitta - Irena Pavlikova - Ondrej Zavila - Pavel Platos - Jose Maria Caridad y Ocerin *

DOMINANT AIR POLLUTION SOURCE DETERMINATION IN THE VICINITY OF COKING PLANT BASED ON STATISTICAL DATA ANALYSIS

The goal of the article is to present the statistical analysis based determination of the dominant air pollution sources in one of the Ostrava pollution monitoring stations. Statistical analyses were based on correlation analysis and quantile-based time pattern analysis. These analyses were able to prove that benzene and toluene pollution is dominantly caused by the same pollution sources. The time pattern analysis then proved the dominance of a nearby cokery. Time pattern analyses also proved traffic to be the dominant source of NO_2 pollution and PM_{10} pollution to be the mix of traffic, heating and industrial sources.

Keywords: Air quality, impact, pollution source.

1. Introduction

The Czech Hydrometeorological Institute (CHMI) [1] operates the Ostrava-Privoz air pollution monitoring station. The station is located in a schoolyard in a mixed residential and industrial urban locality (see Fig. 1).

The station measures concentrations of SO_2 , NO_2 , $\text{PM}_{2.5}$, PM_{10} and VOCs. PM_{10} is sampled and analysed for presence of PAHs and heavy metals. It also measures basic meteorological variables – temperature, air pressure, humidity, wind direction and velocity at 2 m above ground.



Fig. 1 Location of the monitoring station, pollution sources direction and median of PM_{10} and benzene concentration [2]

* ¹Jan Bitta, ¹Irena Pavlikova, ²Ondrej Zavila, ¹Pavel Platos, ³Jose Maria Caridad y Ocerin

¹Institute of Environmental Technology, VSB - Technical University of Ostrava, Czech Republic

²Department of Fire Protection, VSB - Technical University of Ostrava, Czech Republic

³Department of Statistics, Econometrics and Operations Research, Universidad de Cordoba, Spain

E-mail: ondrej.zavila@vsb.cz

The Ostrava-Privoz station is at one of the most polluted sites in the Czech Republic. There are above threshold limit concentrations of PM_{10} and benzene. Threshold limits were exceeded every year in the 2007-2013 period [1].

There are several major air pollution sources which may contribute to high air pollutant concentrations. There are industrial sources: OKK Koksovna Svoboda coking plant to the NE, OKK Koksovna Jan Sverma coking plant to the W, BorsodChem chemical plant to the W, domestic heating sources in the vicinity of the station, Hlucinska street to the E with heavy car traffic and an old ecological burden - the Ostramo oil lagoons - to the SW. The site is within the highly-populated industrial Upper Silesian region; therefore, it is also influenced by the variety of both industrial and non-industrial air pollution sources from both Czech and Polish parts of the region.

The air pollution in the measurement site was analysed in several studies which assessed the air quality in the region. Those studies were based on air pollution dispersion modelling. PM_{10} pollution was analysed in the Air Silesia project [3] and the study for the regional council [4]. NO_2 pollution was one of the National Health Institute study's concerns [5]. Results for the Ostrava-Privoz station site are presented in Table 1.

Contribution of pollution sources to the pollutant concentrations in $\mu g/m^3$ [3], [4] and [5] Table 1

POLLUTION SOURCE	PM_{10} [3]		PM_{10} [4]	NO_2 [5]
	Czech Republic	Poland	Czech Republic	Czech Republic
Domestic heating	7.80	6.50	6.56	0.74
Traffic	8.60	0.50	5.53	17.65
Industry	7.84	3.60	8.66	4.10

The validity of such results can be questioned because of input data inaccuracy and model simplifications. That is why the model result verification is crucial. One of the verification possibilities is the statistical analysis of the pollution monitoring data. More details and examples can be found for example in literature [6] and [7].

2. Methods and data - generally

The goal of this work was to perform some basic statistical analyses which would allow determining dominant air pollution sources for each of the studied pollutant - PM_{10} , NO_2 , benzene and toluene.

The correlation analysis allows grouping pollutants which are produced by the same dominant pollution sources. Each

pollution source has its specific temporal pattern which may be also observed in the air pollution data.

The car traffic is characterised by its week-based periodicity. There is high car traffic from Monday to Friday, low traffic on Saturday and slightly higher traffic during Sunday.

Heat sources (domestic heating, central heating, industrial heating, etc.) are characterised by their year-long periodicity with high heat source utilisation during winter, low or no utilisation during summer, and decreasing/increasing utilisation during the transitional months of spring and autumn.

The air pollution data can also be clustered by the wind direction which may give an insight into which direction are the dominant pollution sources [8].

Data for the analysis were collected between the years 2007-2013. The air pollution data were taken from the Ostrava-Privoz air pollution measurement station and meteorological data were taken from the meteorological station in Mosnov which represents the overall meteorological conditions in the region.

3. Methods and data - statistical properties of air pollution data

According to the literature [8], air pollution data have approximately lognormal statistical distribution. Lognormal distribution is not symmetric and can be characterised by one-sided extremely high values.

These statistical properties cause that commonly used arithmetic mean and variance based methods should not be used. That is why an approach based on median-quantile analyses was used in this work.

The statistical distribution can be tested by Kolmogorov-Smirnov tests. For each of the studied pollutant, this test was performed to confirm the lognormal distribution (SW Statgraphics [9]). All tests confirmed the lognormal distribution for all observed pollutants (see Fig. 2).

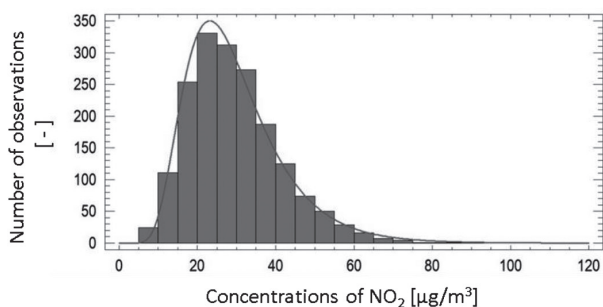


Fig. 2 Histogram of NO_2 concentrations and fitted lognormal distribution

4. Results - Correlation analysis

There were 4 pollutants analysed - PM₁₀, NO₂, benzene and toluene. Correlation analysis confirmed that benzene and toluene are strongly correlated to each other. This means that they share the same dominant pollution sources. This strong correlation is severely weakened from June to August. This suggests the effect of photochemical reactions which mostly occur during those three months when the solar radiation is the strongest. During this period, each pollutant is decomposed at different rates (see Fig. 3). Correlations among PM₁₀, NO₂ and VOCs are lower (0.4-0.6). This suggests different pollution sources that are weighted differently for each pollutant.

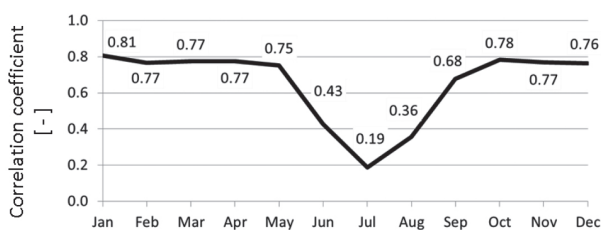


Fig. 3 Correlation relation of benzene to toluene

5. Results - PM₁₀ analysis

The PM₁₀ analysis shows that concentrations were very stable in an annual comparison in 2007-2010 (median 38-38.5 µg/m³). The 2011-2013 values are approx. 10-17% lower (32.2-34.4 µg/m³). This is probably the effect of reduced industrial pollution (cokery batteries modernisation, particulate matter filters in Arcelor Mittal plant, etc.) - see Fig. 4. Monthly-based analysis shows higher and more variable concentrations during winter due to the combination of heat sources' production and occurrence of weather unsuitable for pollution dispersion (see Fig. 5). The analysis of PM₁₀ concentrations clustered by the wind direction shows the presence of an important point source to the NE - OKK Koksova Svoboda cokng plant - and irregular peaks of concentrations from the east caused by particles reemission by car traffic (see Fig. 6).

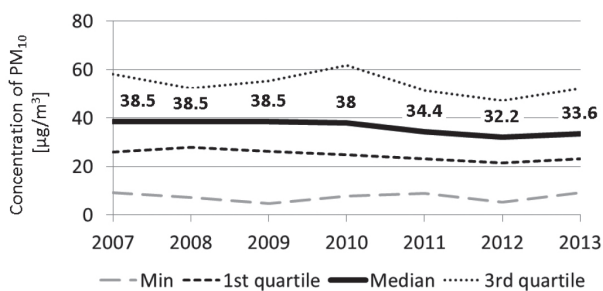


Fig. 4 Analysis of PM₁₀ concentration vs. monitored year

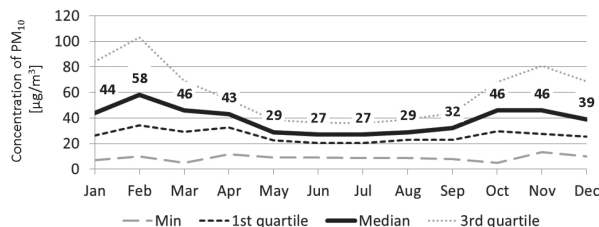


Fig. 5 Analysis of PM₁₀ concentration vs. monitored month

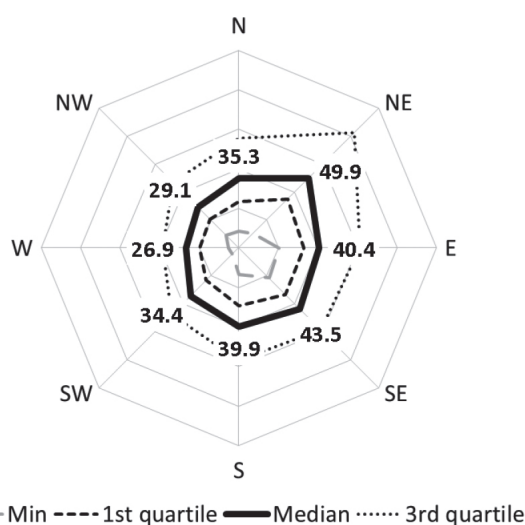


Fig. 6 Relationship of the PM₁₀ concentration [µg/m³] and the wind direction

6. Results - NO₂ analysis

The NO₂ analysis shows that concentrations are falling slightly. It corresponds well with slightly lowering emissions of the car traffic in the Czech Republic (see Fig. 7) [10]. Daily-based analysis shows key effect of the car traffic on the NO₂ concentrations (see Fig. 8). Local frequency of transport can be expressed by number of vehicles that cross the measured region per one day. The latest numbers received in the year of 2010 are:

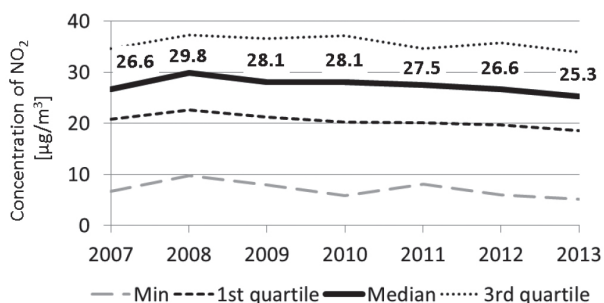


Fig. 7 Analysis of NO₂ concentration vs. monitored year

12613 private cars, 2470 trucks, 536 buses and 129 motor-bikes [11]. Usually, summation of traffic is worked out every five years.

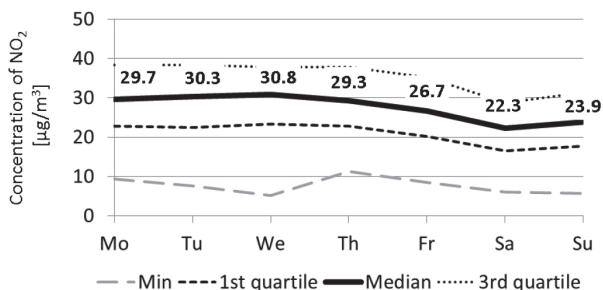


Fig. 8 Analysis of NO₂ concentration vs. monitored day

7. Results - Benzene analysis

The benzene analysis based on monthly comparison shows that in months with the highest solar radiation (May–July), the concentrations drop significantly because of photochemical reactions (see Fig. 9).

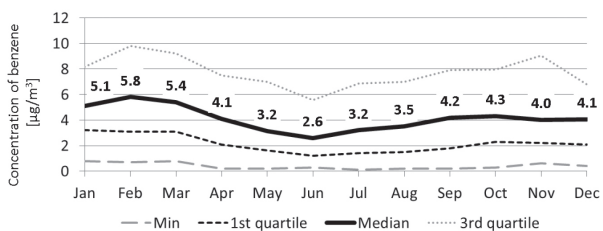


Fig. 9 Analysis of benzene concentration vs. monitored month

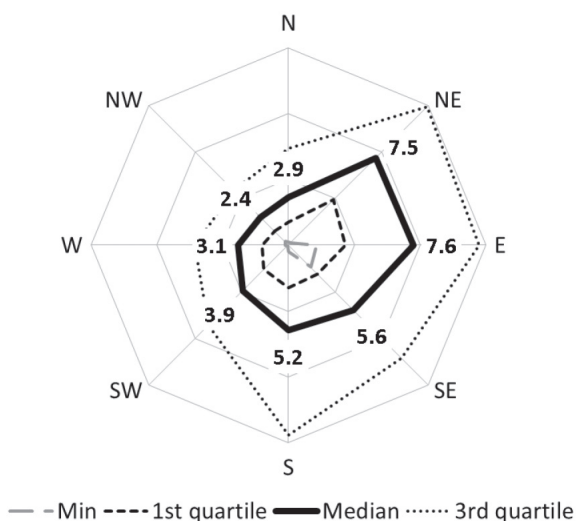


Fig. 10 Relationship of the benzene concentration [µg/m³] and the wind direction

The analysis of benzene concentrations clustered by the wind direction shows the dominance of a point source to the NE – OKK Koksovna Svoboda coking plant (see Fig. 10).

This result is confirmed by the analysis based on annual comparison which shows a steady decline of concentrations and significantly lower values in 2009. This corresponds well with technology improvements in the coking plant and 40% production reduction in 2009 respectively (see Fig. 11).

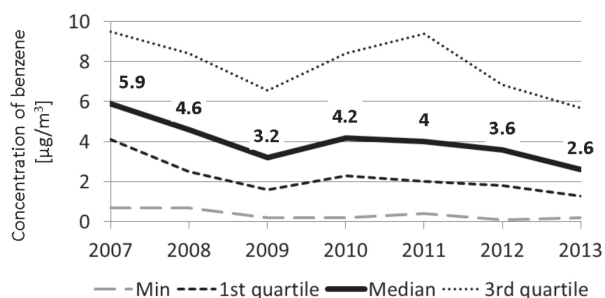


Fig. 11 Analysis of benzene concentration vs. monitored year

8. Conclusion

The correlation and time pattern analyses are simple procedures which may show a presence or a dominance of certain pollution sources.

They may be used for measurement site data analysis and give insight into locally important pollution sources as well as an independent verification method for more detailed air pollution dispersion modelling.

Analyses of the Ostrava-Privoz air pollution monitoring station confirmed the results of the pollution dispersion modelling. PM₁₀ concentrations are the combination of heat sources, car traffic and industrial sources, NO₂ concentrations are dominantly caused by the car traffic, and VOC concentrations are dominantly caused by the OKK Koksovna Svoboda coking plant. Performed analyses do not numerically quantify the influence of certain air pollution sources or their groups. It is to be considered if and how could this approach be further developed to provide such results.

Acknowledgement

This article was financially supported by the Ministry of Education, Youth and Sports of the Czech Republic from the “National Feasibility Program I”, project LO1208 “Theoretical Aspects of Energetic Treatment of Waste and Environment Protection against Negative Impacts”.

References

- [1] Czech Hydrometeorological Institute (CHMI). Columnar Yearbook, [on line], [cit. 2015-2-28], Available at: http://www.chmi.cz/portal/dt?portal_lang=cs&menu=JSPTabContainer/P1_0_Home.
- [2] Google Earth, 2015. Google Earth, [online], [cit. 2015-2-28]. Available at: <http://google-earth.en.softonic.com/>.
- [3] HELLEBRANDOVA, L.: *Information System of Air Quality at Czech - Poland Border in Silesian and Moravian Region (in Czech)*, [online], [cit. 2015-2-28], Available at: http://www.air-silesia.eu/files/file/air_silesia/prezentacje/Informacni_system_kvality_ovzdusi_v_oblasti_Polsko_Ceskeho_pohranici_ve_Slezskem_a_Moravskoslezskem_regionu_projekt_AIR_SILESIA_.pdf.
- [4] JANCIK, P., PAVLIKOVA, I.: Metallurgical Source-contribution Analysis of PM₁₀ Annual Average Concentration: A Dispersion Modeling Approach in Moravian-Silesian Region, *Metalurgija*, vol. 52, No. 4, pp. 497-500, 2013, ISSN 0543-5846.
- [5] HAPALA, P. et al.: *Air Quality Analysis at Ostrava Town and Air Protection Legislature (in Czech)*, [on line], [cit. 2015-2-28], Available at: <http://www.ostrava.cz/cs/urad/magistrat/odbory-magistratu/odbor-ochrany-zivotniho-prostredi/oddeleni-odpadoveho-hospodarstvi-a-ochrany-ovzdusi/analyza-kvality-ovzdusi-v-ostrave/analyza-kvality-ovzdusi>.
- [6] BLAZEK, Z., CERNIKOVSKY, L., KREJCI, B., VOLNA, V.: *The Influence of Meteorological Conditions on Air Quality in the Border Region of Silesia and Moravia - 1st ed. (in Czech)*, Praha : Czech Hydrometeorological Institute, 2013, 182 p. ISBN 978-80-87577-15-8.
- [7] KRYNICKA, J., DRZENIECKA-OSIADACZ, A.: Analysis of variability in PM₁₀ concentration in the Wroclaw agglomeration, *Polish J. of Environmental Studies*, vol. 22, No. 4, pp. 1091-1099, 2013, ISSN 1230-1485.
- [8] United States Environmental Protection Agency (USEPA): *Air Toxics Data Analysis Workbook*, [on line], [cit. 2015-2-28], Available at: http://www.epa.gov/ttnamti1/files/ambient/airtox/workbook/T-Workbook_Secs1-8.pdf.
- [9] Statgraphics Centurion XVII, [on line]. [cit. 2015-2-28], Available at: <http://info.statgraphics.com/statgraphics-home>.
- [10] ISSaR: *Information System of Statistics and Reporting (in Czech)*, [on line], [cit. 2015-2-28], Available at: <http://issar.cenia.cz/issar/page.php?id=500>.
- [11] Road and Motorway Directorate of the Czech Republic: *National-wide Summation of Traffic 2010 (in Czech)*, [on line], [cit. 2015-2-28], Available at: <http://scitani2010.rsd.cz/pages/shop/default.aspx>.

COMMUNICATIONS - Scientific Letters of the University of Zilina Writer's Guidelines

- Submitted papers must be unpublished and must not be currently under review for any other publication.
- Submitted manuscripts should not exceed 8 pages including figures and graphs (in Microsoft WORD - format A4, Times Roman size 12, page margins 2.5 cm).
- Manuscripts written in good English must include abstract and keywords also written in English. The abstract should not exceed 10 lines.
- Submission should be sent: By e-mail - as an attachment - to one of the following addresses: komunikacie@uniza.sk or holesa@uniza.sk (or on CD to the following address: Zilinska univerzita, OVaV - Komunikacie, Univerzitna 1, SK-10 26 Zilina, Slovakia).
- Uncommon abbreviations must be defined the first time they are used in the text.
- Figures, graphs and diagrams, if not processed in Microsoft WORD, must be sent in electronic form (as JPG, GIF, TIF, TTF or BMP files) or drawn in high contrast on white paper. Photographs for publication must be either contrastive or on a slide.
- The numbered reference citation within text should be enclosed in square brackets. The reference list should appear at the end of the article (in compliance with ISO 690).
- The numbered references (in square brackets), figures, tables and graphs must be also included in text - in numerical order.
- The author's exact mailing address, full names, E-mail address, telephone or fax number, the name and address of the organization and workplace (also written in English) must be enclosed.
- The editorial board will assess the submitted paper in its following session. If the manuscript is accepted for publication, it will be sent to peer review and language correction. After reviewing and incorporating the editor's comments, the final draft (before printing) will be sent to authors for final review and minor adjustments
- Submission deadlines are: September 30, December 31, March 31 and June 30.

COMMUNICATIONS

SCIENTIFIC LETTERS OF THE UNIVERSITY OF ZILINA
VOLUME 17

Editor-in-chief:

Prof. Ing. Otakar Bokuvka, PhD.

Editorial board:

Prof. Ing. Jan Bujnak, CSc. - SK
 Prof. Ing. Otakar Bokuvka, PhD. - SK
 Prof. RNDr. Peter Bury, CSc. - SK
 Prof. RNDr. Jan Cerny, DrSc. - CZ
 Prof. Eduard I. Danilenko, DrSc. - UKR
 Prof. Ing. Branislav Dobrucky, PhD. - SK
 Prof. Ing. Pavol Durica, CSc. - SK
 Prof. Dr.hab Inž. Stefania Grzeszczyk - PL
 Prof. Ing. Vladimír Hlavna, PhD. - SK
 Prof. RNDr. Jaroslav Janacek, PhD. - SK
 Prof. Ing. Hermann Knoflacher - A
 Doc. Dr. Zdena Kralova, PhD. - SK
 Doc. Ing. Tomas Lovecek, PhD. - SK
 Doc. RNDr. Mariana Marcokova, CSc. - SK
 Prof. Ing. Gianni Nicoletto - I
 Prof. Ing. Ludovit Parilak, CSc. - SK
 Prof. Ing. Pavel Polednak, PhD. - SK
 Prof. Bruno Salgues - F
 Prof. Dr. Miroslaw Skibniewski, PhD. - USA
 Prof. Andreas Steimel - D
 Prof. Ing. Marian Sulgan, PhD. - SK
 Prof. Dr. Ing. Miroslav Svitek - CZ
 Prof. Josu Takala - SU
 Doc. Ing. Martin Vaculik, PhD. - SK

Address of the editorial office:

Zilinská univerzita
 Office for Science and Research
 (OVaV)
 Univerzitna 1
 SK 010 26 Zilina
 Slovakia

E-mail: komunikacie@uniza.sk

Each paper was reviewed by two reviewers.

Journal is excerpted in Compendex and Scopus.

It is published by the University of Zilina in
 EDIS - Publishing Institution of Zilina University
 Registered No: EV 3672/09
 ISSN 1335-4205

Published quarterly

Single issues of the journal can be found on:
<http://www.uniza.sk/komunikacie>

ICO 00397 563
 August 2015